ALMA MATER STUDIORUM
UNIVERSITÀ DI BOLOGNA

DOTTORATO DI RICERCA IN

AUTOMOTIVE ENGINEERING FOR INTELLIGENT MOBILITY

Ciclo 38

Settore Concorsuale: 09/C1 - MACCHINE E SISTEMI PER L'ENERGIA E L'AMBIENTE

Settore Scientifico Disciplinare: ING-IND/08 - MACCHINE A FLUIDO

DECARBONIZING DIESEL-BASED PROPULSION SYSTEMS: ALTERNATIVE FUELS AND HYBRIDIZATION

Presentata da: Alfredo Maria Pisapia

Coordinatore Dottorato

Davide Moro

Supervisore

Carlo Alberto Rinaldini

Co-supervisore

Enrico Mattarelli

Esame finale anno 2026

Contents

List of figures

List of tables

Acknowledgments

The *Centre of Advanced Powertrain and Fuels* (CAPF) at *Brunel University London, UK*, is gratefully acknowledged for hosting the Ph.D. candidate during his research period abroad and for supporting the development of a dedicated chapter within this thesis.

MathWorks is acknowledged for the MATLAB Academic license granted to the University of Modena and Reggio Emilia.

GAMMA TECHNOLOGIES is acknowledged for the GT-SUITE license granted to the University of Modena and Reggio Emilia.

AVL List GmbH is gratefully acknowledged for granting the AVL FIRE M license to the University of Modena and Reggio Emilia.

Abstract

Meeting climate targets and air-quality standards requires deep, near-term cuts in transport emissions, yet several segments remain hard-to-abate. Heavy-duty and long-haul vehicles demand high energy density, round-the-clock availability and long lifetimes; ultralight aviation faces strict mass and reliability constraints. Full electrification is not always practical on current timescales, and discarding mature internal-combustion technology would ignore decades of proven robustness. This thesis therefore pursues pragmatic engine-centric routes that can be deployed progressively: evolve Diesel architectures with sustainable fuels, with particular focus on hydrogen, and apply hybridization where it meaningfully improves mission efficiency, while keeping performance, durability, and safety margins at the center of design.

The work examines practical, engineering-credible pathways to decarbonize Diesel-based power units across heavy-duty, long-haul, marine, and ultralight aircraft applications. Two complementary routes are pursued within a coherent 0D/1D–3D framework (GT-Power coupled to AVL FIRE-M 3D-CFD): fuel substitution with sustainable alternatives, and hybridization.

At the system level, benchmarking on a 12.9-L heavy-duty platform clarified near-term trade-offs between "drop-in/near drop-in" solutions and redesign. Hydrotreated Vegetable Oil (HVO)/biodiesel behaved as genuine drop-ins in the Diesel configuration, preserving rated power while sustaining high brake thermal efficiency (though the overall decarbonization depends on supply-chain sustainability). Biomethane (CNG) offered clear tailpipe CO_2 advantages in spark-ignited form but at lower rated power and peak efficiency versus the diesel reference. These comparisons mapped the integration envelope for alternatives and motivated a focus on hydrogen as the internal-combustion fuel with the strongest long-term decarbonization potential.

Building on that foundation, the thesis develops and validates a 3D-CFD-guided methodology for diesel–hydrogen Dual-Fuel (DF) operation. After a physically consistent calibration, the study targets the levers that govern high Hydrogen Energy Share (HES) under mechanical and safety constraints (e.g., peak pressure and PPRR in-cylinder limits). The central result is that clever optimization of the diesel injection law, timing, pilot/main splitting, and partial or total suppression of the main, can substantially raise HES while keeping performance near baseline and curbing CO_2 and NO_x. In the conditions explored, controllable heat release rate is maintained even as HES approaches the ultra-high regime (maximum HES = 98%), with the diesel pilot burning in HCCI-like conditions and the overall process following the RCCI behaviour (diesel-hydrogen DF combustion).

To address high-load limitations of DF operation, the thesis culminates in a full-hydrogen, spark-ignited two-stroke concept derived from a production Diesel (Duramax 6.6 L V8) with poppet valves. Tangentially shrouded intake valves and a shallow piston bowl generate strong tumble and high turbulence, improving mixture homogeneity while limiting short-circuiting. Coupled 0D/1D–3D-CFD optimization of gas exchange, scavenging, mixture preparation, and boosting achieves Diesel-comparable full-load performance, near-zero NOx, and high theoretical efficiency, with limited hardware changes (head/piston/valves) that support credible scalability and a favourable technology-readiness outlook.

Looking beyond DF, the thesis developed an ultralight-aircraft Hybrid Power Unit (HPU): a newly designed 2S compression-ignition Diesel (loop-scavenged, supercharged) combined with an axial-flux electric machine and lithium-NMC battery, intended to replace conventional 4S SI gasoline engine (e.g, Rotax 912 ULS/S) with minimal weight penalty and no structural modifications to the fuselage, while operating on Jet-A or diesel fuels. A valveless, dry-sump, air-cooled layout yielded 38.9 kg engine mass (>20 kg lighter than Rotax); overall dry weight exceeded Rotax by only 2–7 kg depending on battery. The engine delivered 68.4 kW @ 4500 rpm with BSFC 230–240 g/kWh (≈–28% fuel vs Rotax). In hybrid use: +6.5% for 5 min (1.4 kWh) or +15% for 5 min (2.4 kWh) respect to the Rotax baseline engine. During cruise at 55–75% the HPU saw –28% fuel consumption, convertible to comparable range gain or ~+30 kg payload. The Estimated CO_2 reductions range from –16% and –37% depending on charging strategy and electricity

Taken together, the results show that decarbonizing Diesel-based power units is feasible through two complementary routes: sustainable fuels (culminating in high/ultra-high hydrogen utilization) and targeted hybridization. The overarching message is evolutionary rather than disruptive: the Diesel engine is not obsolete but a mature, adaptable platform. Re-engineered with advanced simulation, modern combustion strategies, sustainable fuels, and mission-focused hybridization, it can continue to play a relevant, effective role in a lower-carbon mobility landscape across road, marine, and ultralight aviation.

Nomenclature

Abbreviations	
Angle @ 50% of the fuel mass burned	MFB50
Brake Specific Fuel Consumption	BSFC
Brake Thermal Efficiency	BTE
Bottom Dead Center	BDC
Brake Mean Effective Pressure	BMEP
Charging Efficiency	CE
Computational Fluid-Dynamics	CFD
Delivery Ratio	DR
Dual Fuel	DF
Energy Fraction	EF
Electronic Control Unit	ECU
End of Injection	EOI
Exhaust Residual Ratio	ERR
Greenhouse gas	GHG
Heavy-Duty	HD
High-Speed Direct-Injection	HSDI
Hybrid electric Power Unit	HPU
Hybridization Level	HL
Hydrogen Energy Share	HES
Intake Valve Closure	IVC
Internal Combustion Engine	ICE
Late Intake Valve Closing	LIVC
Nikel-Manganese-Cobalt	NMC
Peak Pressure Rise Rate	PPRR
Perfect Displacement	PD
Perfect Mixing	PM
Port Fuel Injection	PFI
Propeller Gearbox	PG
Particulate Matter	PM
Pressure Ratio	PR
Retaining Efficiency	RE
Real Driving Emission	RDE
Scavenging Efficiency	SE
Spark Ignition	SI
Start Of Injection	SOI
Turbine Inlet Temperature	TIT
Turbulent Kinetic Energy	TKE
Technology Readiness Level	TRL
Unburned Hydrocarbons	HC
Unmanned Aerial Vehicle	UAV
Variable Geometry Turbine	VGT
Variable valve actuation	VVA
Volumetric Efficiency	VE
Waste Gate	WG
2-Stroke	2S
4-Stroek	4S
Chemical Formulae	
Carbon dioxides	CO_2

Carbon monoxide	CO
Nitrogen oxides	NOx

Symbols

Air to Fuel Ratio	α
Combustion efficiency	η_c
Crank angle	θ
Engine mean angular velocity	ω_{eng}
Equivalence ratio	ϕ
Mean angular velocity of the in-cylinder flow	ω_T
Relative Air to Fuel Ratio	λ
Specific heat coefficient ratio	k
Stoichiometric Air to Fuel Ratio	α
Supercharging degree	Ψ

Preface

The transition toward sustainable mobility represents one of the most demanding challenges for modern engineering. Within this framework, internal combustion engines remain essential contributors to global transport, powering heavy-duty, marine, and off-road applications where electrification still faces technical and economic barriers. Rather than being discarded, these engines must be reimagined through technological innovation capable of reducing their environmental impact while preserving their intrinsic advantages of efficiency, reliability, and versatility.

This doctoral research, conducted within the PhD programme in *"Automotive Engineering for Intelligent Mobility"* under the project named: *"*Decarbonizing Diesel-Based Propulsion Systems: Alternative Fuels and Hybridization*"*, explores advanced strategies to decarbonize Diesel-based propulsion systems. The work investigates how alternative fuels, hybridization concepts, and unconventional combustion strategies can progressively lower the carbon footprint of Diesel technology and support the transition toward cleaner, more efficient transport solutions. The thesis is therefore focused on the tank-to-wheel perspective, addressing the emissions and performance directly related to the operation of the engine itself.

The research activities were structured around four interconnected studies, each representing a different stage in the technological evolution of the Diesel engine.

The first study investigates a 12.9-L heavy-duty engine originally designed in two versions, Diesel and natural gas, representative of long-haul applications. The analysis evaluates the potential of alternative fuels, including biodiesel, biogas, and hydrogen, as substitutes for conventional Diesel, assessing their influence on engine performance, efficiency, and emissions. The comparative results highlight both the technical feasibility and the environmental benefits associated with these renewable fuels, establishing a baseline for further decarbonization strategies.

The second study focuses on the dual-fuel Diesel–Hydrogen operation. Through a combination of one-dimensional and three-dimensional CFD simulations, the research examines the combustion process, performance, and emission trends when replacing a significant portion of Diesel energy with hydrogen. Particular attention is given to the optimization of the Diesel injection strategy, which is shown to play a crucial role in controlling ignition timing, combustion performances and pollutant formation. The results demonstrate that hydrogen substitution can substantially reduce CO_2 emissions while maintaining comparable efficiency levels to conventional Diesel operation.

Building upon these findings, the third study explores the radical adaptation of a heavy-duty Diesel engine fully converted to operate on hydrogen in a two-stroke configuration. This concept leverages the intrinsic advantages of the 2-stroke cycle (theoretical double power when compared to a 4-stroke engine with the same displacement) to compensate for the performance gap that would otherwise arise when converting a conventional 4-stroke Diesel engine to operate exclusively on hydrogen. The analysis focused on identifying a design capable of delivering performance levels comparable to the original baseline Diesel engine, while taking advantage of the zero-carbon nature of hydrogen combustion with minimal modification of the original engine architecture. Particular attention was given to maintaining low nitrogen oxide emissions through appropriate control of mixture formation and combustion.

The fourth and final study extends the decarbonization concept to the aviation domain. A new two-stroke, air-cooled Diesel boxer engine was designed as the core of a hybrid power unit for an ultralight aircraft. The study compares the proposed configuration with a widely used gasoline competitor, evaluating potential benefits in terms of fuel efficiency, range, and environmental impact. This activity represents the synthesis of the entire research path, combining Diesel efficiency with hybridization and lightweight design principles in a field where energy density and reliability are of paramount importance.

Overall, the thesis provides a unified vision of the Diesel engine as a technology capable of evolving toward carbon neutrality through adaptation rather than replacement. The combined use of biofuels, hydrogen, advanced combustion concepts, and hybrid integration demonstrates that meaningful emission reductions can be achieved without compromising performance or operational flexibility. These results contribute to the ongoing discussion on sustainable propulsion, reaffirming the role of engineering innovation as a driver of realistic and effective decarbonization.

The structure of the thesis reflects the logical progression of this research journey. The first chapter introduces the global context of climate change and transport decarbonization, highlighting the role of Diesel engines and the challenges associated with emissions, regulation, and public perception. The following chapters present the methodologies and findings of each study, organized according to their thematic focus (from fuel substitution and dual-fuel operation to full-hydrogen and hybrid configurations).

Ultimately, this work aims to demonstrate that the Diesel engine is not an obsolete technology, but a mature and adaptable platform that, when reengineered with modern tools and sustainable fuels, can remain a relevant part of the mobility landscape in the decades to come.

1. Introduction

Climate change represents the most pressing global environmental challenge of the 21st century. The continuous increase in global mean surface temperature, primarily driven by anthropogenic greenhouse gas (GHG) emissions, has already altered climate patterns on a planetary scale. According to NASA data, the global average surface temperature has risen by more than 1.2 °C since the late 19th century, with the last decade being the warmest on record since 1880 (see figure 1). Notably, 2024 marked the hottest year ever recorded, further underscoring the accelerating process of global warming that we are now living. This trend is unprecedented in both magnitude and speed when compared to natural variability recorded in paleoclimatic archives.

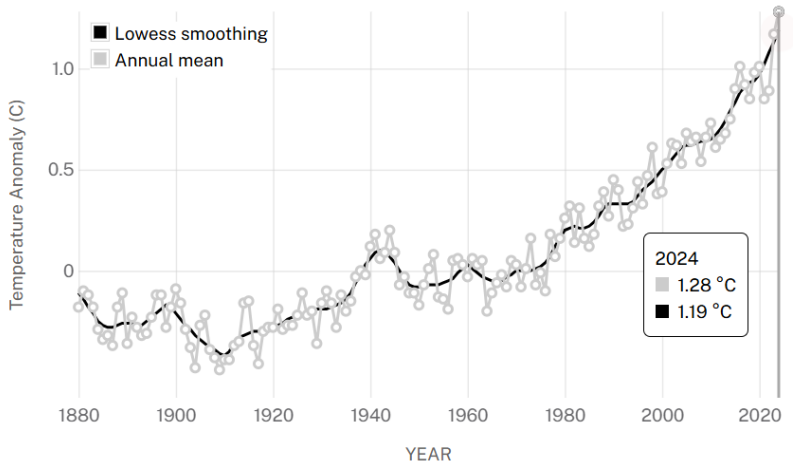

Figure 1. global land-ocean temperature index. Data source: NASA's Goddard Institute for Space Studies (GISS). Credit: NASA/GISS [1].

The warming trajectory is strongly correlated with the sharp increase in atmospheric concentrations of carbon dioxide (CO_2), methane (CH_4), and nitrous oxide (N_2O) since the industrial revolution. As highlighted by Filonchyk et al. in 2024, the combustion of fossil fuels, industrial processes, agriculture, and deforestation are the dominant anthropogenic sources of these gases. CO_2, which accounts for approximately 74% of total emissions [2], has reached atmospheric concentrations exceeding 420 ppm in 2023 [1,3], this human-induced rise is greater than the natural increase observed at the end of the last ice age 20,000 years ago. Methane and nitrous oxide, despite their lower concentrations, have global warming potentials 23 and 296 times higher than CO_2, respectively, further amplifying the greenhouse effect [4].

The enhanced greenhouse effect arises from the ability of these gases to absorb and re-emit infrared radiation emitted by the Earth's surface [5,6]. As a consequence, excess energy is trapped within the atmosphere, perturbing the planetary radiative balance and resulting in global warming. While, as Filonchyk says, natural sinks such as forests and oceans absorb approximately 55% of annual CO_2 emissions, the residual fraction remains in the atmosphere from decades to thousands years [7], ensuring that even immediate emission reductions would not stop warming trends in the short term.

The consequences of this warming are far-reaching. Observations from NOAA confirm an escalation in the frequency and intensity of extreme weather events, including heatwaves, droughts, floods, and tropical cyclones. The cryosphere is particularly affected: Arctic sea ice extent has declined at an average rate of 12.2% per decade since 1981 [1], while mountain glaciers and the Greenland and Antarctic ice sheets are experiencing accelerated mass loss. These cryospheric changes directly contribute to global sea-level rise, currently progressing at a rate of approximately 3.1 mm per year [1,8], endangering coastal infrastructures and ecosystems.

Beyond physical impacts, climate change imposes severe socio-economic challenges. As discussed by Dietz et al. in 2020, the burden of climate change is unevenly distributed, disproportionately affecting low-income regions that contribute the least to global emissions but are the most vulnerable to its effects. This inequity underscores the ethical dimension of climate policy and highlights the necessity of a globally coordinated response [9,10].

The urgency of climate mitigation has driven the global community to establish binding and voluntary agreements[11,12]. The United Nations Framework Convention on Climate Change (UNFCCC), born in 1992, laid the foundation for collective climate action [13]. The Kyoto Protocol (1997) represented the first attempt to impose binding emission reduction targets on developed countries [14], yet its limited participation and scope rendered it insufficient.

A paradigm shift occurred with the Paris Agreement, adopted in 2015 during COP21 [15]. This landmark accord commits all signatory nations to pursue efforts to limit the global average temperature increase to "well below 2 °C" above pre-industrial levels, while striving for a 1.5 °C threshold. Unlike Kyoto, the Paris framework relies on Nationally Determined Contributions (NDCs), allowing countries to tailor mitigation efforts to their socio-economic contexts while providing transparency mechanisms to monitor progress. Despite these advances, current trajectories suggest that existing commitments remain insufficient to meet the 1.5 °C target, necessitating a significant escalation in ambition and implementation.

COP28, held in Dubai in 2023, marked the first official "Global Stocktake" of progress under the Paris Agreement. The outcome emphasized the persistent gap between pledged reductions and the emissions pathways required to achieve climate neutrality by mid-century [16]. The European Union, through its "Fit for 55" package, has set a legally binding objective to cut net GHG emissions by at least 55% by 2030 relative to 1990 levels [17,18]. This policy framework demonstrates the integration of scientific targets into legislative instruments, a crucial step toward achieving long-term decarbonization.

Financial mechanisms are equally essential. The Green Climate Fund, established under the UNFCCC, allocates resources to support mitigation and adaptation initiatives in developing nations. However, despite pledges amounting to USD 100 billion per year [19,20], actual disbursements remain below target, highlighting a persistent gap between commitments and delivery.

The scientific consensus is unequivocal: anthropogenic GHG emissions are the primary driver of observed climate change (IPCC, 2021). Projections indicate that without substantial mitigation, global temperatures could rise by 2.6–3.1 °C by the end of the century [21]. Such warming would exceed adaptation capacities in many regions, leading to irreversible damages to ecosystems, biodiversity, and human societies.

Decarbonization (the progressive reduction and eventual elimination of carbon emissions from human activities) emerges as the cornerstone of climate mitigation. Achieving it requires a systemic transformation of energy, industry, transport, and agricultural sectors. Renewable energy deployment, energy efficiency measures, and carbon capture technologies are already central to national strategies, but their deployment must accelerate dramatically.

In this context, the transport sector deserves particular attention. It accounted for about 8.7 $GtCO_2$-eq in 2019, corresponding to nearly 23% of global energy-related CO_2 emissions [22]. Within transport, road transport is by far the largest contributor, responsible for roughly 70% of these emissions, with passenger cars and freight trucks being the dominant sources, while the remainder coming from aviation, shipping, and rail. In addition, transport emissions have increased by more than 70% since 1990 and, without significant mitigation, are projected to grow by another 16–50% by 2050 [22]. This makes transport not only a substantial contributor to climate change but also a critical area where effective decarbonization policies can deliver meaningful progress.

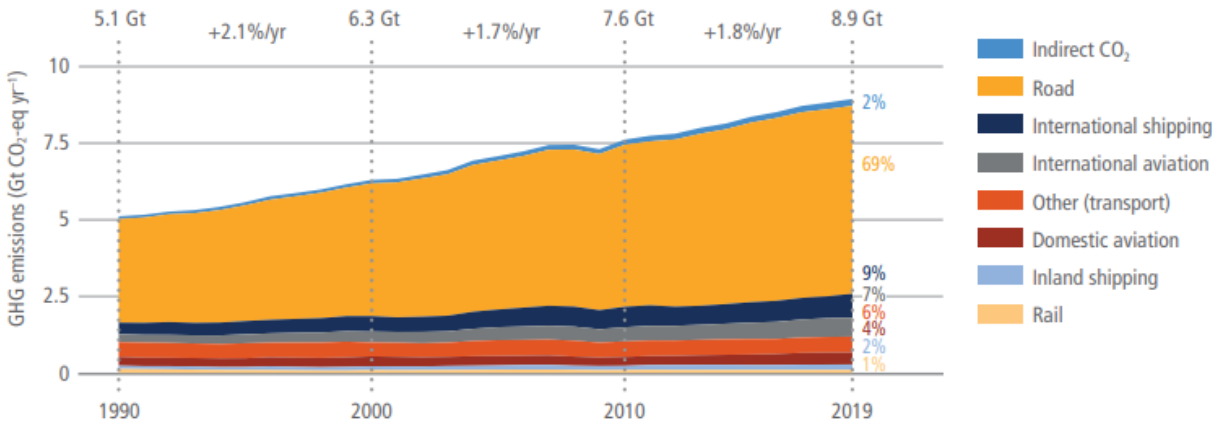

Figure 2 transport global GHG emissions trends [22].

While electrification is advancing in passenger mobility, hard-to-abate sectors such as aviation, maritime, and heavy-duty road transport will continue to rely on combustion-based powertrains in the foreseeable future. This reality emphasizes the importance of exploring hybridization strategies, low-carbon fuels, and innovative combustion concepts as complementary solutions. Addressing transport emissions is thus both an urgent challenge and a strategic opportunity, particularly in the context of internal combustion engines, which are still central to many mobility applications.

Decarbonization is not solely a technological challenge but also a political, social, and economic one. As Dietz argue, transitions are shaped by cultural, institutional, and behavioural dimensions, requiring inclusive governance and equitable policies to ensure public acceptance and global cooperation. Without addressing these systemic factors, technological advances alone will be insufficient to deliver the deep emission reductions required.

1.1. The role of the Diesel engine in automotive and aeronautics sector

1.1.1. Historical and technical relevance of Diesel engines

Since its invention by Rudolf Diesel in 1897, the diesel engine has been one of the cornerstones of modern industrial and transport development. Conceived as a more efficient alternative to the steam engine , the compression-ignition concept quickly demonstrated superior fuel economy and robustness compared to spark-ignition technology [23–25]. These intrinsic advantages soon established the Diesel engine as the preferred solution in applications demanding high durability, reliability, and power-to-fuel efficiency ratios.

During the 20th century, diesel technology underwent continuous refinement. The adoption of turbocharging, originally patented by Alfred Büchi in 1905 and first applied to a large Diesel engine by Brown Boveri in 1924, represented a major milestone, as it allowed a significant increase in specific power by utilizing exhaust gas energy [26–28]. Subsequent innovations, such as direct injection in the 1960s and electronically controlled common-rail systems in the 1990s [29], further boosted efficiency and fuel economy while enabling advanced emission control strategies.

As a result, modern Diesel engines achieve brake thermal efficiencies approaching 47–48% in commercial heavy-duty applications, clearly outperforming the ~30–35% values typical of conventional spark-ignition engines [23]. Recent experimental studies have demonstrated that even higher efficiencies are attainable: the U.S. Department of Energy's SuperTruck II program has set a target of 55% BTE for next-generation heavy-duty engines [30], while Johnson and Joshi (2018) report opposed-piston architectures achieving a BTE of 54.8% under part-load conditions [31]. These results emphasize the unique capability of diesel technology to minimize fuel consumption and CO_2 emissions, consolidating its central role in energy-saving in transport applications.

Beyond efficiency, Diesel engines are renowned for their torque characteristics, delivering high torque at low engine speeds. This makes them ideal for vehicles and machinery operating under heavy load conditions. Their robustness and long service life have further contributed to their global adoption, making diesel engines the backbone of heavy transport, marine propulsion, agricultural machinery, and industrial equipment for over a century.

1.1.2. The role of the Diesel engine in automotive sector

Since their introduction to road transport in the early 20th century, Diesel engines have played a pivotal role in the development of modern mobility and global logistics. Initially confined to trucks and buses, their combination of high fuel efficiency, torque output, and durability made them indispensable for long-distance and heavy-duty applications. As early as the 1940s, Diesel engines had become the preferred powertrain for commercial vehicles, while passenger cars remained dominated by spark-ignition technology. It was not until the 1980s, with the advent of direct injection (DI) and later common-rail fuel systems, that Diesel engines began to penetrate the light-duty market [32].

The introduction of common-rail injection, developed by Denso and Bosch in the 1990s, represented a technological turning point. It enabled precise control of fuel delivery, multi-stage injection, and pressures exceeding 180–200 MPa, significantly improving both efficiency and drivability. By the early 2000s, passenger-car diesel engines were achieving brake thermal efficiencies above 42–43%,

specific power densities of 65 kW/L, and torque levels of 185 Nm/L, rivalling gasoline counterparts while maintaining superior fuel economy. With the evolution of turbocharging, variable geometry turbines, and high-pressure EGR, diesel engines continued to advance; by 2010, peak power and torque densities reached 93 kW/L and 247 Nm/L, respectively[32].

In Europe, these technological gains coincided with favourable tax policies and growing environmental awareness, leading to an unprecedented expansion of the diesel passenger car market. Between 1995 and 2012, diesel vehicles rose from 14.2% to 33.2% in the entire fleet [33,34]. Policymakers and consumers were drawn by the higher efficiency of compression-ignition engines up to 35% more efficient than comparable gasoline engines according to the IPCC Fourth Assessment Report [35], and even 63% higher under certain driving conditions as reported by the U.S. Department of Transportation [32]. However, this growth was not without trade-offs. The higher carbon content of diesel fuel (about 14% more per liter than gasoline) and the rise in vehicle weight and power gradually eroded the CO_2 advantage, which dropped from 5–10% in the 1990s to less than 2% for vehicles registered after 2005.

While the diesel boom in Europe reached its peak in the early 2010s, it has since declined sharply. Stricter emission regulations (Euro VI), the aftermath of the Dieselgate scandal, and the acceleration of hybrid and electric alternatives have all contributed to the shift. Nevertheless, this decline is largely confined to the light-duty sector. In contrast, heavy-duty and long-haul transport continue to rely overwhelmingly on diesel due to its unmatched combination of energy density, availability, and mature refuelling infrastructure.

According to the International Energy Agency (IEA, 2021), heavy-duty road transport represents only a fraction of the global vehicle fleet (8% excluding two and thre-wheelers) but contributes over 35% of total CO_2 emissions from the road sector [36]. This disproportionate share underscores the strategic importance of diesel engines in the decarbonization of logistics and freight transport. Modern heavy-duty diesel engines achieve brake thermal efficiencies exceeding 45%, with advanced aftertreatment systems, including Diesel Oxidation Catalysts (DOC), Diesel Particulate Filters (DPF), and Selective Catalytic Reduction (SCR), ensuring compliance with stringent NO_x and particulate limits.

In addition to their environmental improvements, Diesel engines remain the most practical option for applications that demand long range, high payloads, and continuous operation. Long-haul trucks, intercity buses, agricultural tractors, and construction machinery all benefit from the Diesel engine's high torque at low speeds and its ability to operate efficiently over extended duty cycles. Unlike battery-electric vehicles, which face challenges in range, charging time, and infrastructure, diesel-

powered heavy-duty vehicles maintain operational reliability and flexibility, particularly in regions with limited grid capacity.

Overall, the historical and technical trajectory of diesel technology in road transport demonstrates its central role in global mobility. From the first high-speed direct-injection engines to today's ultra-clean Euro VI-VII systems, diesel has remained a pillar of heavy transport and logistics. While the light-duty sector transitions toward electrification, diesel engines continue to dominate the energy-intensive segments where alternatives remain technically and economically constrained. Their ongoing evolution, through hybridization, alternative fuels, and advanced combustion concepts — ensures that diesel technology will remain an essential component of the road transport sector's path toward decarbonization.

1.1.3. The role of the Diesel engines in the aviation sector

The application of Diesel engines in aviation has a long and fascinating history, marked by alternating phases of enthusiasm and neglect. One of the first successful aviation Diesel engine was the Junkers Jumo 205, developed in Germany in the early 1930s. It was a two-stroke opposed-piston engine, notable for its efficiency and fuel economy compared to gasoline aircraft engines of the time. The Jumo 205 powered aircraft such as the Junkers Ju 86 and the Blohm & Voss Ha 139, demonstrating excellent fuel efficiency and high altitude performance, but its heavy construction and complex maintenance requirements limited its widespread use. Despite these early challenges, the concept proved that compression-ignition could offer tangible benefits for flight propulsion, including greater safety, higher fuel efficiency, and the ability to operate on a range of heavier, less volatile fuels.

A renewed interest in aircraft diesel engines emerged in the 1970s, driven by the oil crises and the growing demand for affordable, efficient propulsion in general aviation. In this context, NASA initiated a series of design studies aimed at evaluating the feasibility of lightweight diesel engines for general aviation [37]. The goal was to reduce operating costs, improve safety, and provide compatibility with multiple fuel types such as Jet-A and diesel fuel, which were already globally available for turbine-powered aircraft. The 70-80s study highlighted one of the most practical motivations for using diesel engines in aviation: fuel availability. While aviation gasoline (AVGAS 100LL) was, and remains, expensive, leaded, and often scarce outside developed regions, diesel and Jet-A fuels are accessible worldwide, ensuring easier refuelling for aircraft operating across remote areas or developing countries.

From an engineering standpoint, the advantages were compelling. NASA's assessment projected that a lightweight aircraft diesel could achieve a Brake Specific Fuel Consumption (BSFC) of 0.36 lb/hp·h (≈219 g/kWh), compared to about 0.45 lb/hp·h for the contemporary gasoline engine (the Continental GTSIO-520-H [38]) [37]. This improvement of nearly 20% in specific fuel consumption translated into 30–40% longer range and substantially lower operating costs. Additional benefits included the elimination of the ignition system, reducing fire risk and maintenance complexity, and inherently better combustion stability under lean conditions. Diesel engines also offered the flexibility to operate at lower specific fuel consumption across a wider power range, which is particularly valuable in cruising regimes typical of small aircraft and unmanned aerial vehicles (UAVs).

While the NASA studies of the 1980s remained mostly conceptual, they laid the groundwork for subsequent development efforts in Europe and the United States. The introduction of modern materials, electronic fuel injection, and turbocharging technology in the automotive industry provided the enabling tools for a new generation of aero-diesel engines designed for general aviation and unmanned systems. A comprehensive review by Gęca et al. (2017 [39]) analyzed over 40 compression ingnition engines developed for aircraft applications, from early prototypes to commercially certified models such as the Austro AE300, SMA SR305, Thielert Centurion, and DeltaHawk DH200 [40–42]. These engines typically achieve brake specific fuel consumptions near 200 g/kWh, corresponding to 35–40% thermal efficiency, while maintaining power-to-weight ratios of around 0.9–1.0 kW/kg — comparable to avgas piston engines of similar displacement.

One of the decisive advantages of these modern designs is their ability to operate directly on Jet-A1, the standard aviation fuel used by turbine aircraft worldwide. This compatibility not only simplifies logistics but also reduces fuel cost by up to 50% relative to AVGAS. In addition, the high energy density of Jet-A1, combined with the superior efficiency of diesel combustion, allows for longer endurance and range, critical attributes for long-range UAVs, surveillance aircraft, and trainer or utility aircraft. Furthermore, advanced designs such as opposed-piston and two-stroke diesel configurations have demonstrated further potential, offering up to 30% lower NO_x emissions, reduced vibration, and compact geometries suitable for light aviation [39].

Nevertheless, the implementation of diesel engines in aviation still faces technical and regulatory challenges. Weight optimization, thermal management, and vibration control remain key issues, as does the certification of new combustion systems under EASA and FAA standards. The certification process itself represents a significant barrier to innovation, as it is lengthy, costly, and often favors incremental improvements over entirely new engine designs. For this reason, many manufacturers prefer to adapt existing engine architectures rather than develop new ones from scratch, in order to

minimize financial risk and shorten time-to-market. This conservative approach, while understandable within the economic framework of general aviation, inevitably slows down the pace of technological advancement and the adoption of disruptive propulsion concepts.

Despite these constraints, the current generation of aero-diesel engines has proven that compression-ignition technology can deliver a viable, efficient, and globally compatible alternative to gasoline engines in aviation. The combination of high efficiency, fuel flexibility, and operational reliability positions diesel engines as a strong candidate for medium-term sustainable propulsion, especially when coupled with hybrid systems or carbon-neutral synthetic fuels. In this sense, the diesel engine continues to embody its original promise: not a relic of the past, but an adaptable technology capable of evolving with the needs of modern aviation.

1.2. Environmental challenges: emission, regulation, perception

Diesel engines, while offering clear advantages in terms of fuel economy and CO_2 reduction per unit of work, are also associated with a set of environmental challenges that have shaped their technological evolution and societal perception. The fundamental trade-off arises from the very nature of compression-ignition combustion [43]: lean, heterogeneous mixtures enable high thermal efficiency but simultaneously promote the formation of nitrogen oxides (NO_x) due to high local flame temperatures, and particulate matter (PM) because of incomplete oxidation in fuel-rich spray regions. In addition, diesel exhaust contains smaller amounts of carbon monoxide (CO) and unburned hydrocarbons (HC), although generally at lower levels than those found in spark-ignition engines. These pollutants, especially NO_x and PM, are directly linked to adverse effects on human health and urban air quality, and have therefore been the primary focus of regulation for more than three decades [44,45].

Technological innovation has progressively reduced these emissions to levels that would have been unthinkable only a few decades ago [46]. Exhaust Gas Recirculation (EGR) systems, introduced in the 1980s, reduce NO_x formation by recirculating a controlled fraction of exhaust gases to lower peak combustion temperatures. Selective Catalytic Reduction (SCR), now standard in heavy-duty and increasingly common in light-duty applications, chemically converts NO_x into nitrogen and water using a urea-based reductant. Meanwhile, Diesel Particulate Filters (DPFs), mandatory in the European Union since Euro 5 for passenger cars, are capable of trapping more than 95% of soot particles, and subsequent regeneration ensures their oxidation into CO_2. The combined effect of these technologies has enabled modern Euro VI and Euro VII diesel engines to reduce NO_x emissions by

about 92% and particulate emissions by more than 95% compared to Euro 1 levels of the early 1990s [47,48].

The regulatory environment has been the main driver of these technological improvements. In the European Union, the progressive tightening of Euro standards since 1992 has forced manufacturers to adopt increasingly sophisticated emission control systems. The Euro 7 regulation, approved in April 2024, entered into force on 1 July 2025 for cars and vans. Compared to Euro 6, it not only confirms strict pollutant limits for NO_x and particulates but also extends testing to a broader set of real-driving conditions and introduces additional requirements for non-exhaust emissions such as brake and tire wear. In the United States, the Environmental Protection Agency (EPA) and the California Air Resources Board (CARB) [49,50] have adopted parallel standards for light-duty and heavy-duty vehicles, with Tier 3 gasoline and diesel requirements converging toward equally stringent levels. In the maritime sector, the International Maritime Organization (IMO) has enforced Tier III NO_x limits in Emission Control Areas since 2016, requiring advanced aftertreatment for new ship engines [51]. Similarly, the International Civil Aviation Organization (ICAO) regulates NO_x emissions from aircraft engines, a framework that also applies to experimental aero-diesel concepts [52].

Despite these significant achievements, the social perception of diesel technology has become increasingly negative. The turning point came with the “Dieselgate” scandal of 2015, when several manufacturers were found to have used defeat devices to manipulate emission results during certification tests [53]. This revelation not only led to massive fines and recalls but also severely undermined public trust in diesel vehicles [54]. Policymakers responded with stricter oversight and urban policies targeting diesel cars specifically. Several European cities, including Paris, Madrid, and Stuttgart, have introduced low-emission zones or outright bans on older diesel vehicles [55]. Simultaneously, taxation schemes have shifted to penalize diesel fuel, while incentives have favoured electrified alternatives.

This regulatory and societal backlash has profoundly influenced consumer behaviour. In Europe, where diesel once accounted for over half of new passenger car sales in the early 2010s (52% [56]), its market share had fallen to below 20% by 2024 (12% [57]). Even hybrid vehicles powered by diesel engines have struggled to gain traction, as their market appeal is overshadowed by the negative public image of diesel technology. While technically modern Euro VI diesels emit far fewer pollutants than their predecessors, the narrative in public discourse continues to equate diesel engines with urban pollution and environmental harm. This disconnection between technical reality and social perception has reshaped the automotive landscape, accelerating the shift toward gasoline, gasoline-hybrid and

electric vehicles, raising fundamental questions about the long-term role of diesel engines in a decarbonized transport system.

1.3. Rationale: adapt, not discard the Diesel engine

The global challenge of decarbonization requires a radical transformation of the energy and transport sectors. However, this transformation must balance ambition with technical feasibility and socio-economic realities. While public discourse in recent years has increasingly portrayed the diesel engine as an outdated and "dirty" technology, the scientific and industrial evidence suggests a more nuanced perspective. Rather than discarding the diesel engine altogether, adapting and decarbonizing this technology offers a pragmatic and effective pathway toward reducing greenhouse gas emissions while ensuring energy security and economic resilience.

The first rationale for maintaining diesel technology lies in its critical role in sectors that are inherently difficult to decarbonize. Heavy-duty road transport, long-haul trucking, agriculture, and construction still depend almost entirely on diesel engines because of their unmatched combination of energy density, fuel availability, robustness, and long operating life [58]. According to the International Energy Agency [59], heavy-duty vehicles account for more than 35% of direct CO_2 emissions from road transport, despite representing only a fraction of the fleet. A similar situation applies to maritime and aviation sectors. Shipping, which carries around 80% of global trade and contributes nearly 4% of global greenhouse gas emissions, has seen pioneering electrification projects such as the Yara Birkeland cargo vessel and the Sparky tugboat [60]. While these cases prove the feasibility of battery-electric solutions for short-range operations, the energy requirements of long-distance ocean-going ships make large-scale electrification economically and technically prohibitive. For the foreseeable future, liquid fuels, and thus combustion engines, remain indispensable in this sector. Aviation faces comparable constraints: although electrification is progressing in small aircraft, drones, and regional flights under 500 km, larger commercial aircraft remain strongly limited by battery weight and energy density. Complete electrification of long-haul flights is not expected before mid-century, leaving sustainable aviation fuels and hybrid solutions as the only viable near- to medium-term alternatives [61].

In this context, abandoning diesel technology would risk undermining both reliability and affordability in key transport sectors. Instead, adapting diesel engines to operate with low-carbon and renewable fuels provides a pragmatic pathway to sustain essential mobility and logistics until zero-emission solutions can be widely deployed. The technological landscape for decarbonizing diesel is

far from static and has expanded significantly in recent years. Hybridization is one of the most immediate and scalable strategies to lower the environmental footprint of diesel engines. By combining internal combustion with electric drives and storage systems, diesel hybrids allow the engine to operate closer to its most efficient points while relying on electric propulsion in low-load or urban conditions. This results in significant fuel savings and pollutant reduction, particularly in stop-and-go applications such as city buses, delivery trucks, and construction equipment. Several studies indicate that hybrid diesel buses can achieve up to 25–30% lower fuel consumption and CO_2 emissions compared to their conventional counterparts, while also reducing noise and improving drivability in urban centers. More recent evaluations confirm that the potential is even greater in specific applications: Zacharof et al. [62] report CO_2 reductions of up to 36% for urban buses, whereas the gains for long-haul heavy-duty trucks are more modest, typically below 10%. These findings illustrate both the value of hybridization where duty cycles are favourable, and the need to complement this approach with other decarbonization pathways, such as renewable fuels, e-fuels, in long-distance and energy-intensive applications.

In this regard, the use of biofuels and renewable diesel has emerged as one of the most mature and immediately deployable solutions. Conventional biodiesel in the form of Fatty Acid Methyl Esters (FAME) has been used for decades, but Hydrotreated Vegetable Oil (HVO) represents a more advanced alternative thanks to its superior stability and cleaner combustion. Advanced biofuels derived from waste biomass and lignocellulosic feedstocks offer well-to-wheel greenhouse gas reductions of 60–80% relative to fossil diesel [63]. These fuels can be used as drop-in replacements or blended with fossil diesel, requiring minimal adaptation of engines or infrastructure (Q8 HVO+ pump can be found in Italy from north to south very easily). Their scalability is linked to sustainable feedstock availability, but they remain an essential element of the near- and mid-term decarbonization portfolio. As underlined by Knothe [64], the production pathway is decisive in shaping the composition and properties of renewable diesel fuels. FAME, obtained via transesterification, retains a significant oxygen content that affects stability and cold-flow behaviour, whereas HVO, produced through hydrodeoxygenation, is almost oxygen-free and chemically closer to fossil diesel. These differences explain why FAME is often blended in limited shares, while HVO can serve as a true drop-in replacement with superior combustion quality.

Synthetic fuels, or e-fuels, have recently gained considerable attention as a long-term decarbonization pathway for compression-ignition engines. These fuels are produced through Power-to-Liquid (PtL) processes that combine hydrogen, generated by electrolysis of water using renewable electricity, with captured CO_2 to form syngas, which can then be converted into liquid hydrocarbons via Fischer–

Tropsch synthesis or methanol-based routes [65]. The resulting products, such as e-diesel and e-kerosene, are chemically similar to their fossil counterparts and can therefore be used as “drop-in” fuels, fully compatible with existing diesel infrastructures and combustion technologies. This compatibility is one of their most significant advantages, as it allows the decarbonization of hard-to-electrify sectors without requiring disruptive changes in distribution networks or vehicle powertrains.

The environmental benefits of e-fuels, however, are strongly dependent on the carbon intensity of the electricity used for their production. Life-cycle analyses show that e-diesel can reduce greenhouse gas emissions by up to 99% compared to fossil diesel when produced with 100% renewable electricity, reaching life-cycle values as low as 1.3 gCO_2eq/MJ. Conversely, if generated with fossil-based electricity, the carbon intensity of e-diesel can exceed 600 gCO_2eq/MJ [66]. This highlights both the promise and the risk of synthetic fuels: their sustainability is contingent upon the rapid decarbonization of the power sector. Despite these challenges, e-fuels represent a versatile solution for heavy-duty road transport, aviation, and maritime applications, where liquid fuels are expected to remain essential for decades. In particular, e-kerosene is considered one of the most promising sustainable aviation fuels, with potential reductions of several megatons of CO_2 by 2030 with affordable costs [67], while e-diesel could substantially lower the carbon footprint of long-haul trucking and shipping [66].

Beyond the adoption of alternative fuels, new combustion strategies have been extensively investigated as a means to further reduce the environmental footprint of diesel engines. Low-temperature combustion concepts such as Homogeneous Charge Compression Ignition (HCCI) and, Reactivity Controlled Compression Ignition (RCCI) have demonstrated the ability to simultaneously achieve high efficiency and ultra-low pollutant emissions. HCCI relies on the auto-ignition of a premixed charge, which lowers peak combustion temperatures and thereby suppresses NO_x formation [68]. RCCI, on the other hand, employs two fuels of different reactivities (typically diesel as a high-reactivity pilot and a gaseous or low-reactivity fuel such as natural gas, methanol, hydrogen or even gasoline, to finely control combustion phasing [69,70]. Early investigations already reported brake thermal efficiencies exceeding 50% while reducing NO_x and soot emissions to near-zero levels [70]. More recent studies have confirmed and extended these findings: for instance, Li et al. (2014) demonstrated through parametric optimization that methanol/diesel RCCI configurations can deliver stable combustion with significantly improved efficiency compared to conventional diesel operation [71]. In their study, the optimum solutions required a high methanol fraction of about 66.5% (≈81% in mass) combined with advanced SOI and moderate EGR (≈34%), which led to an equivalent indicated specific fuel consumption (EISFC) as low as ~165 g/kWh. This corresponded to a marked

efficiency gain relative to conventional diesel operation, while keeping emissions under stringent limits. In particular, NOx was reduced to ~0.07 g/kWh and soot was nearly eliminated (<0.00002 g/kWh), well below Euro VI thresholds, confirming the strong potential of methanol/diesel RCCI to simultaneously achieve ultra-low emissions and high thermal efficiency.

In recent years, and today, research on diesel–methanol dual-fuel RCCI has intensified, reflecting the growing scientific and industrial interest in methanol as a viable low-carbon fuel especially in the marine sector and for heavy duty application. A representative example is the experimental work by Guan et al. [72], conducted at Brunel University, which systematically assessed the combined use of Miller cycle, exhaust gas recirculation, and intake air cooling on a heavy-duty single-cylinder engine. Their results showed that while conventional dual-fuel operation was limited to a methanol substitution of around 28% due to excessive pressure rise rates, the application of Miller cycle and intake air cooling enabled up to 40% methanol energy fraction. Under these optimised conditions, the engine achieved a net indicated efficiency of 47.4% (+3.7% vs. diesel baseline) with a concurrent 37% reduction in NOx emissions, while soot remained negligible (<0.002 g/kWh). These findings highlight the potential of advanced combustion control strategies to unlock the use of methanol in diesel-based engines.

Other contributions from the same research line have expanded this perspective by exploring complementary approaches. For instance, optical diagnostics and kinetic analyses have been employed to clarify ignition and flame development in methanol dual-fuel combustion [73]; studies on injection strategies have shown that split diesel injections can improve mixture homogeneity and reduce pollutant formation [74]. Taken together, this body of work consolidates the view that methanol/diesel RCCI is not only a technically feasible solution but also one of the most actively investigated pathways for extending the role of compression-ignition technology in the decarbonization of transport [75,76].

Hydrogen has recently emerged as one of the most promising low-reactivity fuels for RCCI engines, owing to its unique combination of wide flammability limits, high diffusivity, and zero carbon content. Its use in compression-ignition engines as a secondary fuel has been studied for decades. In the earliest dual-fuel concepts, hydrogen was typically introduced in small amounts through “fumigation” in the intake manifold, which already showed beneficial effects such as lower smoke opacity and reduced CO_2 emissions compared to conventional diesel operation [77,78]. These pioneering investigations laid the groundwork for more advanced approaches such as HCCI and RCCI, where hydrogen plays a central role in controlling combustion phasing and improving efficiency.

Building on the early studies of hydrogen fumigation, which were typically limited to relatively low substitution ratios, subsequent research has focused on strategies to achieve higher hydrogen energy shares in compression-ignition engines [79–82]. One representative example is the work of Chintala and Subramanian [83], who investigated hydrogen enrichment in a diesel/biodiesel dual-fuel engine operated at full load under different control strategies. In the conventional diesel dual-fuel mode (DDM), the maximum hydrogen energy share was limited to about 18%, corresponding to a brake thermal efficiency of 34.8%, a NOx emission level of 9.7 g/kWh, and smoke opacity of 15.4%. By employing retarded diesel injection timing (RDM), the hydrogen share could be increased to 24%, with NOx reduced to 6.1 g/kWh (−37% compared to DDM), albeit with a slight efficiency penalty (29.9%) and higher CO/HC emissions. With port water injection (WDM), the hydrogen energy share reached up to 36%, with NOx further lowered to 6.6 g/kWh (−32% compared to DDM). However, in this configuration the efficiency decreased to 32.7% and smoke opacity rose again to 5.9%. Despite these trade-offs, the study clearly demonstrated that auxiliary control strategies such as injection retardation and water addition can extend the feasible hydrogen substitution well beyond the conventional fumigation limits.

More recently, research has advanced towards configurations capable of sustaining much higher hydrogen substitution ratios with improved efficiency. Hanafi Gharehlar et al. (2024) investigated a diesel–hydrogen RCCI engine and demonstrated that hydrogen could almost entirely replace natural gas as the low-reactivity fuel [84]. In their configuration, obtained at reduced engine load, the diesel pilot contributed only about 22% of the total fuel energy, while hydrogen provided the remaining share (78%). Under these conditions, the brake thermal efficiency exceeded 51%, representing a notable improvement over conventional dual-fuel operation. At the same time, CO_2 emissions were reduced by a factor of four, while unburned methane and formaldehyde were virtually eliminated. CO emissions dropped drastically. by factors of several hundred, and NOx emissions were kept below the Euro VI limit of 0.2 g/kWh through the combined use of exhaust gas recirculation (EGR) and nitrogen dilution.

This outcome was made possible by deliberately operating the engine at low load, a condition that relaxes the constraints on pressure rise rates and combustion phasing, enabling higher hydrogen shares without excessive knock or NOx formation. Such an approach is particularly relevant for fixed-point applications like stationary power generators, where the operating load is stable and can be tuned for optimum efficiency and emissions.

In hydrogen/diesel RCCI, the role of the diesel pilot remains fundamental, as it provides the high-reactivity ignition source that initiates the entire combustion process. The way in which this pilot fuel

is delivered has a decisive influence on overall combustion behaviour, efficiency, and emissions. Experimental studies on light-duty engines have therefore focused on optimising injection strategies. Duan H. et al. (2023) conducted a comparative investigation of single versus double direct injection of the diesel pilot in H_2/diesel RCCI operation [85]. Their results showed that the double-injection strategy not only sustained efficiencies above 50% but also mitigated peak pressure rise rates, improved combustion stability, and lowered NOx formation compared to single injection. As expected, soot and HC emissions were virtually eliminated due to the hydrogen fraction in the fuel blend.

Taken together, these works illustrate the continuous evolution of Diesel–H_2 dual-fuel RCCI concepts: from early enrichment studies to advanced configurations capable of sustaining very high hydrogen shares with high efficiency and ultra-low emissions. This trajectory confirms why hydrogen-assisted RCCI is today regarded as one of the most promising frontiers for adapting compression-ignition technology to the challenges of deep decarbonization. Importantly, the insights gained from these and many other studies reviewed in the literature have provided the foundation and inspiration for the research activities presented in this dissertation, which aim to further explore, validate, and extend the role of hydrogen–diesel RCCI in the path toward sustainable propulsion.

The evidence discussed here in this section reinforces the notion that the “problem” lies not inherently in the diesel engine itself, but in the type of fuel traditionally used to power it. Far from being an obsolete or irremediably “dirty” technology, the compression-ignition engine demonstrates a remarkable ability to evolve when operated with alternative fuels and advanced combustion strategies. By coupling diesel’s robustness and efficiency with low-carbon fuels such as hydrogen, methanol, or advanced biofuels, and by adopting innovative combustion concepts, the engine can continue to serve as a reliable and cost-effective solution in hard-to-abate sectors. While not the definitive long-term endpoint of transport decarbonization, this adaptive pathway ensures that diesel technology remains a relevant and pragmatic contributor to the medium-term transition toward climate neutrality.

2. Sustainable fuels for heavy-duty truck engines: biodiesel, bio-methane and hydrogen

The heavy-duty transport sector plays a crucial role in global logistics, ensuring the movement of goods over long distances and sustaining industrial and commercial activities. In recent years, the continuous growth of freight demand, driven by globalization, e-commerce expansion, and just-in-time production, has led to a steady increase in the number of Heavy-Duty (HD) trucks on the road and, consequently, in fuel consumption and GHG emissions [86]. These vehicles are particularly difficult to electrify, as they require a large amount of stored energy to guarantee operational autonomy comparable to that of conventional Diesel trucks [62]. For this reason, alternative fuels represent one of the most promising short- to mid-term pathways toward decarbonization in this sector, allowing a significant reduction of CO_2 and pollutant emissions while maintaining the high energy efficiency and durability typical of compression-ignition engines.

Among the different strategies under investigation, biofuels are currently the most immediate and practical alternative to fossil Diesel [87]. Their main advantage lies in the ability to achieve a near-neutral CO_2 balance when considering the entire life cycle, as the CO_2 emitted during combustion is approximately compensated by that absorbed during biomass growth. Moreover, biofuels can generally be used in existing Diesel engines with minimal or no hardware modifications, making them ideal *drop-in* candidates for a rapid transition [88].

In this study, two bio-based fuels were analysed: HVOlution by ENI (hereafter referred to as HVO) and compressed bio-methane. Both fuels were tested virtually as substitutes for Diesel and natural gas in the same 12.9 L heavy-duty engine platform, originally developed by the manufacturer in two versions: a direct-injection Diesel and a spark-ignited CNG configuration.

The HVO fuel, derived from hydrotreated vegetable oils, exhibits physical and chemical properties very close to those of standard Diesel, but with a few relevant differences (see Table 1). Its slightly higher lower heating value (44 MJ/kg vs 43 MJ/kg) and lower density (780 vs 840 kg/m³) result in the need to inject a slightly larger fuel volume (around +5–10%) to maintain the same brake output. Furthermore, because of its higher stoichiometric air–fuel ratio (15.0 vs 14.5), the air mass flow rate must be increased to fully exploit its combustion potential. This can be achieved through modest adjustments to the fuel injection and turbocharging systems. The higher cetane number of HVO (≈75 vs 55) also enhances ignition quality and combustion stability, while the absence of sulphur and aromatic compounds contributes to cleaner exhaust gases and reduced particulate emissions.

The bio-methane considered in this work was formulated to replicate the composition and properties of conventional fossil CNG (about 95% CH_4, LHV ≈ 47.5 MJ/kg, see Table 2). As a result, it can be regarded as a fully drop-in alternative, requiring no modifications to the engine hardware or control strategy. This feature makes bio-methane particularly attractive for immediate implementation in existing fleets, as the same 12.9 L engine platform already has a spark-ignited CNG variant offered by the manufacturer. The main trade-off lies in the lower brake performance compared to Diesel, but this is compensated by lower fuel costs per kilometre and reduced CO_2 emissions over the fuel's life cycle.

Table 1: Petrol-diesel and HVO Properties.

	Diesel (EN 590)	HVO
Density (kg/m^3)	840	780
Lower heating value (MJ/kg)	43	44
Energy density (MJ/m^3)	36120	34320
Cetane number	55	75
Stoichiometric air fuel ratio	14.5	15
Heating value of stoichiometric mixture (MJ/kg)	2.96	2.92
Viscosity at 40°C (mm^2/s)	3.67	4.00
Sulfur content (ppm)	<10	<1
Poly-aromatics (%mass)	11	0

Table 2: Reference CNG and Bio-methane properties.

	Reference CNG/Biomethane
Density at 0°C, 1 bar (kg/m^3)	840
Methane Composition (% m/m)	CH_4 95%
Lower heating value (MJ/kg)	47.5
Energy density (MJ/m3)	66.0
Stoichiometric air fuel ratio	16.3
Heating value of stoichiometric mixture (MJ/kg)	2.90
Volume of stoichiometric mixture (MJ/kg)	0.905

On the opposite side of the spectrum, hydrogen offers the unique potential to eliminate CO_2 emissions entirely at the exhaust when used as the sole energy carrier, gaining an increasing attention as a fuel for internal combustion engines [89,90]. Converting a Diesel engine to operate on spark-ignited hydrogen combustion enables clean operation, where the only significant pollutants are nitrogen oxides (NO_x). These can be effectively minimized thanks to hydrogen's extremely wide flammability range, which allows stable combustion under lean or ultra-lean conditions ($\lambda \geq 2$). In such scenarios, NO_x levels can be kept well below Euro VI/VII limits, allowing for a drastic simplification of the after-treatment system—typically limited to a single oxidation catalyst to treat the small amount of unburned hydrocarbons and CO produced by lubricant oil oxidation.

Nevertheless, hydrogen is not a drop-in fuel. Its application in internal combustion engines requires a comprehensive redesign of the fuel and air systems. One of the main challenges is the risk of backflow and backfire, resulting from the possible re-entrainment of hydrogen from the cylinder into

the intake manifold. This issue can be mitigated through precise control of the fuel injection timing and the optimization of valve events [91–93]. Another potential limitation is related to combustion irregularities, such as knocking or abnormal pressure oscillations, which may occur under specific load or mixture conditions if ignition and injection are not properly controlled. Moreover, the storage of hydrogen poses a significant engineering constraint: at 700 bar, the volumetric energy density of hydrogen remains roughly half that of compressed natural gas stored at 250 bar [94]. This means that, for a given tank volume, hydrogen-powered trucks would achieve a shorter driving range unless larger and heavier tanks are adopted.

Finally, hydrogen combustion requires careful mixture preparation and charge formation, as achieving a homogeneous air–fuel distribution is essential to ensure stable operation, avoid local hotspots, and minimize the risk of pre-ignition and knock.

The analysis presented in this chapter was carried out through numerical simulations using the 1D/0D Computational Fluid-Dynamics (CFD) software GT-Power (Gamma Technologies [95]). The model was calibrated with experimental data from both Diesel and CNG engine versions and extended to simulate hydrogen combustion using a predictive model. This approach allowed for a consistent comparison of biodiesel, bio-methane, and hydrogen, providing insights into their respective advantages, limitations, and potential for sustainable application in long-haul heavy-duty transportation.

From this study, a scientific article was produced, titled “Sustainable Fuels for Long-Haul Truck Engines: A 1D-CFD Analysis”, published in 2024 by SAE International [96]. The following pages of this section present and discuss the main results of the work, providing an integrated view of the performance and emission behaviour of biodiesel, bio-methane, and hydrogen when applied to a common HD engine platform.

2.1. Engine configuration and numerical modelling

The analysis presented in this work was carried out on a six-cylinder heavy-duty engine with a total displacement of 12.9 L, representative of a long-haul truck power unit. The same engine platform is produced by the manufacturer in two distinct versions, both based on identical base architecture: a compression-ignition Diesel configuration and a spark-ignition CNG configuration. Table 3 presents the main specifications of the diesel and CNG configuration, while Figure 3 illustrates the engine block.

In its Diesel version, the engine delivers 420 kW at 1800 rpm and a maximum brake torque of 2500 Nm at 1000 rpm, whereas the CNG version reaches 330 kW at 1800 rpm and 2000 Nm at 1200 rpm (see Table 3).

Table 3: Cursor 13-Diesel/ main characteristic [97].

	Diesel Specifics	CNG Specifics
N. cylinders / valve	6/4	
Air boosting system	Turbocharged	
Total displacement (L)	12.9	
Bore x Stroke (mm x mm)	135 x 150	
Maximum power (kW @ rpm)	419 @1800	330 @ 1800
Maximum torque (Nm @ rpm)	2500 @ 1200	2000 @ 1100
Dry weight (kg)	1132	1150

Figure 3: Cursor 13 picture [97]

Although the two versions share the same crankcase and geometric parameters (bore 135 mm, stroke 150 mm, four valves per cylinder), several design differences exist to accommodate the distinct combustion processes. The Diesel engine is equipped with a high-pressure common-rail direct injection system and a Variable Geometry Turbine (VGT), optimized to deliver high air mass flow rates and achieve strong scavenging at full load. Conversely, the CNG version operates with Port Fuel Injection (PFI) and adopts a Waste-Gate (WG) turbocharger. Furthermore, in the gas version, the Intake Valve Closure (IVC) is modified to implement a Miller cycle, reducing charge temperature and increasing knock resistance. In the CNG engine, valve overlap is also minimized to maximize the conversion efficiency of the three-way catalyst.

To evaluate the performance of the different alternative fuels on the same platform, a detailed 1D-CFD model was developed using the GT-Power software (Gamma Technologies, v2022). The Diesel and CNG configurations were first calibrated against experiment data obtained at full-load conditions. The calibrated models were then adapted, when required, to account for the use of sustainable fuels. For the hydrogen case, where no experimental dataset was available, a dedicated model was derived from the original Diesel configuration equipped with a VGT turbine. The combustion system design was based on a chamber geometry proposed in the literature: the Diesel injector was replaced by a spark plug, while a hydrogen injector was positioned between the two intake valves. Moreover, the intake port design was modified to enhance tumble generation during the intake stroke, and both valve lift profiles and timings were optimized to support hydrogen combustion.

In the Diesel configuration, load is controlled by the injected fuel mass, combined with the actuation of the EGR valve and the VGT rack position. In contrast, the CNG version relies on a single throttle valve upstream of the plenum to regulate the intake mass flow, while a PID controller adjusts the wastegate valve opening to reach the boost target. A virtual ECU reproduces the response of the main sensors and actuators, while a cylinder deactivation strategy is implemented under part-load conditions. In both versions, a backpressure valve is included downstream of the turbine to account for the exhaust pressure associated with the after-treatment system, which is not explicitly modeled.

This calibrated 1D model serves as the foundation for the evaluation of the alternative fuels discussed in the following sections.

2.2. Experimental validation of the 0D/1D-CFD Models

To ensure that the developed 1D/0D-CFD models could be reliably employed as predictive tools, a comprehensive calibration and validation process was carried out using experimental data acquired under full-load operating conditions. Both the Diesel and the CNG configurations of the 12.9 L heavy-duty engine were considered. This step was essential to verify the model accuracy before extending its application to the analysis of alternative fuels.

The Diesel engine model was first validated by comparing the main brake performance parameters with experimental measurements. As reported in Figure 4, the agreement between simulations and experiments is excellent in terms of brake torque, brake power, and brake thermal efficiency (BTE), with a maximum deviation of about 3 % observed in BTE at high engine speed. Subsequently, the gas-exchange parameters were analysed, as shown in Figure 5, which compares volumetric efficiency and the characteristic pressures in the intake and exhaust systems (namely the compressor inlet (P_1), intercooler outlet (P_5), and turbine inlet/outlet (P_3/P_4)). The close agreement on compressor inlet and turbine outlet pressures confirms that the flow losses within the ducts were correctly represented in the model. Likewise, the accurate reproduction of intercooler outlet and turbine inlet pressures demonstrates that the turbocharger operation was properly captured, ensuring a realistic description of the overall air-path dynamics. Finally, Figure 6 presents the validation of the turbine inlet gas temperature (T_3), which is a key indicator of the thermal loading acting on the turbine.

Since this quantity depends on combustion development, heat transfer and component efficiencies, the close match between simulation and experiment provides further evidence of the physical robustness of the Diesel engine model.

A similar validation procedure was applied to the CNG spark-ignition configuration. As illustrated in Figure 7, the correlation between simulation and experimental data is again very good for brake torque, brake power, and BTE, with deviations comparable to those observed for the Diesel model. Figure 8 shows the comparison of volumetric efficiency and manifold pressures, confirming that the simplified air-path layout with waste-gate control was effectively represented. Finally, Figure 9 compares the turbine inlet temperatures, demonstrating that the model is able to capture with satisfactory accuracy the main thermal and gas-dynamic phenomena of the real engine.

Overall, the calibration and validation activities confirmed that both the Diesel and CNG models are capable of reproducing the engine thermodynamics and gas-exchange processes within acceptable error margins. The validated models thus provide a reliable virtual test bench for the subsequent numerical evaluation of biodiesel and bio-methane but also of hydrogen combustion concepts presented in the following sections.

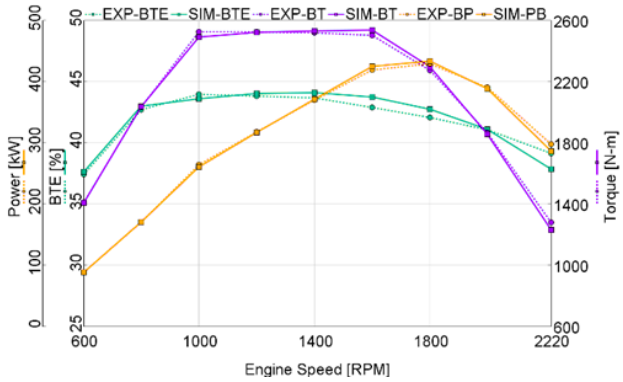

Figure 4: Brake torque, power and BTE comparison between simulation and experimental data (stock Diesel engine)

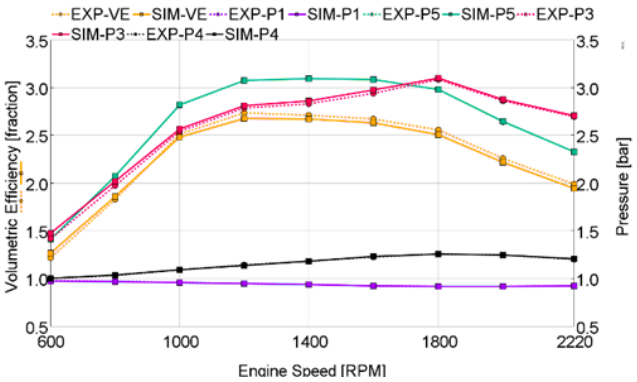

Figure 5: Volumetric efficiency and average pressure in the intake and exhaust manifolds comparison between simulation and experimental data (stock Diesel version).

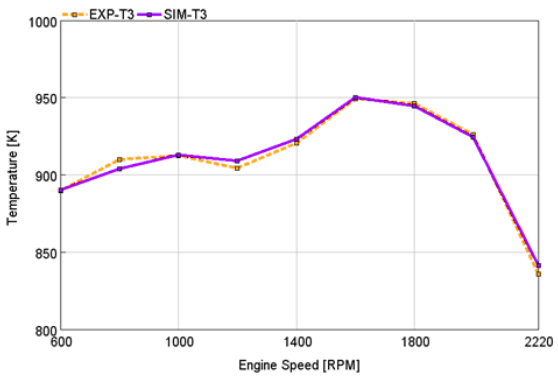

Figure 6: Turbine inelt temperature comparison between simulation and experimental results (stock Diesel engine).

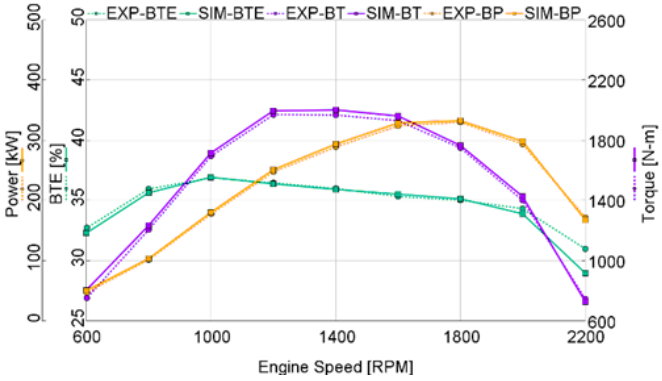

Figure 7: Brake torque, power and BTE comparison between simulation and experimental data (stock CNG engine).

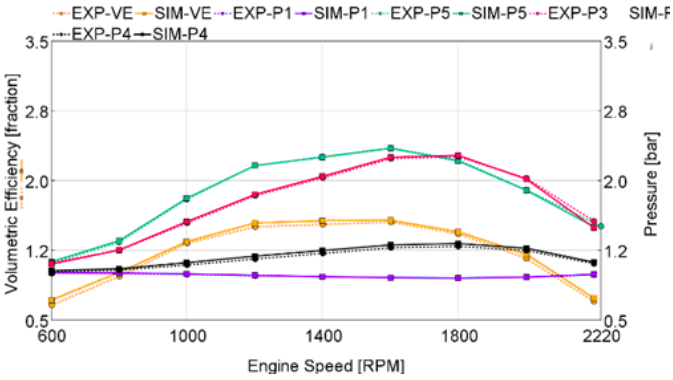

Figure 8: Volumetric efficiency and average pressure in the intake and exaust manifolds comparison between simulation and experimental data (stock CNG engine).

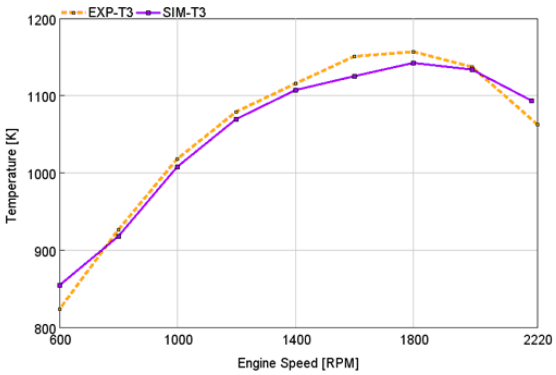

Figure 9: Turbine inlet temperature comparison between simulation and experimental data (stock CNG engine)

2.3. Numerical optimization of the hydrogen-fuelled Engine.

After validating the numerical models of the Diesel and CNG configurations, the simulation framework was extended to investigate the feasibility of converting the same 12.9 L heavy-duty engine to spark-ignited hydrogen operation. The main goal was to assess whether a hydrogen-fueled configuration could achieve comparable brake performance to the CNG version while drastically reducing pollutant emissions and maintaining acceptable thermal and mechanical constraints. This step represents a crucial milestone in the overall research path, as it bridges the conventional combustion systems with a fully carbon-free alternative, preserving the robustness and efficiency of the original Diesel platform.

The optimization was performed entirely through 1D-CFD simulations using the previously validated *GT-Power* model. The hydrogen engine was derived from the baseline Diesel configuration equipped with a Variable Geometry Turbine (VGT). This choice was motivated by the substantially higher air mass flow required by hydrogen combustion. Although hydrogen possesses a higher lower heating value than natural gas (≈120 vs 47 MJ/kg), its stoichiometric air–fuel ratio is nearly five times higher (≈80 vs 17). Consequently, to reach the same brake power level, a much greater air mass must be supplied to the cylinders, particularly under lean operation ($\lambda \approx 2.4–2.5$). Such conditions make the use of a flexible and efficient boosting system essential. The VGT allows fine control of both boost pressure and exhaust backpressure, ensuring proper air delivery across the full engine speed range and facilitating transient response. In contrast, a fixed-geometry or WG-controlled turbine, such as that used in the CNG version, would not be able to accommodate the wide variation in air demand associated with hydrogen combustion without significant efficiency penalties.

The combustion process was simulated using a predictive quasi-dimensional model (SI-Turb), previously calibrated [98] with experimental data. The reference engine used for SI-Turb previous calibrations was a 2.0 L turbocharged direct-injection hydrogen prototype with a variable geometry turbine [99,100]. The reference setup of that engine featured lean combustion ($\lambda \approx 2.5$), delayed spark timing and a Miller cycle (early intake valve closing) to balance efficiency, performance and NO_x formation. As illustrated in Figure 11 (a-c), the results obtained from the calibrated GT-Power model are in close agreement with the experimental measurements. Both the global performance indicators (Brake Mean Effective Pressure (BMEP), BTE and VE) and the in-cylinder quantities (pressure and heat-release rate (HRR)) are well reproduced, confirming the capability of the predictive combustion model to capture the fundamental thermodynamic and combustion processes of the hydrogen engine, despite the simplified numerical approach. It must be emphasized that the predictive capability of the model is strictly bounded to the operating range used for its calibration.

The accuracy of the numerical simulations cannot be guaranteed under conditions that significantly differ from those experimentally tested. For this reason, in the present work the combustion parameters were kept as close as possible to the reference prototype, maintaining the relative air–fuel ratio between 2.4 and 2.5 and adopting similar spark timings. Furthermore, the geometry of the combustion chamber and the intake ports was assumed to be consistent with that of the experimental engine, scaled according to the bore of the 12.9 L unit (Figure 10 shows the chamber geometry considered in the quasi-dimensional model). This ensured that the simulated flow and combustion characteristics remained representative of a realistic HD hydrogen configuration.

Once the hydrogen engine model was properly defined and the combustion setup established, a numerical optimization campaign was conducted to identify the most efficient and clean operating conditions for this configuration. The optimization focused on achieving a balance between brake performance, efficiency, and emissions, while ensuring reliable operation within realistic thermal and mechanical limits.

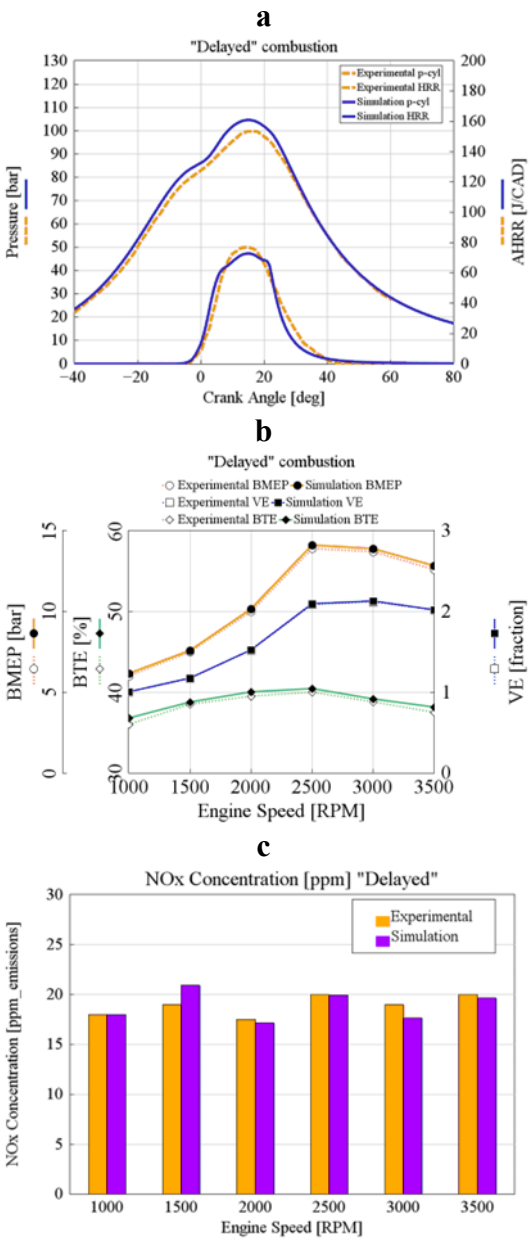

Figure 11: Calibration results of the predictive quasi-dimensional combustion model for the 4T H2 engine. a) in cylinder pressure and HRR trace at full load @2500 rpm; b) average BTE, volumetric efficiency VE, BMEP; c) Nox concentration at full load for the whole engine speed range considered (1000-3500 rpm)

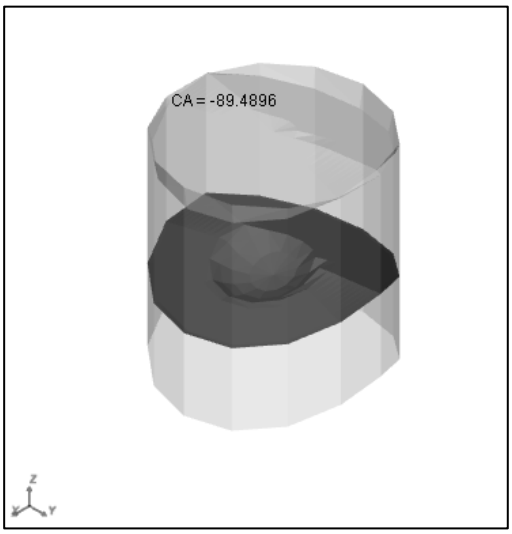

Figure 10: combustion chamber geometry implemented in the GT-Power quasi-dimensional predictive model.

The following objectives and constraints were defined for the hydrogen-fuelled configuration:

- Target performance: Achieve brake power and torque comparable to the stock CNG engine (330 kW @ 1800 rpm, 2000 Nm @ 1200 rpm).
- Efficiency target: Maximize Brake Thermal Efficiency (BTE) in all operating points.
- Emissions constraint: Maintain NO_x concentrations below 20 ppm across the entire speed–load map.

- Mechanical and thermal limits:
    - Peak in-cylinder pressure Pmax < 120 bar
    - Turbine inlet temperature TIT < 850 °C
    - Fraction of residual gases at IVC < 25 %
- Combustion and control constraints:
    - Fuel injection start after intake valve closure (IVC) to prevent backfire.
    - IVC not later than Bottom Dead Center (BDC).
    - Spark timing and boost pressure to be optimized concurrently to ensure smooth and stable combustion.

Within these boundaries, the optimization parameters included:

- Intake and exhaust valve lift profiles and timings (IVA, IVC, EVO, EVC);
- VGT rack position (controlling boost pressure and backpressure);
- Spark advance (governing combustion phasing and BTE).

The optimization procedure was carried out through iterative simulations on a predefined speed–load grid, ensuring that each solution respected all the above constraints. The operating strategy was based on lean combustion ($\lambda = 2.4–2.5$) to minimize NO_x formation, combined with a delayed spark timing to control peak pressure and temperature levels. This approach leverages hydrogen's wide flammability range and fast burning rate to achieve clean and efficient combustion, while avoiding the risks of knocking or irregular combustion that may occur under rich or stoichiometric conditions.

The results of the optimization are summarized from Figure 12 to Figure 16, which report the main control and combustion quantities of the hydrogen-fuelled configuration across the speed–load map. The analysis verifies compliance with the design targets (performance, NO_x, and mechanical/thermal limits) and clarifies the engine behaviour under ultra-lean operation.

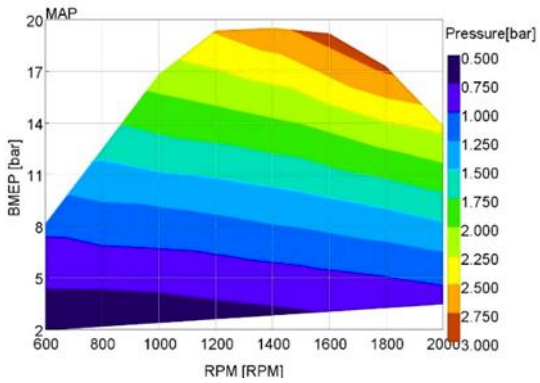

Figure 12: Intake Manifold Air Pressure (MAP) as function of engine speed and BMEP for the optimized hydrogen engine.

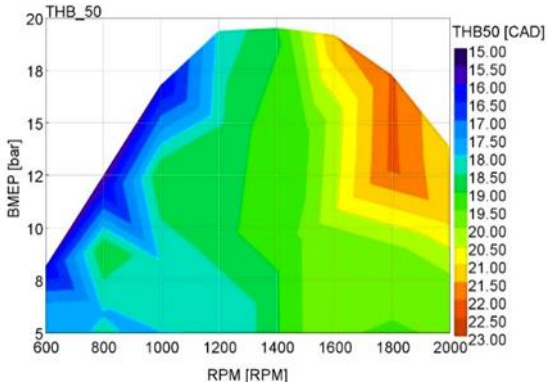

Figure 13: THB50 map as function of engine speed and BMEP for the optimized hydrogen engine.

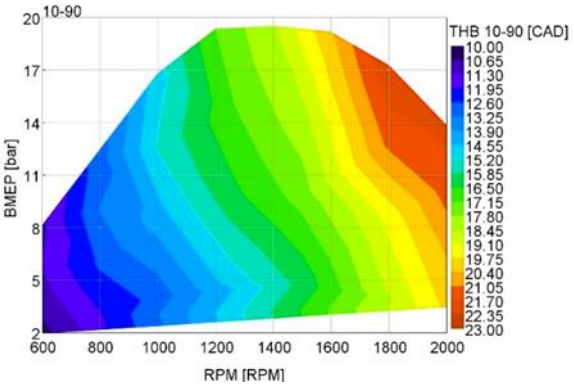

Figure 14: THB10-90 map as function of engine speed and BMEP for the optimized hydrogen engine.

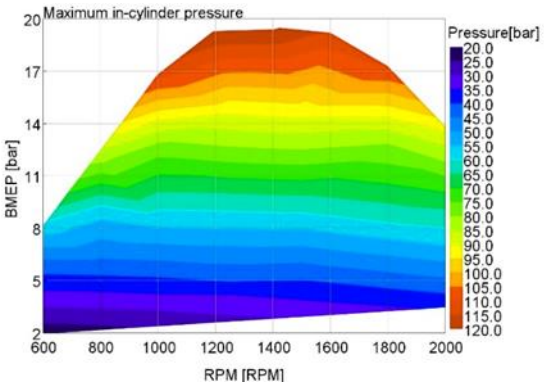

Figure 15: Max in-cylinder pressure map as function of engine speed and BMEP for the optimized hydrogen engine.

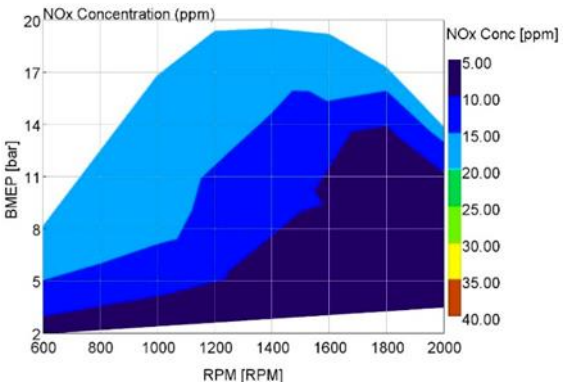

Figure 16: NOx concentration (ppm) map as function of engine speed and BMEP for the optimized hydrogen engine.

Figure 12 shows the intake manifold absolute pressure (MAP). At part load, control is shared between VGT rack (primary lever) and throttle (secondary at lower loads): load is first reduced by opening the rack to drop boost with minimal pumping losses; only at lower loads does the throttle close to keep the target λ while maintaining stability. Figure 13 reports the map of THB50, defined as the crank angle corresponding to 50% of the total heat released. At low and medium speeds, the combustion phasing is more advanced, while at higher speeds and loads it is progressively delayed to control the maximum in-cylinder pressure and turbine inlet temperature. The optimized values of THB50 range

between 15° and 18° aTDC, representing a good compromise between efficiency and mechanical stress. Figure 14 presents the THB10-90 combustion duration. Durations remain comparatively short (~10–22° CA) over the map, which is a proof of a fast combustion. Figure 15 presents the map of maximum in-cylinder pressure (Pmax). The results show that the peak pressure always remains below the imposed limit of 120 bar across the full operating range. This confirms that the optimization process succeeded in controlling the in-cylinder pressure evolution through the combined adjustment of spark timing and VGT position.

Figure 16 shows the NO_x concentration predicted by the simulations. The NO_x values are below 20 ppm at all operating points, with an average value below 15 ppm over more than half of the map. These results confirm that the ultra-lean hydrogen combustion strategy is effective in minimizing NO_x emissions while maintaining stable engine operation.

The optimized hydrogen configuration satisfies all the imposed constraints. The air-path and combustion parameters are properly balanced, ensuring low NO_x emissions, controlled peak pressure, and consistent combustion behaviour across the full speed–load range.

2.4. Final comparison: full load

Three alternative fuels are theoretically compared in the following two section using the same 12.9 L heavy-duty engine platform described before: biodiesel (HVO), bio-methane, and hydrogen. According to the adopted hypotheses, the bio-methane configuration provides the same results as the CNG engine, since the two fuels share identical physical and chemical properties. Similarly, replacing conventional Diesel fuel with HVO leads to negligible differences in combustion characteristics. In this case, the injection rates were slightly adjusted to achieve the same brake power as the Diesel engine, while the volumetric efficiency was increased by about 4 % at full load to compensate for the lower fuel density and the higher stoichiometric air–fuel ratio of HVO. The non-dimensional burn-rate curves were assumed to remain unchanged with respect to the Diesel reference. Based on these assumptions, the comparison focuses on the global thermodynamic performance and emissions behaviour of the three alternative fuels under both full-load and partial-load operating conditions.

Figure 17 to Figure 24 summarize the main thermodynamic and performance parameters predicted by the 1D-CFD simulations for the three combustion concepts at full load condition. The HVO and hydrogen configurations exhibit very similar trends in volumetric efficiency, as both operate with the same VGT system. Conversely, the bio-methane engine, characterized by stoichiometric combustion, requires considerably less air, with a peak volumetric efficiency of about 1.55 compared to 2.7 for

the other two fuels as shown in Figure 17. Consistent with this, the boost pressure curves show a maximum value of roughly 3 bar for biodiesel and hydrogen, and about 2.4 bar for bio-methane (see Figure 18). The hydrogen engine demonstrates a more efficient use of boost pressure at medium-to-low speeds compared to the Diesel baseline. For instance, at 1200 rpm the hydrogen configuration achieves a volumetric efficiency of 2.3, only slightly lower than the 2.5 observed for the Diesel case, despite operating with a significantly lower boost pressure (2.15 vs. 2.85 bar). This improvement is related to the optimized valve lift profile and timing, which introduce a small overlap period that enhances the air-exchange process. The advantages of this strategy are further illustrated in Figure *19* a-b, which presents the compressor map at full load. The hydrogen engine consistently operates at lower boost pressures than the Diesel/HVO version across almost the entire speed range, and the operating points fall in a region of higher compressor efficiency. With the turbine rack maintained in a more open position, both the compressor and turbine work under favourable conditions reducing losses.

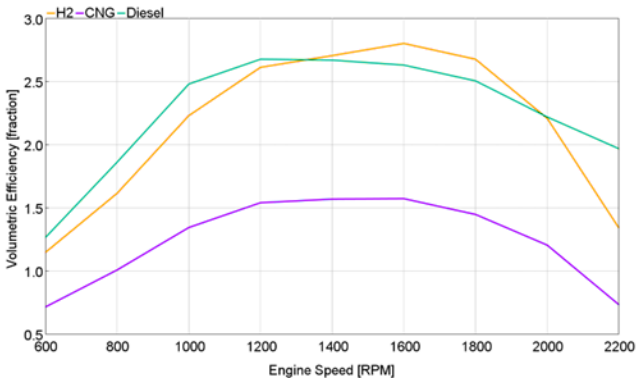

Figure 17: Volumetric efficiency comparison among CNG/biomethane, hydrogen and diesel/HVO engine at full load.

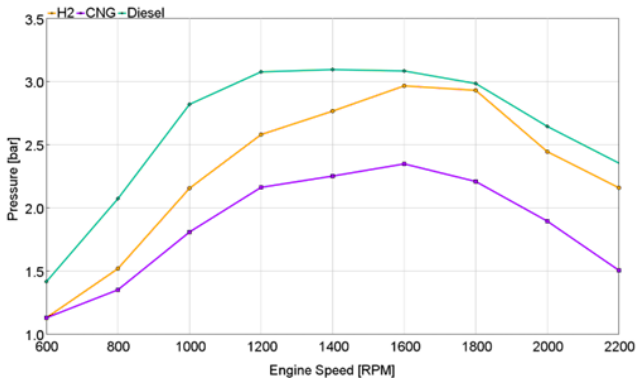

Figure 18: Boost pressure comparison among CNG/biomethane, hydrogen and Diesel/HVO engine at full load.

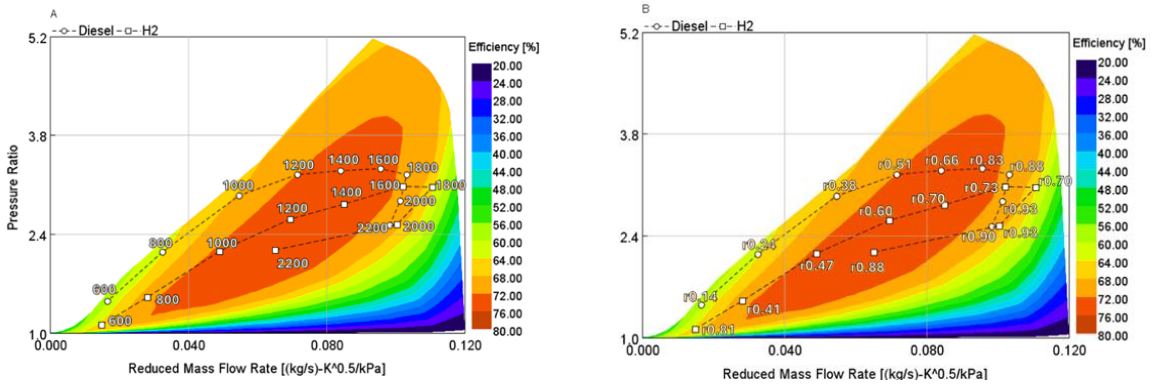

Figure 19: Compressor working condition comparison between Diesel/HVO and the hydrogen engine at full load. a) operating points with engine speed. b) operating points with rack position.

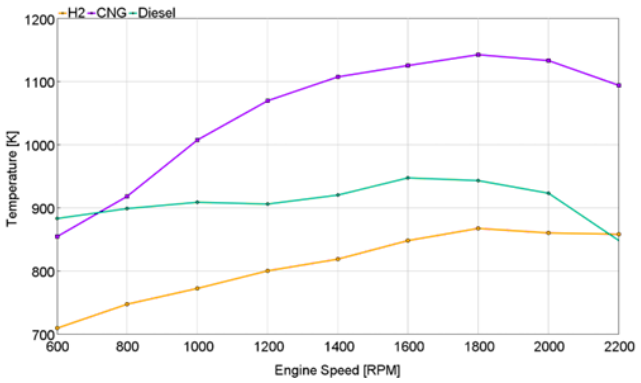

Figure 20: TIT comparison among CNG/biomethane, Hydrogen and Diesel/HVO engine at full load.

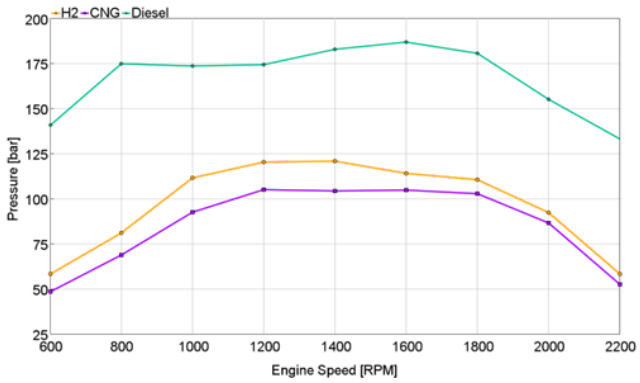

Figure 21: peak cylinder pressure comparison among CNG/biomethane, Hydrogen and Diesel/HVO engine at full load.

Figure 20 and Figure 21 compare the TIT and the maximum in-cylinder pressure. The hydrogen engine shows slightly higher peak pressures than the bio-methane configuration (approximately 120 vs. 105 bar), but the TIT is significantly lower (peak values around 880 K compared to 1150 K). As a result, the hydrogen configuration experiences lower thermal stress on the piston, exhaust manifold, and turbine, while the gas-pressure-induced loads remain comparable. This behaviour aligns with expectations, as the hydrogen engine operates under ultra-lean conditions, whereas the bio-methane engine relies on stoichiometric combustion.

The brake torque, brake power, and BTE curves, shown in Figure *22*, Figure *23* and Figure *24*, confirm that the hydrogen and bio-methane engines deliver nearly identical performance, as imposed during the setup of the hydrogen model to match the reference CNG configuration, approximately 20% lower than the Diesel/HVO configuration. This reduction in output is primarily due to emission-control limitations. In the Diesel/HVO cases, pollutant reduction depends on a complex after-treatment system combining oxidation catalyst, particulate filter, and SCR unit. The bio-methane configuration employs a simpler three-way catalyst, which constrains the maximum allowable exhaust-gas temperature and thus limiting the output power. For the hydrogen configuration, the most restrictive constraint is the control of NOx emissions: increasing load further would make compliance difficult without adopting an equally complex after-treatment system.

As shown in Figure *24*, the Diesel/HVO configuration achieves the highest BTE values, mainly due to its higher compression ratio and lower heat losses compared with the CNG/bio-methane case. Despite this disadvantage, the hydrogen engine matches the Diesel efficiency at low engine speeds and remains consistently more efficient than the CNG/bio-methane configuration throughout the operating range.

Overall, the full-load results confirm that the biodiesel configuration effectively reproduces Diesel performance with minimal recalibration, the bio-methane configuration ensures clean operation at lower efficiency, and the hydrogen configuration combines low thermal stress and moderate mechanical loads with near-Diesel efficiency with the advantage of zero CO_2 emissions at the tail pipe.

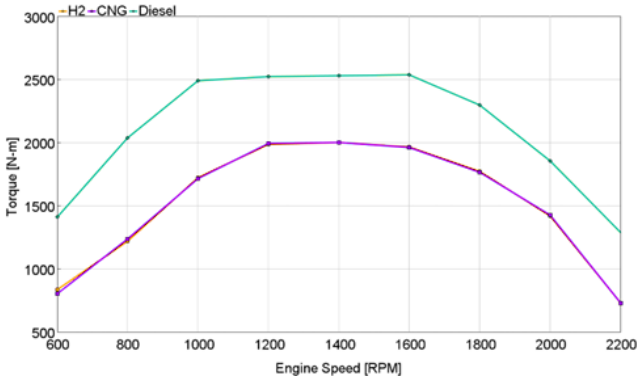

Figure 22: Brake torque comparison among CNG/biomethane, Hydrogen and Diesel/HVO engine at full load.

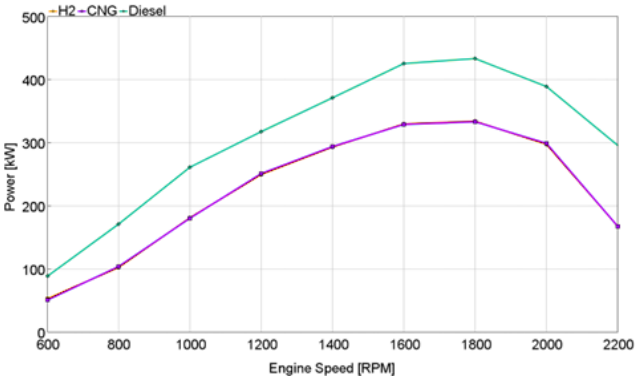

Figure 23: Brake power comparison among CNG/biomethane, Hydrogen and Diesel/HVO engine at full load.

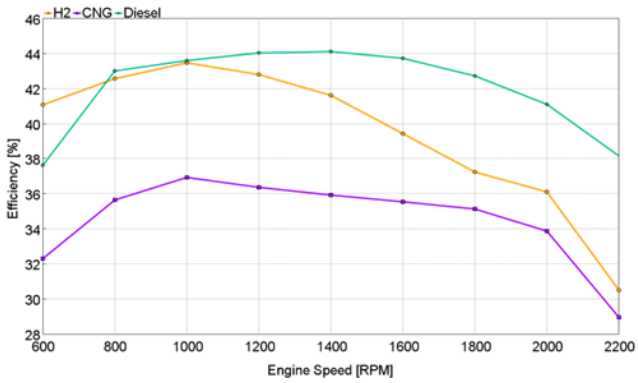

Figure 24: BTE comparison among CNG/biomethane, Hydrogen and Diesel/HVO engine at full load.

2.5. Final comparison: partial load

Partial-load operation was investigated with particular reference to the twelve reference points defined by the European Stationary Cycle (ESC) procedure [101]. The control strategy applied in the simulations varies depending on the engine type. For the CNG/bio-methane configuration, a stoichiometric mixture was maintained over the entire operating range to ensure the highest conversion efficiency of the three-way catalyst. Within the model, the curve of burnt fuel remains unchanged from full to partial load, at constant speed. Although this represents a simplified assumption, the influence on the predicted brake performance is limited, since the turbulent combustion process shows only a weak dependence on the initial charge pressure. Particular attention was paid to the coordination between the WG and the throttle valve to minimize pumping losses. At

medium-to-high loads, the brake output was regulated by the WG position while the throttle remained fully open, whereas at low loads the throttle was progressively closed and the WG held open to reduce airflow and maintain the target mixture strength.

A comparable strategy was adopted for the hydrogen configuration, following the same approach described before. For the HVO case, instead, the engine load was controlled by adjusting the injected fuel quantity. The turbine rack position was kept as open as possible to limit pumping losses, while ensuring compliance with the minimum air–fuel ratio required at each speed to avoid exceeding the smoke limit.

Figure 25 compares the BTE obtained for the twelve ESC operating modes. The letters A, B, and C correspond to low, medium, and high engine speeds respectively, while the accompanying number indicates the percentage of load (for instance, *A50* refers to 50 % load at low speed). The Weighted Average efficiency (*WA*) was calculated from the twelve modes, excluding idle, according to the regulatory weighting factors.

The Diesel/HVO configuration clearly achieves the highest overall efficiency, while the CNG/bio-methane version shows the lowest values. The hydrogen engine nearly matches the HVO performance at low speed, although the difference becomes more pronounced at higher speeds. On a weighted basis, the hydrogen configuration attains an average efficiency of about 37 %, compared with 41 % for HVO and 34 % for CNG/bio-methane.

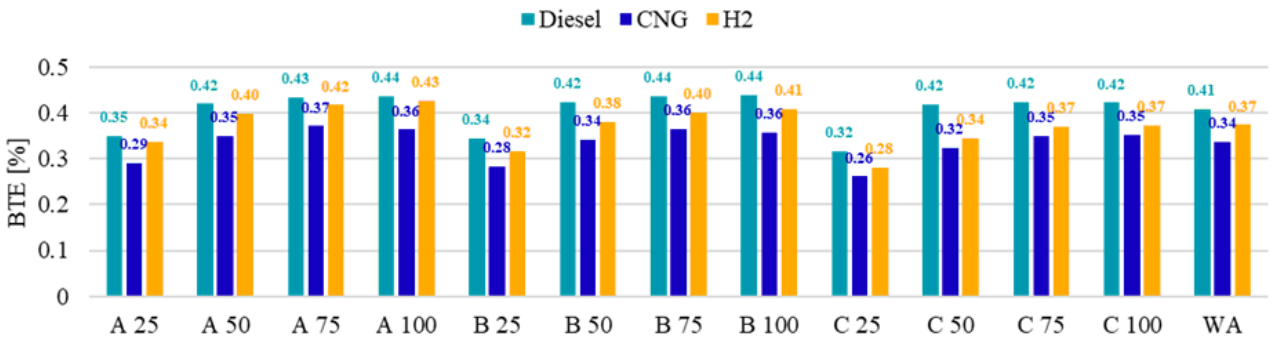

Figure 25: Comparison among HVO, bio-methane and hydrogen. BTE at different operating condition (ESC test). WA= Weighted Average.

2.6. Final remarks and conclusions

The comparative numerical analysis confirms that all the investigated fuels (HVO, bio-methane, and hydrogen) represent technically viable options for reducing the environmental impact of HD engines.

However, none of them can be considered a universal solution, as each presents distinct advantages and limitations depending on the specific application scenario.

Biodiesel demonstrates the highest brake performance and thermal efficiency among the analysed fuels (max brake power= 420 kW and BTE_{max}=44%), behaving as a true drop-in alternative that can be adopted in existing Diesel engines with minimal calibration adjustments. Its main strengths lie in the immediate applicability and compatibility with current hardware, which make it a short-term option for carbon reduction in HD fleets. Nevertheless, the complex and costly exhaust after-treatment system required to meet stringent emission limits, along with uncertainties regarding large-scale feedstock availability, may limit its long-term sustainability.

Bio-methane also offers straightforward integration into existing spark-ignited natural gas engines, ensuring clean combustion and lower CO_2 emissions compared to fossil fuels. However, its BTE remains lower than that of biodiesel and hydrogen (BTE_{max}=37%), and the fuel storage system is more demanding and expensive than that of liquid fuels, even though less critical than for hydrogen. Availability and logistics of renewable methane could also represent constraints for future deployment on a wide scale.

Green hydrogen emerges as the most environmentally promising solution, providing virtually zero CO_2 emissions and drastically reduced NO_x levels without the need for complex after-treatment systems when engine runs in lean/ultra-lean fuel mixtures. The simulated configuration achieved power and torque levels comparable to the CNG/bio-methane engine (by design, as imposed during the hydrogen model setup) while offering higher thermal efficiency (max brake power= 330 kW, BTE_{max}=43.8%), particularly at low and medium speeds. These results indicate that spark-ignited hydrogen engines can approach the efficiency of Diesel systems and even rival fuel-cell performance in specific conditions. On the other hand, hydrogen combustion still poses significant challenges, including high-pressure on-board storage, safety considerations, and the current lack of a mature production and distribution infrastructure. Moreover, the engine conversion requires non-negligible hardware modifications, involving the redesign of the combustion chamber, the fuel injection and ignition systems.

Within the broader scope of this PhD research, this activity focused on evaluating the technical feasibility and environmental potential of alternative sustainable fuels as substitutes for fossil ones, with the aim of extending the life of Diesel engine technology for HD transport applications. This topic is particularly relevant considering the complexity of electrifying this sector, where internal combustion engines are still indispensable for energy density and operational flexibility.

The analysis showed in these pages, represented an essential step in the overall PhD research path, as it provided a comprehensive evaluation of the potential of sustainable fuels for HD engines and clarified the trade-offs between performance, efficiency, and emissions. The results obtained in this phase offered the necessary background to identify the most promising directions for further investigation. Among the considered fuels, hydrogen emerged as the most interesting option for long-term decarbonization, despite its intrinsic challenges related to storage, infrastructure, and combustion control. Its outstanding properties, such as the absence of CO_2 emissions and the potential for ultra-lean, clean combustion, make it a strong candidate for future HD applications.

In recent years, hydrogen has gained growing attention within the scientific and industrial communities, becoming a central element of the European Hydrogen Strategy which identify it as a key enabler of the energy transition [89,90]. This context further motivated the decision to focus the following phase of this PhD work on hydrogen utilization in internal combustion engines, aiming to explore its real potential and limitations in a more advanced and physically detailed framework.

For this reason, the next chapters will be devoted to the dual-fuel Diesel–hydrogen combustion concept, investigating the in-cylinder phenomena mainly through 3D-CFD analyses. This methodological shift, from system-level comparison to detailed combustion modelling, allows a deeper understanding of hydrogen's behaviour in Diesel-based architectures, providing insight into its capability to significantly reduce CO_2 emissions while maintaining the efficiency and robustness that characterize conventional compression-ignition engines.

3. Numerical exploration of diesel-hydrogen dual-fuel combustion: up to 80% of hydrogen share

3.1. Introduction to the dual fuel combustion concept

Dual-fuel (DF) combustion is a hybrid strategy that combines two fuels of different reactivities to control ignition and combustion phasing inside compression-ignition engines. The high-reactivity fuel (typically diesel) is directly injected into the combustion chamber to act as the ignition source, while the low-reactivity fuel is premixed with air before intake, forming a homogeneous or partially stratified charge. This configuration enables ignition control via the diesel pilot injection while maintaining the high thermal efficiency typical of compression ignition operation. Although DF operation is often associated with modern low-carbon combustion strategies, it is not a new concept. This operating mode was already known in the previous century, not only for diesel-methane configurations but also with other gaseous fuels as demonstrated for instance by the work by Elliott and Davis in 1951, where several gaseous fuels, including natural gas, propane, butane, and hydrogen, were tested in a diesel engine under DF conditions [102].

Over the years, DF operation has attracted growing interest as a viable pathway to reduce the environmental impact of compression-ignition engines. As summarized by Wei and Geng (2016), natural gas, the most extensively studied gaseous fuel in DF applications, offers an illustrative example of the potential advantages of this concept. Natural gas is characterized by a higher hydrogen-to-carbon ratio, lower aromatic content, and cleaner combustion compared with diesel, which results in significant reductions in CO_2 and PM emissions under properly optimized conditions [103,104]. These benefits arise primarily from the lower carbon content and the more homogeneous combustion process typical of premixed gaseous fuels. At the same time, DF operation presents typical challenges such as higher HC and CO emissions at low load ([105–107]) and increased NO_x formation at high load, which underline the importance of controlling the diesel pilot injection and mixture formation [105,106].

Table 4: hydrogen physicochemical properties [108,109]

Property	Value
Carbon content (mass %)	0
Molar mass (g/mol)	2.016
Density (@1bar, 273 K; kg/m^3)	0.089
Lower Heating Value (LHV) (MJ/kg)	119.9
Stoichiometric air-to-fuel ratio (α_{st}) (-)	34.1
LHV* = LHV/α_{st} (MJ/kg)	3.52
Volumetric energy content (@1bar, 273 K; MJ/m^3)	10.7
Boiling point (K)	20
Auto-ignition temperature (K)	853
Minimum ignition energy in air (@1 bar, α_{st}; mJ)	0.017
Quenching distance (@1 bar, 298 K, α_{st}; mm)	0.64
Laminar flame speed in air (@1 bar, 298 K, α_{st}; m/s)	1.85
Diffusion coefficient in air (@1 bar, 273 K; m^2/s)	8.5 x 10^{-6}
Flammability limit in air (volume %)	4-76
Flammability limit in air (λ)	10-0.14
Adiabatic flame temperature (@1 bar, 298 K, α_{st}; K)	2480
Octane number ([RON+MON]/2)	130+
Cetane number (-)	/

In this context, hydrogen has been studied as an alternative fuel for internal-combustion engines for many decades, owing to its wide flammability range, high diffusivity, and clean-burning nature (see Table 4). Nevertheless, the growing global effort toward carbon neutrality, together with the rapid progress in hydrogen production, storage, and infrastructure, has further pushed research into diesel–hydrogen DF engines, positioning them as a promising pathway to drastically reduce CO_2 emissions without abandoning compression-ignition technology.

Building upon the consolidated knowledge developed in the field of diesel–methane DF combustion, and leveraging the previous experimental and numerical investigations conducted by the research group on this topic [110–112], the present work represents a natural evolution of that scientific pathway. The methodologies, modelling approaches, and diagnostic experience gained in studying diesel–methane DF operation have provided a solid foundation and a technical springboard for addressing the more demanding conditions of diesel–hydrogen DF combustion, where the nearly carbon-free nature of the gaseous component introduces new opportunities, but also new challenges, in terms of ignition control, mixture formation, and emission behaviour.

3.2. Objectives

The first part of this research focused on numerically exploring the potential and limitations of hydrogen–diesel DF combustion in a light-duty compression-ignition engine. While the adoption of hydrogen in internal combustion engines has been widely studied, most investigations have been limited to spark-ignited or fully hydrogen-fuelled configurations. In contrast, the DF mode offers the possibility to progressively replace diesel with hydrogen, maintaining the advantages of compression ignition while significantly reducing carbon-based emissions. This activity led to the publication of a scientific paper titled *"Exploring Hydrogen–Diesel Dual Fuel Combustion in a Light-Duty Engine: A Numerical Investigation."* [113].

The main objective of this study was to investigate the feasibility of replacing a significant portion of the energy conventionally supplied by diesel fuel with hydrogen, while preserving the original engine architecture with minimal modifications. The analysis aimed to evaluate the potential of such an approach in terms of combustion stability, efficiency, and mechanical integrity. Particular emphasis was placed on the influence of the diesel injection strategy, since the baseline injection law was originally optimized for conventional diesel operation.

To achieve these objectives, a 3D-CFD numerical campaign was carried out using a model previously validated against experimental data under both conventional diesel and hydrogen–diesel conditions. Two representative operating points of a light-duty 2.8 L High-Speed Direct-Injection (HSDI) diesel engine were considered, covering partial- and full-load regimes. For each operating condition, the total injected energy was kept constant while progressively increasing the hydrogen contribution up to 80% of the total fuel energy.

The numerical approach adopted in this work allowed isolating the intrinsic effects of hydrogen substitution on mixture formation, ignition delay, and combustion development. A dedicated parametric sweep of the start of injection (SOI) was carried out at each hydrogen share to investigate the role of injection phasing in controlling the combustion and maximizing overall efficiency.

The results of this activity provided a first comprehensive insight into the behaviour of hydrogen–diesel DF combustion in a light-duty compression-ignition engine, establishing the foundation for the subsequent optimization work presented in the following sections.

3.3. Engine description and modelling framework

The reference engine is a 2.78 L, in-line, 4-Stroke HSDI diesel for automotive use, manufactured by FCA-VM Motori in Cento (FE), Italy, featuring four valves per cylinder, common-rail injection and six-hole injectors. The combustion chamber is an omega-shaped bowl in the piston (bowl volume 32.8 cm³, squish height 0.9 mm); the main geometric data include are summarized Table 5.

Table 5: Main features of the HSDI 4-Stroke selected engine.

Engine Parameter	**Value/Description**
Engine Type	HSDI 4-Stroke Diesel, EURO IV
Cylinders	4 in-line
Total displacement (L)	2.78
Bore × Stroke (mm)	94 × 100
Connecting rod length (mm)	159
Compression ratio	17.5:1
Swirl ratio	1.8
N. of valves per cylinder	4
Exhaust valve opening (°CA AFTD)	114
Intake valve opening (°CA AFTD)	337
Exhaust valve closing (°CA AFTD)	389
Intake valve closing (°CA AFTD)	590
Air Metering	Turbocharger with VGT + Intercooler
Injection System	Common rail
Max. Injection press. (MPa)	160
Number of injector holes	6
Injector hole protrusion (mm)	2
Injector hole distance from injector axis (mm)	1.35
Injector hole diameter (mm)	0.153
Max. brake power (kW@rpm)	130@3800
Max. brake torque (Nm@rpm)	440@1750
Max. peak in-cylinder pressure (bar)	150
Max. Engine Speed (rpm)	4600

Figure 26: Cross section of a 60° sector of the combustion chamber with injector shape

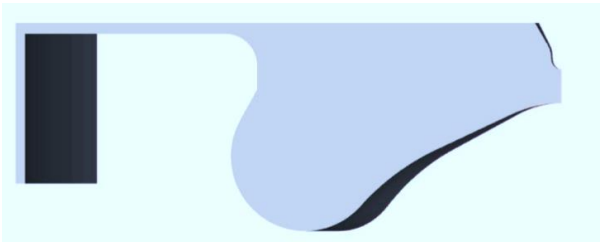

Figure 27: Computational grid at TDC

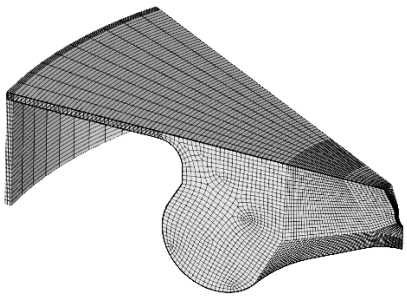

Table 6: Main models used for 3D-CFD AVL FIRE M setup

Physical/Numerical model	Model adopted
Turbulence model	k-zeta-f
Wall treatment	Hybrid
Wall heat transfer model	Standard
Breakup model	Kelvin-Helmhotz/Rayleigh-Talor
Wall interaction model	Kunke
Turbulent dispersion model	Solved
Fuel evaporation model	Dukowicz
Diesel surrogate (gas phase)	C_7H_{16}
Combustion model	AVL WCFM-3Z
Auto ignition model	Two-Stage
Laminar flame speed	AVL database
Auto ignition delay	AVL database
NOx model	Thermal mechanism

Table 7: Main features of the computational grid.

Mesh property	Value
Volume cell size (mm)	1.3 (0.65 from -30 to +30 °CA AFTDC)
Boundary layer thickness (mm)/n. of layers	0.1/2
Number of cells @ TDC	~70,000
Crevices: thickness × height (mm)	0.8 × 12.7

The 3D-CFD analysis was carried out on a sector model corresponding to one injector hole (60° of the full geometry), exploiting the geometric symmetry of the six-hole injector. This approach allows the numerical cost to be significantly reduced while maintaining a physically accurate representation of spray evolution and combustion development within the chamber. The computational domain is shown in Figure 26.

The moving mesh was generated using AVL FAME M (see Figure 27), while the simulations were performed in AVL FIRE M [114], solving the Reynolds-Averaged Navier–Stokes (RANS) equations with the k–zeta–f turbulence model as closure [115]. The main models adopted for the simulation are summarized in Table 6. Fuel atomization and breakup were modelled through the Kelvin–Helmholtz/Rayleigh–Taylor (KH–RT) approach [116], while the gas phase was modelled with n-heptane (C_7H_{16}) as diesel surrogate. Combustion was simulated using 3-Zones Extended Coherent Flame Model (ECFM-3Z, [117]), which can capture both diffusion-controlled and premixed combustion modes. This model provides an excellent compromise between accuracy and computational cost, since it relies on the AVL laminar flame-speed database, allowing an efficient yet physically consistent representation combustion processes.

The swirl ratio imposed at intake-valve closure was 1.8, and the piston–liner crevice volume was included in the computational domain to correctly reproduce the effective compression ratio as shown

in Figure 26 and Figure 27. The main mesh characteristics are summarized in Table 7. A mesh and time-step sensitivity analysis was conducted to ensure numerical independence of the results. Three different average cell sizes were considered: 1.3 mm, 0.65 mm, and 0.2 mm, while three crank-angle steps (0.25°, 0.1°, and 0.01° CA) were tested during the injection and combustion phases. The analysis was performed at 4000 rpm – 13.5 bar BMEP, corresponding to the full-load diesel operation. The results showed that the meshes with 0.65 mm and 0.2 mm average cell size provided identical in-cylinder pressure traces and heat-release profiles, confirming grid independence. Therefore, the 0.65 mm mesh was adopted for all simulations as the best compromise between resolution and cost. Similarly, the time-step sensitivity study revealed that 0.1° CA produced the same peak pressure as 0.01° CA, and was therefore chosen for the main campaign to minimize computational time. The detailed results of the mesh and time-step sensitivity analyses are omitted for brevity reason.

The 3D-CFD model was then validated against the selected diesel experimental data (2400 rpm – 10.5 bar BMEP and 4000 rpm-13.5 bar BMEP), whose main parameters are listed in Table 8. Figure 28 compares the simulated and measured in-cylinder pressure and Apparent Heat-Release Rate (AHRR; equation (1)). The agreement is good in both cases, although the model slightly underestimates the peak AHRR at all loads. The main combustion parameters: gross indicated mean effective pressure (IMEP*; equation (2)), peak pressure, and combustion phasing (CA10, CA50, CA90), are reported in Table 9 and Table 10, confirming the small and acceptable error between simulated results and experimental data.

$$\mathrm{AHRR} = \frac{\mathrm{k}}{\mathrm{k}-1}\mathrm{p}\frac{\mathrm{dV}}{\mathrm{d}\theta} + \frac{1}{\mathrm{k}-1}\mathrm{V}\frac{\mathrm{dp}}{\mathrm{d}\theta} \quad (1)$$

$$\mathrm{IMEP}^{*} = \frac{1}{V_d}\int_{\mathrm{IVC}}^{\mathrm{EVO}} \mathrm{pdV} \quad (2)$$

Table 8: Diesel validation cases: main parameters for experiments and numerical simulations.

Engine Parameter	2400 rpm-10.5 bar BMEP		4000 rpm-13.5 bar BMEP	
	Exp.	Num.	Exp.	Num.
Pressure @ IVC (bar)	2.5	2.5	1.5	1.5
Trapped mass (mg/cycle/cyl)	1283.5	1283.5	1640.2	1639.1
Diesel mass (mg/cycle/cyl)	52.00	52.00	69.70	69.60
Disel SOI pilot (°CA AFTDC)	-14.7	-14.7	-	-
Disel in pilot injection (mass%)	1.1	1.1	-	-
Diesel SOI pre (°CA AFTDC)	-0.6	-0.6	-	-
Diesel in pre injection (mass%)	2	2	-	-
Diesel SOI main (°CA AFTDC)	10.5	10.5	-12.0	-9.0
Diesel in main injection (mass%)	96.8	96.8	100	100
Residuals * (mass%)	7	7	5	5
EGR (mass%)	0	0	0	0
Swirl ratio (-)	1.8	1.8	1.8	1.8
Head temperature	-	500	-	500
Liner temperature	-	480	-	480
Piston temperature	-	520	-	520

*based on the results of a validated GT-Power model of the full engine

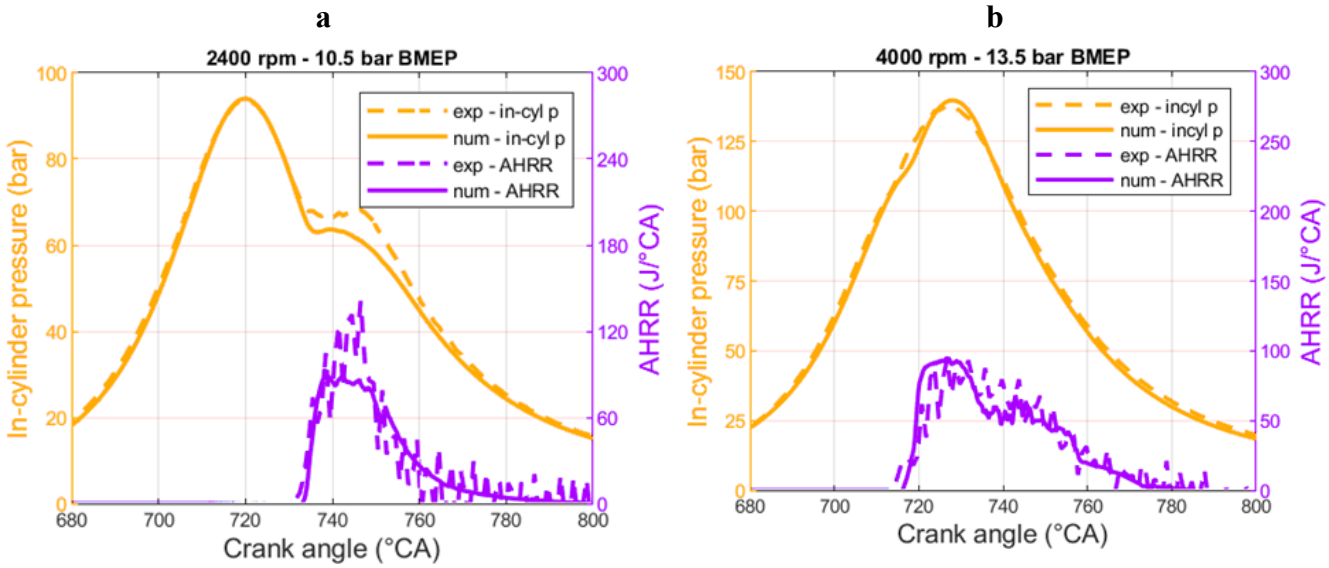

Figure 28: Experimental vs numerical comparison in terms of in-cylinder pressure and AHRR: a) 2400 rpm-10.5 bar BMEP. a) 4000 rpm-13.5 bar BMEP.

Table 9:Experimental vs numerical comparison in terms of IMEP*, peak in-cylinder pressure and combustion phasing parameters: 24000 rpm -10.5 bar BMEP.

Engine parameter	Exp.	Num.	Absolute error
IMEP* (bar)	11.30	10.61	0.69
Peak in-cylinder pressure (bar)	93.74	93.97	0.23
CA10 (°CA AFTDC)	17.5	17.8	0.3
CA50 (°CA AFTDC)	24.5	27.0	2.5
CA90 (°CA AFTDC)	38.5	43	4.5
Δθ10-90 (°CA)	21.0	25.2	4.2

Table 10: Experimental vs numerical comparison in terms of IMEP*, peak in-cylinder pressure and combustion phasing parameters: 4000 rpm -13.5 bar BMEP.

Engine parameter	Exp.	Num.	Absolute error
IMEP* (bar)	21.70	21.25	0.27
Peak in-cylinder pressure (bar)	138.00	139.70	1.6
CA10 (°CA AFTDC)	2.8	2.9	0.1
CA50 (°CA AFTDC)	17.8	18.8	1
CA90 (°CA AFTDC)	42.8	46.0	3.2
Δθ10-90 (°CA)	40.0	43.1	3.1

Table 11: Main features of the DF optical accessed engine

Engine Parameter	Value/Description
Engine type	4-stroke, single cylinder, optically accessible
Stroke (mm)	92
Bore (mm)	85
Cylinder volume displacement (cm3)	522
Combustion bowl volume (cm3)	19.7
Compression ratio	16.5:1
Number of valves	4
EVO (CA °AFTDC)	116
IVO (CA °AFTDC)	344
EVC (CA °AFTDC)	380
IVC (CA °AFTDC)	588
Diesel injection system Common rail	
Number of holes	7
Cone angle of fuel jet axis (deg)	148
Hole diameter (mm)	0.141
Hydrogen PFI injection system	
Number of holes	1
Maximum injection pressure (bar)	5

Following the validation under conventional diesel operation, a dedicated calibration of the DF configuration was carried out to ensure that the model could reliably reproduce hydrogen–diesel combustion behaviour. Since no experimental data were available for the VM 2.8 L engine operating in DF mode, the CFD setup was first tuned and validated on a single-cylinder optically accessible research engine, operated in DF hydrogen–diesel mode at 2000 rpm. This engine, whose main specifications are reported in Table 11, was specifically modified by the researchers of the CNR-STEMS laboratory to operate under DF conditions [118,119]. It featured a seven-hole injector and hydrogen supplied through the intake manifold. It should be noted that this optically accessible engine is similar to the reference VM engine considered in this work, thus providing a representative test platform for model calibration.

Table 12: Comparison between experimental data and numerical results of the CNR-STEMS hydrogen-diesel DF single cylinder optically accessible engine.

Engine parameter	Exp.	Num.	Absolute error
Engine speed (rpm)	2000		-
IMEP* (bar)	4.38	4.88	0.5
Experimental peak in-cylinder pressure (bar)	60.2	59.8	0.4
CA10 (°CA AFTDC)	-0.8	0.2	1
CA50 (°CA AFTDC)	9.4	9.6	0.2
CA90 (°CA AFTDC)	22.2	24.8	2.6
CA10-90 (°CA)	23	24.6	1.6

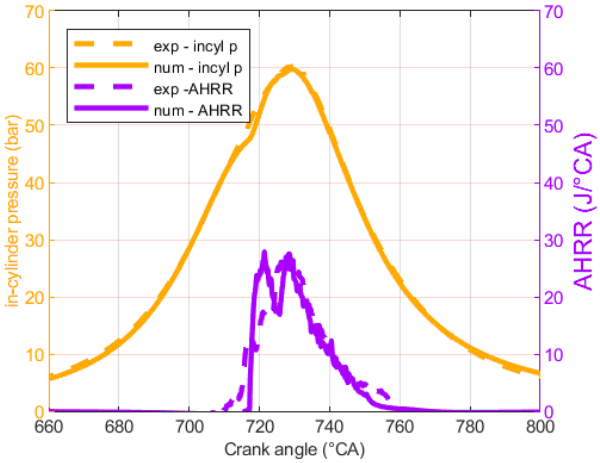

Figure 29: Comparison between experimental and numerical in-cylinder pressure and AHRR of the single cylinder, optically accessible H2-D DF engine.

The calibration procedure focused on adapting the combustion and injection sub-models to capture the specific characteristics of DF operation. In particular, the parameters governing auto-ignition delay, flame development, and premixed burning in the ECFM-3Z model were adjusted to match the measured in-cylinder pressure and AHRR. The comparison between simulated and measured traces showed a very good agreement in terms of pressure evolution, ignition delay, and combustion phasing, while maintaining an accurate prediction of IMEP* and overall combustion efficiency. The validation results, summarized in Table 12 and Figure 29, confirm the capability of the model to reproduce the key features of hydrogen–diesel DF combustion across different operating conditions.

Once the calibration was completed, the same validated setup was transferred to the 2.78 L VM engine model, without introducing further tuning parameters, ensuring a consistent and physically based methodology for the subsequent numerical campaign.

The validated sub-model parameters derived from this calibration were then implemented in the CFD model of the VM engine. This approach ensured that the numerical investigation of hydrogen–diesel DF combustion on the VM engine was carried out on a reliable and experimentally grounded modelling framework.

3.4. Experimental setup

The experimental investigations used to support the numerical work were carried out on two distinct engine test benches, located at the Department of Engineering “Enzo Ferrari” of the University of Modena and Reggio Emilia (UNIMORE) and at the CNR-STEMS research center. Both facilities

were employed to characterize the combustion and performance behaviour of the two engines considered in this study: the 2.8 L VM Motori diesel engine, which represents the reference configuration, and the single-cylinder optically accessible research engine used for DF calibration.

The first experimental campaign was conducted on the 2.8 L, four-cylinder turbocharged diesel engine described in Table 5. Tests were performed at the UNIMORE engine laboratory using an Apicom FR400 BRV eddy-current dynamometer, controlled by Apicom Horus software. The test bench was equipped with standard sensors for monitoring air and exhaust pressure and temperature, together with a Coriolis flow meter for accurate measurement of diesel fuel consumption. The in-cylinder pressure was recorded by means of a Kistler piezoelectric transducer connected to a charge amplifier and synchronized with an optical encoder. A high-frequency indicating system enabled crank-angle-resolved acquisition with an angular resolution of 0.3° CA. The data acquisition system was based on National Instruments Compact RIO hardware, while real-time data processing was handled by Alma Automotive software.

The second experimental setup, located at the CNR-STEMS laboratory, was employed for the characterization of the hydrogen–diesel DF combustion. The test engine is a single-cylinder compression-ignition research engine (see Table 11), equipped with an extended piston featuring a 46 mm flat sapphire window on the crown, which provides optical access to the combustion chamber. A 45° mirror integrated into the piston directs the optical signal towards high-speed visible and infrared cameras, allowing visualization of the entire combustion process. The engine retains its original four-cylinder common-rail injection system, managed by an open ECU, which enables full control of injection timing, pressure, and duration.

For the hydrogen supply, a port fuel injector was installed on the intake manifold, fed by a compressed gas line regulated at 5 bar. The injector operates once the exhaust valves are closed, ensuring homogeneous mixing of hydrogen and air without short-circuiting. The ECU synchronizes the diesel and hydrogen injection systems, with a delay unit ensuring precise timing alignment between the two injection events.

Additional instrumentation includes:

- Air flow and pressure monitoring: Intake air is filtered, dehumidified, and conditioned in temperature and pressure; the Sensyflow FMT500-IG measures the air mass flow rate.
- Gaseous fuel system: The hydrogen line is equipped with a pressure regulator, flame arrester, and flame trapper. The hydrogen mass flow rate is measured using a Brooks thermal mass flow meter.

- Data acquisition: In-cylinder pressure is measured via a piezoelectric transducer, while the signals of the diesel and PFI injectors are recorded prior to the injectors. Data are acquired every 0.2° CA, with a 200-cycle average used to compute the AHRR via thermodynamic analysis.

This combined experimental framework enabled both model validation under diesel operation and model calibration under hydrogen–diesel DF conditions, providing a robust experimental foundation for the CFD analysis presented in this work.

3.5. Simulation methodology

The updated CFD model of the VM 2.8 L diesel engine was employed to investigate the influence of increasing hydrogen energy contribution on the combustion process and engine performance at both partial and full-load operating conditions, namely 2400 rpm – 10.5 bar BMEP and 4000 rpm – 13.5 bar BMEP, respectively.

For each operating point, a series of simulations was carried out by progressively increasing the hydrogen energy share (H_2 energy share) to 20 %, 40 %, 60 %, and 80 % of the total fuel energy supplied in the corresponding diesel case. The total injected energy was maintained constant across all simulations. The progressive substitution of diesel fuel was achieved by reducing the mass injected during the main injection event, as illustrated in Figure 30, while keeping the injection pressure and nozzle geometry unchanged.

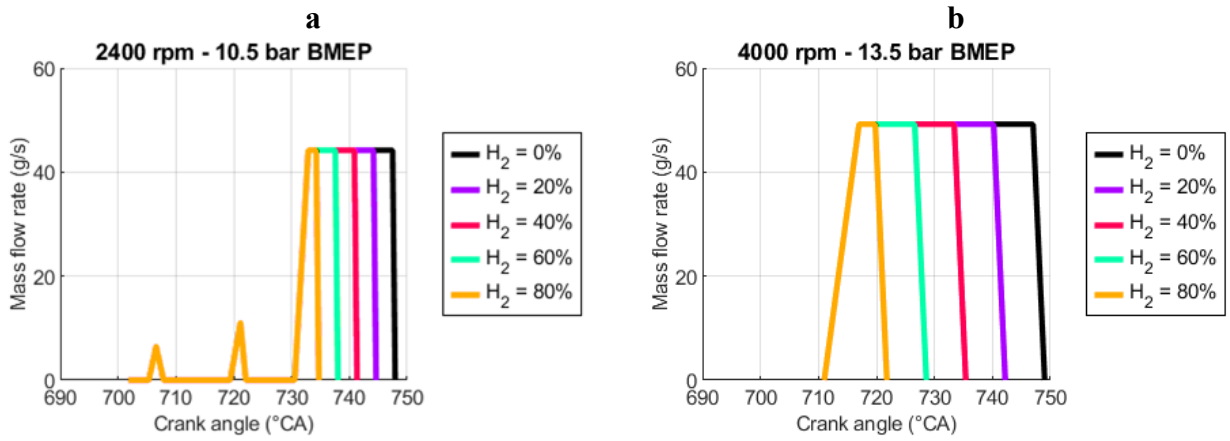

Figure 30: Diesel fuel injection strategy for Diesel (black line) and hydrogen-diesel DF operation with increasing H2 energy share: a) 2400 rpm – 10.5 bar BMEP; (b) 4000 rpm – 13.5 bar BMEP

Although port-fuel injection of hydrogen typically leads to a decrease in volumetric efficiency due to displacement of intake air, this phenomenon was not explicitly considered in the present CFD analysis. Instead, it was assumed that the total trapped mass at intake-valve closure (IVC) remained constant for all cases. This modelling approach allows isolating the pure effect of hydrogen substitution on mixture formation, ignition, and combustion development, without the confounding influence of varying boundary conditions. Such an assumption is still physically consistent, as the same conditions can be achieved experimentally by suitably adjusting the turbocharger control to compensate for the air displacement effect.

After evaluating the effect of increasing hydrogen substitution on the combustion behaviour, an additional parametric sweep of the Start of Injection (SOI) was performed for each operating point. This analysis was motivated by the progressive transition of DF combustion from diffusion-dominated to premixed-dominated as the diesel fraction decreases. Consequently, the optimization of the diesel injection phasing becomes essential to recover combustion efficiency and maintain stable operation.

At partial load (2400 rpm), the entire three-pulse injection pattern (pilot, pre, and main) was rigidly shifted in the crank-angle domain, preserving the relative spacing between the pulses. At full load (4000 rpm), characterized by a single main injection, the SOI was varied individually within a suitable range to cover both advanced and retarded combustion regimes.

This methodology enabled the systematic evaluation of the influence of hydrogen energy share and diesel injection timing on the main combustion metrics (namely in-cylinder pressure, AHRR, IMEP*, combustion efficiency, and peak pressure-rise rate (PPRR)) while ensuring consistent thermodynamic boundary conditions across all simulations.

The ultimate objective of these analyses was to recover or even surpass the efficiency observed under conventional diesel operation, demonstrating the feasibility of achieving efficient hydrogen–diesel DF combustion through optimized injection phasing and minimal hardware modifications.

3.6. Results and discussion: Partial load case

Starting from the reference diesel operation at 2400 rpm and 10.5 bar BMEP, representative of a partial-load condition, a progressive replacement of diesel fuel with hydrogen was performed up to a hydrogen energy share of 80 %. The injected diesel mass was proportionally reduced in order to maintain a constant total energy input for each case.

The increase of the hydrogen fraction in the intake mixture leads to a gradual enrichment of the premixed charge. Figure 31 reports the variation of the hydrogen–air equivalence ratio (ϕ_{H_2}) as a function of the hydrogen energy share, calculated according with equation (3):

$$\phi_{H_2} = \frac{\alpha_{s,H_2}}{\left(\frac{m_{a,TOT} - m_{a,D}}{m_{H_2}}\right)} \quad (3)$$

Where:

$\alpha_{s,H2}$ = stoichiometric air-to-fuel ratio for hydrogen (34.0)

$m_{a,TOT}$ = total air mass trapped at IVC

$m_{a,D}$ = air mass reacting with diesel (under stoichiometric assumption)

m_{H2} = trapped hydrogen mass at IVC.

As shown in Figure 31, the equivalence ratio increases with the hydrogen share, reflecting the higher hydrogen concentration in the premixed mixture. In the numerical analysis, the total trapped mass at IVC was kept constant, neglecting the volumetric efficiency penalty typically associated with port-fuel-injected hydrogen. This assumption allows isolating the effects of hydrogen substitution on combustion, although similar conditions can be experimentally reproduced by appropriately controlling the turbocharger operation.

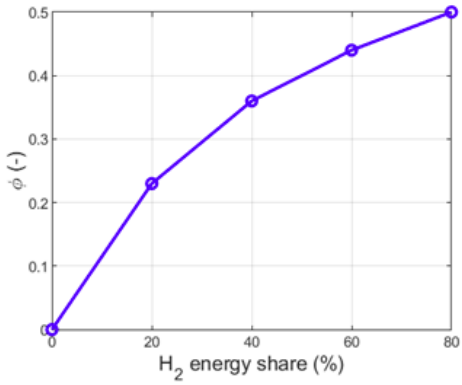

Figure 31: Equivalence ratio variation of the hydrogen-air premixed charge with increasing hydrogen energy share at partial load (2400 rpm – 10.5 bar BMEP).

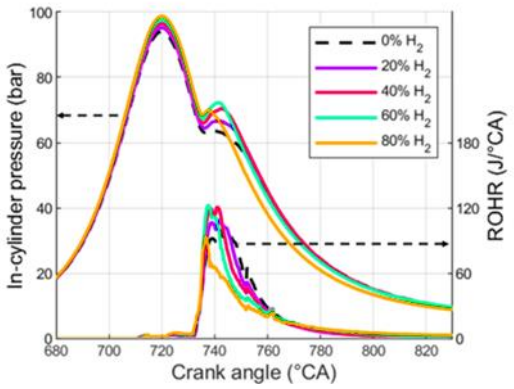

Figure 32: effect of increasing hydrogen energy share on in-cylinder pressure and ROHR at partial load (2400 rpm – 10.5 bar BMEP).

The influence of the hydrogen energy share on the in-cylinder pressure and Rate of Heat Release (ROHR) is shown in Figure 32, while Figure 33 summarizes the corresponding trends of key combustion parameters: peak pressure, PPRR, IMEP*, combustion efficiency (ηc), combustion phasing (CA10, CA50, CA90), and combustion duration (CA10–90). It should be noted that in the

following discussion the ROHR refers to the total rate of heat release, while AHRR represents the difference between the heat released by combustion and the wall heat flux. As the hydrogen energy contribution increases, the in-cylinder pressure at the end of compression (corresponding to the first pressure peak) rises slightly, from about 94 bar to 98.7 bar, mainly due to the higher specific heat ratio γ (equation (4)) of hydrogen–air mixtures compared to air alone.

$$\gamma = \frac{c_p}{c_v} \qquad (4)$$

Where c_p and c_v are specific heat at constant pressure and specific heat at constant volume respectively.

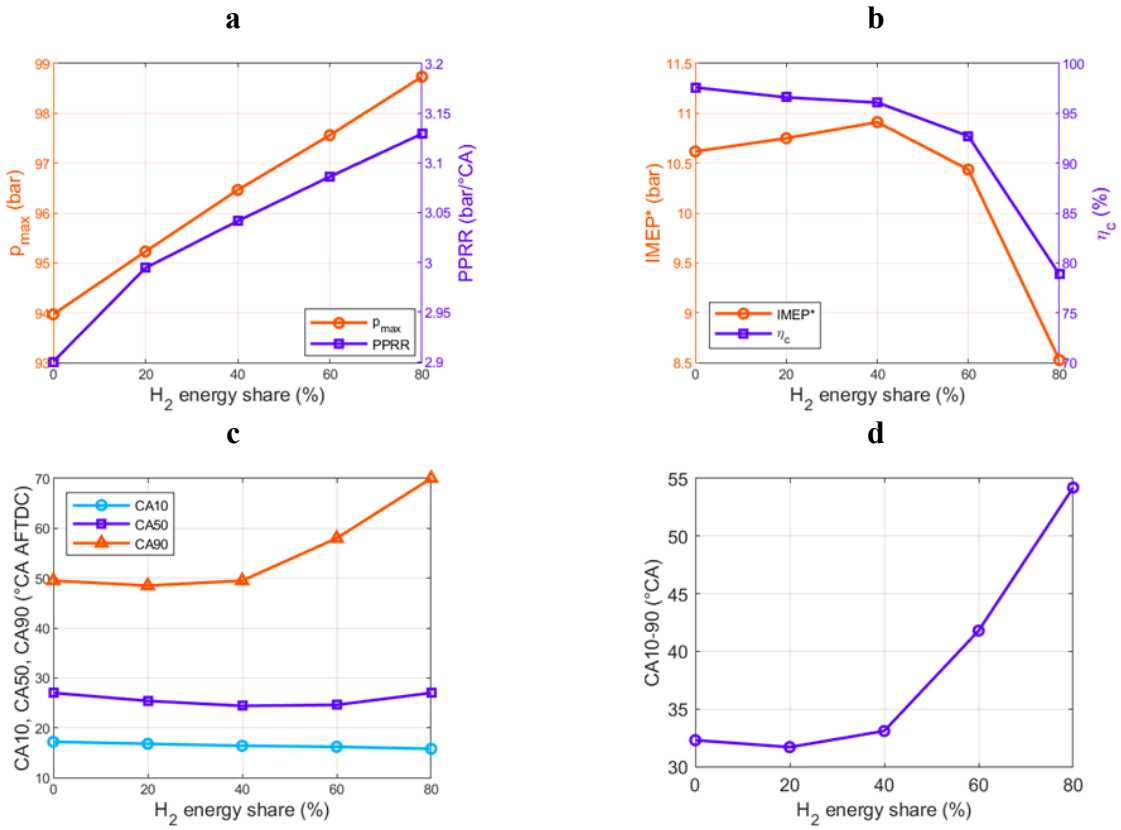

Figure 33: Effect of increasing hydrogen energy share on the main combustion characteristics at partial load (2400 rpm – 10.5 bar BMEP): a) peak in-cylinder pressure and PPRR; b) IMEP* and combustion efficiency; c) combustion phasing parameters; d) turbulent combustion duration.

The PPRR shows only a modest variation, increasing from 2.9 to 3.1 bar/°CA as the diesel is progressively replaced by hydrogen (Figure 33-a). During combustion, the second pressure peak grows up to approximately 60 % H_2-ES, then decreases at 80 %. This behaviour is linked to the corresponding ROHR evolution, which becomes progressively faster up to 60 % H_2-ES due to the

enhanced premixed burning, but then slows down because the reduced diesel quantity provides a weaker ignition source for the leaner mixture.

The IMEP* trend (Figure 33-b) confirms this behaviour. A moderate substitution (up to 40 % H_2-ES) results in an increase of IMEP* by approximately 2.7 % (from 10.6 to 10.9 bar) compared with the diesel baseline, due to faster and more efficient combustion phasing. Beyond this threshold, the performance deteriorates, with a maximum reduction of about 19.6 % at 80 % H_2-ES (down to 8.5 bar). This drop is mainly attributed to a decrease in η_c, which worsens continuously with increasing hydrogen share (maximum reduction ≈ 19.2 %, Figure 33-b). The reduced η_c is probably due to the increase of ϕ_{H_2} and, consequently, of the premixed hydrogen mass that cannot completely burn because of flame quenching near the combustion chamber walls and the mass of hydrogen trapped in the crevices. However, up to 40 % H_2-ES, the combustion is faster, as evidenced by the CA50 shift toward TDC (Figure 33-c), improving thermal efficiency and outweighing η_c. At higher substitution levels, however, both the combustion duration (CA10–90) (Figure 33-d) and the combustion completeness deteriorate, resulting in lower IMEP*.

To further improve the performance of DF operation at low hydrogen substitution ratios and to recover the efficiency losses observed at higher hydrogen shares, a Design of Experiments (DOE) was carried out by varying the SOI of the diesel pilot, pre, and main injections. The analysis was performed by rigidly advancing the entire diesel injection pattern with respect to the baseline diesel case, maintaining the same relative spacing between the three pulses. As shown in Figure 34, the SOI of each injection event was shifted progressively from 5° to 30° CA in steps of 5° CA, producing a total of six injection timings for each hydrogen energy share condition. The same procedure was applied to all DF simulations at partial load, ensuring a consistent comparison among operating modes.

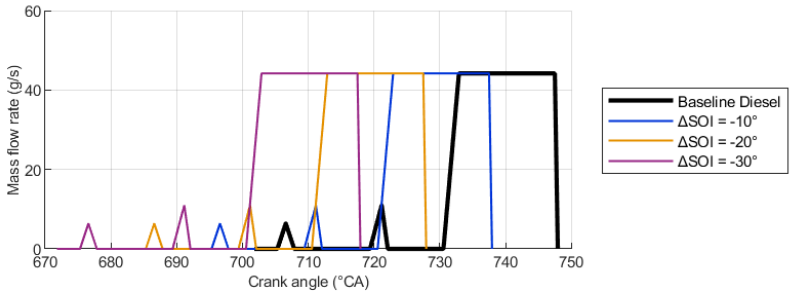

Figure 34: Effect if SOI variation on diesel fuel injection law for the Diesel case at partial load (2400 rpm -10.5 bar BMEP)

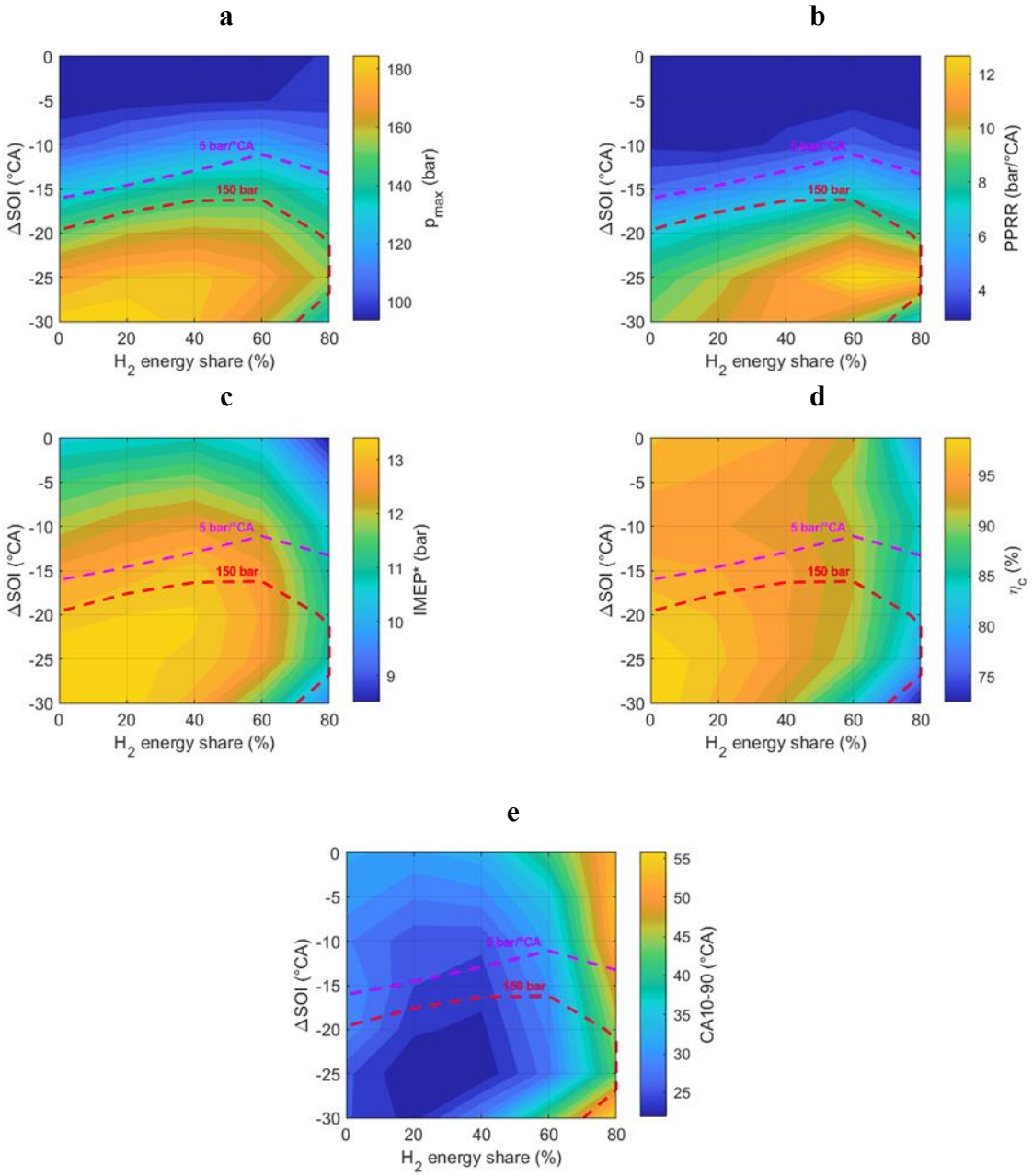

Figure 35: Effect of hydrogen energy share and diesel fuel SOI on the main combustion characteristics at partial load (2400 rpm -10. Bar BMEP): a) peak in-cylinder pressure; b) PPRR; c) IMEP*; d) ηc; IMEP*; e) CA10-90.

The influence of the SOI variation on the main combustion parameters is reported in Figure 35, which presents contour maps of peak in-cylinder pressure, PPRR, gross IMEP*, and η_c as a function of both hydrogen energy share and SOI variation (ΔSOI). From these results, it can be observed that the trends of IMEP* and ηc as a function of the hydrogen share (previously shown in Figure 33-b) are generally confirmed across all injection timings, except for extreme advances (ΔSOI = −25° and −30° CA). At these conditions, the excessive advancement of the injection causes premature combustion, leading to lower overall efficiency as the hydrogen share increases. In general, IMEP* increases with

the advancement of the diesel injection. The maximum performance improvement is achieved for low hydrogen substitution levels (≈ 20 % hydrogen energy share) and large SOI advances (ΔSOI between −25° and −30° CA), corresponding to an average IMEP* gain of about 27 % relative to the baseline diesel operation. However, two operational constraints were imposed to ensure mechanical integrity and acceptable noise levels:

- Maximum in-cylinder pressure: 150 bar;
- Maximum PPRR: 5 bar/°CA.

The first constraint corresponds to the maximum pressure sustainable by the engine structure, while the second limit is associated with combustion noise and vibration. At this operating point, the baseline diesel case shows a PPRR = 2.9 bar/°CA; thus, the PPRR threshold of 5 bar/°CA was considered the more restrictive condition for the partial load condition. As a result, the optimal injection advance for each DF configuration was defined as the SOI shift corresponding to the maximum IMEP* that does not exceed the PPRR limit. This represents the best compromise between performance enhancement and controlled combustion dynamics.

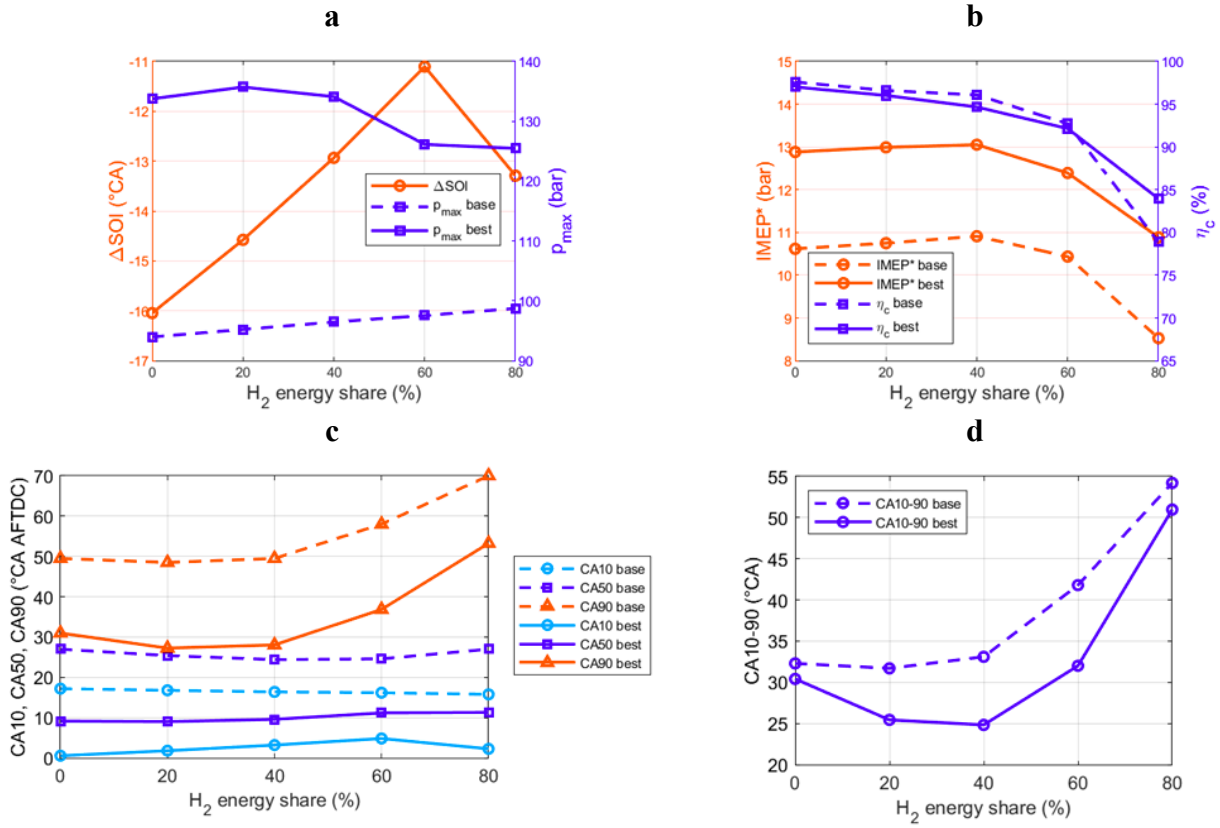

Figure 36: Comparison among baseline Diesel, optimized Diesel and optimized hydrogen Diesel DF cases in terms of: a) peak in-cylinder pressure; b) IMEP* and combustion efficiency; c) combustion phasing; d) combustion duration at partial load (2400 rpm - 10.5 bar BMEP)

The resulting optimized injection strategies and the corresponding combustion outcomes are presented in Figure 36. As shown in Figure 36-a, the required injection delay (ΔSOI) decreases progressively with the hydrogen energy share up to about 60 %, and then slightly increases at 80 % hydrogen energy share. This trend is linked to the interplay between ignition delay and mixture reactivity as the proportion of premixed hydrogen increases.

The optimized cases exhibit peak pressures higher than the baseline diesel and DF configurations, but always below the 150 bar limit. The combustion efficiency η_c (Figure 36-b) worsens with increasing hydrogen share due to the higher equivalence ratio of the premixed mixture and the corresponding flame quenching near the chamber walls and within crevice volumes. Even after optimization, η_c remains lower than the baseline diesel case, with reductions ranging from 0.6 % to approximately 14 %. Despite this decline in combustion efficiency, the optimized cases show a clear improvement in IMEP* across all hydrogen shares (Figure 36-b), with the maximum gain of +22.9 % occurring at 40 % hydrogen energy share. This improvement results from an optimal combustion phasing (CA50 ≈ 10° ATDC) achieved through the SOI advance, regardless of the hydrogen content (Figure 36-c). Furthermore, the combustion duration (CA10–90) decreases up to 40 % of the hydrogen energy share (Figure 36-d), further enhancing performance. At higher hydrogen shares (60–80 %), the combustion duration increases again, and η_c continues to decline, reducing the IMEP* benefit.

In summary, advancing the diesel injection timing proves to be an effective strategy to enhance the performance of hydrogen–diesel DF operation at partial load. At low hydrogen shares, early injection phasing significantly improves efficiency, while at high substitution levels, it enables the recovery of performance losses caused by reduced combustion efficiency. Nonetheless, combustion efficiency cannot be completely restored through injection-timing optimization alone, as flame quenching and incomplete oxidation remain limiting factors of the DF combustion process.

3.7. Results and discussion: Full load case

After the analysis of the partial-load condition, attention was next focused on the full-load operation, which represents the second investigated case in this study. This operating point corresponds to 4000 rpm and 13.5 bar BMEP, and was selected to evaluate the behaviour of hydrogen–diesel DF combustion under high-load, high-temperature conditions, where both air–fuel mixing and pressure rise rates play a crucial role in determining engine performance and mechanical reliability.

As in the partial-load simulations, diesel fuel was progressively replaced by hydrogen, increasing the hydrogen energy share from 0% (pure diesel operation) up to 80% of the total fuel energy, while

keeping the overall energy input constant. The corresponding diesel injection law was modified accordingly (Figure 30), reducing the injected diesel mass during the main injection event to maintain equal energy supply. Figure 37 shows the variation of the equivalence ratio of the premixed hydrogen–air mixture ϕ_{H_2}, calculated according to (3), as a function of the hydrogen energy share.

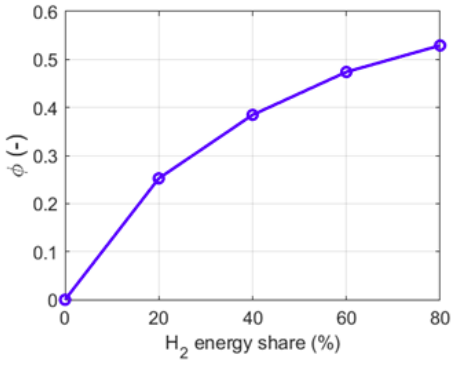

Figure 37: Variation of the equivalence ratio of the H2-air premixed charge with increasing hydrogen energy share at full load (4000 rpm – 13.5 bar BMEP).

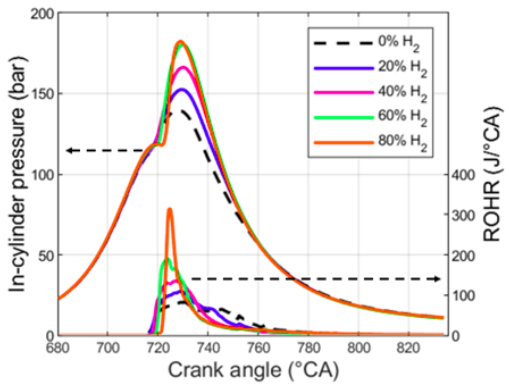

Figure 38: Effect of increasing hydrogen energy share on in-cylinder pressure and ROHR at full load (4000 rpm – 13.5 bar BMEP)

The introduction of hydrogen into the full-load operation notably influences both combustion characteristics and engine performance. As shown in Figure 38 and Figure 39-a, the peak in-cylinder pressure increases significantly when diesel is progressively substituted by hydrogen, rising from approximately 139.7 bar in conventional diesel operation to about 182.3 bar at 80% hydrogen energy share. This pressure rise is consistent with similar observations reported in literature for DF engines operating at medium-to-high loads [120–122]. It mainly stems from the ROHR as the combustion process transitions from diffusion-controlled to premixed-dominated. Such a strong increase in pressure, however, represents one of the main challenges in extending the hydrogen energy share to very high levels under full-load conditions, as it can easily lead to excessive mechanical stress and high combustion noise. Nevertheless, as will be demonstrated in the following sections, this issue can be effectively mitigated by appropriately optimizing the diesel injection law, which allows controlling the in-cylinder pressure rise while preserving the benefits of hydrogen enrichment.

Hydrogen's high laminar flame speed and wide flammability range accelerate the combustion process, promoting rapid energy release within a shorter crank-angle window. However, an increase in ignition delay is also observed as the hydrogen energy share rises. This effect can be attributed to two concurrent factors:

1. To maintain the same total trapped mass at IVC as the hydrogen fraction increases, the intake temperature must be reduced, leading to lower temperatures at the end of compression;
2. Hydrogen tends to absorb part of the heat released during the low-temperature combustion phase of diesel, thereby delaying the onset of high-temperature reactions.

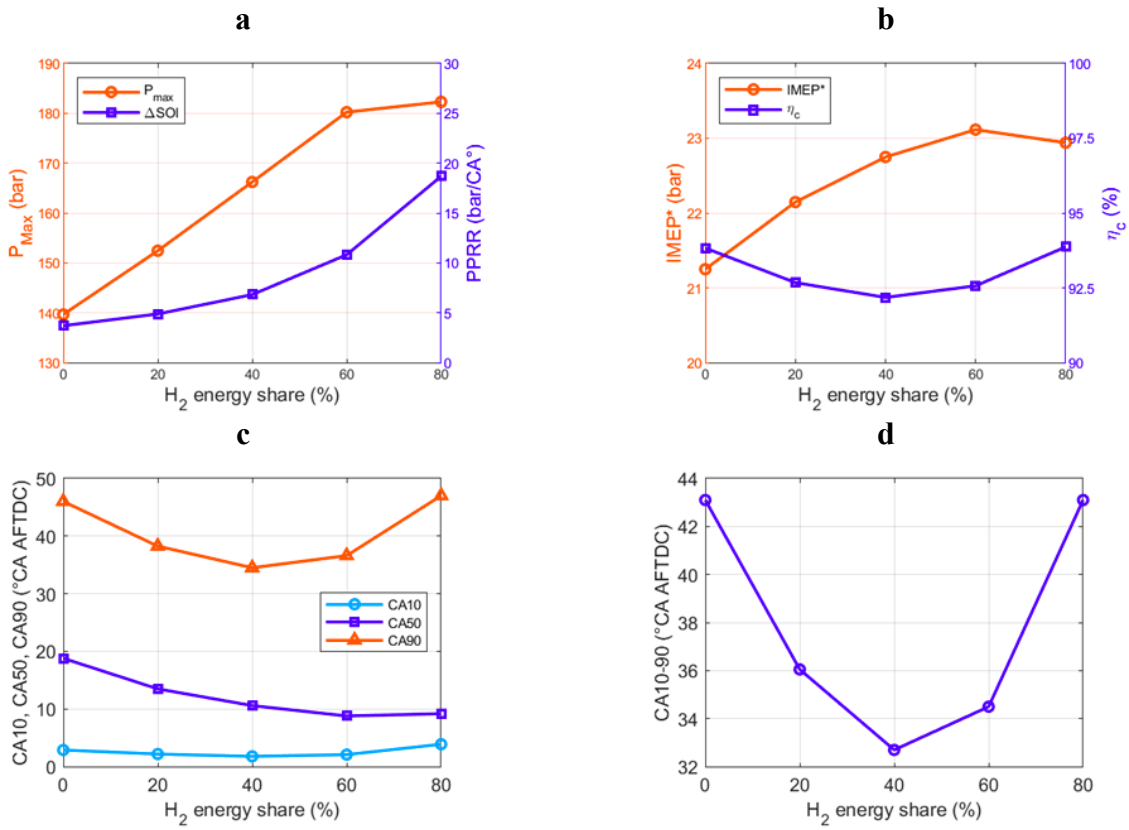

Figure 39: Effect of increasing hydrogen energy share on the main combustion characteristics at full load (4000 rpm – 13.5 bar BMEP): a) peak in-cylinder pressure and PPRR; b) IMEP* and combustion efficiency; c) combustion phasing parameters; d) turbulent combustion duration.

Regarding combustion phasing, Figure 39-c shows that CA10 is almost unaffected by hydrogen substitution, while CA50 shifts markedly toward TDC, decreasing from 18.8° ATDC in the diesel case to 9.2° ATDC at 80% hydrogen energy share. The latter part of combustion, represented by CA90, initially advances up to 40% H_2 energy share but then retards at higher hydrogen contents. Consequently, the combustion duration (CA10–90) shortens up to 40% hydrogen energy share, reaching 33° CA (about 10° shorter than diesel operation), and then lengthens again due to the slower oxidation of the outer premixed zones (Figure 39-d).

The corresponding in-cylinder pressure and ROHR traces for the various hydrogen shares are presented in Figure 38. They confirm a progressive shift from the two-stage, diffusion-like diesel combustion toward a predominantly single-peaked premixed behaviour, with steeper ROHR slopes as hydrogen concentration increases.

In terms of performance, Figure 39-b shows that the IMPE* increases with hydrogen substitution, peaking at 23.1 bar for 60% H_2-ES, which corresponds to an improvement of about 9% compared with the diesel baseline. This performance gain is primarily driven by the enhanced thermal efficiency, as the faster combustion moves the energy release closer to TDC.

The η_c, on the other hand, exhibits a non-monotonic trend: it slightly decreases up to 40% H_2-ES (reaching 92.2%, i.e., −1.7% compared with diesel) and then gradually recovers to values comparable to the diesel case at 80% hydrogen substitution. Therefore, the overall trend of IMEP* can be explained by the combined effect of the combustion efficiency and the thermodynamic efficiency. As the hydrogen fraction increases, η_c decreases due to incomplete oxidation of the premixed charge, while the faster combustion rate and the advance of CA50 toward TDC lead to an increase in thermoduric efficiency. At moderate hydrogen shares (up to approximately 60% hydrogen energy share), the improvement in thermodynamic efficiency outweighs the loss in η_c, resulting in a net increase in IMEP*. Beyond this threshold, the efficiency penalty associated with incomplete combustion becomes dominant, causing a gradual reduction in IMEP*.

However, it should be highlighted that in all simulated cases, the maximum in-cylinder pressure exceeds the mechanical limit of 150 bar for the reference engine (Table 5), with PPRR increasing dramatically and reaching almost 19 bar/°CA at 80% hydrogen energy share (Figure 39). Such high pressure gradients would cause severe mechanical stress and excessive combustion noise. Therefore, an optimization of the diesel injection strategy becomes essential to achieve efficient DF operation under full-load conditions while keeping mechanical loads and NVH levels within acceptable limits.

To achieve efficient DF operation while keeping mechanical stresses and noise within acceptable limits, an optimization of the diesel injection timing was carried out. A DOE was performed varying the SOI of the main injection within the range −3° CA to +6° CA relative to the baseline diesel case, using 1° CA increments (Figure 40). The same SOI sweep was applied to all the hydrogen substitution levels, from 0 % to 80 % hydrogen energy share. Where intermediate combinations of SOI and hydrogen energy share were not directly simulated, linear interpolation was used to estimate the results.

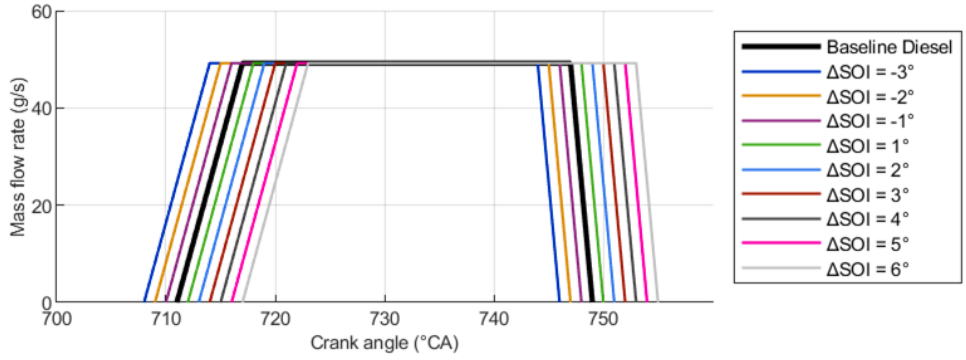

Figure 40: Effect of SOI variation on Diesel fuel injection law for the Diesel case at full load (4000 rpm – 13.5 bar BMEP)

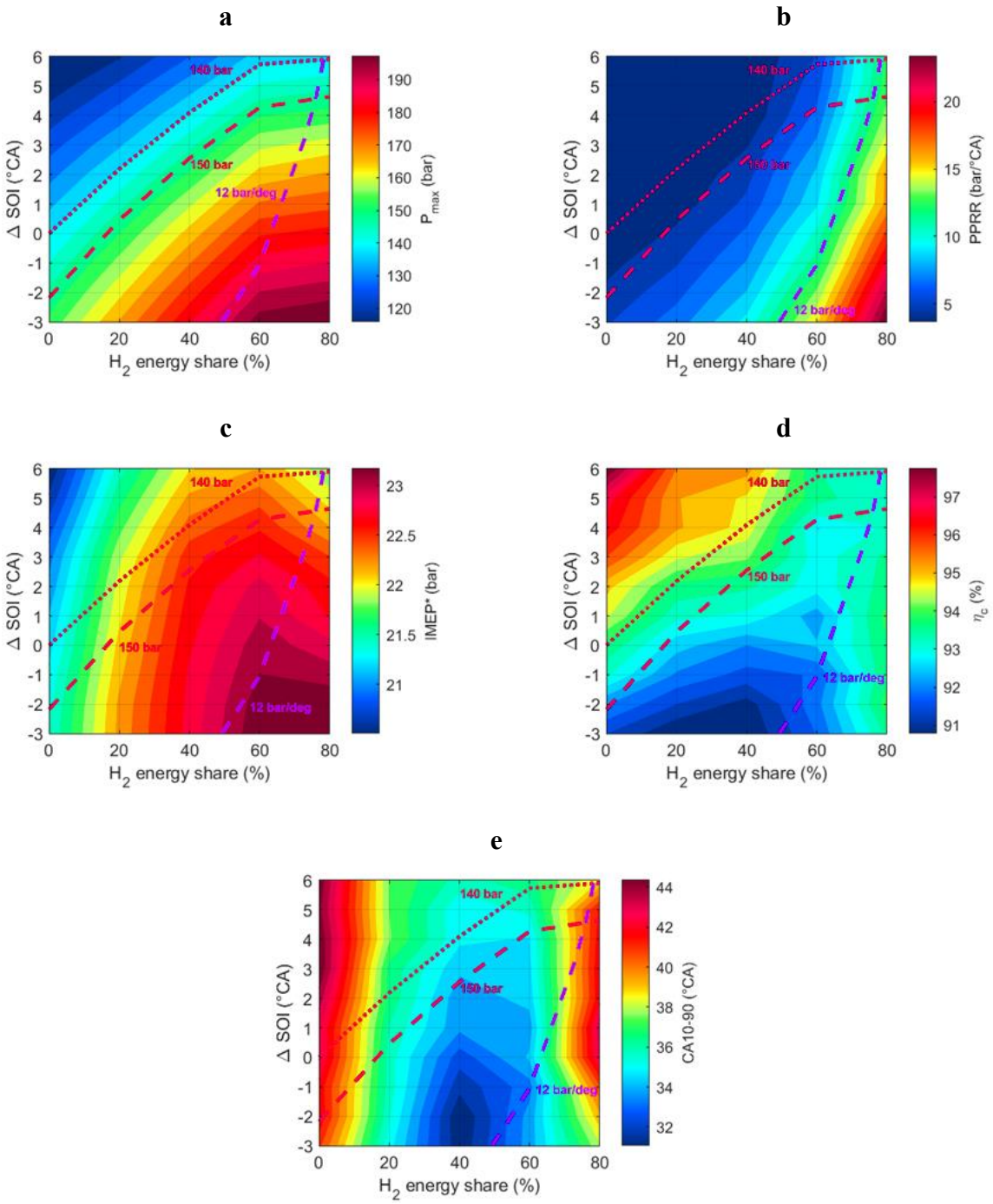

Figure 41: Influence of hydrogen energy share and Diesel fuel SOI on the main combustion characteristics at full load (4000 rpm – 13.5 bar BMEP): a) peak in-cylinder pressure; b) PPRR; c) IMEP*; d) combustion efficiency; e) CA10-90.

The effects of the SOI variation on the main combustion parameters are summarized in Figure 41, which reports contour maps of peak in-cylinder pressure, PPRR, IMEP*, and η_c as a function of hydrogen energy share and ΔSOI. Three reference boundaries are drawn on these maps:

- the red dashed line indicates the maximum allowable peak pressure for the engine (150 bar);
- the red dotted line corresponds to the peak pressure of the baseline diesel operation (140 bar);

- the magenta dashed line marks the acceptable PPRR limit for this load condition (12 bar/°CA).

As shown in Figure 41-a, the peak pressure rises with both increasing hydrogen share and advanced SOI, following the same trend observed for the baseline diesel case. At the same time, the map highlights that the reference diesel engine operates with a certain margin, as its 140 bar peak pressure remains below the 150 bar threshold, suggesting that a 2° CA advance could be introduced without surpassing the structural limit. In this full-load condition, the pressure limit proves to be the most restrictive constraint, more so than the PPRR limit. However, the sensitivity of these two parameters differs from what was observed at partial load. While at low load the two constraints were nearly parallel, at full load the effect of hydrogen substitution on PPRR is much stronger, resulting in almost vertical PPRR-limit contours on the map. Consequently, the maximum allowable hydrogen energy share without exceeding the 12 bar/°CA PPRR limit and keeping $\Delta SOI \leq +6°$ CA is approximately 78.4 %.

Regarding performance, Figure 41 shows that IMEP* depends primarily on the hydrogen energy share, while the influence of SOI timing is less pronounced. Advancing the main injection in the full-diesel case by about 2° CA yields a small gain of 0.8 % in IMEP*, though at the expense of a 1.9 % drop in η_c. The combustion efficiency map (Figure 41-d) reveals that η_c reaches its maximum for ΔSOI values between +3° CA and +6° CA and low hydrogen shares (below 20 %). However, for higher hydrogen fractions, advancing the injection generally produces no benefit or even a worsening in efficiency, since the early combustion phasing increases wall heat losses and promotes incomplete oxidation in peripheral regions.

The CA10–90 map (Figure 41-e) further confirms that the shortest combustion durations are obtained for slightly retarded injections (negative ΔSOI) and intermediate hydrogen shares (20–60 %), where a balanced mixture reactivity and phasing minimize the overall burning interval.

Based on the contour maps discussed above, the optimal SOI for each hydrogen energy share was determined as the value that maximized IMEP* while keeping both the peak in-cylinder pressure and PPRR within the prescribed limits (150 bar and 12 bar/°CA, respectively). The resulting optimized injection timings are reported in Figure 42, together with the corresponding ΔSOI values for diesel and DF operation. The results show that the optimal SOI must be progressively delayed (i.e., less advanced) as the hydrogen energy share increases, in order to maintain both the peak pressure and the PPRR within the admissible range. This trend becomes particularly evident beyond 40% hydrogen energy share, where the increase in mixture reactivity and combustion intensity requires later injection timings to mitigate excessive pressure gradients. It is also worth noting that, under the baseline DF

configuration, the absence of any SOI adjustment leads to peak pressures above the structural limit, confirming that injection re-phasing is essential for safe full-load operation.

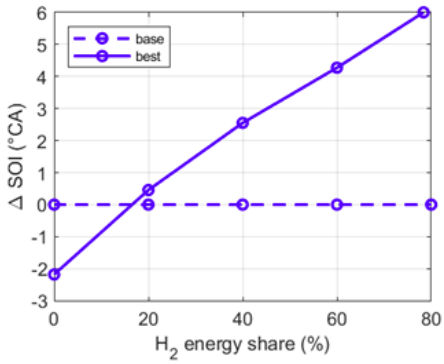

Figure 42: SOI comparison between baseline and optimized (best) Diesel fuel injection strategy for different hydrogen energy shares.

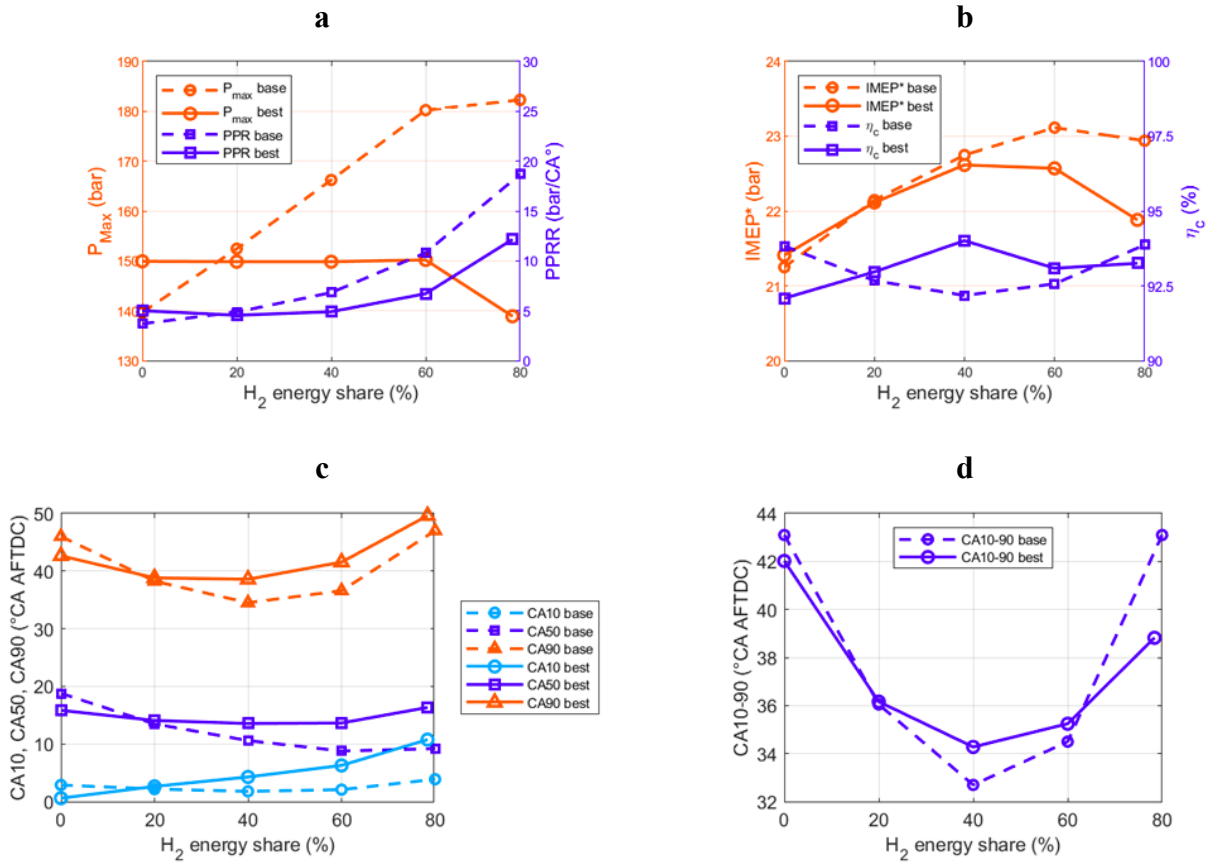

Figure 43: Comparison between the main combustion characteristics before and after the Diesel fuel SOI optimization at full load (4000 rpm – 13.5 bar BMEP): a) peak in-cylinder pressure and PPRR; b) IMEP* and combustion efficiency; c) combustion phasing parameters; d) turbulent combustion duration

The comparison between baseline and optimized cases is shown in Figure 43, which reports the evolution of peak pressure and PPRR (Figure 43-a), IMEP* and combustion efficiency η_c (Figure 43-b), combustion phasing parameters (Figure 43-c), and combustion duration (Figure 43-d). As

illustrated, the optimized injection strategy effectively reduces both peak pressure and PPRR, ensuring compliance with mechanical limits while maintaining stable combustion.

In terms of performance, the optimized diesel case (ΔSOI = −2.18° CA) yields a marginal IMEP* gain of about 0.2 bar (≈0.8%) compared with the baseline diesel, accompanied by a 1.9% reduction in η_c due to slightly more advanced phasing. More interestingly, all the optimized DF configurations show higher IMEP* values than both the baseline and optimized diesel cases, demonstrating that the use of hydrogen can enhance indicated efficiency even when injection timing is adjusted to limit mechanical loads.

Among all conditions, the configuration with 40% H_2 energy share and ΔSOI = +2.55° CA stands out as the most favourable. This case delivers the highest IMEP* and η_c among the optimized DF setups, achieving a +1.2 bar (+5.6%) improvement in IMEP* and a +2.1% increase in η_c compared to the optimized diesel case. Such improvement results from an optimal combustion phasing, with CA50 located around 10° ATDC, which enhances the thermodynamic efficiency of the cycle while maintaining acceptable pressure gradients. In addition, the combustion duration (CA10–90) decreases significantly up to 40% hydrogen share (Figure 43-d), confirming faster combustion development.

For higher hydrogen fractions (≥ 60% hydrogen share), the combustion duration increases again, while η_c progressively worsens due to enhanced flame quenching near the chamber walls and partial oxidation in the peripheral zones of the combustion chamber. As a consequence, the overall IMEP* improvement tends to diminish, though the optimized DF cases still outperform the baseline diesel operation in terms of indicated efficiency.

At the maximum admissible hydrogen share (78.4% H_2-ES) (corresponding to the maximum SOI advance (+6° CA) allowed by the constraints) the optimized configuration still shows better performance than the diesel case. In particular, IMEP* increases by 0.47 bar (+2.2%) and η_c by 1.3% with respect to the optimized diesel, while peak pressure and PPRR remain below the imposed limits (Figure 43-a). These results demonstrate that hydrogen can effectively replace a substantial portion of diesel fuel (roughly 80%) even at full load, maintaining or improving performance while preserving safe operating conditions.

To further clarify the influence of hydrogen substitution and injection phasing on the full-load behaviour, two representative operating points were selected and compared with the baseline diesel case. The first corresponds to the 40% H_2–DF configuration, which achieved the highest IMEP* and combustion efficiency among all optimized cases, while the second represents the maximum

admissible hydrogen substitution (78.4%), associated with the structural and PPRR limits. The corresponding optimized SOI values are ΔSOI = +2.55° CA and ΔSOI = +6° CA, respectively.

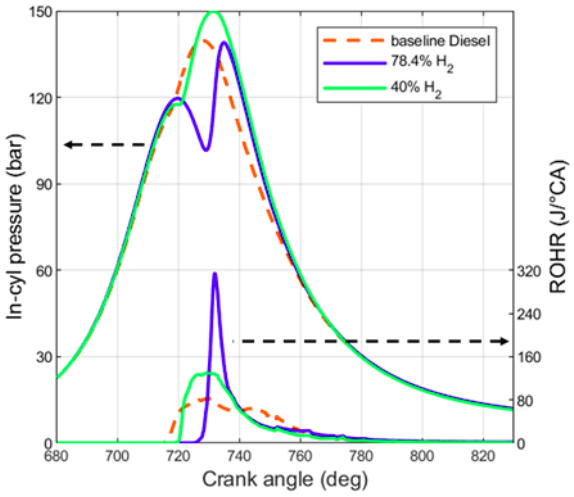

Figure 44: Comparison between baseline Diesel operation and optimized 80 % hydrogen energy share combustion at full load (4000 rpm – 13.5 bar BMEP) in terms of in-cylinder pressure and ROHR

Figure 44 compares the in-cylinder pressure and ROHR traces for these three cases. The 40% hydrogen energy share configuration exhibits the highest peak pressure, reaching 150 bar, compared to 139.7 bar for the baseline diesel and 138.9 bar for the 78.4% hydrogen share case. This indicates that the moderate hydrogen share combined with advanced injection timing allows the combustion to be phased very close to TDC, maximizing thermodynamic efficiency without exceeding the structural limit. The 78.4% H_2–DF case, on the other hand, displays the sharpest ROHR profile and a distinctive double-peak pressure shape, which reflects the highly premixed nature of the mixture and the occurrence of a secondary heat-release phase. This more abrupt combustion behaviour explains why the PPRR in this case reaches the imposed limit of 12 bar/°CA.

The quantitative comparison, summarized in Table 13, confirms the performance trends observed in the contour maps. The 40% hydrogen share configuration provides the best overall compromise between performance and combustion quality, showing a +6.4% increase in IMEP* relative to the baseline diesel (from 21.25 bar to 22.61 bar) and a +5.6% gain compared to the optimized diesel case. η_c also slightly improves (+0.2%), while the combustion duration (CA10–90) shortens by 8.8° CA, confirming a faster and more complete combustion process. At the 78.4% H_2–DF condition, performance remains superior to the baseline diesel, though with smaller gains: IMEP* increases by +2.96%, and $\eta_c$decreases slightly (−0.6%) due to incomplete oxidation in the peripheral regions of

the chamber. The combustion duration is still reduced compared to diesel (−4.3° CA). These results clearly demonstrate that efficient full-load DF operation can be achieved up to very high hydrogen substitution levels, provided that injection timing is properly optimized.

Table 13: Comparison between Diesel and optimized 80 % H2-D DF

	Diesel	**Opt. Diesel**	**40 % H_2 H_2-D DF**	**78 % H_2 H_2-D DF**
Hydrogen energy share (%)	0	0	40	80
ΔSOI (°CA)	0	-2.18	-2.55	-6.00
Max in-cylinder pressure (bar)	139.7	150.0	150.0	138.9
PPRR (bar/°CA)	3.71	5.01	4.91	12.00
IMEP* (bar)	21.25	21.41	22.61	21.88
η_c (%)	93.82	92.09	94.01	93.25
CA10-90 (°CA)	43.1	42.0	34.3	38.8

From both the general analysis and the evaluation of the selected operating points, it can be concluded that, at full load, the transition from diesel to hydrogen–diesel DF operation inevitably requires optimization of the main injection timing to limit mechanical stress and combustion noise. The results highlight that intermediate hydrogen substitution levels (≈ 40%) yield the best trade-off between efficiency, combustion stability, and pressure-rise rate, offering substantial performance improvements compared to the pure diesel mode. At higher hydrogen shares, the combustion process becomes more abrupt and premixed, leading to higher PPRR values and requiring retarded SOI to remain within mechanical limits. These necessary timing delays partially counteract the potential thermal-efficiency gains, making it more difficult to exceed diesel performance. Nonetheless, with the optimized SOI, the engine is capable of maintaining safe operation even at nearly 80% hydrogen substitution, achieving performance levels comparable to or slightly higher than diesel.

3.8. Final remarks and conclusions

This numerical study investigated the implementation of hydrogen–diesel DF combustion in a light-duty compression-ignition engine, focusing on the influence of increasing hydrogen substitution on combustion behaviour and engine performance, as well as on the optimization of the diesel injection strategy. Two operating points were analyzed: a medium-load / medium-speed condition (2400 rpm – 10.5 bar BMEP) and a high-load / high-speed condition (4000 rpm – 13.5 bar BMEP).

At partial load, the following main conclusions can be drawn:

- Increasing the hydrogen energy share up to 40% results in an IMEP* improvement due to a faster and more efficient combustion process. At higher hydrogen shares, however, IMEP* decreases, reaching its lowest value at 80% hydrogen energy share.
- The performance deterioration observed at high substitution levels is primarily caused by a reduction in combustion efficiency, associated with incomplete oxidation of the premixed hydrogen–air mixture and flame quenching near the chamber walls.
- By advancing the diesel injection timing, the performance at low hydrogen shares can be further enhanced. At higher hydrogen fractions, injection phasing optimization enables the recovery of IMEP* losses, in some cases even exceeding the diesel baseline performance. Nonetheless, combustion efficiency remains lower than in conventional diesel combustion and cannot be fully restored through injection advancement alone.

Under full-load conditions, the analysis revealed the following trends:

- Hydrogen substitution leads to a significant increase in both peak in-cylinder pressure and pressure rise rate, often exceeding the engine's structural limits. To ensure safe operation, retarding the diesel injection timing becomes necessary. For each hydrogen share, an optimal SOI was identified to maintain both peak pressure and PPRR within acceptable limits.
- The highest IMEP* is achieved around 40% H_2 energy share, where the combustion process is still relatively stable and thermally efficient. At higher substitution levels, the combustion becomes more abrupt and efficiency slightly decreases, resulting in overall performance comparable to or slightly below the diesel baseline.
- Two optimized configurations were identified: (I) 40% hydrogen energy share, $\Delta SOI = +2.55°$ CA, maximizing IMEP* (+6.4% vs diesel baseline) and achieving the highest combustion efficiency; (II) 78.4% hydrogen share, $\Delta SOI = +6°$ CA, enabling the maximum feasible hydrogen share under the imposed constraints, with a modest performance improvement (+2.96% IMEP*) and a small decrease in combustion efficiency.

These results highlight that injection timing optimization plays a pivotal role in enabling the conversion of conventional diesel engines to DF operation, enhancing performance while respecting mechanical and acoustic limits. In particular, the diesel injection law determines not only the combustion onset but also the entire phasing of the heat release, acting as the key control parameter for the DF process.

In this study, the optimized injection strategy allowed achieving hydrogen energy shares up to approximately 80% while maintaining acceptable peak pressures and PPRR, even at high load. The DF mode investigated here can be regarded as a Reactivity-Controlled Compression Ignition (RCCI)-type combustion, where a late diesel injection serves as the ignition source for a largely premixed hydrogen–air charge. This configuration enables an effective and relatively simple control of the combustion initiation: by retarding the diesel injection, it is possible to offset the natural tendency of hydrogen to accelerate the combustion process, thereby maintaining an optimal combustion phasing (CA50 ≈ 10° ATDC) and avoiding excessive in-cylinder pressure peaks.

The outcomes of this work therefore demonstrate that hydrogen–diesel DF operation is not only feasible but also highly promising for improving the efficiency and sustainability of compression-ignition engines. Moreover, the findings achieved here laid the foundation for the subsequent optimization steps, in which different diesel injection strategies were investigated compare to the ones studied in this section, allowing the hydrogen energy share to be further increased up to 86% while maintaining stable and efficient combustion.

4. CFD-driven optimization of diesel injection: toward 86% hydrogen share

The research activity presented in this section focuses on the optimization of diesel injection strategies for hydrogen–diesel DF operation in a light-duty compression-ignition engine. The study was conceived to further improve combustion efficiency and reduce pollutant emissions by exploiting the diesel injection law as a key control parameter for the ignition and combustion process. To this end, a combined experimental and numerical approach was adopted, enabling the development of a CFD-driven optimization framework capable of correlating injection parameters, hydrogen utilization, and pollutant formation mechanisms.

Experimental tests were carried out on a single-cylinder research engine derived from a light-duty diesel unit and specifically modified to operate under DF conditions. The experimental campaign provided the reference data required for the calibration and validation of the combustion and emission sub-models integrated in the CFD environment. Once validated, the numerical model was used to perform a systematic analysis of the effect of the injected diesel mass on the overall combustion process. The objective was to evaluate whether a single, small diesel injection could be sufficient to ensure a stable ignition and controlled combustion development, while maximizing the hydrogen contribution to the total fuel energy. This approach enabled the identification of operating conditions that combine high hydrogen energy shares with stable combustion and acceptable in-cylinder pressure levels, providing a robust framework for assessing both the performance and emission behaviour of hydrogen–diesel DF operation at low-to-medium/high engine loads.

While the general objective of this activity was to further extend the achievable hydrogen substitution, its motivation arises directly from the findings of the previous study discussed in the previous section. That work analysed hydrogen–diesel DF combustion under both partial and full-load conditions, showing two distinct limitations. At partial load, excessive hydrogen substitution led to poor combustion efficiency and incomplete oxidation if not properly controlled, whereas at full load, the high reactivity and fast flame speed of hydrogen resulted in steep pressure gradients and peak pressures close to the mechanical limits of the engine. A similar trend was also observed in the present activity, confirming that the impact of hydrogen substitution strongly depends on the engine load. At low-to-medium/high loads, large hydrogen fractions may reduce the combustion efficiency, while at higher loads, the faster flame development tends to intensify pressure rise and mechanical stress. Under those conditions, the maximum feasible hydrogen energy share was found to be approximately

86%, already corresponding to a virtual 86% reduction in CO_2 emissions compared to conventional diesel operation.

Building on these results, the present study was carried out at low-to-medium/high load conditions, where the lower in-cylinder stresses allow for higher hydrogen fractions without exceeding the structural constraints of the engine. Moreover, this work expands the previous investigation by introducing a dedicated modelling of pollutant emissions (including NO_x, CO, and CO_2) based on calibrated sub-models, thus providing a more complete picture of both the combustion and emission processes in hydrogen–diesel DF engines. This research activity resulted in the publication of the paper entitled *"CFD-Driven Optimization of Diesel Injection for a Hydrogen–Diesel Dual-Fuel Engine"* [123].'

4.1. Engine specification and experimental setup

The experimental and numerical analyses were performed on a three-cylinder, naturally aspirated, four-stroke Diesel prototype engine designed for off-road applications. The engine has a total displacement of 1028 cm^3, with a bore and stroke of 75.0 × 77.6 mm and a compression ratio of 17.5:1. Each cylinder is equipped with two valves (one intake and one exhaust), and the intake port has a swirl-type configuration to promote in-cylinder charge motion. The piston bowl features a non-cantered omega shape and the injector is a six-holes diesel injector, centrally aligned with the bowl axis. The electronically controlled common-rail system is equipped with a three-piston pump capable of delivering injection pressures up to 1400 bar. The intake and exhaust valve lift profiles are shown in Figure 45, where the valve overlap amounts to approximately 27° CA. The main specifications of the reference engine are summarized in Table 14.

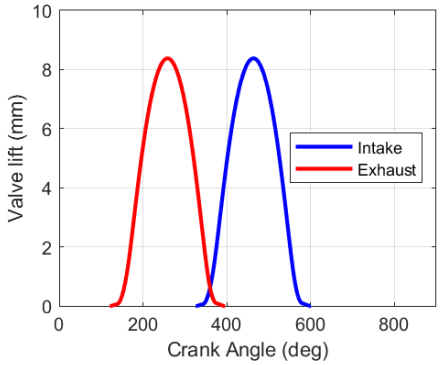

Figure 45: Intake and exhaust valve lift profiles.

Table 14: Main features of the reference engine.

Engine parameter	Description
Engine type	4-Stroke Diesel
Combustion mode	Compression
Cylinders	3, in-line
Total displacement (cm3)	1028
Bore × Stroke (mm × mm)	75.0 × 77.6
Compression ratio	17.5:1
N. of valves per cylinder	2
Exhaust valve opening (EVO; °CA aFTDC)	142
Intake valve opening (IVO; °CA aFTDC)	347
Exhaust valve closing (EVC; °CA aFTDC)	374
Intake valve closing (IVC; °CA aFTDC)	579
Air Metering	Naturally aspirated
Injection system	Direct, Common
Max injection Pressure (bar)	1400
N of injector per cylinder × N of holes per	1× 6
Injector hole protrusion (mm)	1
Injector hole distance from injector axis	2
Max. brake power (kW@rpm)	15@3600
Max. brake torque (Nm@rpm)	60@2000

This prototype engine was modified by the STEMS-CNR research center to enable DF operation with hydrogen port injection. Thanks to its simple design and robust mechanical architecture, this engine represents an ideal platform for the conversion from full-diesel to hydrogen–diesel DF operation, as well as for a detailed experimental characterization of the combustion process under this innovative configuration.

To support the numerical analysis and validate the combustion model under hydrogen–diesel DF operation, an experimental campaign was carried out on the modified engine at the STEMS-CNR facilities. Initially, the engine was operated with conventional diesel fuel to establish a baseline reference, and then progressively transitioned to DF mode by introducing hydrogen through the intake manifold.

Diesel consumption was monitored by a gravimetric balance, while the common-rail injection system, controlled via the Electronic Control Unit (ECU), delivered two injections per cycle (a pilot and a main). Torque was measured using a dynamometric load cell, and the intake air flow rate was measured with a hot-wire anemometer. During all tests, the EGR system was mechanically disabled to ensure repeatable and interference-free combustion conditions.

For DF operation, a dedicated hydrogen injection system was designed and assembled in the laboratory. The hydrogen supply line included a 200-bar storage cylinder, a pressure regulator, a mass flow meter, and a fuel rail feeding three port fuel injectors (PFI), each positioned in front of an intake

valve. The gaseous injectors, originally designed for CNG operation, were operated at 5 bar and were capable of delivering up to 1700 cc/min at 4 bar. Hydrogen injection timing was synchronized with the intake valve opening by means of electronic delay units linked to the engine trigger signal, ensuring that the injection was completed before the valve closure to reduce hydrogen backflows and backfire risks. To guarantee safe operation, the hydrogen system was equipped with two safety valves and a flame arrestor to prevent backfire or leakage incidents.

In-cylinder pressure was measured using three piezoelectric pressure transducers mounted in the cylinder head through modified glow-plug adapters. A multi-channel acquisition system recorded the pressure data, hydrogen and diesel mass flow rates, and injector actuation signals. For each operating point, 200 consecutive cycles were acquired and ensemble-averaged to minimize cycle-to-cycle variations.

All tests were performed at a constant engine speed of 2000 rpm, varying the hydrogen injection duration to achieve different loads. Three dual-fuel operating conditions were investigated, corresponding to 30%, 50%, and 70% of the maximum torque output. Before switching to DF operation, the engine was operated in pure diesel mode to obtain the baseline data. In DF mode, diesel provided roughly 10% of the total power output (about 5 Nm), acting as the ignition source for the hydrogen–air mixture.

The main parameters of the tested operating conditions are summarized in Table 15, which also reports the global air-to-fuel ratio (λ_g) and the hydrogen energy share (HES), computed according to Equations (5) and (6):

$$\lambda_g = \frac{\dot{m}_{air}}{\alpha_{st,H_2} \cdot \dot{m}_{H_2} + \alpha_{st,D} \cdot \dot{m}_D} \quad (5)$$

$$HES = \frac{\dot{m}_{H_2} \cdot LHV_{H_2}}{\dot{m}_{H_2} \cdot LHV_{H_2} + \dot{m}_D \cdot LHV_D} \times 100 \quad (6)$$

where $\dot{m}_{H_2}$, $\dot{m}_D$, and $\dot{m}_{air}$ are the mass flow rates of hydrogen, diesel, and air respectively (kg/h), and LHV_{H_2} and LHV_D represent the lower heating values of hydrogen and diesel (kJ/kg).

Table 15: Main parameters of the tested operating points.

	10% load	30% load	50% load	70% load
Engine speed × IMEP (rpm × bar)	2000×0.7	2000×1.9	2000×3.2	2000× 4.6
Brake Torque (Nm)	5.5	15.5	26.5	37.5
Brake Power (kW)	1.15	3.25	5.55	7.85
Diesel mass flow rate (kg/h)	0.66	0.67	0.71	0.69
H_2 mass flow rate (kg/h)	0	0.27	0.37	0.44
Diesel Fuel Mass (mg/cyl/cycle)	3.65	3.72	3.96	3.82
H_2 Fuel Mass (mg/cyl/cycle)	0	1.50	2.05	2.43
λ_g (-)	6.21	3.02	2.46	2.2
HES (%)	0	53.2	59.2	64.0
Diesel injection strategy	Pilot + Main			
H_2 injection strategy	Single injection			

4.2. 0D/1D-CFD modelling and validation

To reproduce the global behaviour of the tested engine and provide consistent boundary conditions for the subsequent 3D-CFD simulations, a 0D/1D model was first developed using GT-Power (Gamma Technologies. [95]). The model represents the entire engine system, including the intake and exhaust manifolds, and was designed to capture the relevant thermodynamic and fluid-dynamic interactions between the gas-exchange system and the in-cylinder domain.

The model geometry was constructed to replicate the real engine configuration in detail, with particular attention to the intake and exhaust line lengths, diameters, and valve timing. Calibration was performed by comparing simulated results with experimental measurements, focusing on the pressure losses in the manifolds, the in-cylinder heat transfer correlation, and the exhaust back-pressure. Two different experimental datasets were employed for the calibration phase:

- a full-load operation map in conventional diesel mode across 1400–3600 rpm, used to tune the general gas-dynamic response of the system (not discussed in detail here);
- and the load sweep in DF hydrogen–diesel operation at 2000 rpm, corresponding to 10%, 30%, 50%, and 70% load, described previously in the experimental section.

Combustion within the 0D/1D environment was not directly simulated but instead imposed through the experimental AHRR, obtained by applying the first law of thermodynamics to the in-cylinder pressure data. This approach ensures that the in-cylinder energy release and heat transfer reproduce the experimental combustion characteristics with high fidelity. The AHRR was calculated according to Equation (7):

$$AHRR = \frac{k}{k-1} p \frac{dV}{d\theta} + \frac{1}{k-1} V \frac{dp}{d\theta} \quad (7)$$

where k is the ratio of specific heats, p the instantaneous in-cylinder pressure, $V$the instantaneous cylinder volume, and θ the crank angle.

The validated 0D/1D-CFD model accurately reproduced the experimental trends of both cycle-averaged quantities (including brake power, torque, thermal efficiency, air mass flow rate, and peak in-cylinder pressure) and instantaneous in-cylinder pressure traces, showing very good agreement across all tested operating conditions (Figure 46 and Figure 47).

Once validated, the GT-Power model was employed to generate time-resolved boundary conditions for the 3D-CFD simulations, ensuring full consistency between the global gas-dynamic system and the in-cylinder flow field analysed in detail within the following section.

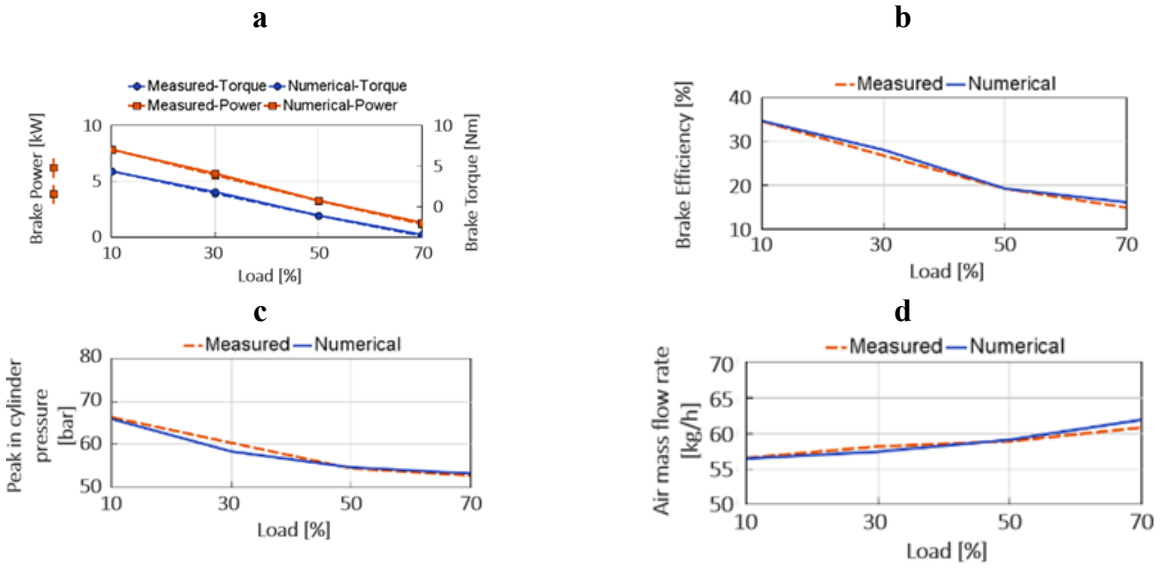

Figure 46: Comparison between measured and numerical (0D/1D-CFD) (a) brake power and torque, (b) brake efficiency, (c) peak in-cylinder pressure, (d) air mass flow rate at 10%, 30%, 50% and 70% load.

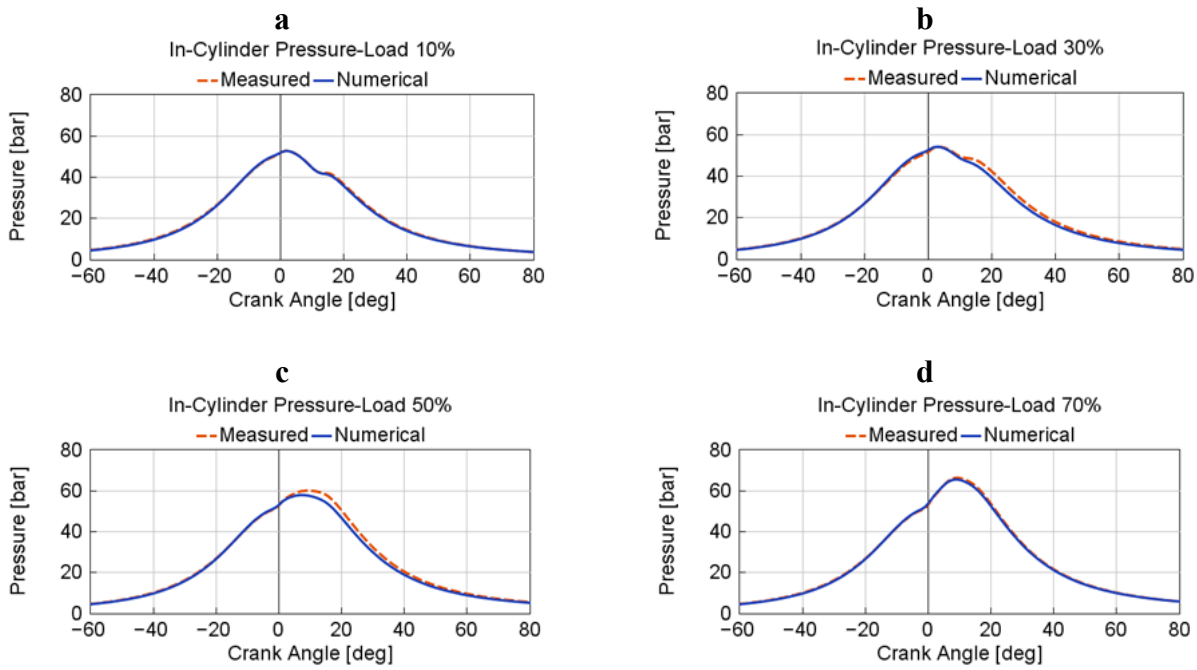

Figure 47: Comparison between measured and numerical (0D/1D-CFD) in-cylinder pressure traces for (a) 10 % load, (b) 30 % load, (c) 50 % load and (d) 70 % load.

4.3. 3D-CFD modelling and validation

The 3D-CFD simulations were carried out using AVL FIRE M, with the aim of reproducing the in-cylinder processes of the hydrogen–diesel DF engine described before. The modelling strategy followed a stepwise approach, beginning with the definition of the main physical sub-models, followed by a sequence of non-reactive and reactive simulations, and concluding with the optimization of the diesel injection strategy.

The simulations were based on the Reynolds-Averaged Navier–Stokes (RANS) approach, adopting the k–zeta–f turbulence model as the closure formulation, which provides accurate near-wall predictions and improved representation of swirl and tumble motion. Spray atomization of the diesel fuel was described using the Kelvin–Helmholtz/Rayleigh–Taylor (KH–RT) breakup model, while n-heptane (C_7H_{16}) was selected as the surrogate for commercial diesel fuel in the gas-phase combustion calculations. The Dukowicz evaporation model and the Schiller–Naumann drag law were used to describe liquid–gas interactions and droplet dynamics.

Combustion was simulated through the ECFM-3Z, which provides a good compromise between physical fidelity and computational cost. This model accounts for both premixed and diffusion-controlled combustion regimes, and was coupled with AVL's laminar flame speed and auto-ignition delay databases to ensure reliable representation of hydrogen–diesel interactions.

Regarding emissions, the model accounted for the formation of CO, CO_2, and NO_x. CO and CO_2 were calculated by solving a two-step global oxidation mechanism (Equation (8) and (9)), representing the partial oxidation of the surrogate fuel to CO and its subsequent conversion to CO_2. Reaction (9) was neglected under globally lean conditions. The formation of NO_x was captured using the extended Zeldovich thermal mechanism, a widely recognized approach for thermal NO prediction in diffusion and premixed combustion [124,125].

$$C_nH_mO_l + \left(n + \frac{m}{4} - \frac{l}{2}\right) O_2 \rightarrow nCO_2 + \frac{m}{2}\, H_2O \quad (8)$$

$$C_nH_mO_l + \left(\frac{n}{2} - \frac{l}{2}\right) O_2 \rightarrow nCO + \frac{m}{2}\, H_2 \quad (9)$$

The moving mesh was created using AVL FAME M, whose automated workflow allows the motion of both piston and valves. The computational domain included the cylinder, intake, and exhaust ports, as shown in Figure 48. Polyhedral cells were adopted to balance numerical accuracy, computational efficiency, and geometrical fidelity. The global cell size was set to 1.5 mm, with localized refinements in the spray region (down to 0.4 mm) and within the combustion chamber, where the cell size was reduced to 0.5 mm during the injection and combustion phases. The boundary layer mesh consisted of two layers of 0.1 mm thickness each, for a total of approximately 6.1×10^5 cells at top dead centre (TDC). Table 16 summarized further mesh details

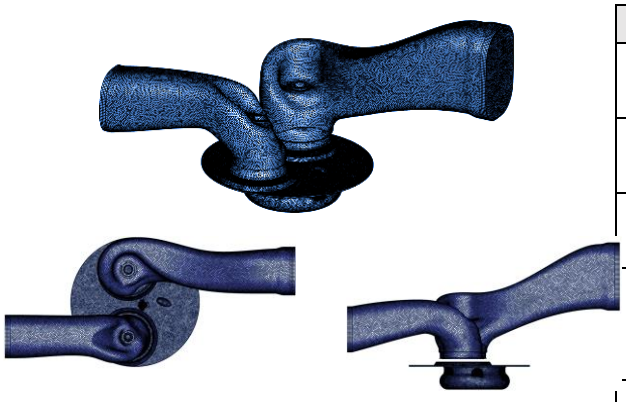

Figure 48: Prospective, up and side views of the computational grid.

Table 16: Computational grid details

Property	Value
Target cell Size (mm)	1.5
Injection refinement (mm)	0.4
Cylinder volume cell size (mm)	1.5 (0.5 from -30 to +30 °CA AFTDC)
Boundary layer thickness (mm)/n. of layers	0.1/2
Number of cells @ TDC	609,627

The 3D-CFD simulations were organized in three sequential stages:

1. Cold-flow simulations were carried out over two complete engine cycles, starting from EVO aiming at obtaining a coherent in-cylinder flow field, matching experimental trapped mass. Combustion and fuel injection were disabled, while boundary conditions for pressure, temperature, and composition were imported from the validated 0D/1D-CFD model. Combustion was replicated through a simple reinitialization of the cylinder before EVO. This ensured full consistency between the overall gas-dynamic system and the in-cylinder flow field keeping computational costs low. The comparison between simulated and experimental trapped mass at IVC (Figure 49) confirmed the reliability of this approach.

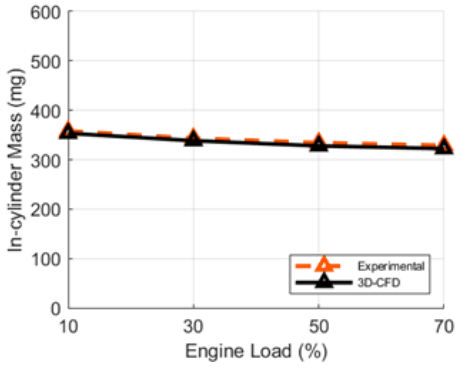

Figure 49: Experimental ad numerical (3D-CFD) comparison in terms of total in-cylinder trapped mass.

2. Reactive simulations were then performed between IVC and EVO to calibrate the combustion model. The initial charge consisted of a perfect premixed charge made up of air, hydrogen, and residual gases, with flow fields coming from the cold-flow stage. Although the assumption of a perfectly premixed hydrogen-air mixture introduces some simplification, it is justified by the geometry of the intake system and by the early port injection of hydrogen (at 346° CA bTDC), which guarantees sufficient time for homogenization before the diesel pilot injection.

3. Injection-strategy optimization followed the combustion calibration. Starting from the validated setup, different diesel injection strategies were tested to minimize diesel consumption while maintaining stable operation and comparable performance to the baseline diesel engine. The goal was to assess whether a single, reduced diesel injection could ensure reliable ignition and combustion stability while maximizing the hydrogen share.

The investigated operating points were defined in accordance with the experimental tests, covering four engine loads (10 %, 30 %, 50 %, and 70 %) at constant speed (2000 rpm). For each condition,

the trapped hydrogen mass, the corresponding relative air–fuel ratios for both fuels, and the injected diesel mass were extracted at IVC and are summarized in Table 17. This table also provides a direct comparison between the calibrated 3D-CFD setup and the experimental data, confirming the close alignment of the numerical model with the measured operating conditions.

The relative air–fuel ratios for hydrogen and diesel were computed as:

$$\lambda_{H_2} = \frac{\alpha_{H_2}}{\alpha_{H_2,st}} \quad (10)$$

$$\lambda_D = \frac{\alpha_D}{\alpha_{D,st}} \quad (11)$$

where $\alpha_{H_2}$and $\alpha_D$represent the actual air-to-fuel ratios for hydrogen and diesel, respectively, while $\alpha_{H_2,st} = 34.00$and $\alpha_{D,st} = 15.18$are the corresponding stoichiometric ratios.

In accordance with the experimental configuration, the diesel injection strategy consisted of two injection events: a pilot and a main pulse. The SOI angles were set to 12.8° bTDC for the pilot and 2.2° aTDC for the main injection. Minor adjustments were applied during calibration to better match the experimental pressure traces, remaining within the uncertainty margin of the test measurements.

Table 17: Comparison between main experimental and numerical parameters.

Engine Parameters	10%-load		30%-load		50%-load		70%-load	
	Exp	Num	Exp	Num	Exp	Num	Exp	Num
H_2 trapped mass (mg/cyl/cycle)	0	0	1.50	1.45	2.05	2.03	2.42	2.42
Diesel mass (mg/cyl/cycle)	3.65	3.65	3.72	3.71	3.96	3.96	3.82	3.82
λ_{H_2} (-)	-	-	6.51	6.41	4.57	4.49	3.80	3.69
λ_D (-)	6.21	6.07	5.81	5.72	5.30	5.16/	5.40	5.23
Swirl ratio (-)	-	2.2	-	2.2	-	2.2	-	2.2
Head temperature (K)	-	500	-	500	-	500	-	500
Liner temperature (K)	-	480	-	480	-	480	-	480
Piston temperature (K)	-	550	-	550	-	550	-	550

The calibration of the combustion model was based on the comparison between simulated and experimental in-cylinder pressure and AHRR at the four load levels. AHRR was derived from the first law of thermodynamics assuming no blow-by and a constant polytropic coefficient (k = 1.4) during compression and expansion, while the gross indicated mean effective pressure (IMEP*) was calculated as:

$$IMEP^* = \frac{1}{V_d}\int_{IVC}^{EVO} p\ dV \qquad (12)$$

The comparison between experimental and numerical results (Figure 50 a-d) showed excellent agreement for all load points. Table 18 summarizes the main performance and combustion-phasing indicators (IMEP*, peak pressure, PPRR, and CA10–CA90) together with their absolute deviations. Errors remained small in all cases, confirming the robustness of the calibration.

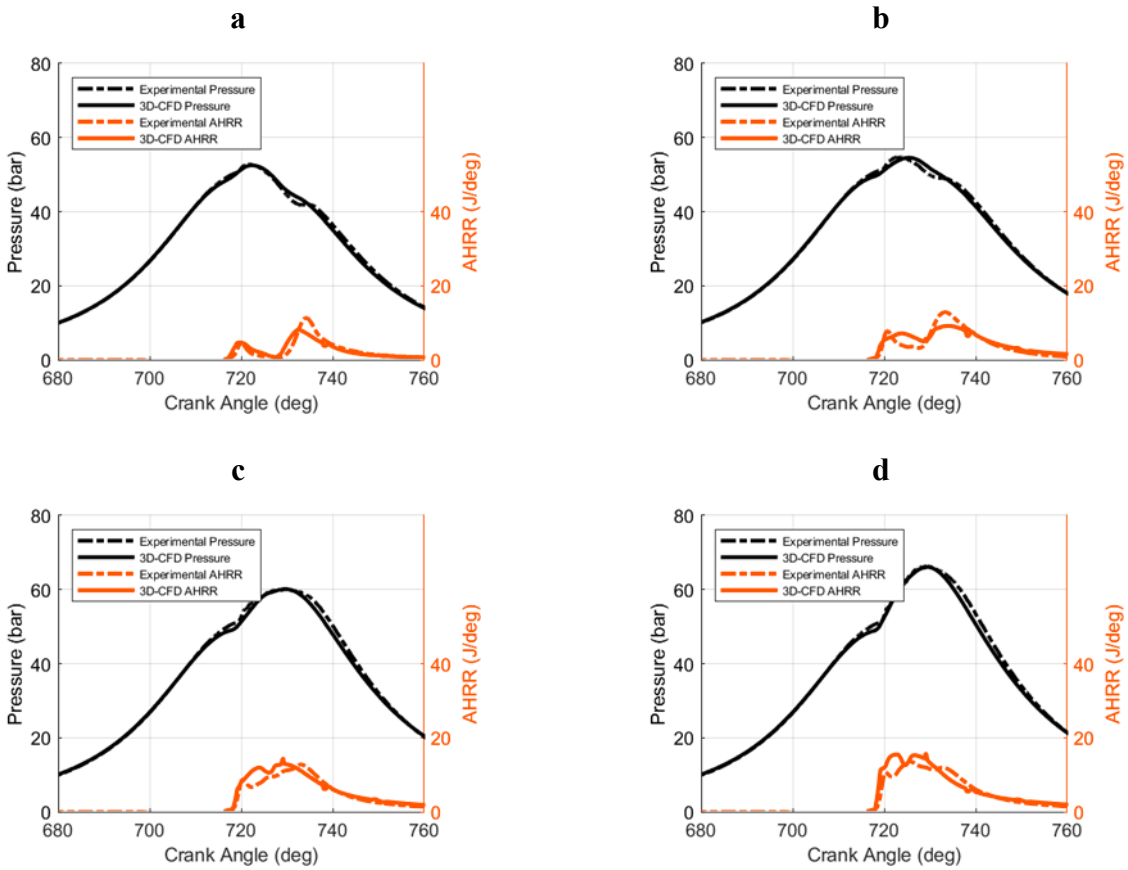

Figure 50: Experimental vs numerical (3D-CFD) comparison in terms of in cylinder pressure and AHRR: a) 10% load, b) 30% load, c) 50% load, d) 70% load.

Table 18: Comparison between experimental and numerical (3D-CFD) IMEP*; peak in-cylinder pressure; PPRR; combustion phasing parameters for the considered operating points.

Engine Parameter	**10% load**		**30% load**		**50%load**		**70%load**		**Absolute error**			
	Exp.	**Sim**	**Exp.**	**Sim**	**Exp.**	**Sim**	**Exp.**	**Sim**	**10%load**	**30%load**	**50%load**	**70% load**
IMEP* (bar)	1.93	1.92	3.67	3.78	5.02	5.12	5.69	5.7	0.01	0.11	0.10	0.01
Peak in-cylinder Pressure (bar)	52.9	52.5	54.8	54.6	60.1	60.1	66.3	66.1	0.40	0.20	0.00	0.2
PPRR (bar/deg)	1.55	1.54	1.57	1.55	1.72	1.57	2.46	2.53	0.02	0.02	0.15	0.1
CA10 (°CA aFTDC)	4.30	2.38	3.34	3.81	3.00	2.93	2.40	1.82	1.9	0.5	0.1	0.6
CA50 (°CA aFTDC)	15.9	15.0	15.6	16.3	13.7	12.9	12.3	11.0	0.9	0.7	0.6	1.3
CA90 (°CA aFTDC)	34.1	35.0	36.4	39.6	35.1	37.5	34.8	37.1	0.9	3.2	2.4	2.3
Δθ 10-50 (°CA)	11.6	12.6	12.3	12.5	10.7	10.0	9.9	9.2	1.0	0.2	0.7	0.7
Δθ 10-90 (°CA)	29.8	32.6	33.6	35.8	32.1	34.6	32.4	35.3	2.8	2.2	2.5	2.9

Crank angle	C_7H_{16} mass fraction	Temperature	
720 °CA	(a)	(e)	
	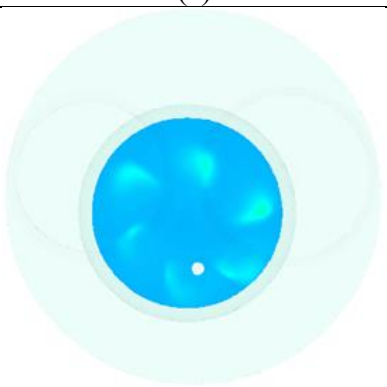	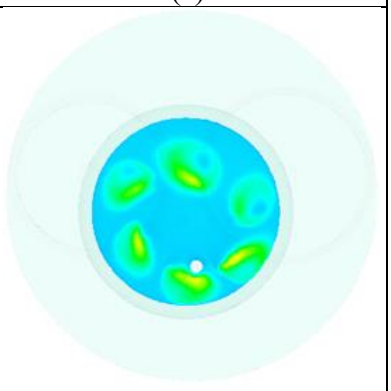	
725 °CA	(b)	(f)	
	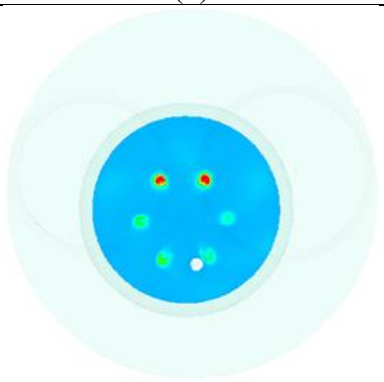	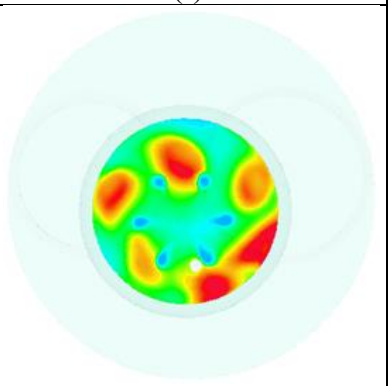	
730 °CA	(c)	(g)	
	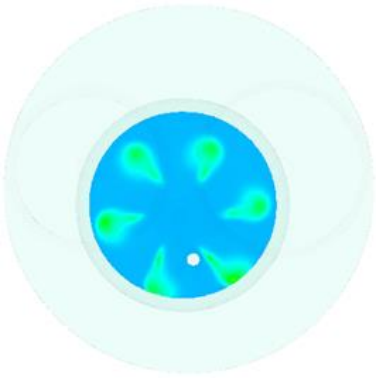	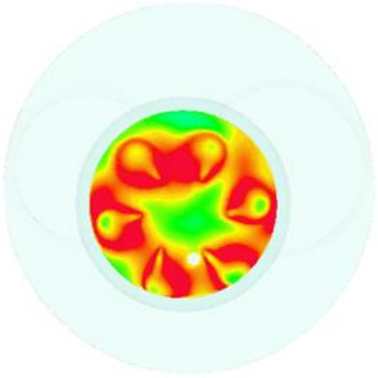	
735 °CA	(d)	(h)	
	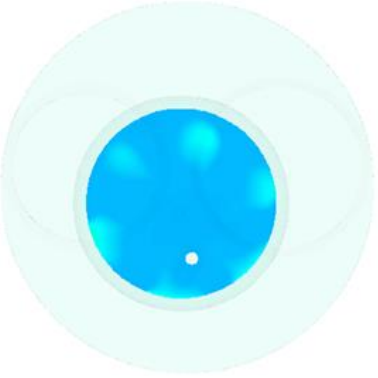	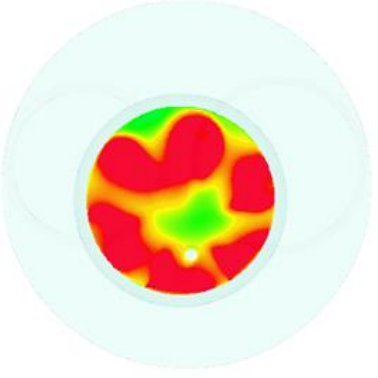	

Figure 51: Spatial distribution of in-cylinder C7H16 mass fraction and temperature on a cut plane perpendicular to the cylinder axis at 720°CA (a,e), 725 °CA (b,f), 730 °CA (c,g) and 735 °CA (d,h) for the 70% load case.

At 70 % load, the spatial distributions of C_7H_{16} mass fraction and temperature at different crank angles (Figure 51) reveal that the premixed hydrogen–air mixture is reliably ignited by the pilot diesel spray. Combustion initiates in the pilot injection region and progressively propagates throughout the premixed charge, resulting in a stable and well-controlled process. When the main injection occurs, the reaction is already well established, and its overall impact on combustion development is comparatively limited. Indeed, as highlighted in Figure 51 c and g, at around 730° CA, when the main injection penetrates the combustion chamber, it enters regions already characterized by high local temperatures. These areas correspond to zones previously ignited by the pilot spray, where hydrogen combustion has already consumed a significant portion of the available oxygen. As a consequence, the diesel injected during the main event burns under oxygen-deficient and high-temperature conditions, which are favourable to soot formation. This behaviour is consistent with experimental evidence, where an increase in particulate emissions was observed under this DF working condition.

A final comparison between simulated and measured emissions of CO_2, CO, and NO_x is shown in Figure 52 a-c. To reconcile the quantitative levels, a single multiplicative correction factor (one for each species) was applied to the numerical results, following a methodology previously adopted in similar works. This correction is mainly justified for the carbon-based emissions by (I) the use of n-heptane as a diesel surrogate, which differs in carbon content from the commercial diesel used experimentally, and (II) the possible contribution of lubricating-oil combustion, not accounted for in the model.

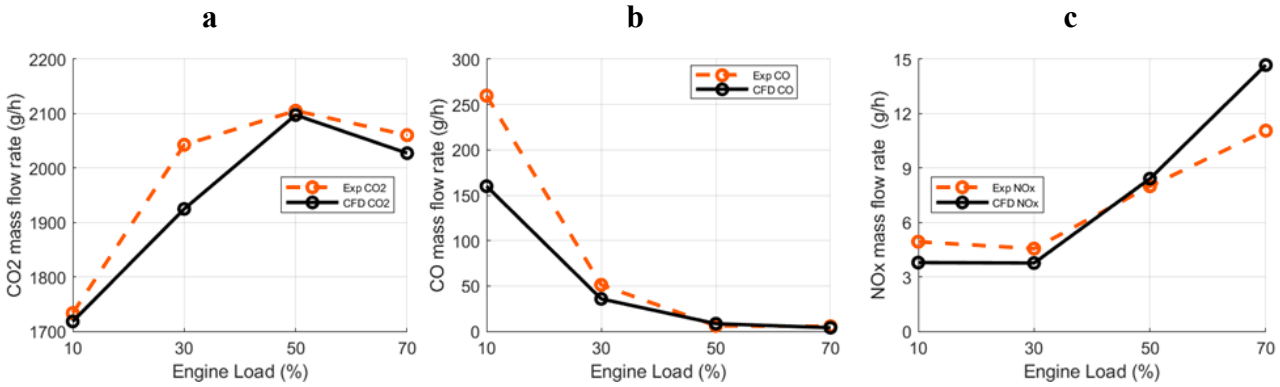

Figure 52: Experimental and numerical (3D-CFD) comparison in terms of emissions: a) CO2, b) CO and c) NOx.

After correction, the agreement between simulations and experiments was satisfactory across all species and operating conditions, confirming the model's ability to reproduce the dominant emission trends in hydrogen–diesel DF combustion.

The following tendencies were consistently captured:

- CO_2 emissions varied moderately with the injected diesel quantity, a tendency captured by both simulations and experiments;
- CO emissions decreased with higher hydrogen content, due to enhanced oxidation promoted by higher local temperatures and leaner mixtures;
- NO_x emissions increased with the hydrogen fraction, consistent with the faster heat-release rate observed (see MFB50 in Table 18), which led to higher peak temperatures and enhanced thermal NO formation.

Both the experiments and the simulations were conducted without EGR, a factor that explains the relatively high NO_x levels observed.

4.4. Injection optimization

Following the successful validation of the combustion model, a third simulation phase was devoted to the optimization of the diesel injection strategy under hydrogen–diesel DF operation. The primary objective of this activity was to evaluate the potential reduction of carbon-based emissions (CO and CO_2) and NO_x through a progressive decrease of diesel fuel usage, while maintaining combustion stability and performance (IMEP* and efficiency) comparable to the baseline configuration.

As previously described, the reference diesel strategy consists of two injections per cycle (a pilot and a main event). Starting from this baseline, a parametric sweep was carried out by progressively reducing the mass of the main injection in steps of 25 %, from 100 % (baseline case) down to complete removal (0 % main injection), while keeping the pilot event unchanged in both duration and timing. This resulted in a total of five distinct configurations, including the full-diesel baseline.

Figure 53 illustrates the evolution of the diesel injection law for the 50 % engine load. As shown, while the pilot pulse remains constant across all cases, the main event becomes progressively shorter until it is entirely removed. To ensure comparability between operating points, the energy reduction associated with diesel removal was compensated by an equivalent energy contribution from hydrogen, introduced through the premixed gaseous charge. This approach allowed isolating the effect of diesel substitution on combustion and emissions while maintaining a constant total energy input to the engine.

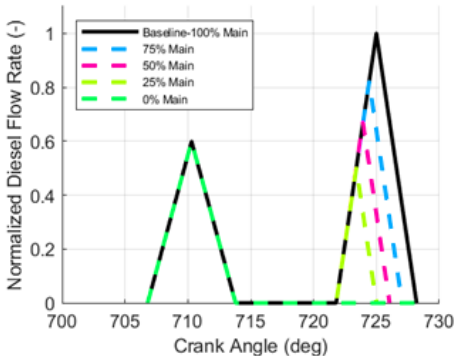

Figure 53: Diesel injection profiles at 50% engine loa, from baseline to reduced main cases.

To quantify the substitution level in a normalized form, the Energy Fraction (EF) parameter was defined as:

$$EF = \frac{E_D + E_{H_2}}{E_{D,full\ load}} \quad (13)$$

where E_D and E_{H_2} are the energy contributions of diesel and hydrogen at a given DF operating point, respectively, and $E_{D,full\ load}$ represents the total energy provided by diesel fuel under full-load, conventional diesel operation. These quantities are computed as:

$$E_D = m_D \cdot LHV_D \quad (14)$$

$$E_{H_2} = m_{H_2} \cdot LHV_{H_2} \quad (15)$$

$$E_{D,full\ load} = m_{D,full\ load} \cdot LHV_D \quad (16)$$

During the previous cold-flow and combustion calibration simulations, the analysis was carried out at fixed engine loads. However, once part of the diesel energy was replaced by hydrogen, the same load could no longer be maintained, as the substitution altered the global working condition of the engine. Consequently, engine load was no longer a consistent reference variable, and the Energy Fraction (EF) was adopted as the primary comparative metric across all cases. The correspondence between baseline engine loads and their associated EF values is reported in Table 1.

Table 19: Correspondence between engine load and Energy Fraction (EF) values.

Baseline load cases				**Corresponding EF**			
10%	30%	50%	70%	EF0.22	EF0.47	EF0.58	EF0.64

Table 20: Diesel and hydrogen injection strategies for each energy fraction.

property	%main	EF0.22	EF0.47	EF0.58	EF0.64
Injected diesel mass (mg/cyl/cycle)	**100%**	3.65	3.71	3.96	3.82
	75%	3.08	3.10	3.34	3.22
	50%	2.51	2.49	2.72	2.62
	25%	1.94	1.88	2.1	2.03
	0%	1.37	1.27	1.48	1.43
Main diesel injection peak velocity (m/s)	**100%**	115	100	100	130
	75%	93	93	93	100
	50%	82	82	82	82
	25%	55	55	55	55
	0%	0	0	0	0
H_2 mass (mg/cyl/cycle)	**100%**	0	1.45	2.03	2.42
	75%	0.21	1.68	2.27	2.65
	50%	0.42	1.89	2.51	2.88
	25%	0.62	2.08	2.71	3.13
	0%	0.83	2.34	2.94	3.29

For each EF condition, Table 20 summarizes the parameters modified during the optimization campaign—namely, the injected diesel mass, the total hydrogen trapped in the cylinder at IVC, and the estimated peak injection velocity of the main diesel event. The baseline configuration (100 % main injection) is included for reference.

This systematic variation of the diesel injection profile, compensated by a proportional increase in hydrogen, enabled a detailed investigation of the transition from dual-fuel to near-hydrogen operation. Through this method, it was possible to assess the influence of the pilot-only combustion mode, evaluating whether a single small diesel injection could effectively ensure stable ignition and controlled combustion, while maximizing the hydrogen energy share up to approximately 86 % under the least critical operating conditions.

4.5. Results and discussion

The results of the injection optimization campaign are presented in this section, focusing on the combined effects of diesel reduction and hydrogen substitution on combustion behaviour, performance, and emissions.

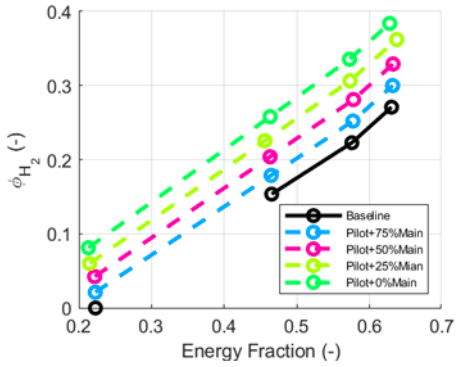

Figure 54: Φ_{H_2} across all injection strategies.

Figure 54 reports the Φ_{H_2} for all the simulated configurations, including the baseline cases. The lowest investigated EF (EF = 0.22) corresponds to conventional diesel operation, whereas all other conditions represent DF operation. As the main diesel mass was progressively reduced and the hydrogen contribution increased, the premixed hydrogen–air mixture became richer. Nevertheless, all configurations remained within the lean or ultra-lean regime, ensuring safe and stable combustion without knocking tendency.

The combustion efficiency (defined as the ratio between the accumulated heat release and the total chemical energy supplied by both fuels) is shown in Figure 55-a. Two distinct behaviours were observed depending on the energy fraction. At low EF (EF = 0.22), any reduction or suppression of the main diesel injection led to a marked efficiency drop, reaching values as low as 0.61 when the main injection was completely removed. Under these conditions, hydrogen contributed little to the combustion process and, in some zones, its presence even hindered diesel ignition by displacing air and reducing local oxygen availability. Conversely, at higher EF values, the combustion efficiency of the reduced-main strategies was nearly identical to that of the baseline configuration. This indicates that at high hydrogen substitution levels, and with sufficient global energy input, combustion remains complete and stable even when diesel injection is minimized.

The Gross Indicated Efficiency (GIE), which quantifies the ratio of the indicated work to the total input chemical energy between intake valve closing (IVC) and exhaust valve opening (EVO), was computed as:

$$GIE = \frac{IMEP^* \cdot V_d}{E_D + E_{H_2}} \quad (17)$$

where V_d denotes the engine total displacement.

As shown in Figure 55-b, at EF = 0.22, the progressive reduction of the main injection mass caused a significant loss in GIE, mirroring the drop in combustion efficiency. However, as the energy fraction increased, reduced-main cases achieved GIE values comparable to, or even slightly higher than, the baseline.

The most favourable condition was observed at EF = 0.47 with a 50 % main-injection reduction, which yielded a 3 % improvement in GIE relative to the corresponding baseline configuration. This improvement resulted from a faster combustion rate during the early stages of heat release, as confirmed by the shorter combustion durations and the shift of the CA50 toward TDC.

The crank-angle intervals CA10–90 and CA10–50 (Figure 55 d-e) were reduced in most reduced-main cases, reflecting a faster overall burn rate. Consequently, combustion phasing advanced (Figure 55-f), leading to higher peak in-cylinder pressures (Figure 55-g) and pressure-rise rates (PPRR) (Figure 55-h). Even at the most severe condition (EF = 0.64 with 0 % main injection), the increases in peak pressure (+5.1 bar) and PPRR (+1.3 bar/°CA) remained well within the structural limits of the engine.

The emissions of CO_2, CO, and NO_x as a function of EF are reported in Figure 55 i-m. As expected, both CO_2 and CO decreased proportionally with the reduction of diesel fuel. The evolution of NO_x, however, exhibited a more complex trend. Although the faster hydrogen combustion could in principle raise flame temperatures, NO_x emissions decreased when the main diesel injection was strongly reduced or completely eliminated. This counterintuitive behaviour is explained by the transition from localized high-temperature diesel combustion to a lean, premixed hydrogen-air regime. In all simulated cases, the hydrogen relative air–fuel ratio λ_{H_2} remained above 2.7, a condition under which hydrogen combustion is known to produce negligible thermal NO_x [126]. Therefore, increasing diesel replacement with hydrogen consistently led to lower NO_x formation.

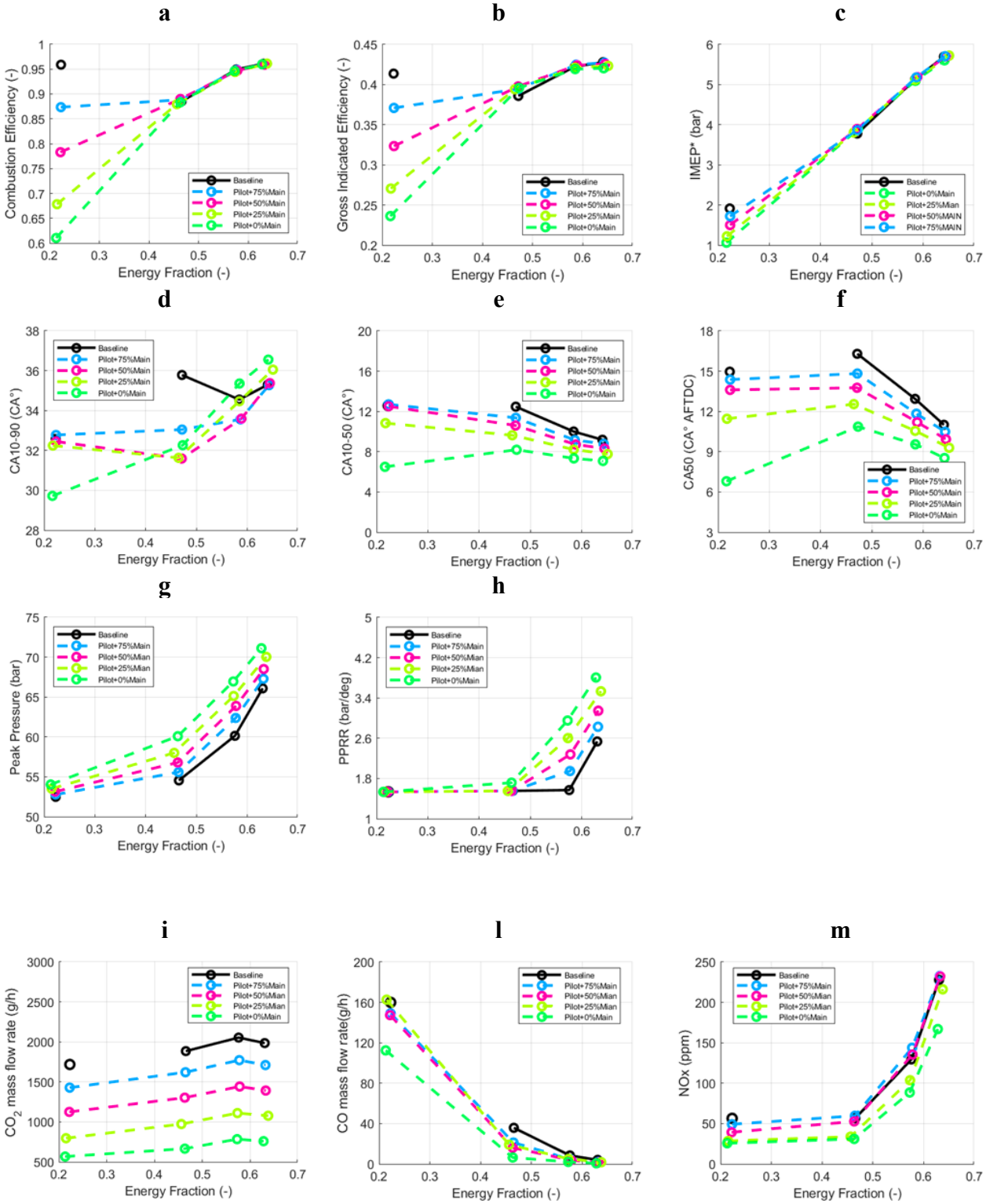

Figure 55: Comparison of main engine performance parameters for all studied injection strategies.

From these analyses, several key findings emerge:

- At EF0.22, reducing the main diesel injection significantly worsened both combustion efficiency and GIE, offering no performance benefit.
- At EF0.47, a 50 % main-injection reduction slightly increased GIE while simultaneously decreasing carbon-based emissions, providing the best trade-off between performance and environmental impact.
- At higher energy fractions (EF0.58 and EF0.64), GIE values remained similar across all injection strategies, but eliminating the main injection further reduced CO_2, CO, and NO_x emissions.

Based on these results, an optimized diesel injection configuration was identified for each energy fraction, aiming to maintain engine performance close to the baseline while minimizing emissions:

- 100 % main injection at EF0.22 (diesel operation);
- 50 % main injection at EF0.47;
- 0 % main injection at EF0.58 and EF0.64.

It is worth noting that the EF0.22 case corresponds to pure diesel operation, since at such a low load hydrogen combustion was incomplete and contributed negligibly to the total heat release. Consequently, full-diesel mode was retained as the optimal solution for this condition. At the opposite end, the EF0.64 configuration represents the condition with the highest hydrogen energy share, reaching approximately 86 % of the total fuel energy. This demonstrates that, under medium-high load conditions, it was possible to further extend hydrogen substitution compared to the full-load case analysed in the previous study, while maintaining stable combustion and respecting the mechanical constraints of the engine. The performance and emission results of the optimized cases are summarized in Table 21, in comparison with the corresponding baseline dual-fuel configurations.

Table 21: Comparison between the optimized and the baseline DF cases in terms of the main thermodynamic and combustion parameters and engine emissions.

	GIE		**Peak Pressure**		**CA10-90**		**Injected Diesel**		**CO_2**		**CO**		**NO_x**	
	val.	**Δ%.**	**val.**	**Δ%**	**val.**	**Δ%**	**val.**	**Δ%**	**val.**	**Δ%.**	**val.**	**Δ%**	**val.**	**Δ%**
	(bar)	**(%)**	**(bar)**	**(%)**	**(°CA)**	**(%)**	**(g/h)**	**(%)**	**(g/h)**	**(%)**	**(g/h)**	**(%)**	**(ppm)**	**(%)**
EF0.22	0.41	0.0	52.5	0.0	32.6	0.0	657.0	0	1718	0.0	160	0.0	56.5	0.0
EF0.47	0.40	+2.8	56.8	+4.0	31.6	-11.7	448.2	-32.9	1303	-32.3	16.2	-54.8	52.8	-7.0
EF0.58	0.42	-0.7	63.9	+6.3	35.4	+2.5	266.4	-62.6	785	-62.5	2.09	-75.5	88.5	-31.6
EF0.64	0.42	-1.8	71.1	+11.4	36.5	+3.4	257.4	-62.6	760	-62.4	0.77	-81.1	167	-26.7

Figure 56 a-c compare the in-cylinder pressure and AHRR traces for the baseline and optimized cases at EF0.47, EF0.58, and EF0.64. In the optimized configurations, combustion was noticeably faster, with a sharper and earlier AHRR peak compared to the baseline. This acceleration in heat release produced higher peak pressures and PPRR values, consistent with the trends already summarized in Table 21.

Further insight into the mechanisms governing NO_x formation is provided in Figure 57 a-c. Although the average in-cylinder temperature increased in the optimized cases due to the higher hydrogen content, NO_x emissions were consistently lower than in the corresponding baseline cases. Up to the onset of the main diesel injection, the temporal evolution of NO_x formation was almost identical between the two strategies. After that point, however, the trends diverged markedly, particularly in configurations where the main injection was suppressed. This confirms that the reduction or elimination of the main injection was the primary driver behind the observed NO_x reduction, despite the slightly higher overall temperatures.

A closer look at the temperature fields in Figure 58 a-h (for EF0.64) further supports this interpretation. At 720° CA, both the baseline and optimized cases displayed nearly identical temperature distributions, since the pilot injection was unchanged. From 730° CA onward, the baseline case developed localized hot spots typical of conventional diesel combustion, while the optimized configuration exhibited a more homogeneous temperature field, with smoother gradients and no pronounced high-temperature zones. This behaviour confirms that the removal of the main diesel injection effectively suppresses the formation of the localized hot regions responsible for thermal NO_x production.

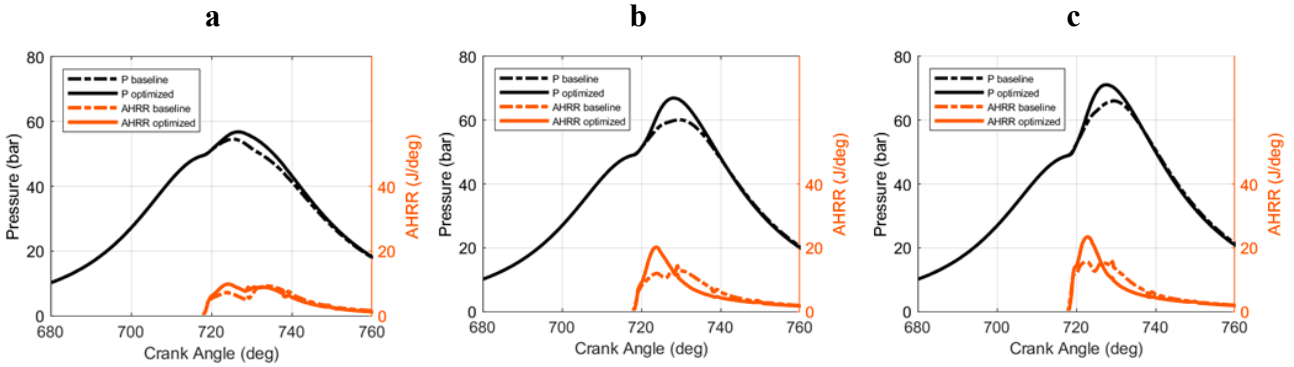

Figure 56: Comparison of in-cylinder pressure and AHRR between baseline and optimized DF cases at: a) EF0.47, b) EF0.58, and c) EF0.64.

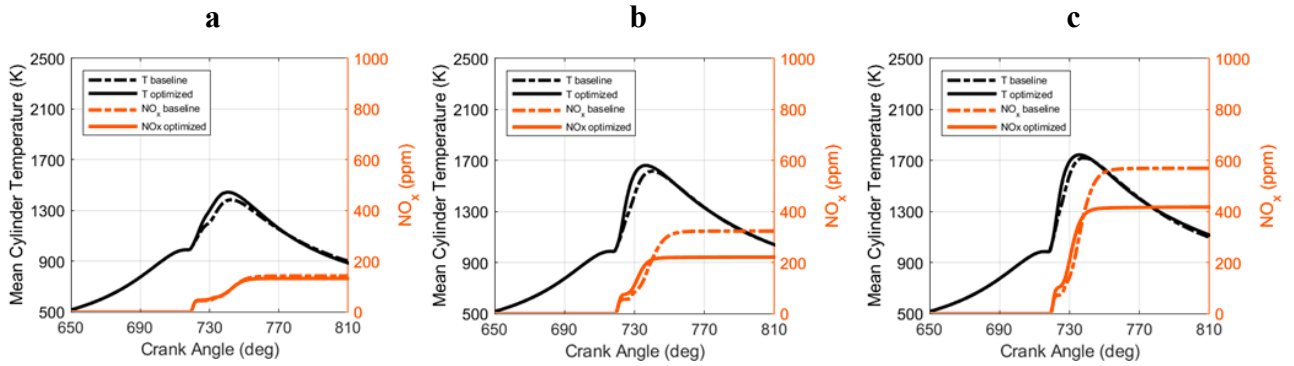

Figure 57: Comparison of average in-cylinder temperature and NO_x formation over the engine cycle for baseline and optimized configurations at: a) EF0.47, b) EF0.58, and c) EF0.64.

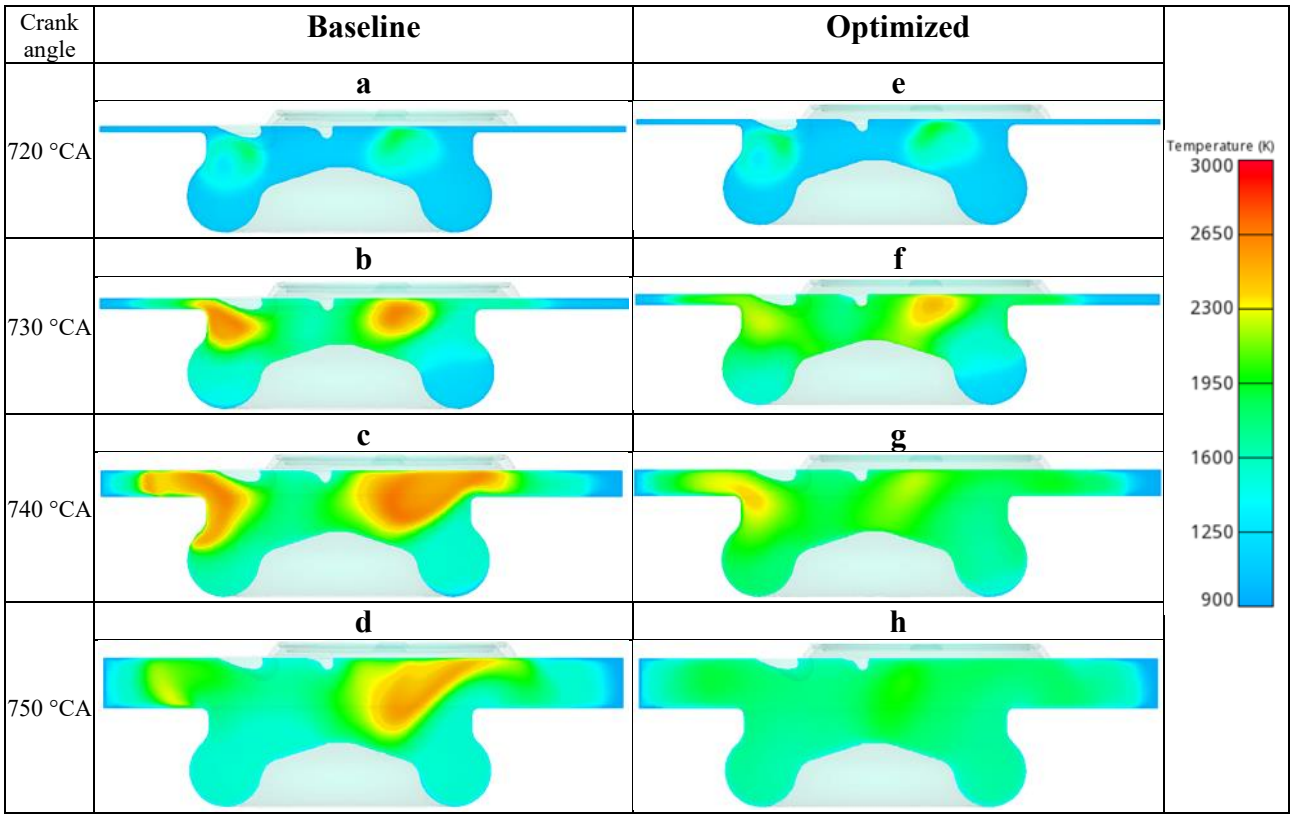

Figure 58: Spatial distribution of in-cylinder temperature on a cut plane that includes both the cylinder and the injector axis at 720 °CA (a, e), 730 °CA (b, f), 740 °CA (c, g), and 750 °CA (d, h) for the EF0.64 case. Comparison between baseline and optimized cases.

4.6. Conclusions and final remarks – transitioning to advanced combustion strategies

In this part of the work, the analysis focused on hydrogen–diesel DF combustion in a modified compression-ignition engine, combining experimental measurements with both 0D/1D and 3D-CFD simulations. The main objective was to understand how the diesel injection strategy influences the combustion process, and whether a gradual reduction, or even the complete removal, of the main diesel injection could enhance efficiency while further lowering emissions. To ensure comparability across different operating conditions, the analyses were performed at various Energy Fractions (EFs), representing the ratio between the total energy supplied by the fuels (diesel + H_2) and the reference energy of the full-load diesel operation.

The results highlighted distinct behaviours depending on the operating load:

- At low load (EF = 0.22), hydrogen combustion proved unstable and incomplete due to the extremely lean mixture, making full diesel operation the only viable configuration to guarantee ignition and combustion stability.
- At medium load (EF = 0.47), reducing the main injection by 50 % improved the gross indicated efficiency by about 3 %, while significantly decreasing diesel consumption (–33 %), CO_2 (–32 %), CO (–55 %), and NO_x (–7 %).
- At higher loads (EF = 0.58–0.64), the main injection could be completely eliminated with negligible efficiency penalties (–0.7 % to –1.8 %), still achieving marked reductions in fuel consumption and emissions (more than 60 % less diesel and CO_2, about 80 % less CO, and roughly 30 % less NO_x).

Although the average in-cylinder temperature slightly increased due to the faster hydrogen combustion, NO_x emissions continued to decrease as the main diesel injection was reduced. This behaviour was attributed to the transition from diffusion-controlled diesel flames to an ultra-lean, premixed hydrogen–air combustion regime, as confirmed by the 3D-CFD simulations showing a more homogeneous temperature field and the absence of localized hot spots in the optimized cases.

In the previous study (see paragraph 3 *"Numerical exploration of diesel-hydrogen dual-fuel combustion: up to 80% of hydrogen share"*), the optimization of the diesel injection timing had proven effective in improving combustion phasing and recovering performance losses at high hydrogen substitution levels, achieving results comparable (or even superior) to those of the baseline Diesel operation, while reducing carbon-based emissions. Building on that foundation, and moving

toward an increasingly reduced use of fossil fuel within the combustion process, the present work focused instead on the injected diesel quantity, keeping the pilot injection unchanged in both timing and duration. This approach made it possible to investigate whether a small pilot injection alone could ensure stable ignition and combustion when most of the energy was supplied by hydrogen. The results showed that, at medium-medium/high load, stable operation could indeed be achieved with a single, small pilot event, allowing the hydrogen energy share to increase up to 86 % without exceeding the engine's mechanical limits. These findings clearly demonstrate the central role of the diesel injection law in governing the dual-fuel combustion process.

The results obtained in this section also provided a conceptual and methodological bridge toward the next phase of the research. Once the influence of the diesel injection law was fully characterized under medium–high load conditions, the analysis naturally evolved toward the development of advanced low-temperature combustion modes. By shifting the diesel injection to much earlier crank angles, the strategy progressively transitioned into a Reactivity-Controlled Compression Ignition (RCCI) with a HCCI-like regime. As will be discussed in the following chapter, this new configuration (tested at BMEP = 6 bar) enabled a hydrogen energy share exceeding 95 %, reducing the diesel contribution to below 5 % of the total energy input. This approach represents a further step toward nearly carbon-free engine operation, while retaining the controllability and ignition stability typical of dual-fuel systems.

5. 3D-CFD-guided optimization of advanced dual-fuel combustion: toward ultra-high hydrogen shares

Building upon the previous optimization of diesel injection strategies from low to high hydrogen substitution ratios, the next stage of this research focused on pushing the DF concept to its physical limits. The primary goal of this investigation was to assess how far the Hydrogen Energy Share (HES) could be increased while maintaining combustion stability, acceptable pressure-rise rates, and high efficiency. This phase therefore represents the transition from optimized RCCI operation to advanced DF combustion regimes, characterized by highly premixed, low-temperature burning conditions.

This activity was carried out as part of the author's Ph.D. research at Brunel University London, under the supervision of Prof. Xinyan Wang, within the Centre for Advanced Powertrain and Fuels (CAPF). The professor and his research group, provided support and the experimental data required for the calibration of the CFD framework and for the subsequent optimization of diesel injection strategies discussed in this chapter. The collaboration enabled the development of a high-fidelity numerical model capable of accurately reproducing the in-cylinder processes of a single-cylinder heavy-duty Diesel engine operated in DF Diesel–hydrogen mode.

Previous results showed in the previous chapters, demonstrated that, at moderate hydrogen shares, careful calibration of the diesel pilot injection allows for significant improvements in efficiency and partial reduction of CO and CO_2. However, the increase in hydrogen content also led to steeper heat-release rates and higher in-cylinder pressures, which imposed structural and thermal limits on the engine operation. To overcome these constraints, the present work explores more advanced injection strategies aimed at reducing the diesel energy fraction while promoting a more homogeneous charge preparation (a prerequisite for achieving ultra-clean combustion with minimal pollutant formation).

The analysis was conducted at low-load operating conditions, where the mechanical constraints are less restrictive and the predictive capability of the combustion and emission models is more reliable. Starting from the previously calibrated CFD setup, a systematic two-step optimization was performed:

1. In the first phase, different mass splits and timings of pilot and main injections were investigated to promote an RCCI-type combustion, in which the diesel triggers the ignition of the premixed hydrogen–air charge.
2. In the second phase, the diesel quantity was progressively reduced and advanced, leading to a single, early injection that burns under HCCI-like conditions, while hydrogen continues to

behave as the low-reactivity fuel, being ignited by the auto-ignition of the diesel pilot according to the RCCI principle.

In this configuration, the diesel acts as a distributed ignition source initiating the combustion of the hydrogen–air mixture, while hydrogen provides almost the entire energy contribution. This combined approach allowed exploring a wide range of reactivity-controlled conditions, ultimately achieving hydrogen energy shares up to 98 %, and providing new insight into the physical limits and potential of DF diesel–hydrogen combustion.

5.1. Yuchai YC6K engine description

The experimental and numerical activities were carried out on a single-cylinder research engine derived from the Yuchai YC6K six-cylinder heavy-duty Diesel engine, specifically modified by Brunel "Centre of Advanced Powertrain and Fuels" to operate in DF condition. The short block and crankcase assembly were entirely re-engineered by AVL, featuring two counter-rotating balance shafts to minimize mechanical vibrations and ensure smooth operation in steady and transient conditions. This configuration was developed to reproduce the thermodynamic behaviour of a large-bore commercial engine under fully controlled laboratory conditions, enabling flexible operation with both conventional and alternative fuels. The engine's main specifications are reported in Table 22.

Table 22: Single cylinder engine specification.

Engine parameter	Description
Bore × Stroke (mm × mm)	129 × 155
Cylinder displacement (cc)	2026
Connecting rod length (mm)	256
Geometric compression ratio	16.8
Max. in-cylinder pressure (bar)	180
Max PPRR (bar/deg)	15
Max. engine speed (rpm)	1900
Piston	Re-entrant diesel bowl
N. of valves	4
Intake/Exhaust valve Diameter (mm/mm)	43.9 / 40.4
Intake cam duration (CAD, mm)	Variable
Exhaust cam duration (CAD, mm)	5250, 14
Exhaust cam timing (AFTDC)	Open: -227 Close: 18
Diesel injector	Central DI Bosch CRIN 3.22, 8 Hole 150°, 0.176 mm hole diameter, Common Rail, 2200 bar max pressure

The engine features a bore and stroke of 129 and 155 mm, respectively, yielding a displacement of 2.03 L. The geometric compression ratio is 16.8:1, though the effective compression ratio can vary depending on the intake valve closing strategy adopted via the variable valve actuation system. The engine operates up to 1900 rpm and is capable of reaching peak in-cylinder pressures of approximately 180 bar under full-load Diesel operation. Independent lubrication and cooling circuits are employed, equipped with thermostatic control to reproduce stable temperature conditions during testing.

The cylinder head adopts a four-valve layout (two intake, two exhaust) driven by dual overhead camshafts. The most distinctive feature of the research engine is the hydraulic Variable Valve Actuation (VVA) system installed on the intake camshaft, which enables implementation of advanced Miller-type cycles [127].

The VVA system, developed by Jacobs Vehicle Systems, relies on a lost-motion hydraulic mechanism that decouples the valve motion from the fixed cam profile. A high-pressure oil circuit, controlled by an electro-hydraulic solenoid valve, regulates the oil flow to the lost-motion chamber, thereby adjusting the effective intake valve timing and duration independently of the camshaft rotation. A schematic view of the solenoid assembly is depicted in Figure 59. This configuration allows real-time modulation of the IVC, making it possible to reproduce both Late Intake Valve Closing (LIVC) and the Second Intake Valve Opening (2IVO, [128]), which introduces a brief secondary opening of the intake valve during the exhaust stroke to acting as a controllable internal EGR (iEGR). By delaying the intake valve closure through LIVC, instead , the effective compression ratio decreases while maintaining the expansion ratio constant, leading to an overall improvement in thermal efficiency and a reduction of in-cylinder temperatures. Such a configuration is particularly advantageous for dual-fuel and RCCI modes, where it promotes homogeneous mixture formation and avoids excessive pressure-rise rates. Figure 60 illustrates various advanced lift profile that can be obtained by varying the actuation parameters of the VVA system.

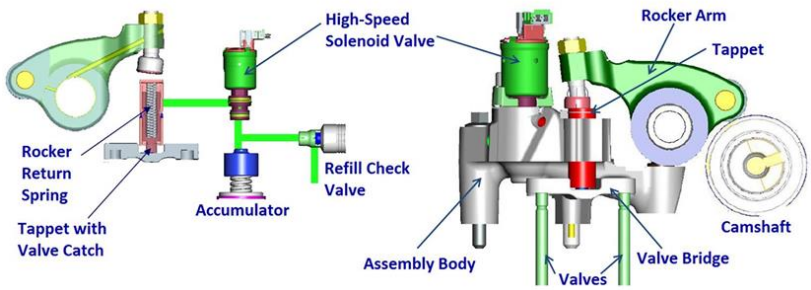

Figure 59: Lost-motion intake VVA system with collapsing tappet on the valve side of the rocker arm [129].

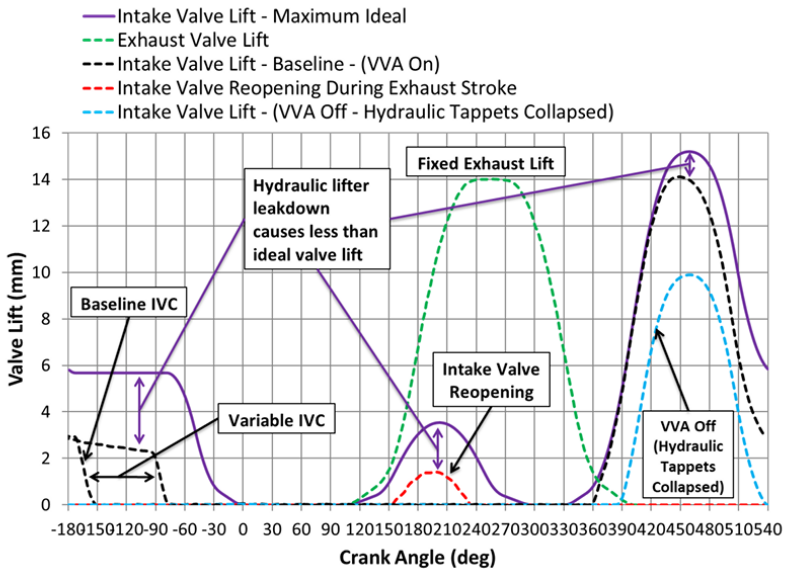

Figure 60: Possible intake valve lift profiles enabled by the hydraulic VVA system [129,130]

Valve lift is monitored using a MicroStrain S-DVRT-8 displacement transducer. The exhaust valve train retains a conventional fixed cam profile, with an opening duration of approximately 245 CAD and a maximum lift of about 14 mm.

The engine is coupled to an eddy-current dynamometer (Froude Hofmann AG150) capable of both torque and speed control. The Diesel circuit is based on a Bosch CRIN 3.22 common-rail injection system, featuring a centrally located eight-hole injector with 0.176 mm nozzle diameter and a spray cone angle of 150°. Injection pressure is provided by a Bosch CP4-S2 high-pressure pump, capable of delivering up to 2200 bar, and is managed by a Bosch CR.8 electronic control unit (ECU). The system enables fully independent control of injection pressure, injection timing, and mass split between pilot and main injections, allowing flexible operation from conventional Diesel combustion to advanced dual-fuel strategies.

Fuel mass flow in both the supply and return lines is measured through Coriolis mass flow meters (Endress + Hauser Promass 83A), ensuring accurate instantaneous consumption and heat-release estimation. The high-pressure lines and common-rail accumulator are thermally insulated and equipped with pressure sensors for safety and repeatability.

The air path employs a closed-loop external boosting system designed to maintain constant intake pressure throughout the operating range. A variable-speed electrically driven compressor supplies the intake charge, while a water-cooled intercooler regulates the intake air temperature. Both pressure and temperature sensors (PT100 and piezo-resistive transducers) are installed upstream and downstream of the plenum to ensure accurate boundary control.

The experimental setup is also equipped with a high-pressure cooled EGR (HPL) loop, which allows the introduction of recirculated exhaust gases when required. However, it is important to note that for all the operating points analysed in this work, the EGR system was deactivated, in order to isolate the effects of hydrogen substitution and diesel injection strategy on combustion behaviour and emissions. This configuration ensures stable and repeatable intake conditions, providing a well-controlled environment for the calibration and validation of the CFD model under DF operation.

Exhaust emissions were measured using a modular analytical system designed for heavy-duty single-cylinder applications. A dedicated sampling probe was positioned downstream of the exhaust manifold, ensuring representative raw-gas sampling. The sampling line was heated and insulated to prevent condensation and preserve gas composition. Major gaseous species (CO, CO_2, NO_x, O_2, and THC) were quantified using a HORIBA MEXA-7170 DEGR analyser, while soot concentration was determined with an AVL 415SE smoke meter operating according to the Filter Smoke Number method. The sampling system includes a back-pressure stabilization tank and a particle filter upstream of the analysers.

All engine parameters were monitored and recorded through an integrated data acquisition system developed in MATLAB/Simulink and interfaced with National Instruments hardware. Cycle-resolved in-cylinder pressure was measured using a piezoelectric pressure transducer (Kistler 6052C) and a charge amplifier (Kistler 5011B), synchronized with a 720 ppr optical encoder mounted on the crankshaft, ensuring a resolution of 0.5 CAD. All signals were acquired and averaged over at least 200 consecutive cycles to ensure stability and repeatability.

5.2. 3D-CFD modelling and validation

The 3D-CFD simulations were performed using AVL FIRE M, with the aim of reproducing the in-cylinder processes of the hydrogen–diesel DF engine described previously. The modelling activity was structured as a two-step process: first, a calibration phase of the combustion model under baseline operating conditions, and second, the optimization of the Diesel injection strategy to maximize hydrogen utilization and overall efficiency.

Since no coupled 0D/1D CFD model was developed, the analysis was limited to the in-cylinder processes, neglecting the flow phenomena occurring in the intake and exhaust ports. Consequently, the computational domain was restricted to the compression and expansion strokes, ranging from IVC to EVO. The in-cylinder flow field was initialized by prescribing a swirl ratio consistent with the corresponding experimental condition, while the thermodynamic properties of the trapped charge

(pressure and temperature) were defined to ensure both the same in-cylinder pressure at IVC and the same total mass as measured during the experiments. Wall temperatures for the piston crown, cylinder liner, and head were assigned according to literature, while valve and injector geometries were defined with the same lift profiles and timings as used experimentally. This procedure allowed the numerical setup to reproduce the experimental boundary conditions with good fidelity, while significantly reducing computational cost.

The simulations were based on the Reynolds-Averaged Navier–Stokes (RANS) formulation, adopting the k–ζ–f turbulence model as closure. Spray atomization of Diesel fuel was described by the Kelvin–Helmholtz/Rayleigh–Taylor (KH–RT) breakup model, while n-heptane (C_7H_{16}) was employed as the surrogate for commercial Diesel in gas-phase reactions. Combustion was modelled with the ECFM-3Z approach, which captures both premixed and diffusion-controlled combustion regimes. This model was coupled with AVL's laminar flame-speed and auto-ignition delay databases to ensure an accurate representation of hydrogen–Diesel interactions across a broad range of operating conditions.

The emission sub-models accounted for CO, CO_2, and NO_x formation. CO and CO_2 were predicted through a two-step global oxidation mechanism, describing the partial oxidation of the surrogate fuel to CO and its subsequent conversion to CO_2, while the second step was neglected under globally lean conditions. NO_x formation was modelled using the extended Zeldovich thermal mechanism. A summary of the physical and chemical sub-models adopted in this work is reported in Table 6, consistent with those described in the previous chapters.

The computational domain included, as mentioned before, only the engine cylinder, which was simulated in full-size configuration since the detailed CAD geometry of the combustion chamber and valve seats was available. This allowed an accurate representation of the in-cylinder flow field and of the spray–wall interaction zones during the combustion process. A representative view of the computational mesh is shown in Figure 61.

The mesh was generated using AVL FIRE™ Mesh, adopting a base cell size of 3 mm in the bulk volume. Two conical refinement regions were defined one for each injector hole, with characteristic cell sizes of 0.4 mm and 0.2 mm, in order to capture droplet breakup and vapor–air mixing in the near-nozzle region. Additionally, during the combustion phase, a refinement down to 1 mm was activated within the chamber to better resolve the flame front and local mixture gradients. At top dead centre, the mesh consisted of approximately 1.13×10^6 cells (see Table 23). The cylinder mesh refinements had been adapted to the injection strategy adopted so, different meshes with same mesh parameters but different refinement timing were created.

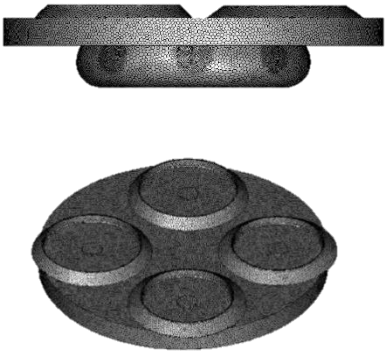

Figure 61: Side and prospective views of the computational grid.

Table 23: Computation grid details.

Property	Value
Target cell Size (mm)	3
1st and 2nd Injection refinements (mm)	0.4 and 0.2
Cylinder volume cell size (mm)	3 (1 from -20 to +40 °CA AFTDC)
Boundary layer thickness (mm)/n. of layers	0.1/2
Number of cells @ TDC	1,130,000

Table 24: main parameters of the tested operating points of the single cylinder engine.

IMEP (bar)	**6**			**12**			**18**		
λ_g (-)	**2.15**	**2.42**	**2.56**	**1.56**	**2.03**	**2.89**	**1.32**	**1.39**	**1.51**
λ_{H_2} (-)	3.42	3.79	4.07	2.45	3.20	4.57	4.37	4.57	4.92
Engine speed (rpm)	1218	1218	1218	1213	1213	1213	1213	1213	1213
Brake Torque (Nm)	71.0	70.7	70.4	159.5	162.7	165.7	257.5	258.0	258.4
Brake Power (kW)	9.0	9.0	8.9	20.2	20.6	21	32.6	32.6	32.7
Diesel mass flow rate (kg/h)	0.796	0.758	0.791	1.45	1.47	1.50	4.72	4.63	4.60
H_2 mass flow rate (kg/h)	0.6	0.6	0.6	1.14	1.14	1.15	0.91	0.91	0.91
Diesel Fuel Mass (mg/cyl/cycle)	21.79	20.76	21.64	39.8	40.4	41.2	129.8	127.3	126.3
H_2 Fuel Mass (mg/cyl/cycle)	16.4	16.4	16.4	31.3	31.3	31.6	25.0	25.0	25.0
HES (%)	67	68	67	69	68	68	35	35	36
Diesel injection strategy	Pilot + Main								
Hydrogen injection strategy	Single Injection								

The calibration of the 3D-CFD model was carried out on a total of nine operating points, covering three engine loads at the same engine speed and three air-to-fuel ratios for each load condition. For each case (low, mid, high load), the compressor boost pressure was adjusted to obtain three distinct λ_{H_2} values of the hydrogen-air mixture and global λ_{H_2}, while maintaining the same engine speed and injected mass of both fuels. The main parameters characterizing these operating points are summarized in Table 24, which reports the values of engine load (IMEP*), the injected diesel mass, the injected hydrogen mass, Hydrogen Energy Share (HES) etc.

The model calibration was performed by comparing the in-cylinder pressure trace and the corresponding apparent heat release rate (AHRR) calculated from both experiments and simulations using the first law of thermodynamics. A good agreement between CFD and experimental results was achieved for the pressure evolution and heat-release shape across the entire operating range as

illustrated in Figure 62. Once the combustion behaviour was matched, the comparison was extended to macroscopic performance indicators, including the indicated mean effective pressure (IMEP*), maximum pressure, PPRR, and η_c. The IMEP* and $\eta_{c,}$ were calculated according to the same formulation reported in the previous chapters.

Special attention was also paid to the prediction of pollutant emissions. Although the ECFM-3Z model was able to accurately reproduce the overall combustion process and its phasing, the emission sub-models showed limited capability in capturing the experimental trends of CO, CO_2, and NO_x formation. The absolute values of these species were affected by systematic deviations, which were partially reduced through the application of empirical scaling factors. These corrections can be physically justified, especially for the carbon-based species, by the use of n-heptane as a surrogate for Diesel fuel, whose carbon content differs from that of the real fuel, thus influencing the predicted oxidation rates. Despite the improved correlation obtained after the application of the correction factors, the absolute error remained significant in some operating conditions (see Figure 63), with the exception of the low-load case (IMEP= 6 bar), where a satisfactory agreement was achieved for CO_2 and NO_x. For this reason, the emission results provided by the CFD simulations should be considered reliable only in relative terms, that is, for analysing trends and sensitivities, but not in absolute magnitude.

Overall, the calibration ensured a satisfactory match between the numerical and experimental datasets, providing a reliable baseline for the subsequent optimization of the Diesel injection strategy. Calibration results are reported in Table 25, Table 26 and Table 27, where both performance parameters and emissions are compared to experimental data.

Since the aim of the research was to explore the upper limit of the hydrogen energy share, the analysis following the calibration phase focused on progressively reducing the Diesel quantity and investigating new injection strategies through a systematic parametric study, as detailed in the next section.

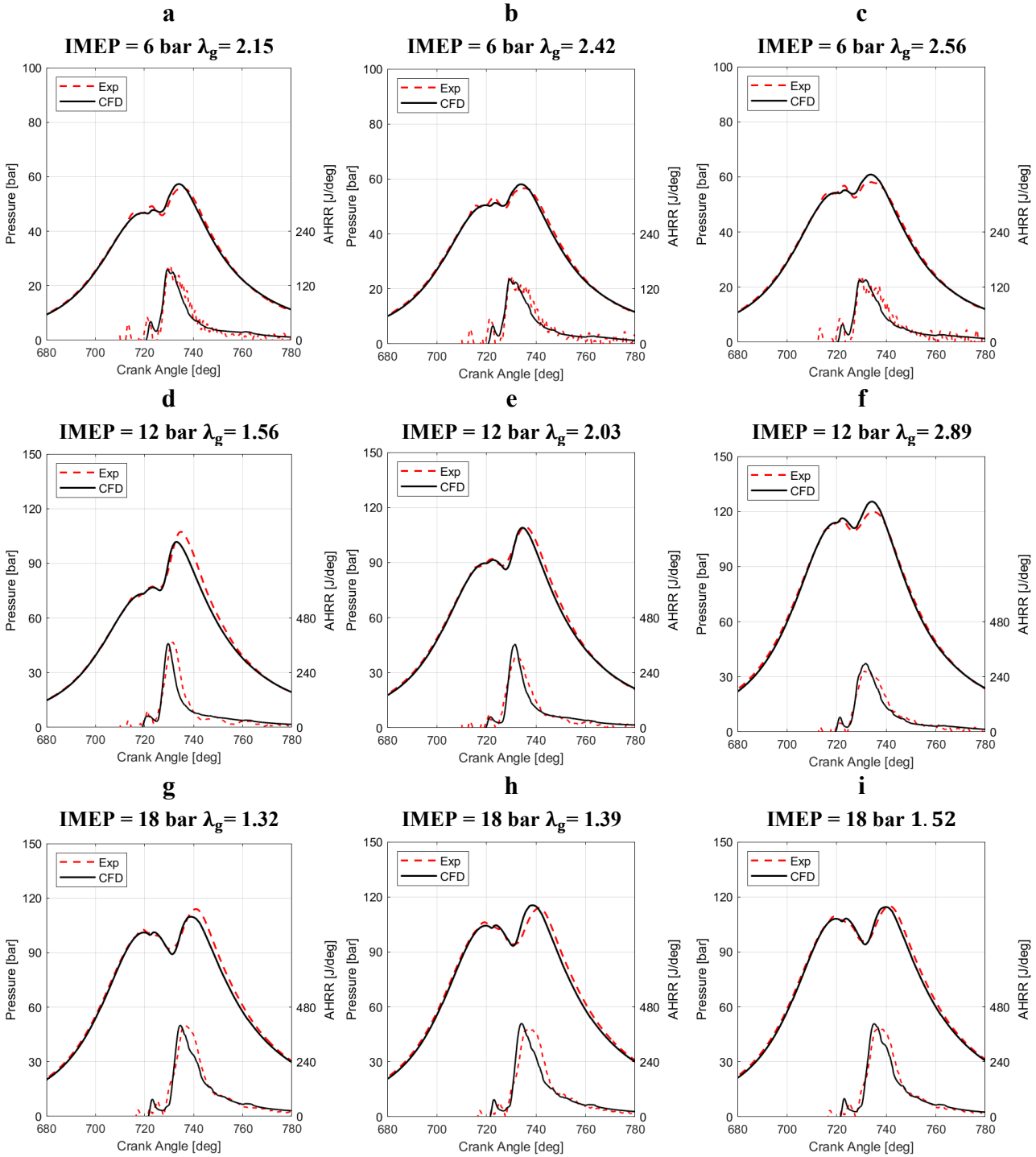

Figure 62: Comparison of in cylinder pressure and AHRR for the 9 studied cases: a) IMEP = 6 bar λ_g= 2.15, b) IMEP = 6 bar λ_g= 2.42, c) IMEP = 6 bar λ_g= 2.56, d) IMEP = 12 bar λ_g= 1.56, e) IMEP = 12 bar λ_g= 2.03, f) IMEP = 12 bar $\lambda_{2.89}$= 4.57, g) IMEP = 18 bar λ_g= 1.32, h) IMEP = 12 bar λ_g= 1.39, i) IMEP = 12 bar λ_g= 1.52.

Table 25: Comparison between experimental and numerical (3D-CFD) IMEP*; peak in-cylinder pressure; PPRR; combustion phasing parameters for the low load working point (IMEP = 6 bar).

	IMEP = 6 bar								
Engine Parameter	**λ_g= 2.15**		**λ_g= 2.42**		**λ_g= 2.56**		**Absolute error**		
	Exp.	**Sim**	**Exp.**	**Sim**	**Exp.**	**Sim**	**λ_g= 2.15**	**λ_g= 2.42**	**λ_g= 2.56**
IMEP* (bar)	6.40	6.70	6.42	6.64	6.45	6.72	0.30	0.22	0.28
Peak in-cylinder Pressure (bar)	56.6	57.3	57.24	58.0	58.8	60.9	0.70	0.86	2.10
PPRR (bar/deg)	2.56	2.61	2.63	2.069	2.31	1.87	0.05	0.19	0.45
CA10 (°CA aFTDC)	728.2	728.9	728.3	728.8	728.2	728.8	0.7	0.5	0.6
CA50 (°CA aFTDC)	735.1	735.4	736.1	736.1	736.7	736.2	0.3	0.0	0.5
CA90 (°CA aFTDC)	757.0	770.8	761.7	771.7	762.0	771.8	13.8	10.0	9.8

Table 26: Comparison between experimental and numerical (3D-CFD) IMEP*; peak in-cylinder pressure; PPRR; combustion phasing parameters for the mid load working point (IMEP = 12 bar).

	IMEP = 12 bar								
Engine Parameter	**λ_g= 1.56**		**λ_g= 2.03**		**λ_g= 2.89**		**Absolute error**		
	Exp.	**Sim**	**Exp.**	**Sim**	**Exp.**	**Sim**	**λ_g= 1.56**	**λ_g= 2.03**	**λ_g= 2.89**
IMEP* (bar)	12.38	12.08	12.52	12.71	12.68	13.41	0.30	0.19	0.70
Peak in-cylinder Pressure (bar)	107.5	101.8	109.9	109.0	125.4	119.9	5.7	0.0	5.1
PPRR (bar/deg)	5.88	7.23	3.90	6.23	3.54	3.65	1.35	2.33	0.11
CA10 (°CA aFTDC)	727.6	727.7	728.6	729.2	728.8	728.4	0.1	0.6	0.4
CA50 (°CA aFTDC)	733.1	734.2	734.8	735.5	735.9	735.4	1.2	0.7	0.5
CA90 (°CA aFTDC)	755.6	773.7	753.4	771.6	753.0	767.5	18.1	18.2	14.5

Table 27: Comparison between experimental and numerical (3D-CFD) IMEP*; peak in-cylinder pressure; PPRR; combustion phasing parameters for the mid load working point (IMEP = 12 bar).

	IMEP = 18 bar								
Engine Parameter	**λ_g= 1.32**		**λ_{H_2}= 1.39**		**λ_{H_2}= 1.52**		**Absolute error**		
	Exp.	**Sim**	**Exp.**	**Sim**	**Exp.**	**Sim**	**λ_{H_2}= 4.37**	**λ_{H_2}= 4.57**	**λ_{H_2}= 4.92**
IMEP* (bar)	18.46	18.00	18.49	18.20	18.62	18.41	0.46	0.29	0.21
Peak in-cylinder Pressure (bar)	114.1	109.8	114.0	115.4	115.0	114.5	4.3	1.4	0.5
PPRR (bar/deg)	5.44	5.00	5.35	5.15	5.39	4.63	0.44	0.20	0.76
CA10 (°CA aFTDC)	732.5	732.7	732.8	732.2	733.0	732.9	0.2	0.6	0.1
CA50 (°CA aFTDC)	740.2	741.1	740.6	740.2	740.8	740.7	0.9	0.4	0.1
CA90 (°CA aFTDC)	766.4	779.6	766.1	776.8	766.2	774.7	13.2	10.7	8.5

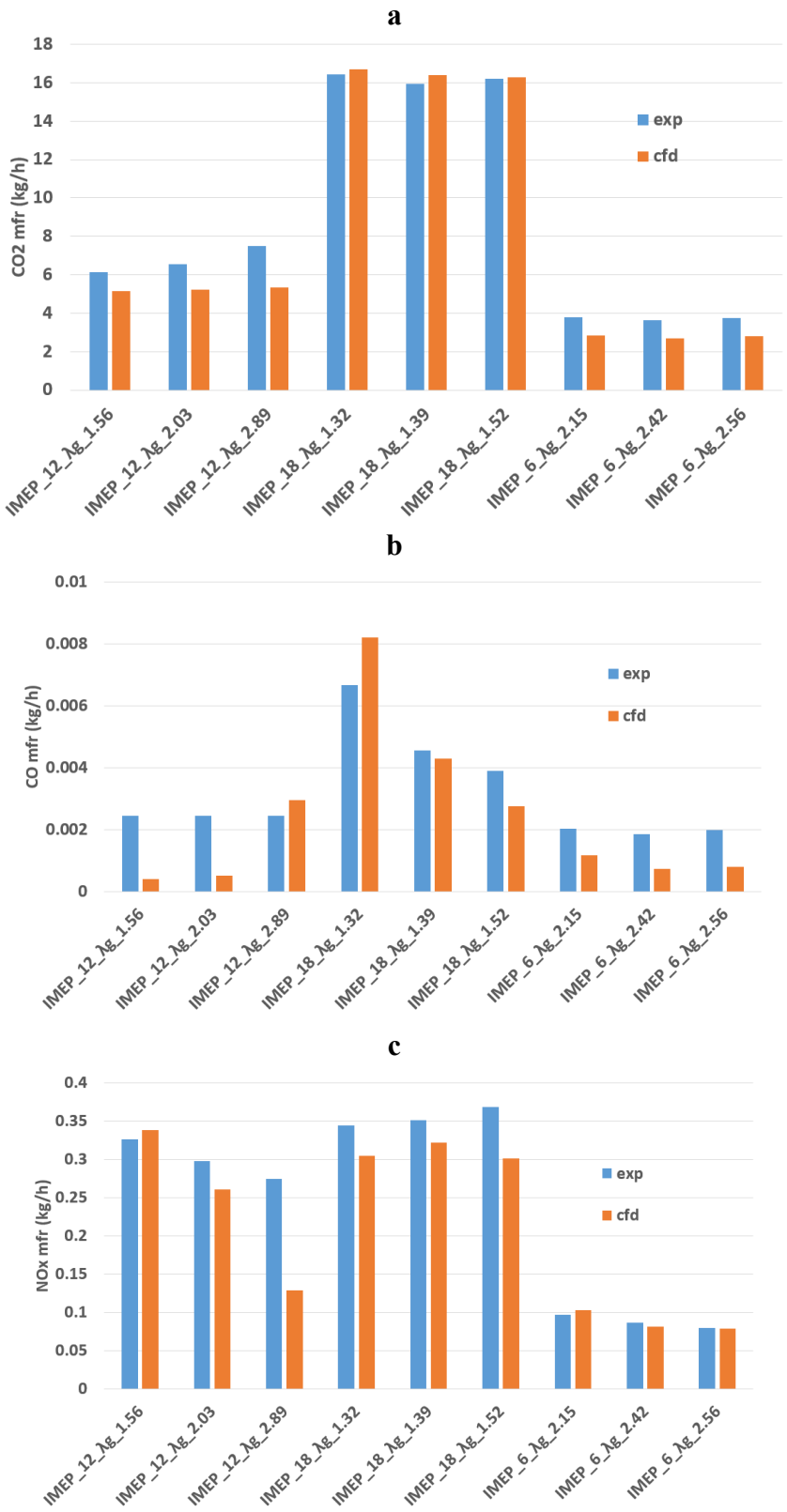

Figure 63: comparison between experimental and numerical simulation in terms of emissions mass flow rates: a) CO2, b) CO c) NOx.

5.3. Diesel injection optimization – RCCI combustion with advanced diesel injections

Building upon the calibrated 3D-CFD model described in the previous section, an optimization campaign was carried out to identify diesel injection strategies capable of improving combustion efficiency and reducing emissions while maintaining operation within the structural limits of the engine. Previous analyses demonstrated that, at high-load conditions, increasing the HES provides limited benefit, since the faster combustion of the premixed hydrogen–air mixture leads to a sharp rise in in-cylinder pressure and PPRR. Conversely, at low load the mechanical constraints are less critical, and the emission sub-models show better predictive reliability. For these reasons, the optimization was performed at low-load conditions (IMEP = 6 bar, $\lambda_g = 2.56$), where both the baseline maximum in-cylinder pressure and PPRR are well below the mechanical thresholds, allowing a safe exploration of more advanced combustion concepts.

In this part of the work, the focus was placed on promoting a RCCI-type combustion. In this regime, the diesel fuel is injected sufficiently in advance so that it has time to mix with the air during the compression stroke. As the temperature and pressure rise, the diesel undergoes auto-ignition, initiating the combustion process of the low-reactivity fuel, which in this case is hydrogen. The early diesel injection therefore controls the onset of combustion, acting as a reactive trigger that governs the ignition timing and stabilizes the subsequent burning of the hydrogen–air mixture. The main goal of this phase was to identify injection strategies that would allow the formation of a partially premixed charge capable of auto-igniting in a controlled manner, thus reproducing the characteristic behaviour of RCCI combustion. The second experimental design (DOE), aimed at exploring even earlier injection strategies and more homogeneous conditions, will be discussed in the following section.

To investigate these effects, a DOE was performed by varying the diesel injection parameters at the selected load point. The total diesel mass was kept constant with respect to the baseline case, while the mass split between pilot and main injections and the SOI angles were systematically varied. Four mass-split strategies were tested (0–100, 10–90, 25–75, and 50–50 (pilot–main)) each combined with different injection timings according to the following matrix:

Table 28: Tested diesel split, SOI of the pilot and main for the DOE analysis

Diesel mass split (pilot%-main% of the total diesel mass injected)	0-100	10-90	27-75	50-50
SOI pilot	640	650	680	-
SOI main	650	680	710	720

Cases where the pilot injection occurred after the main were excluded by design, and the injection pressure was kept constant at 1139 bar, consistent with the baseline condition among all tested combinations, only those satisfying the structural constraints of the engine were retained, namely Pmax < 130 bar and PPRR < 15 bar/°CA (see Table 22). The pressure-rise rate proved to be the most restrictive condition, eliminating several cases with highly advanced diesel injections. A summary of the investigated configurations and their structural feasibility is reported in Table 29, which lists the pilot/main split, SOIs, and indication of the cases that met the constraints.

Table 29: DOE matrix for Diesel injection optimization at low load, indicating split ratio, injection timings, and structural feasibility ✓/✗ and including the baseline case.

Split	SOI pilot	SOI main	Structural feasibility
10-90 (**baseline**)	716	723	-
0-100	-	640	✗
	-	650	✗
	-	660	✗
	-	670	✗
	-	680	✗
	-	690	✗
10-90	640	650	✗
	640	680	✗
	640	710	✗
	650	680	✗
	650	710	✗
	650	720	✓
	680	710	✗
	680	720	✓
25-75	640	680	✗
	640	710	✗
	640	720	✓
	660	680	✗
	660	710	✗
	660	720	✓
	680	710	✗
	680	720	✓
50-50	640	680	✗
	640	710	✗
	640	720	✗
	660	680	✗
	660	710	✗
	660	720	✗
	680	710	✗
	680	720	✗

From this DOE, the configuration maximizing efficiency while remaining within structural limits corresponded to a 25–75 mass split, with SOIs at 660° CA (pilot) and 720° CA (main). The comparison between this optimized case and the baseline is illustrated in Figure 64, showing the in-cylinder pressure and AHRR.

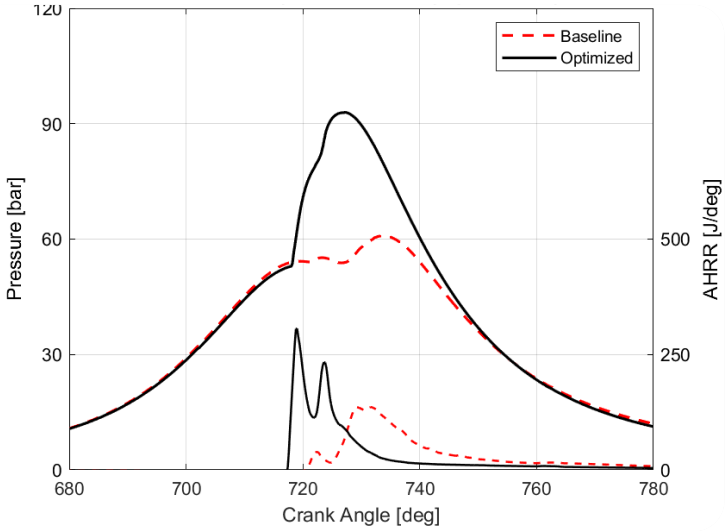

Figure 64: Comparison between baseline and optimized cases: in-cylinder pressure and AHRR (IMEP = 6 bar).

The optimized configuration exhibits a two-stage heat-release pattern: the first Diesel pulse, injected 60° CA before TDC, initiates a reactive premixed zone that triggers the ignition of the hydrogen-air mixture slightly before TDC; the second, larger diesel injection after TDC sustains the combustion process and supplies additional energy. This configuration promotes an RCCI-like combustion mode in the first phase, where the early diesel ignition acts as the initiator of the hydrogen–air charge, while the late diesel injection contributes mainly to diffusion-controlled burning.

The optimization led to a substantial improvement in overall performance, as summarized in Table 30. The GIE increased by 9.3 %, CO emissions decreased by 48.6 %, indicating enhanced oxidation of diesel and hydrogen, whereas the higher combustion temperatures, promoted by the faster HRR, resulted in an 85.6 % increase in NO_x. The unburned hydrocarbon (HC) emissions increased by 37.3%, caused by incomplete oxidation of the diesel injected during the second pulse, which burned in locally oxygen-deficient regions. The higher temperature and more concentrated heat-release phasing also produced a 52.7 % increase in Pmax, confirming that the mechanical limits constrain further advancement of the injection.

Table 30: Comparison between baseline and optimized cases: GIE, Pmax, PPRR, CA10–90, CO_2, CO, NO_x

GIE		Peak Pressure		PPRR		CA10-90		CO_2		CO		NO_x		HC	
val.	Δ%.	val.	Δ%	val.	Δ%	val.	Δ%	val.	Δ%.	val.	Δ%	val.	Δ%	val.	Δ%
(bar)	(%)	(bar)	(%)	(°bar/CA)	(%)	(CA)	(%)	(g/h)	(%)	(g/h)	(%)	(ppm)	(%)	(mg/h)	(%)
0.51	+9.3	93.0	+52.7	12.9	+592	43.6	-14.5	2428	0	0.417	-48.6	1455	85.6	1.01	+37.3

From a combustion standpoint, these results indicate that it is not feasible to advance the entire diesel injection without exceeding the mechanical limits of the engine. Only a portion of the diesel can be injected early to promote ignition of the premixed hydrogen–air mixture, while the remainder must be introduced later to sustain combustion and control its duration. However, the late diesel injection, taking place when the hydrogen combustion is already underway, burns in oxygen-depleted zones and leads to the formation of additional hydrocarbons. This observation suggests that the second diesel pulse could be suppressed or substituted with additional hydrogen, thereby exploiting the reactive mixture already present in the chamber.

In summary, the RCCI-type strategy successfully improved the overall thermodynamic performance of the DF diesel-hydrogen engine, achieving a 9.3 % increase in. Nevertheless, the results revealed that such improvement in efficiency did not translate into a clear advantage in terms of emissions. While CO was significantly reduced, both NO_x and HC emissions increased as a consequence of the higher in-cylinder temperature and the incomplete oxidation of the diesel injected during the late phase of combustion. These findings indicate that, although RCCI operation provides an efficient combustion mode, in this configuration the engine still suffers from the intrinsic drawbacks, namely, the coexistence of diffusion flames and oxygen-depleted regions. To overcome these limitations, attention was therefore shifted toward more homogeneous combustion modes with just a single injection. As observed in previous works, the removal of the main diesel injection proved effective in reducing NO_x emissions, mainly due to the suppression of localized high-temperature regions that typically develop during the late diffusion-controlled phase. Combining this approach with a strongly advanced single diesel injection, capable of achieving a homogeneous or partially homogeneous auto-ignition (HCCI-like), can further mitigate NO_x formation by promoting a smoother and more uniform heat-release process. In such conditions, the charge has sufficient time to mix and evaporate before ignition, resulting in a lower-temperature and cleaner combustion regime that will be the the focus of the next section.

5.4. Diesel injection optimization – ultra-high hydrogen energy share combustion

After optimizing the dual-injection strategy for RCCI operation, the analysis was further extended to enhance the reactivity control of the mixture by reducing the diesel contribution and advancing its injection timing. The objective of this second optimization phase was therefore not to abandon the RCCI concept, but rather to refine it by inducing an HCCI-like combustion behaviour of the diesel fuel. In this configuration, the Diesel quantity was significantly reduced compared to the baseline, and the single injection was performed much earlier in the cycle. This combination allows the small amount of diesel to completely (or almost completely) mix with the in-cylinder charge during the compression stroke. As a result, the Diesel droplets fully evaporate before ignition, forming a homogeneous or partially-homogenous mixture that auto-ignites under compression according to the HCCI principle. The diesel therefore acts as a distributed ignition source, initiating combustion uniformly across the chamber rather than through localized flame fronts, while the hydrogen remains the dominant energy carrier. This refined strategy preserves the RCCI nature of the process but integrates an HCCI-like diesel combustion phase, achieving a smoother and cleaner heat release with minimal pollutant formation.

Based on the results discussed previously (see chapter 4), the main diesel injection was first completely removed and replaced by an equivalent quantity of hydrogen, leading to a HES of 96%. Since the combustion remained stable, the diesel pilot quantity was further reduced, resulting in configurations with HES of 98% and 99%. To systematically assess the influence of the diesel timing under these highly premixed conditions, a DOE was conducted for each HES level. The SOI was varied between 645° and 710° CA in 5° increments, and from 710° to 720° CA in 2° steps, covering a broad range of early injection timings. All cases were simulated under the same operating conditions as the baseline (IMEP = 6 bar, $\lambda\_g = 2.56$), with constant injection pressure (1139 bar). The DOE results for each hydrogen share are summarized in Figure 65, which reports the in-cylinder pressure and AHRR traces for all simulated SOIs while Table 31 reports further macroscopic information about the three studied HES. As can be observed from the table, the air–hydrogen mixture is consistently ultra-lean, a particularly relevant aspect since premixed combustion under such lean conditions leads to inherently low flame temperatures and, consequently, very limited NO_x formation.

Table 31: Main constant parameters of the simulated points of the DOE analysis compared with the baseline DF configuration (HES = 67%)

HES	λ_g		λ_{H_2}		Injected diesel (g/h)		Injected hydrogen (g/h)	
	val.	Δ%	val.	Δ%	val.	Δ%	val.	Δ%
67% (baseline)	2.56	0	4.07	0	791	0	600	0
96%	2.71	+5.86	2.84	-30.2	92	-88.4	860	+44.1
98%	2.72	+6.25	2.78	-31.5	48	-93.9	870	+46.1
99%	2.73	+6.64	2.76	-32.2	24	-97.0	880	+47.3

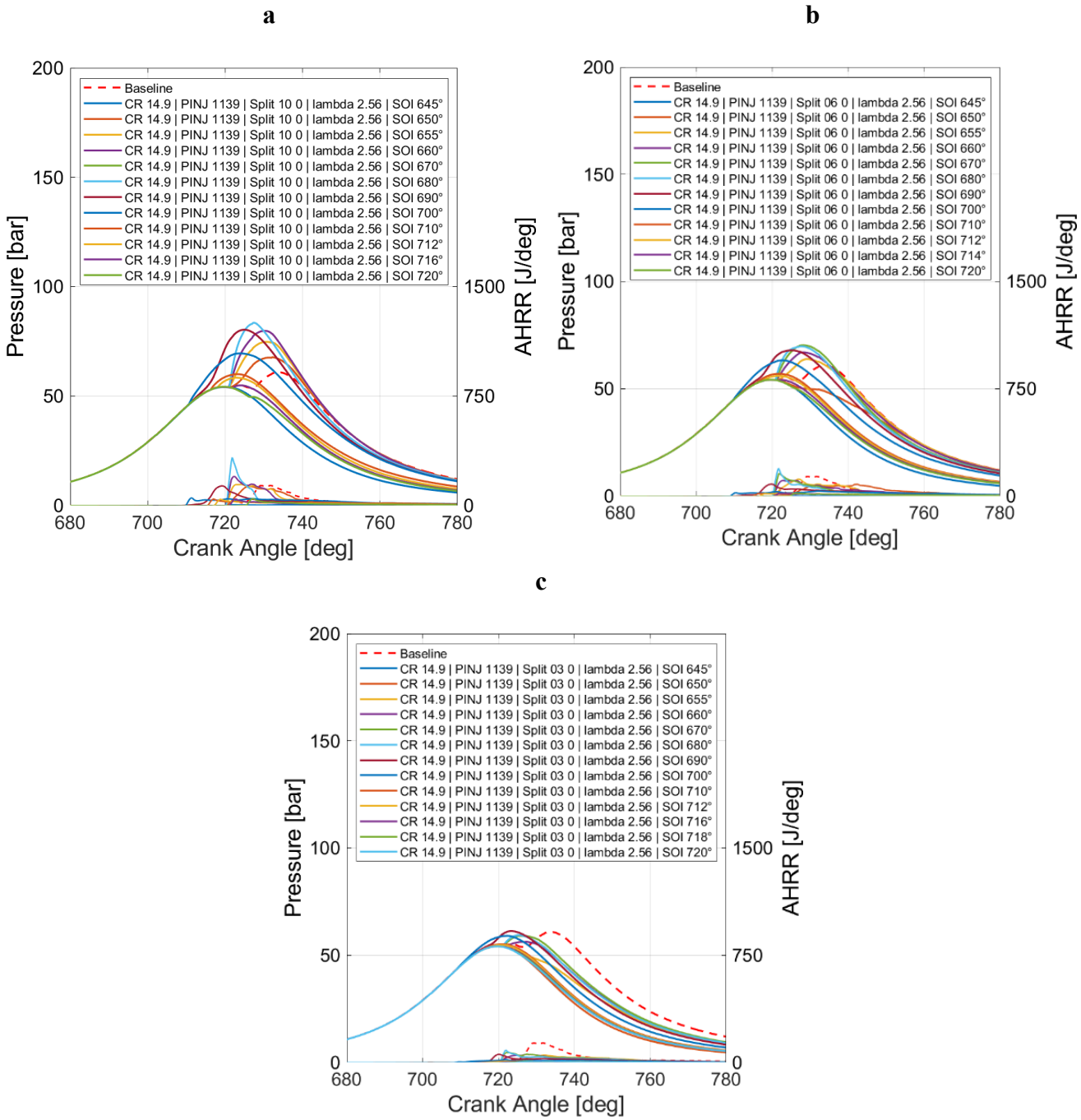

Figure 65: In-cylinder pressure and AHRR traces for all SOI timings from DOE analysis. a) HES= 96, b) HES= 98% c) HES=99%.

The results of the DOE highlight clear differences in combustion behaviour among the three hydrogen-energy-share levels. For the 96 % and 98 % HES configurations, more than half of simulated cases exhibit stable combustion, conversely, the 99 % HES configuration fails to sustain a stable reaction: in every tested SOI, the expansion pressure remains markedly lower than in the baseline, and the AHRR traces reveal a weak heat release. This behaviour confirms that, at such an extreme hydrogen share, the diesel quantity becomes insufficient to initiate a self-sustained ignition of the ultra-lean hydrogen–air mixture (diesel is reduced by 97% respect to baseline, see Table 31), regardless of the injection timing.

Given these results, the subsequent analysis focuses exclusively on the 96 % and 98 % HES configurations, which proved to be the most promising and physically meaningful operating conditions.

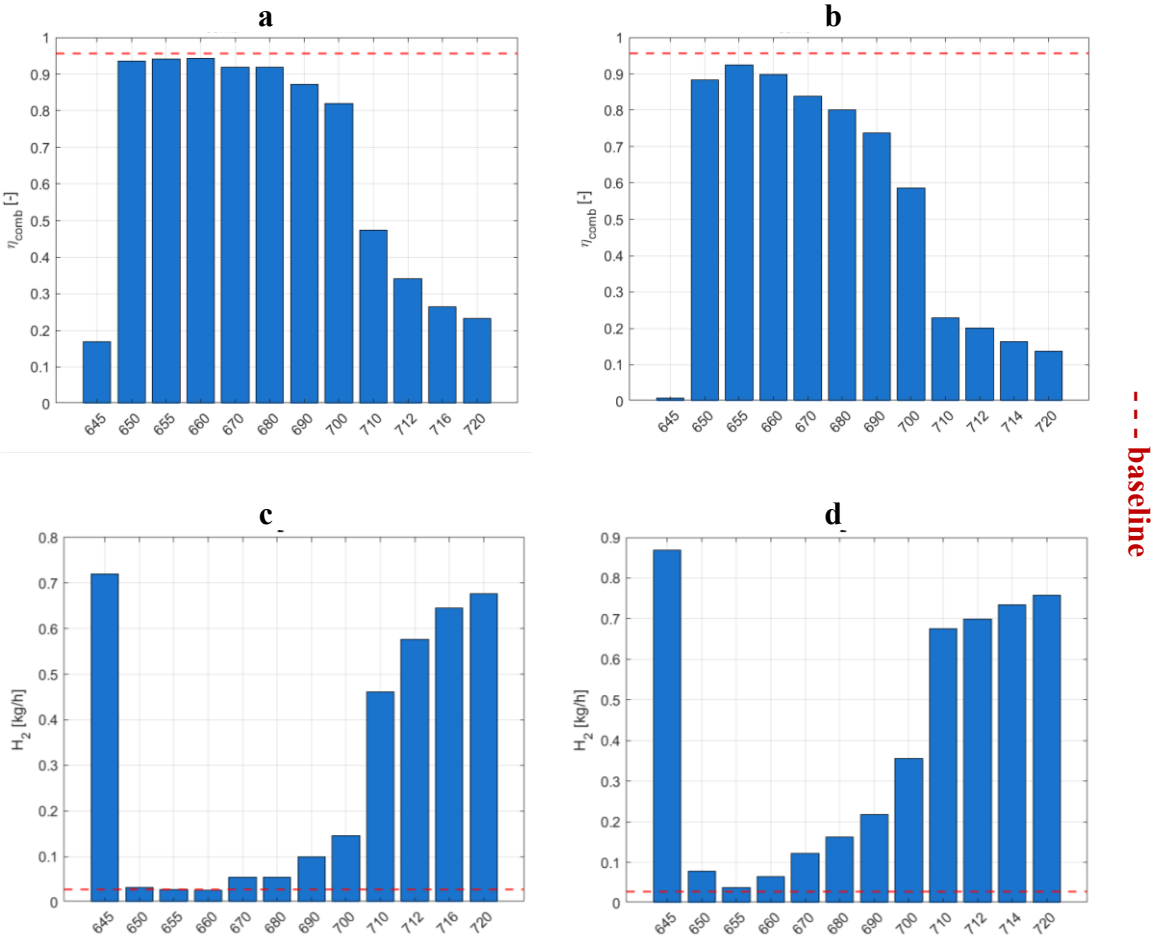

Figure 66: Combustion efficiency and hydrogen residuals at EVO for all DOE cases: a) ηc, HES = 96%; b) ηc, HES = 98%; c) hydrogen residuals at EVO, HES = 96%; d) hydrogen residuals at EVO, HES = 96%.

The combustion efficiency in both 96% and 98% HES cases was generally lower than the baseline, as shown in Figure 66, due to the increased presence of unburned hydrogen in the crevice regions and

the stronger flame-quenching effect at the cylinder walls. The hydrogen-rich mixture, being uniformly distributed in the chamber, enhances these losses because the peripheral zones do not fully react before the end of combustion. This trend is confirmed by the hydrogen emission mass flow rate, which shows higher residual hydrogen compared to the baseline (see Figure 66 c-d).

As expected, CO_2 emissions decreased proportionally to the reduction in diesel usage, reflecting the higher hydrogen energy contribution (from 67% in the baseline to 96–98%). The NO_x emissions, on the other hand, dropped dramatically, becoming nearly zero for the most advanced SOI timings in both 96% and 98% HES cases. The corresponding bar charts for CO_2 and NO_x, reported in Figure 67 a-d, show the CO_2 reduction with respect to the base line (red dashed line) and the NO_x injection timing dependency.

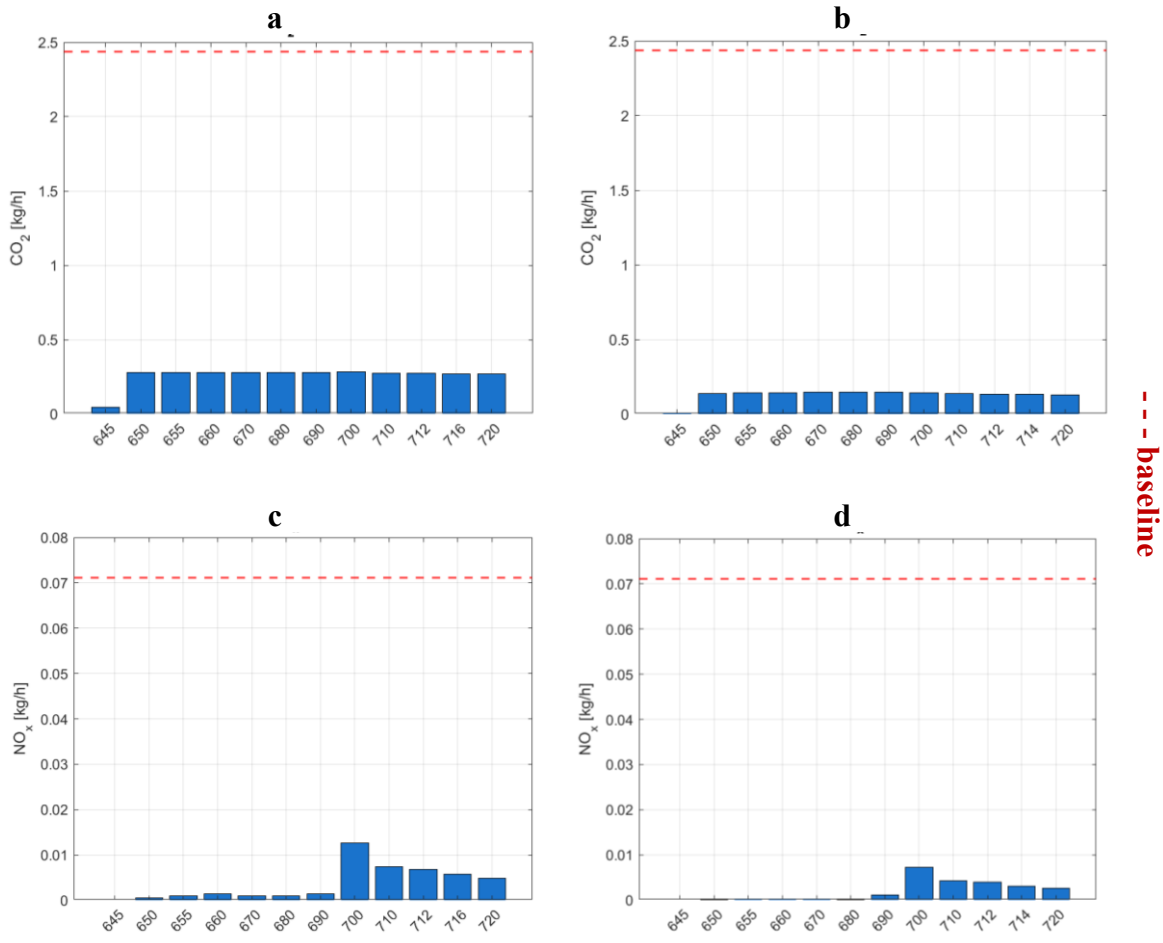

Figure 67: CO_2 and NO_x emissions for all DOE cases: a) CO_2 emissions, HES = 96%; b) CO_2 emissions, HES = 98%; c) NO_x emissions, HES = 96%; d) NO_x emissions, HES = 96%.

From the DOE results, the optimal conditions were identified as:

- HES = 96%, SOI = 660° CA, which minimizes NO_x emissions while maintaining a +4.4% increase in GIE compared to the baseline.
- HES = 98%, SOI = 655° CA, which achieves near-zero NO_x and the lowest efficiency penalty among all tested cases (see Figure 66).

A comparison between the baseline and the optimized conditions is presented in Table 32, showing the main performance and emission metrics comparison between baseline and optimized HCCI-like cases (HES = 96%, 98%).

Table 32:Comparison between baseline and optimized RCCI/HCCI like cases (HES=96%, 98%), in terms of GIE, Peak pressure, Combustion duration, ηc, CO2, CO, NOx emissions.

	GIE		**Peak Pressure**		**CA10-90**		**η_c**		**CO_2**		**CO**		**NO_x**	
	val.	**Δ%.**	**val.**	**Δ%**	**val.**	**Δ%**	**val.**	**Δ%**	**val.**	**Δ%.**	**val.**	**Δ%**	**val.**	**Δ%**
	(bar)	**(%)**	**(bar)**	**(%)**	**(°CA)**	**(%)**	**(-)**	**(%)**	**(g/h)**	**(%)**	**(g/h)**	**(%)**	**(ppm)**	**(%)**
Baseline HES=67%	0.465	0	60.9	0	43.6	0	0.96	0	2.81	0	0.81	0	855	0
HES=96%	0.485	+4.4	79.8	+31	31.5	-12.1	0.94	-1.3	0.32	-88.6	0.39	-52	16.83	-98.0
HES=98%	0.459	-1.2	63.7	+5	33.4	-10.2	0.93	-3.2	0.17	-94.0	1.30	+60	2.44	-99.7

The comparison between the optimized configurations at HES 96 % and 98 % and the baseline case also highlighted in Figure 68 shows the main differences in pressure development and combustion dynamics. As expected, moving from the dual-injection RCCI configuration to the single-injection HCCI-like diesel strategy leads to a reduction in mechanical load, reflected by lower in-cylinder peak pressures and PPRR. Both high-HES cases show smoother pressure traces and broader heat-release profiles with respect to the double injection strategy, confirming a more gradual and distributed combustion process. At the same time, the absence of the second diesel injection eliminates the diffusion-controlled tail that characterized the previous RCCI operation, resulting in a single, well-shaped AHRR peak dominated by the premixed hydrogen combustion. The lower PPRR values, together with the flatter AHRR curves, indicate a significant mitigation of combustion noise and mechanical stress on the engine components. These findings demonstrate that advancing the diesel injection and increasing the hydrogen share not only improve combustion uniformity but also allow operating within safer mechanical limits respect to the RCCI-double injection strategy.

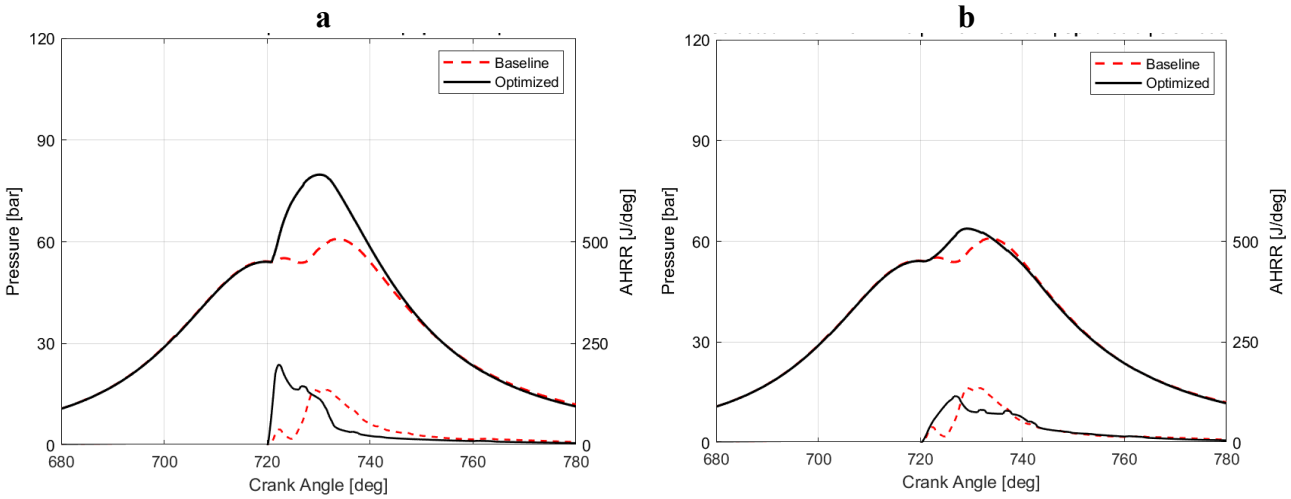

Figure 68: In-cylinder pressure and AHRR comparison between the DF baseline case and the optimized cases: a) HES=96% pilot SOI= 660° CA, b) HES = 98% pilot SOI 655° CA.

The optimized configuration exhibits a more uniform and overall lower temperature distribution, despite a higher average bulk temperature within the cylinder. This agrees with thermal NO_x formation that is primarily governed by localized temperature peaks, which are strongly mitigated in the hydrogen-enriched case. The same behaviour is evident in Figure 69, which report the mean in-cylinder temperature and the corresponding NO_x levels, showing that even if average in-cylinder temperature is higher than baseline (case HES = 96%), the NO_x emissions are significantly lower.

Figure 70 provides a spatial view of the in-cylinder temperature field at representative crank angles, illustrating the different combustion characteristics between the baseline and the optimized configurations. Despite the higher mean in-cylinder temperature observed in the optimized case (Figure 69), the temperature field appears much more uniform, with the absence of localized hot spots typically associated with the diffusion-controlled phase of the main diesel injection. At approximately 732 °CA, it can be seen that the baseline case exhibits well-defined high-temperature zones corresponding to the diffusion flame region, whereas in the optimized configuration such zones disappear, confirming the elimination of diffusion combustion due to the removal of the main injection.

Furthermore, when compared with the conditions discussed in the previous chapter (see chapter 4), the strongly advanced pilot injection results in a broader and more evenly distributed ignition region. The diesel injected early in the cycle has sufficient time to mix with the surrounding charge, leading to auto-ignition over a wider portion of the chamber and under partially premixed conditions. This

behaviour, clearly visible around 723 °CA in Figure 70, results in a more distributed heat-release pattern and lower local peak temperatures, effectively suppressing thermal NO_x formation.

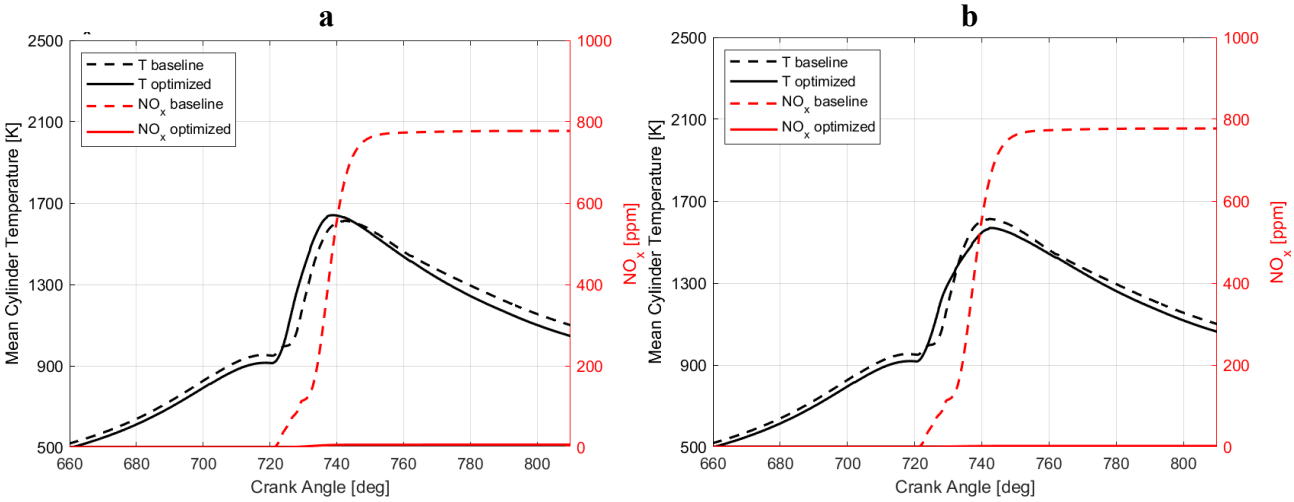

Figure 69: Average in-cylinder temperature and NOx formation plots of the optimized cases, compared with the baseline DF case. a) opt., HES=96% vs baseline b) opt. HES=98% vs baseline.

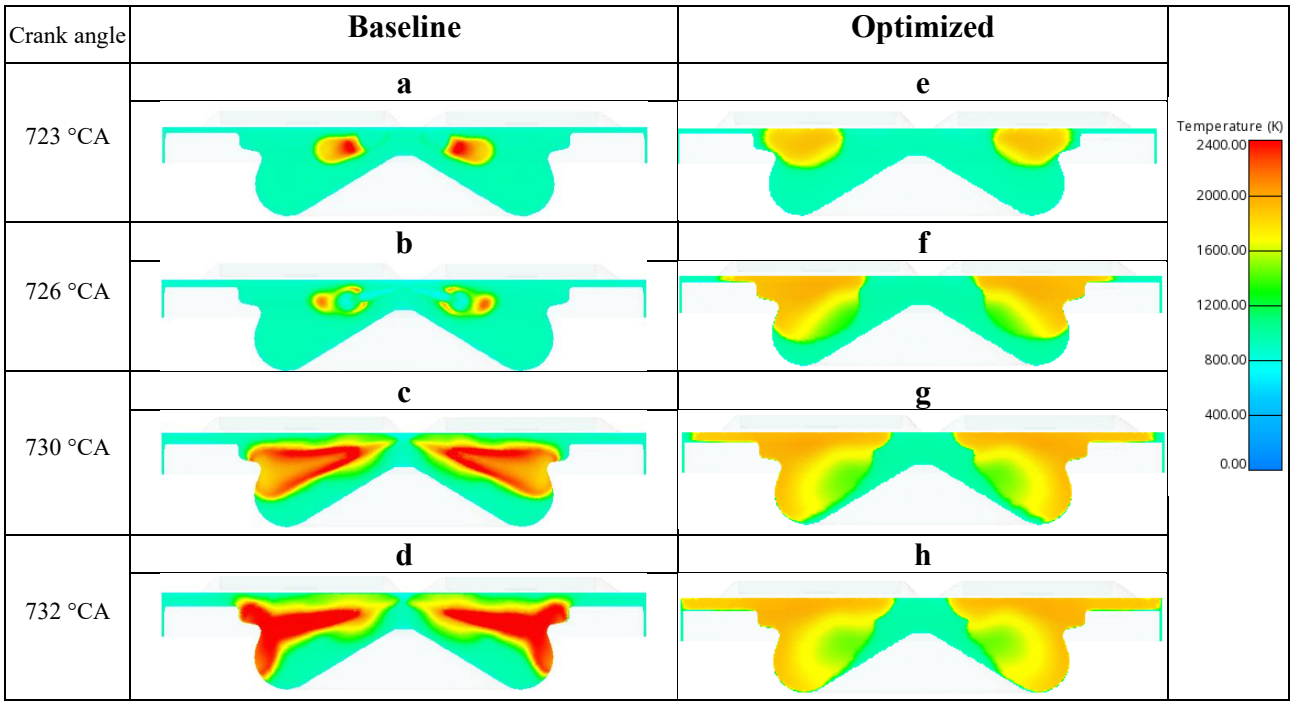

Figure 70: In-cylinder temperature map for baseline (a-d) and optimized 96% HES case (e-h).

These findings demonstrate that increasing the hydrogen share and adopting a single, strongly advanced diesel injection effectively promote a partially homogeneous combustion regime, characterized by smooth heat release and extremely low pollutant formation. The 96% HES configuration, in particular, achieved an GIE gain of +4.4% over the baseline and produced NO_x

emissions corresponding to roughly half the Euro 7 regulatory limit (see Table 32), while maintaining stable operation and nearly zero carbon emissions.

Figure 71: Optimized case vs Euro 7 comparison in terms of NOx emissions.

CA°	Opt.	Euro 7	RDE
NOx (mg/kWh)	115	200	260

Overall, this phase of the study confirms that ultra-high hydrogen energy shares can deliver a super-clean and efficient combustion process under low-load conditions. Future work should investigate the feasibility of transferring these results to higher loads, where peak pressure and temperature constraints become more critical. Potential strategies include operating under ultra-lean conditions, adopting water injection, or employing variable valve actuation to reduce the effective compression ratio. Such approaches could further extend the range of stable operation and pave the way toward near-zero emissions diesel-hydrogen DF engines.

5.5. Key outcomes and transition to full hydrogen-fuelled engine configuration

The optimization campaign carried out in this section proved to be a decisive step in extending the hydrogen capability of the DF diesel-hydrogen engine. Through a systematic refinement of the diesel injection law, it was possible to reach ultra-high hydrogen energy shares (up to 98 %) while maintaining combustion stability and mechanical integrity. The injection strategy was shown to play a crucial role in controlling mixture formation, ignition phasing, and pollutant formation, demonstrating that proper calibration of the diesel pilot can dramatically reduce NO_x emissions and pressure-rise rates. These results confirm that, within the DF diesel–hydrogen framework, injection optimization represents the key enabler for achieving low-temperature, clean, and efficient operation.

The achieved configuration successfully addressed the main limitations observed in previous studies, effectively mitigating diffusion-controlled combustion and promoting a more homogeneous, HCCI-like auto-ignition of the Diesel pilot. However, the investigation was conducted under low-load conditions, where the mechanical and thermal stresses on the engine are moderate and the hydrogen combustion process remains stable. At higher loads, the elevated in-cylinder temperatures and pressure gradients could compromise combustion stability, leading to abnormal ignition or excessive pressure rise. Future research should therefore focus on extending the current strategy to medium and

high-load operation, possibly through ultra-lean mixtures, water injection, or variable valve actuation to reduce the effective compression ratio and maintain controllable combustion phasing.

It should be emphasized that the present activity represents an exploratory CFD-based investigation. Although the models were applied within their validated range and carefully calibrated against available experimental data, dedicated experimental campaigns are required to confirm the observed trends and to fully validate the combustion and emission predictions under ultra-high hydrogen energy shares. This need becomes even more critical considering the HCCI-like nature of the diesel combustion process adopted in the most advanced cases, which differs substantially from baseline, conventional DF operation with late diesel injection.

Finally, this study marks a conceptual boundary within the present thesis. Having demonstrated that diesel can be reduced to negligible quantities while maintaining stable DF operation, the next logical step is to explore a fully hydrogen-fuelled engine configuration, derived from the same diesel architecture but equipped with a spark-ignition system instead of the compression-ignition pilot. This evolution represents the natural continuation of the current research path and will be the focus of the following chapter.

6. Full-hydrogen spark-ignition 2-stroke engine conversion: a CFD-base pathway toward zero emission operation

In recent years, hydrogen internal combustion engines have gained remarkable attention as a promising solution to drastically reduce greenhouse gas (GHG) emissions while retaining the robustness, scalability, and cost-effectiveness typical of conventional engine technology. The growing number of scientific studies devoted to this field confirms the interest of the research community in exploring hydrogen as a carbon-free energy carrier capable of supporting the decarbonization of the transport and energy sectors [109,131,132].

Hydrogen-fuelled spark-ignition (SI) engines operating on the 4-stroke (4S) cycle have been extensively studied since the 1980s [132]. After appropriate optimization, these engines can achieve stable, efficient, and clean operation under ultra-lean conditions (typically $1.8 < \lambda < 2.7$) [133–135]. However, they also present well-known challenges, such as pre-ignition and backfire risks due to hydrogen's very low ignition energy and wide flammability limits. Additionally, when operated with very lean mixtures, the need for large air mass flow rates makes turbocharging or supercharging almost mandatory to sustain acceptable performance [136,137]. Nevertheless, conventional boosting systems are often insufficient to guarantee both low-speed torque and high-speed power, especially when the reference engine was originally designed for Diesel operation.

During the research activities conducted as part of this PhD project at Brunel University London, an extensive numerical campaign was devoted to the study of dual-fuel diesel–hydrogen combustion in a HD engine. Through a 3D-CFD-based optimization of the diesel injection strategy, the potential of DF operation with ultra-high hydrogen energy shares (up to 98%) was clearly demonstrated, together with a significant reduction in pollutant emissions. However, the study also revealed the intrinsic limitations of the concept, particularly under high-load conditions, where maintaining efficient combustion and acceptable pressure rise rates becomes increasingly challenging.

Building upon these outcomes, the complete replacement of diesel with hydrogen emerged as a natural evolution of the research pathway. The next logical step was therefore to explore a fully hydrogen-fuelled engine concept, capable of combining zero-carbon operation with high performance and simplified hardware. In this context, the 2-stroke (2S) cycle offers a particularly attractive alternative to conventional 4-stroke (4S) designs, as the doubled firing frequency can compensate for the volumetric efficiency losses typical of ultra-lean hydrogen combustion, without increasing the engine displacement.

Among the possible 2S architectures, those employing intake and exhaust poppet valves represent an especially compelling option. Originally investigated by Toyota [138], Ricardo [139] and Honda [140–143] for gasoline engines, and later by Renault for Diesel applications [144,145], this configuration can be derived from existing 4S platforms with minimal modification. In particular, only the cylinder head (comprising the combustion chamber and the gas exchange ports) requires a complete redesign, while the lubrication and crankcase systems can remain substantially unchanged.

The work presented in this chapter therefore investigates, through an integrated 0D–1D/3D-CFD methodology, the feasibility of converting a Duramax 6.6 L V8 Diesel engine into a 2-stroke hydrogen-fuelled spark-ignition unit. The objective is to preserve the main geometric features of the base engine while optimizing the scavenging and mixture formation processes to achieve both high brake thermal efficiency (>35%) and ultra-low NO_x emissions (<20 ppm) without the need for exhaust after-treatment.

This analysis represents the culmination of the PhD research pathway on hydrogen application on diesel based-engines, translating the experience gained in DF operation into the conceptual design of a fully hydrogen-powered architecture.

6.1. Numerical methodology for the 2-stroke hydrogen development

The investigation was carried out through an integrated numerical approach combining 0D/1D-CFD and 3D-CFD simulations within a structured iterative design loop. The overall strategy followed the same logic previously adopted for the DF studies, where 0D/1D models were used to set the initial and boundary conditions for the 3D-CFD domain, while the outcomes of the 3D analyses were in turn used to refine and recalibrate the 0D/1D framework. This reciprocal exchange allowed a progressive improvement of both predictive accuracy and physical consistency throughout the design process.

A preliminary 0D/1D engine model was developed in GT-Power [95] starting from a set of empirical assumptions derived from the original 4S Diesel configuration. Several major modifications were introduced to adapt the architecture to the 2S valved concept. The intake and exhaust port geometries were completely redesigned, and the valve lift profiles were optimized to ensure proper flow exchange and minimize short-circuiting. Simulations suggested slightly larger exhaust valves compared to the intake pair, in order to enhance the scavenging efficiency while respecting mechanical feasibility constraints.

A two-stage boosting system was then integrated into the model, combining a mechanically driven supercharger equipped with an intercooler in series with a VGT turbocharger. The displacement of the supercharger and its drive ratio relative to the crankshaft were optimized through steady-state simulations, whereas the turbocharger selection was based on both steady and transient analyses.

The engine control strategy was also redefined to suit hydrogen operation. In addition to spark-timing control, a bypass valve was introduced on the supercharger to regulate charge pressure, complementing the conventional turbine rack control. No EGR loops were necessary, as the charge composition and in-cylinder λ could be finely adjusted through the coordinated actuation of the turbine rack, supercharger bypass, hydrogen injection rate, and spark advance. Load control was achieved by modulating these parameters rather than throttling, thus avoiding pumping losses. At low loads, cylinder deactivation could be obtained by simply omitting the fuel injection in one or more cylinders.

A 0D scavenging sub-model was implemented to capture the essential features of the 2S gas-exchange process, including the correlation between trapped and escaping charge fractions and the instantaneous cylinder composition. This scavenging curve, which plays a central role in the overall engine efficiency prediction, was initially derived from 3D-CFD data and continuously updated as new simulation results became available.

Combustion was represented using a quasi-dimensional predictive model for hydrogen, based on the SI-Turb approach implemented in GT-Power. The burn rate model was preliminarily calibrated using experimental data from a 4S hydrogen prototype developed by Dumarey and subsequently refined to reflect the new 2S configuration. Given the different flow structure of the new combustion chamber (characterized by tumble-dominated motion rather than swirl) the quasi-dimensional turbulence sub-model was recalibrated from scratch using the information extracted from 3D cold-flow scavenging simulations. The accuracy of this model was found to be crucial for reliable predictions of combustion rate and pressure evolution. The hydrogen injector model was also updated to account for the specific characteristics of gaseous fuel injection, which have a direct influence on scavenging and mixture formation.

The 3D-CFD analyses were performed using AVL FIRE M, with the moving mesh generated through AVL FAME M [114]. A Reynolds-Averaged Navier–Stokes (RANS) approach with a k–ζ–f turbulence closure [115] was adopted, given its robustness in reproducing in-cylinder flow structures in internal combustion engines. The computational mesh employed polyhedral cells, chosen as a good compromise between accuracy and computational efficiency. This cell topology allows a faithful

representation of the complex geometry of the combustion chamber and ports while maintaining low distortion, even in narrow regions such as the valve seats.

The computational domain encompassed the entire combustion chamber, together with the intake and exhaust ports (Figure 72 a-b). Downstream portions of the exhaust duct were simplified, as the flow field beyond the valve seats has a negligible influence on the scavenging process. Such simplifications considerably reduced meshing time without compromising result reliability. Local refinements were applied in the vicinity of the valves and near the hydrogen injection straws to properly resolve regions with high velocity gradients and small-scale vortices.

The main mesh characteristics are summarized in Table 33, while Table 34 lists the principal physical models adopted in the CFD setup. Figure 73 illustrates grid details in the valve region and around the injector tip, highlighting the adaptive refinement strategy employed in the most critical zones.

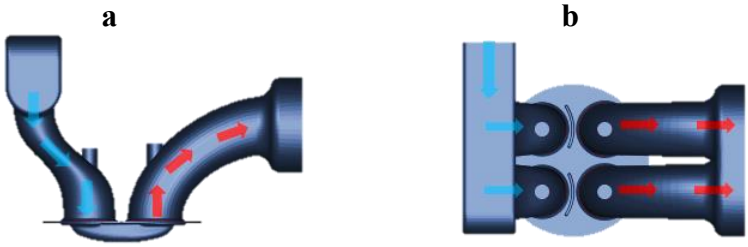

Figure 72: views of the computational domain: a) side view, b) top view.

Table 33: Computational grid details.

Target cell Size (mm)	2
Intake/exhaust valve refinement (mm)	0.5
Injection refinement	Coarse cone: depth: 28 mm; cell size: 0.6 mm
	Medium cone: depth: 14 mm; cell size: 0.5 mm
	Fine cone: depth: 7 mm; cell size: 0.15 mm
Boundary layer thickness (mm)/n. of layers	0.4/2
Max. number of cells	1,914,200

Table 34: 3D-CFD models and sub-models details.

Compressibility	Variable density, compressible
Turbulence model	k-zeta-f
Turbulence wall treatment	Hybrid [cita Popovac e Hanjalic]
Wall function	Two Layer wall function [cita Cheing e Launder]

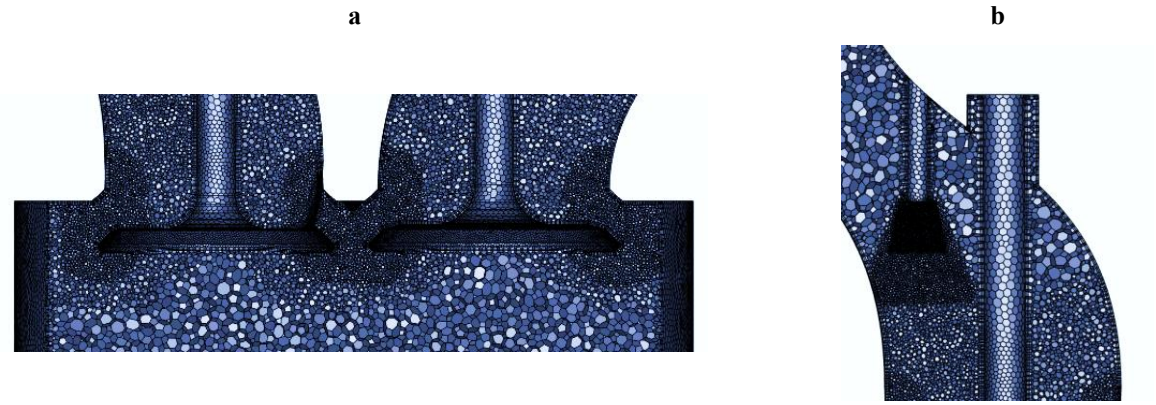

Figure 73: Computational grid details: a) valve refinement b) hydrogen injector refinement.

The 3D-CFD campaign was organized into two phases.

- In the first phase, the analysis focused on the scavenging process, aimed at assessing the delivery ratio, trapping efficiency, and fresh charge fraction for different engine speeds. The corresponding scavenging curves were then exported to update and recalibrate the 0D/1D GT-Power model.
- In the second phase, the hydrogen injection process was explicitly simulated to investigate the in-cylinder mixture formation and to evaluate fuel–air homogeneity at the spark timing.

Three full-load operating conditions were analysed: 1200 rpm, 1600 rpm, and 3000 rpm. The first two correspond to: low, medium and max engine speed. The 3000 rpm case, characterized by the shortest available mixing time, was used as the reference for the optimization of injection timing and strategy, since an adequate mixture formation at this speed ensures easier calibration at lower operating points.

6.2. Reference engine characteristics and the new concept design

The baseline configuration considered for this study is the Duramax 6.6 L V8 Turbo Diesel engine, whose main technical specifications are summarized in Table 35. This engine, originally designed for marine and HD applications, represents a robust and well-documented platform for conversion to alternative fuels.

Table 35: Baseline Diesel engine characteristics.

Engine characteristic	Value/description
Type:	4-Stroke, 6.6 ℓ V8 Turbo Diesel
Displacement:	6604 cc
Engine orientation:	Longitudinal
Compression ratio:	16.0:1
Valve configuration:	Overhead valves
Valves per cylinder:	Four
Valve lifters:	Mechanical roller
Firing order:	1 2 7 8 4 5 6 3
Bore x stroke:	103 mm x 99 mm
Fuel System:	DI with high pressure common rail
Fuel type:	Ultra low sulfur Diesel and B20 bioDiesel
Brake power:	332 kW @ 2800 rpm*
Brake Torque:	1234 Nm @ 1600 rpm*
Maximum Powered Speed:	3450 rpm
Emissions control:	Cooled Exhaust Gas Recirculation (EGR) + Selective Catalytic Reduction (SCR)+Diesel Particulate Filter (DPF)+intake throttle
Cylinder Block:	Cast iron
Cylinder head:	Cast aluminum
Intake manifold:	Cast aluminum
Exhaust manifold:	Cast nodular iron with steel pipe extension
Main bearing caps material:	Cast nodular iron
Crankshaft:	Forged steel
Camshaft:	Steel
Connecting rod:	PM iron
*GM tested per SAE J1349	

In the 4S hydrogen version developed by Dumarey, approximately 20 % of the original Diesel components were replaced or redesigned to adapt the unit to Spark Ignition (SI) operation. The key modifications involved the turbocharging system, pistons and piston rings, valves and valve seats, the hydrogen injection system, and the electronic control unit, which was updated in both hardware and software. Additional components such as the ignition system, intake manifold, and crankcase ventilation circuits were also re-engineered to accommodate the new combustion process.

Compared to the Diesel baseline, the hydrogen 4S variant benefits from a much simpler and more cost-effective after-treatment system, as the formation of conventional pollutants is nearly eliminated under ultra-lean steady-state operation. The resulting decrease in exhaust backpressure also contributes to lowering the overall pumping losses.

For the transition to the 2S spark-ignition configuration, further modifications were required with respect to Dumarey's 4S hydrogen engine. The additional components specifically introduced for the 2S concept include:

- newly designed cylinder heads, optimized for simultaneous valve operation;
- redesigned valves and camshafts, with specific timing and lift profiles;
- a mechanically driven supercharger coupled to the crankshaft and equipped with a bypass valve;
- an additional charge-air cooler downstream of the supercharger;
- a re-shaped piston bowl, tailored for tumble-enhanced mixture formation;
- and a low-pressure port fuel-injection system for hydrogen delivery.

Preliminary evaluations indicate that nearly two-thirds of the original Diesel hardware could be retained without substantial modification. This high level of component carry-over makes the 2S hydrogen engine concept economically attractive and feasible even for retrofitting scenarios.

From a design standpoint, the 2S architecture is expected to significantly reduce the performance gap that still separates the hydrogen 4S engine from its Diesel counterpart, while maintaining durability and reliability standards. Accordingly, the following operational limits were set for the design process: maximum in-cylinder pressure of 180 bar, maximum pressure rise rate of 5 bar/°CA, and maximum turbine inlet temperature of 850 °C. The 2S cycle inherently supports these constraints, since, for an equal brake torque, the BMEP is halved compared to the 4S version. Consequently, the target BMEP for the 2-stroke configuration does not exceed 12 bar, allowing reduced mechanical stress while preserving output power.

Designing a 2S engine with overhead valves introduces one of the most critical challenges of the entire project: optimizing the scavenging process while both intake and exhaust valves are simultaneously open. The development effort must balance three often conflicting requirements. First, the engine must ensure a sufficiently high fresh-charge flow rate within the very short time window available for gas exchange, especially at high speeds. Second, the removal of residual combustion products must be efficient enough to prevent hot gas pockets that could trigger auto-ignition in subsequent cycles. Finally, short-circuiting of air and fuel through the exhaust valves must be minimized, since any fresh charge loss directly penalizes thermal efficiency.

The latter aspect is particularly relevant because air losses increase the pumping power absorbed by the supercharger. The penalty is twofold: the supercharger must supply more air than the stoichiometric requirement, and the resulting exhaust flow, diluted with excess air, carries lower enthalpy into the turbine, thereby reducing the compressor outlet pressure and increasing the supercharger pressure ratio.

To alleviate short-circuit losses, the intake valve geometry was modified through the introduction of shrouds (thin walls attached to the upper portion of the valve head, partially masking the curtain area on the exhaust-facing side). This solution, first explored by Toyota and Honda in the 1990s [140–142], deflects the incoming charge away from the exhaust valves and promotes a more coherent tumble-type flow inside the cylinder.

In the present study, both radial and tangential shroud orientations were investigated, but only the latter configuration is discussed here, as it produced the most favourable results. The final design closely resembles the tangential shrouds previously adopted by Honda. The main geometric parameters of the shrouded valves are summarized in Figure 74, where the normalized shroud height ($h^* = 0.222$), maximum thickness ($w^* = 0.042$), and angular coverage ($\theta = 95°$) are reported with respect to the 36 mm valve seat diameter.

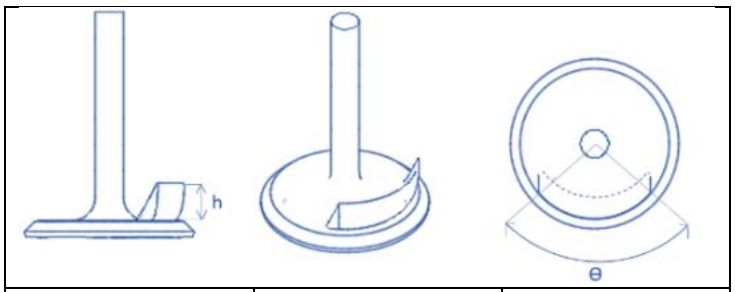

h*	w*	Θ
0.222	0.042	95°

Figure 74: Intake valve shrouds of the hydrogen 2S engine: side, perspective and up views.

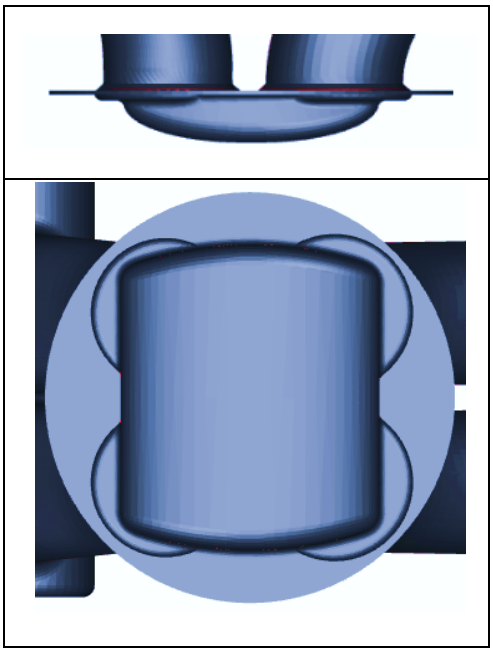

Figure 75: Combustion chamber views of the hydrogen 2S engine: side and bottom view.

The added mass due to the shroud is below 10 %, and the asymmetry can be dynamically balanced by a small rib positioned opposite to the shroud. Although manufacturing such valves is more complex and costly than standard ones, their mechanical integrity and durability are not expected to be compromised. The asymmetry of the curtain flow induced by the shroud promotes a well-organized tumble motion, which plays a decisive role in air–fuel mixing and flame propagation in SI engines. Based on these observations, the combustion chamber was redesigned to enhance and sustain the tumble vortex while generating additional radial motion (squish) near TDC. The resulting shallow-bowl chamber geometry, illustrated in Figure 75, guides the in-cylinder flow along a smooth U-shaped path and produces a wide squish region as the piston approaches TDC.

During the intake phase, hydrogen is supplied through two injection straws per cylinder, positioned in the intake ports and operating at approximately 10 bar under choked (sonic) conditions. The injectors are oriented to deliver the fuel jet through the portion of the valve curtain opposite the exhaust side, maintaining a high injection momentum. This configuration minimizes both hydrogen short-circuiting and volumetric efficiency losses, as the compact high-velocity jet occupies a smaller portion of the flow area under the valve.

Figure 76 presents the intake port layout with the corresponding straw geometry. Each straw features a circular nozzle of 3 mm diameter, a protrusion of 16.2 mm into the port, and a lateral offset of 12.0 mm from the valve axis. Since the ratio between upstream and downstream pressures always exceeds the critical value, the flow remains choked under all operating conditions. Consequently, the mass flow rate depends solely on the upstream pressure and the injector geometry, remaining nearly insensitive to manifold pressure variations.

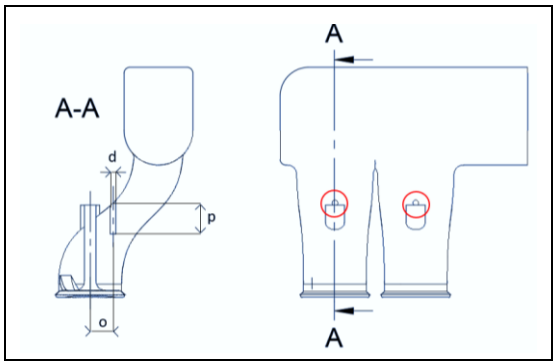

p	d	o
16.2 mm	3 mm	12 mm

Figure 76: Intake port section with straws view.

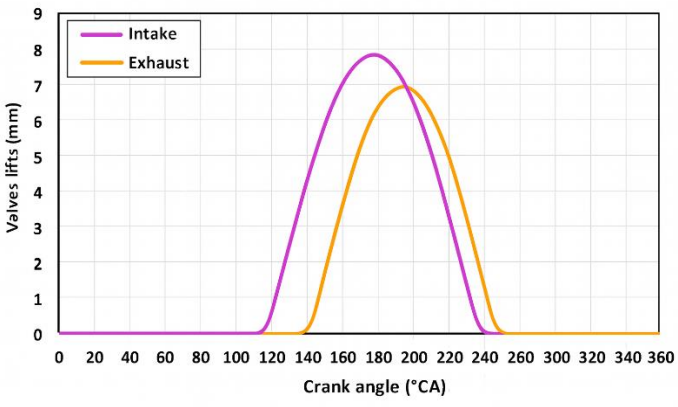

Figure 77: Optimized valve lift profile (without clearance).

An essential factor in the scavenging optimization is the definition of the valve actuation profiles and timing. The opening durations were set to guarantee the required mass flow rate without excessive boost pressure, and thus without increasing pumping losses, while respecting the mechanical constraints of the valvetrain. Valve overlap was minimized to reduce charge short-circuiting, although this required careful balancing: advancing the exhaust opening excessively would lower expansion work, whereas delaying intake closure too much could lead to charge expulsion back into the port, significantly increasing backfire risk. The final valve laws were obtained through an iterative optimization procedure involving both 3D-CFD simulations and 1D analyses. The optimized lift profiles are shown in Figure 77. The exhaust valves open 70° CA before BDC and close symmetrically after it, while the intake valves are delayed by roughly 20° CA, with closure occurring about 75° CA after BDC (approximately 5° CA after exhaust closure). The maximum intake lift is limited to 7 mm (relatively small compared to the 36 mm valve seat diameter) which keeps the peak gas velocity concentrated in the valve curtain region, reducing hydrogen stagnation near the valve seat and consequently minimizing the backfire risk.

6.3. Scavenging analysis without fuel

The first stage of the numerical investigation focused on assessing the effectiveness of the proposed 2S configuration in terms of its scavenging behaviour, excluding the influence of hydrogen injection. This preliminary step was essential to isolate the aerodynamic characteristics of the gas-exchange process and to evaluate the capability of the intake and exhaust systems to ensure adequate charge renewal.

The analysis was carried out by adopting a set of dimensionless parameters commonly used in the literature to describe 2S scavenging [146–148]. These include the Delivery Ratio (DR), Scavenging Efficiency (SE), Charging Efficiency (CE), and Retaining Efficiency (RE), all of which are defined as time-dependent quantities throughout the gas-exchange period.

The DR quantifies the normalized mass of fresh charge supplied to the cylinder and is defined as:

$$DR = \frac{m_{a,delivered}}{\rho_a V_d} \quad (18)$$

where $m_{a,delivered}$is the instantaneous mass of air delivered to the cylinder, $\rho_a$is the ambient air density, and $V_d$the displaced volume. At the end of the process, DR corresponds to the volumetric efficiency.

The SE measures the purity of the in-cylinder charge at a given time and is defined as the ratio between the mass of trapped fresh air ($m_{a,trapped}$) and the total cylinder mass (m_{cyl}):

$$\mathrm{SE} = \frac{\mathrm{m_{a,trapped}}}{\mathrm{m_{cyl}}} \quad (19)$$

The CE expresses the normalized mass of trapped fresh charge with respect to the reference volume:

$$CE = \frac{m_{a,trapped}}{\rho_a V_d} \quad (20)$$

Finally, the RE assesses the fraction of delivered air that remains trapped in the cylinder at the end of scavenging:

$$E = \frac{m_{a,trapped}}{m_{a,delivered}} \quad (21)$$

At the end of the process, RE coincides with the global trapping efficiency and indirectly quantifies the fresh charge lost through short-circuiting.

Since all these parameters depend on the thermodynamic state during scavenging, two additional indices were considered to characterize the operating conditions. The supercharging degree (Ψ) is defined as:

$$\Psi = \frac{\rho_{int} V_{cyl}}{\rho_a V_d} \quad (22)$$

where ρ_{int} represents the average density of the fresh charge upstream of the intake valves and $V_{cyl}$is the mean cylinder volume during scavenging. Another key boundary condition is the pressure ratio (PR), given by the ratio between intake and exhaust pressures. The interaction between Ψ and PR determines the overall flow rate of fresh air entering the cylinder.

To interpret the results, two reference models traditionally used for scavenging analysis were recalled [146–148]. The Perfect Displacement (PD) model represents an ideal situation in which the incoming fresh charge completely displaces the burnt gases without mixing. In this case, no short-circuiting occurs until the cylinder is fully filled, and DR equals CE, while RE remains unity. Once the cylinder reaches its full capacity (DR ≥ Ψ), SE stays equal to 1, and RE decreases proportionally to Ψ/DR. Conversely, the Perfect Mixing (PM) model assumes instantaneous and uniform mixing between incoming and residual gases, implying that the exhaust gas composition mirrors that of the cylinder contents. For identical operating conditions, the PM model yields lower CE, SE, and RE values compared to PD. The actual performance of real engines typically falls between these two extremes; ideally, the behaviour should remain closer to PD. Results worse than PM indicate excessive fresh charge losses, leading to decreased efficiency and increased emissions.

Another relevant parameter in scavenging characterization is the Tumble Ratio (TR), defined as:

$$TR = \frac{\omega_T}{\omega_{eng}} \quad (23)$$

where ω_T is the mean angular velocity of the in-cylinder flow around the tumble axis, and ω_{eng} is the crankshaft speed. This index quantifies the capacity of the intake flow to generate organized motion, which plays a crucial role in mixture preparation and combustion stability.

The scavenging simulations were performed at three full-load operating points (1200, 1600, and 3000 rpm), each characterized by distinct intake and exhaust conditions derived from the calibrated 0D/1D model. The corresponding values of Ψ and PR are summarized in Table 36. As expected, both supercharging degree and pressure ratio increase with engine speed, to compensate for the reduced gas-exchange time and to achieve the required performance targets.

Table 36: Boundary condition for the scavenging analysis.

Engine speed (rpm)	**1200**	**1600**	**3000**
Ψ	1.86	3.18	3.55
Intake pressure (bar)	2.09	3.56	4.00
Intake temperature (K)	313	313	313
Exhaust pressure (bar)	1.99	3.18	3.23
PR (p_{int}/p_{exh})	1.05	1.12	1.24

3D-CFD scavenging simulation results are summarized in Figure 78, where CE, RE and TR are shown for the three working condition. The optimized scavenging system consistently exhibited performance superior to the perfect mixing model, which is particularly encouraging given the

intrinsic difficulty of limiting short-circuiting in valved two-stroke engines. The overall results are consistent with those reported in previous research by Nakano, Sato, and colleagues [141–143] and reported in figure .

The evolution of RE as a function of DR showed a similar trend at all speeds. Initially, RE = 1 (perfect displacement), followed by a gradual decrease once a portion of the fresh charge begins escaping through the exhaust. The transition from the PD to mixed behaviour occurs at different DR values depending on the engine speed: around 0.25 at 1200 rpm, 0.4 at 1600 rpm, and 0.6 at 3000 rpm. After this transition, RE decreases smoothly with increasing DR, as short-circuiting becomes more likely. Nevertheless, at high DR values (around DR = 1), RE remains within 0.92–0.95 for all speeds, confirming the robustness of the proposed design.

The computed TR values were particularly significant, exceeding 5 at valve closure across all operating points. Such high turbulence levels are markedly greater than those typically observed in 4S engines and are expected to enhance air–fuel mixing and combustion efficiency. For each speed, TR increased with DR until reaching a maximum slightly before intake valve closure. This behaviour reflects the influence of the momentum flux through the intake valves and the near-constant dissipation rate of turbulence during the process. At a fixed DR, however, TR decreases as speed increases: for example, at DR = 1.25, TR values were 7.3, 5.8, and 5.5 at 1200, 1600, and 3000 rpm, respectively, indicating higher turbulence dissipation at elevated speeds.

The SE was analysed as a function of the normalized filling index (DR/Ψ). For all cases, SE values exceeded DR/Ψ, as the volume of expelled hot gas was replaced by denser cold air (see Figure 79). Increasing engine speed slightly improved SE at comparable filling levels, likely due to the higher PR, which enhances the momentum of the incoming flow and promotes a more compact front of fresh charge sweeping the chamber.

To further interpret the process, a residuals chart was generated (Figure 80), plotting the Exhaust Residual Ratio (ERR) versus the Cylinder Residual Ratio (CRR = 1 − SE). The PM model corresponds to the line y = x, while PD is represented by y = 1. The CFD results lie between these two limits, closer to PD, confirming the effective scavenging characteristics of the proposed configuration. The best-fit line derived from the simulated data (used in the GT-Power model) approximates a hybrid behaviour, nearly perfect displacement for CRR > 0.9, and gradually approaching perfect mixing at lower residual fractions.

Finally, the spatial distribution of the fresh charge and residual gases at intake valve closing (IVC) was analysed for the most critical operating condition (3000 rpm). The oxygen concentration field

and velocity vectors at IVC (Figure 82) demonstrate a uniform distribution of the fresh charge, without significant residual pockets. The velocity maps confirm the presence of a strong, coherent tumble vortex about the x-axis (ω_T), which is expected to promote further homogenization of the charge before ignition. Overall, the results indicate that the redesigned intake system and shrouded valve geometry provide efficient scavenging, limited short-circuit losses, and high turbulence intensity, creating the ideal foundation for stable and clean hydrogen combustion in the subsequent analysis.

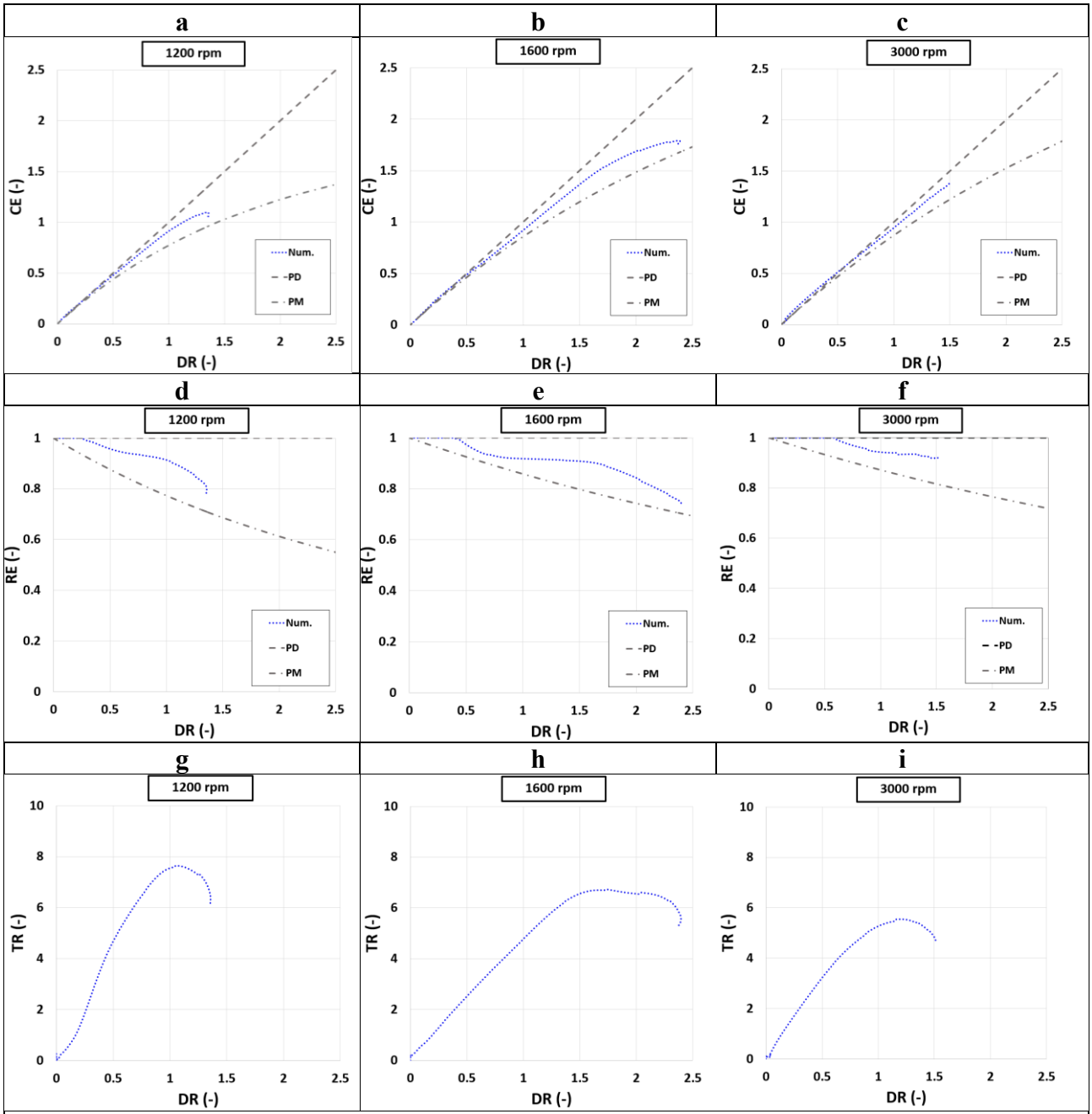

Figure 78: CE (a-c), RE (d-e), TR (g-h) versus DR during scavenging process, at 1200, 1600 and 3000 rpm without fuel injection.

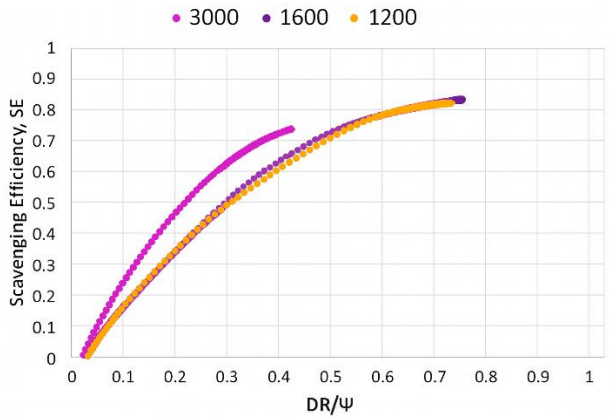

Figure 79: SE plotted as a function of the cylinder filling index DR/ Ψ at 1200, 1600 and 3000 rpm, without fuel injection.

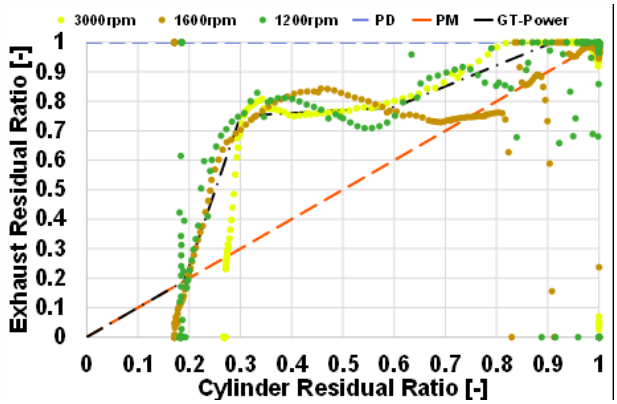

Figure 80: Residual chart, for 1200, 1600 and 3000 rpm with GT-Power fit curve. Fuel injection is not included here.

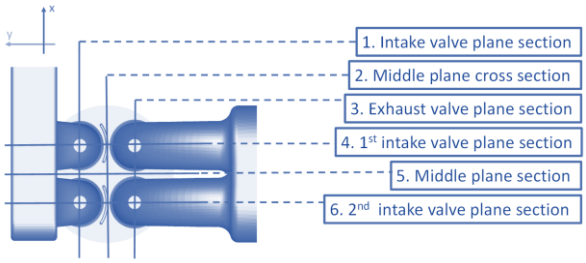

Figure 81: Definition of the cutting planes adopted for the analysis of the scavenging process.

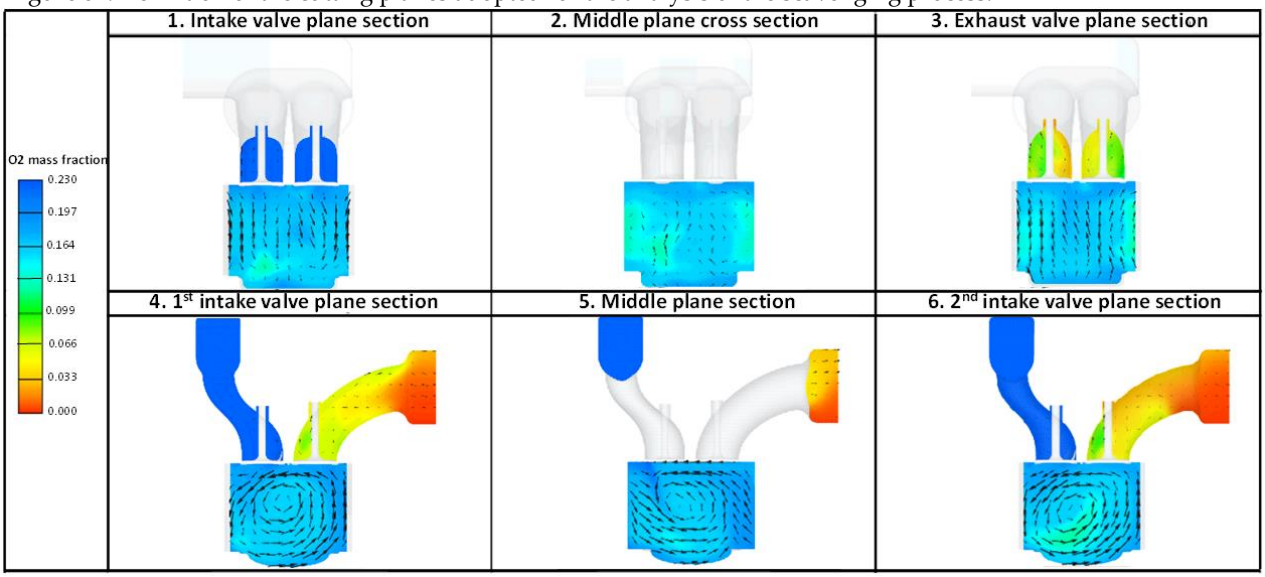

Figure 82: Oxygen distribution and velocity field shown at IVC on the six cutting planes defined in Figure 81. Engine speed: 3000, no fuel injection.

6.4. Calibration of the GT-Power model

The results of the three-dimensional CFD analyses were not limited to the evaluation of the scavenging behaviour, but were also used to enhance the predictive capability of the GT-Power model. The integration between the two simulation environments made it possible to combine the accuracy of 3D- CFD modelling with the flexibility and computational efficiency of system-level simulations.

The most significant update introduced in the 0D/1D framework concerned the scavenging sub-model, which was recalibrated using the information obtained from the 3D-CFD campaign. The residuals curve derived from the 3D simulations replaced the default empirical formulation previously adopted, allowing the 0D/1D model to reproduce the specific behavior of the newly designed 2S configuration. This modification enabled a more accurate representation of the relationship between trapped mass, delivered mass, and short-circuiting phenomena.

Additionally, corrections were applied to the valve discharge coefficients, derived from the flow characteristics predicted by 3D-CFD under varying pressure ratios and valve lifts. These refinements improved the accuracy of the effective flow areas used in the 0D/1D model and ensured a consistent correspondence between the boundary conditions of the two approaches.

To verify the quality of the calibration, several global parameters describing the scavenging process were compared between the 1D and 3D simulations performed under identical operating conditions. The evaluation included the DR, representing the normalized amount of fresh air supplied to the cylinder; the CE, indicating the mass of trapped air available for combustion; theTE, describing the system's ability to retain the delivered charge; and the fraction of residual gas remaining in the cylinder, obtained as the complement of the Scavenging Efficiency (1 – SE). The unsteady mass-flow rates through the intake and exhaust valves were also analyzed to confirm the temporal consistency of the flow predictions.

The comparison showed an excellent agreement between the 1D and 3D models across all operating conditions. This outcome is particularly relevant considering that a single calibration setup was used for every case, without any parameter adjustments specific to engine speed or load. The validated 0D/1D model therefore provides a reliable and computationally efficient tool for system-level performance studies and for subsequent optimization of the air-handling and control strategies.

It should be emphasized that this calibration phase represents only an intermediate step within a broader iterative design loop.

6.5. Injection and fuel mixture preparation analysis

The development and optimization of the hydrogen injection strategy were carried out through an extensive campaign of 3D-CFD multi-cycle simulations, in which both the scavenging and compression phases were explicitly modelled. Each case included five consecutive engine cycles, which proved sufficient to achieve convergence in terms of hydrogen concentration within the intake port, cylinder, and exhaust regions. As in the previous analyses, the initial and boundary conditions were derived from the calibrated GT-Power 0D/1D model, ensuring full consistency between system-level and CFD predictions.

Because combustion was not included in the 3D simulations, the in-cylinder thermodynamic fields (pressure, temperature, and species mass fractions) were reinitialized ten crank-angle degrees before the EVO at the end of each cycle. This allowed the flow and species fields to reach a steady periodic behaviour while maintaining realistic residual gas distributions.

The multi-cycle analysis focused on the most demanding operating condition, corresponding to the maximum engine speed and power output (3000 rpm), with a global equivalence ratio of 0.5. Different hydrogen injection timings were tested, while maintaining the nominal mass flow rate of 7.9 g/s and an injection pressure of 8 bar. The most effective configuration was obtained for a start of injection (SOI) at 185° crank angle and an end of injection (EOI) at 236.5°, resulting in a total duration of 51.5° CA, as illustrated in Figure 83.

Under these conditions, approximately 96% of the injected hydrogen was retained within the cylinder at IVC, while only 4% escaped through the exhaust. The amount of fuel remaining in the intake manifold was negligible, implying that the risk of backfire was virtually eliminated. This limited short-circuit fraction, achieved at the most critical operating point and in an early development phase, represents a promising result, especially since the small quantity of unburned hydrogen in the exhaust would be completely oxidized in the downstream flow without requiring any after-treatment.

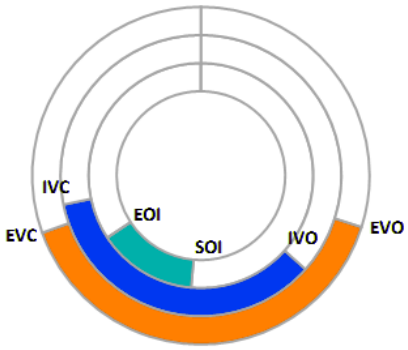

Figure 83: Polar diagram showing intake and exhaust valve timing and hydrogen injection duration.

Another remarkable outcome concerns the homogeneity of the air–fuel mixture at spark timing, assumed to occur 15° BTDC. The mixing process, illustrated in Figure 84, was analysed on cutting plane 6 (as defined in Figure 81). The results show that hydrogen forms a compact jet entering the cylinder through the intake-valve curtain opposite to the exhaust. Guided by the strong tumble vortex, the fuel stream flows along the liner, reaches the piston bowl, and is then deflected upward while maintaining a coherent trajectory along the cylinder wall. Approximately 40° CA after the SOI, a small portion of hydrogen reaches the exhaust valves, which are already closing at that point. This explains the very limited fuel loss observed at the exhaust.

After both valve pairs are closed, the tumble-driven motion continues to promote an efficient redistribution of the trapped charge. The time evolution of the in-cylinder equivalence ratio, shown in Figure 85, highlights the progressive homogenization of the mixture during the compression stroke. Between BDC (1620° CA) and TDC (1800° CA) of the fifth cycle, the standard deviation of the equivalence ratio decreases continuously, reaching values below 5% of the mean at the time of ignition.

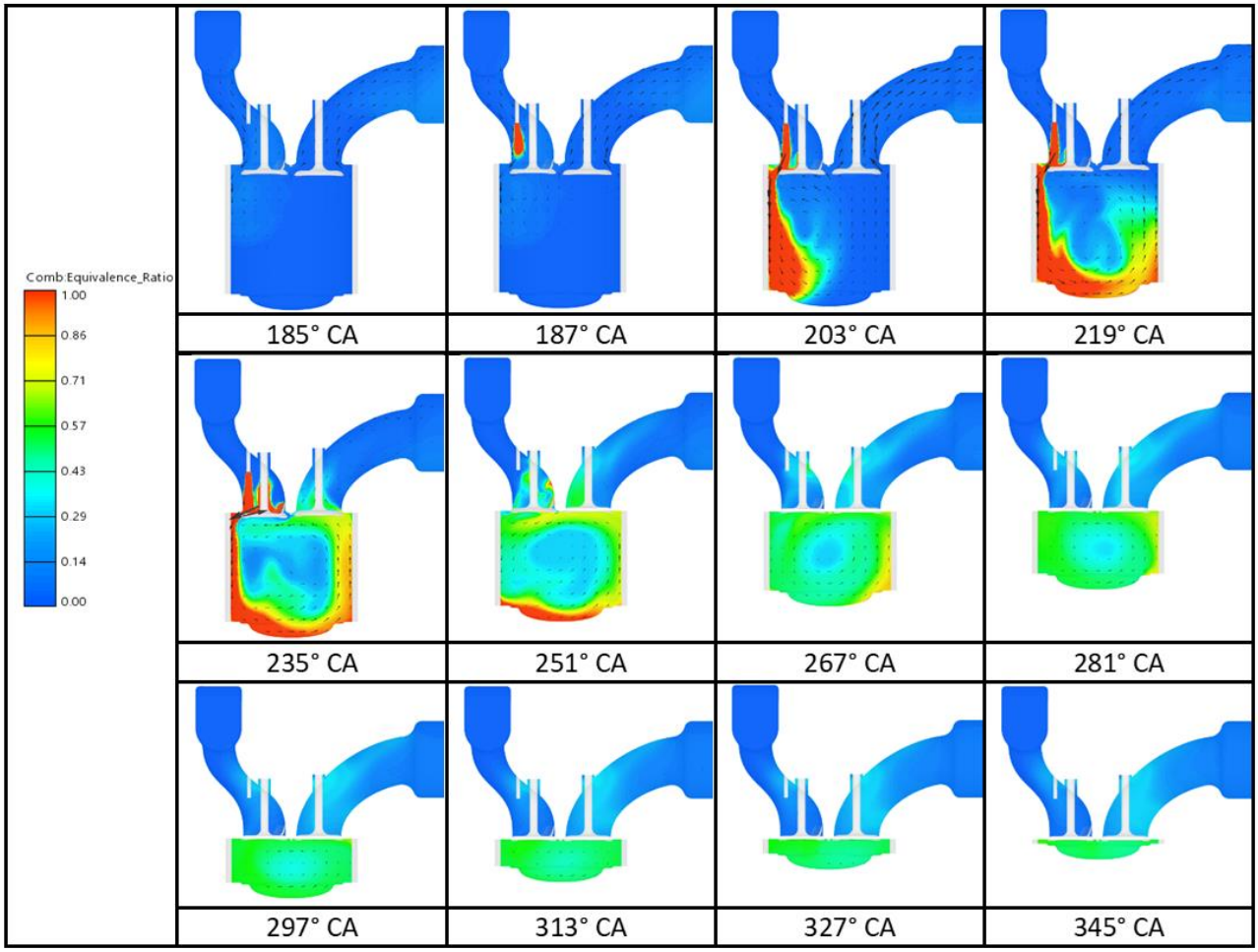

Figure 84: Evolution of the equivalence ratio on cutting planes 6 (see Figure 81) for different crank-angle positions during the fifth cycle (engine speed 300 rpm, equivalence ratio 0.5, SOI = 185 °CA, EOI = 236.5° CA ATDC, Spark Timing = 345° ATDC).

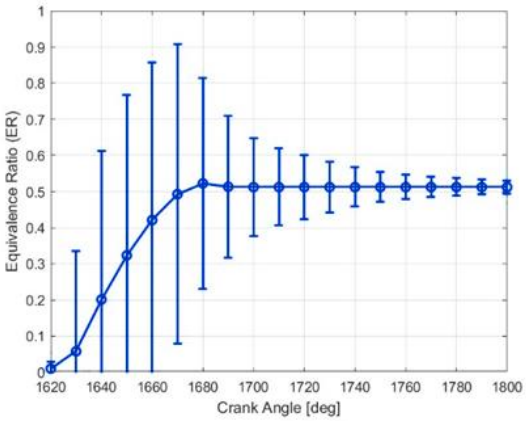

Figure 85: Mean value and standard deviation of in-cylinder equivalence ratio during the fifth cycle (1620° -1800° CA). Engine speed 3000 rpm, equivalence ratio 0.5, SOI = 185 ° CA, EOI = 236.5° CA, spark at 345° CA.

At spark timing, the equivalence-ratio distribution across the six reference planes (Figure 86) confirms the high level of mixture uniformity within the chamber. The minimum and maximum local values, 0.48 and 0.58 respectively, are confined to narrow peripheral zones that occupy a negligible fraction of the total volume and are therefore not expected to affect flame propagation or combustion stability significantly.

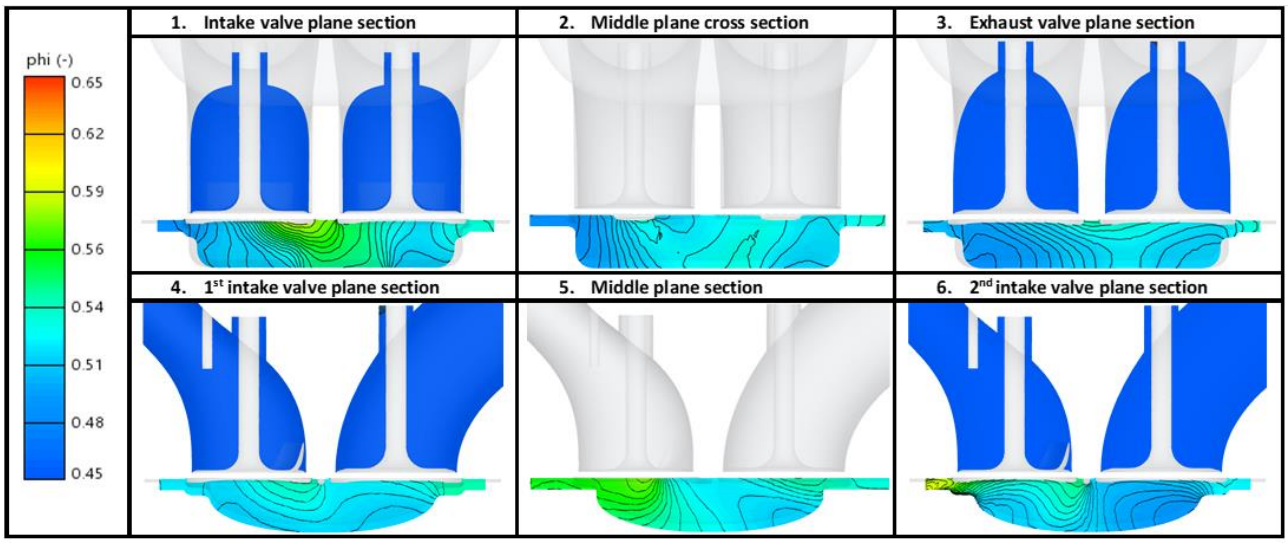

Figure 86: Equivalence-ratio distribution at spark timing (-15° CA BTDC) across six cutting planes (engine speed 3000 rpm, equivalence ratio 0.5, SOI = 185° CA, EOI = 236.5° CA).

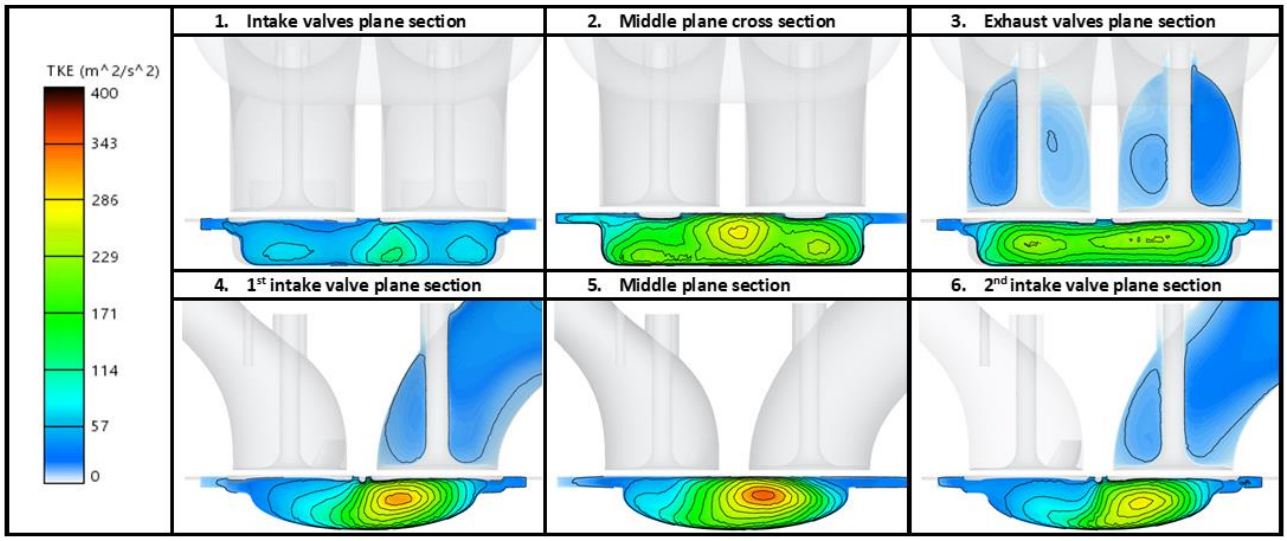

Figure 87: Turbulent kinetic energy distribution at spark timing (-15° CA BTDC) across the same cutting planes.

The last aspect analysed concerns the turbulent kinetic energy (TKE), a key indicator of the charge-motion intensity at the time of ignition. As shown in Figure 87, the TKE distribution at 15° BTDC is not uniform, with the highest values concentrated near the central region of the chamber, immediately below the spark-plug position. Peak TKE levels of 350–400 m^2/s^2 are consistent with the dissipation of the strong tumble vortex generated during scavenging and are indicative of favourable turbulence conditions for stable and complete combustion.

In summary, the multi-cycle simulations confirmed that the proposed injection strategy ensures excellent fuel retention, minimal short-circuiting, and highly homogeneous mixture formation. The combination of tangential shrouded valves, optimized port geometry, and strong tumble generation provides the right flow structure for clean and efficient hydrogen combustion, paving the way for the subsequent combustion analysis.

6.6. Full load performance analysis

The overall engine performance under full-load conditions was evaluated using the GT-Power 1D model, previously recalibrated with the 3CFD-derived scavenging and mixture-formation results discussed in the earlier sections. Combustion and NOx emissions were predicted through a quasi-dimensional hydrogen combustion model, calibrated against experimental data obtained from the 4S hydrogen engine developed by Dumarey.

A key aspect of this analysis concerned the design and matching of the two-stage supercharging system, composed of a variable-geometry turbocharger, a centrifugal compressor, and a mechanical

supercharger. For the latter component, a positive displacement unit with an integrated bypass valve was selected. The supercharger was placed downstream of the turbocharger compressor, a configuration preferred for two main reasons:

1. operating on a pre-compressed charge allows the supercharger to achieve the required pressure ratio with a smaller displacement and reduced overall dimensions;
2. in a V8 configuration, this arrangement enables compact integration between the cylinder banks, with the supercharger and charge cooler positioned centrally within the engine “V”.

Previous investigations on valved two-stroke engines [149] suggest that the supercharger should operate at peak power with a pressure ratio between 1.6 and 1.8, corresponding to the region of highest isentropic efficiency on the performance map. At lower speeds, the supercharger continues to assist the turbocharger in maintaining the target boost level, without requiring an excessive reduction of the turbine nozzle area. This prevents a rise in exhaust backpressure that would otherwise penalize the airflow rate, even in the presence of high boost pressures. At the same time, it is important to avoid operating points with pressure ratios below unity, which would indicate that the supercharger is no longer compressing the air but rather dissipating energy (a situation typically associated with low-speed conditions and undersized units).

The optimization of the boosting system relied on experimental compressor and turbine maps, minimizing the use of scaling factors. The resulting operating points for the full-load conditions are reported in Figure 88 and Figure 89, showing the locations of the simulated points on the maps of the supercharger and turbocharger compressor, respectively. For the supercharger (Figure 88), all operating points except 800 rpm fall within regions of isentropic efficiency above 60%, and the rotor speed remains safely below the mechanical limit, ensuring quiet and reliable operation. The turbocharger compressor map (Figure 89) also exhibits a well-distributed set of points, maintaining high efficiency and a wide margin from both surge and choke boundaries.

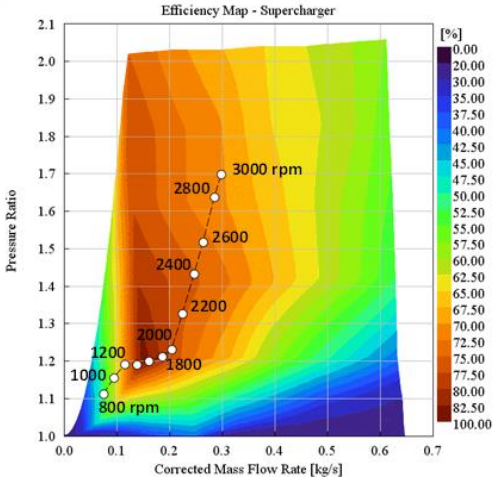

Figure 88: Operating points at full load on the supercharger map.

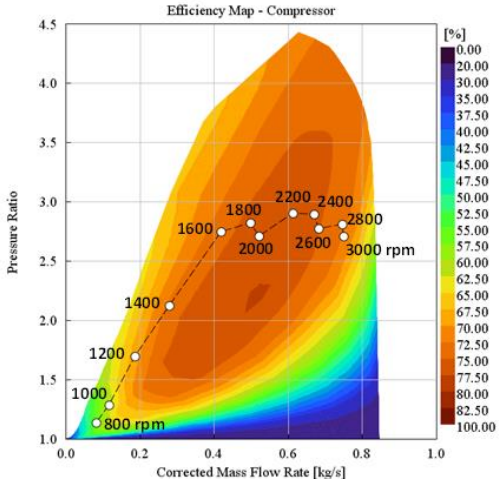

Figure 89: Operating points at full load on the turbocharger compressor map.

The resulting scavenging parameters at full load are illustrated in Figure 90. The DR, CE, TE, and residual gas fraction were plotted as functions of engine speed. From 1600 to 3000 rpm, CE remains nearly constant between 1.5 and 1.8, while TE increases from 0.78 to 0.90. The DR remains in the range of 1.9–2.1, indicating that the volumetric filling capacity of the engine remains stable across the operating range. Although the trapped residual gas fraction is relatively high (between 17% and 25%) it is expected to be uniformly mixed with the fresh charge due to the intense turbulence generated during the scavenging and compression phases, thus minimizing the risk of hot spots or knock phenomena.

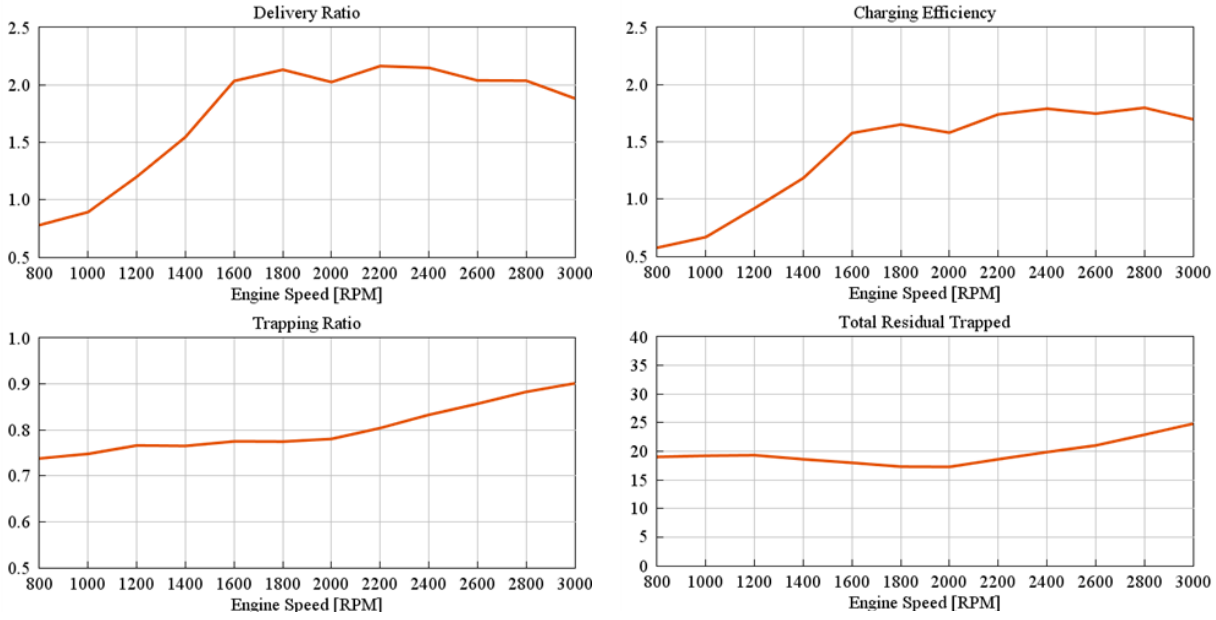

Figure 90: Scavenging parameters at full load as functions of engine speed: DR (volumetric efficiency), trapping ratio, charging efficiency, and residual gas fraction.

The combustion-related parameters, summarized in Figure 91, were obtained by imposing an in-cylinder relative λ of 2.2 and adjusting the spark timing to achieve a 50% mass fraction burned (MFB50) at 15° CA ATDC. This setup yielded stable combustion, with a combustion duration (BD1090) between 25° and 55° CA, and NOx concentrations below 20 ppm. These conditions are consistent with those observed in the 4S hydrogen prototype by Dumarey, confirming that the 2S layout preserves the same lean-burn operating characteristics.

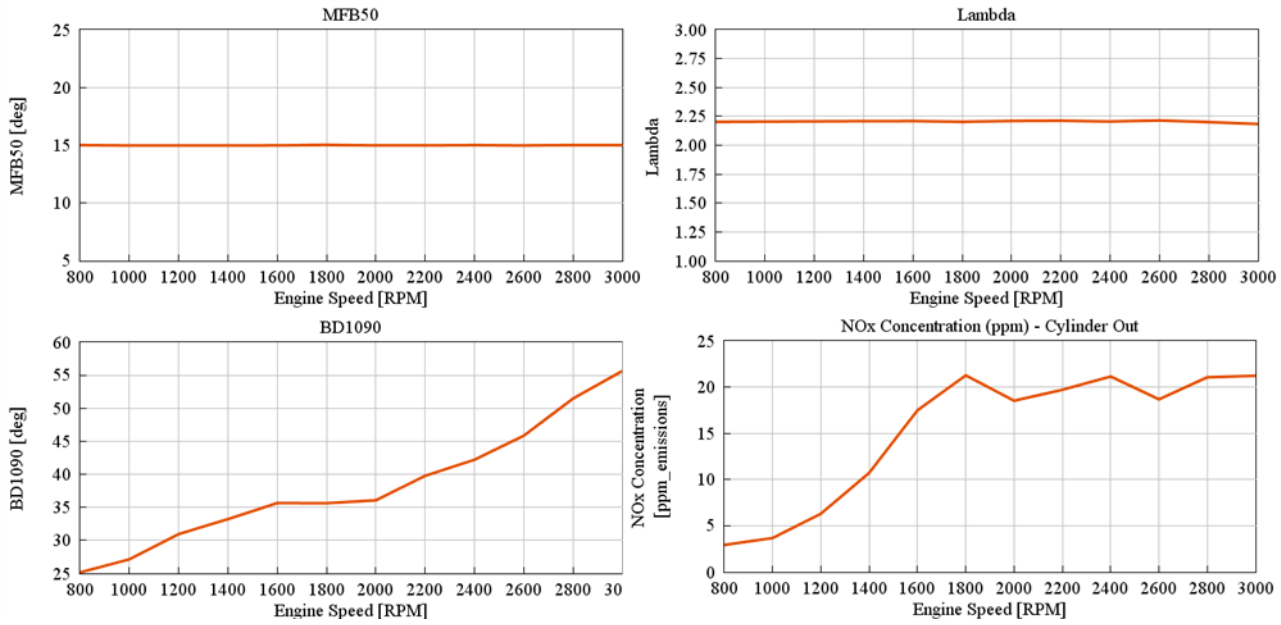

Figure 91: Combustion parameters at full load: MFB50, air–fuel ratio, combustion duration and NOx emissions.

The engine's Mean Effective Pressures (MEPs) are presented in Figure 92, where the gross indicated, friction, supercharger, and brake MEPs are compared. The gross indicated and brake values closely match those measured on the 4S hydrogen engine, but the 2S configuration delivers significantly higher torque and power due to one combustion event per crank revolution.

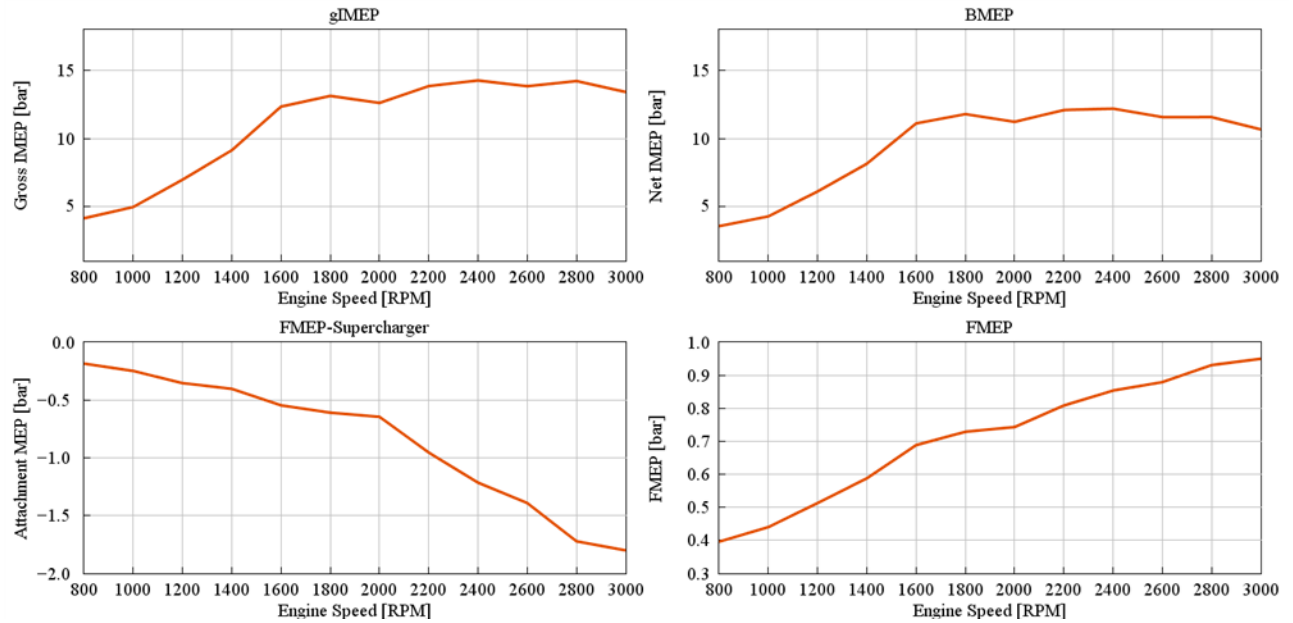

Figure 92:MEP plots as function of Engine RPM at full load: Gross IMEP, BMEP, FMEP-Supercharger, FMEP.

The resulting brake torque and power curves are shown in Figure 93, confirming that the proposed 2S hydrogen engine reaches the same full-load performance as the reference Diesel engine. However, as expected, the Diesel version still achieves a slightly higher BTE due to its higher compression ratio and more favourable thermodynamic cycle.

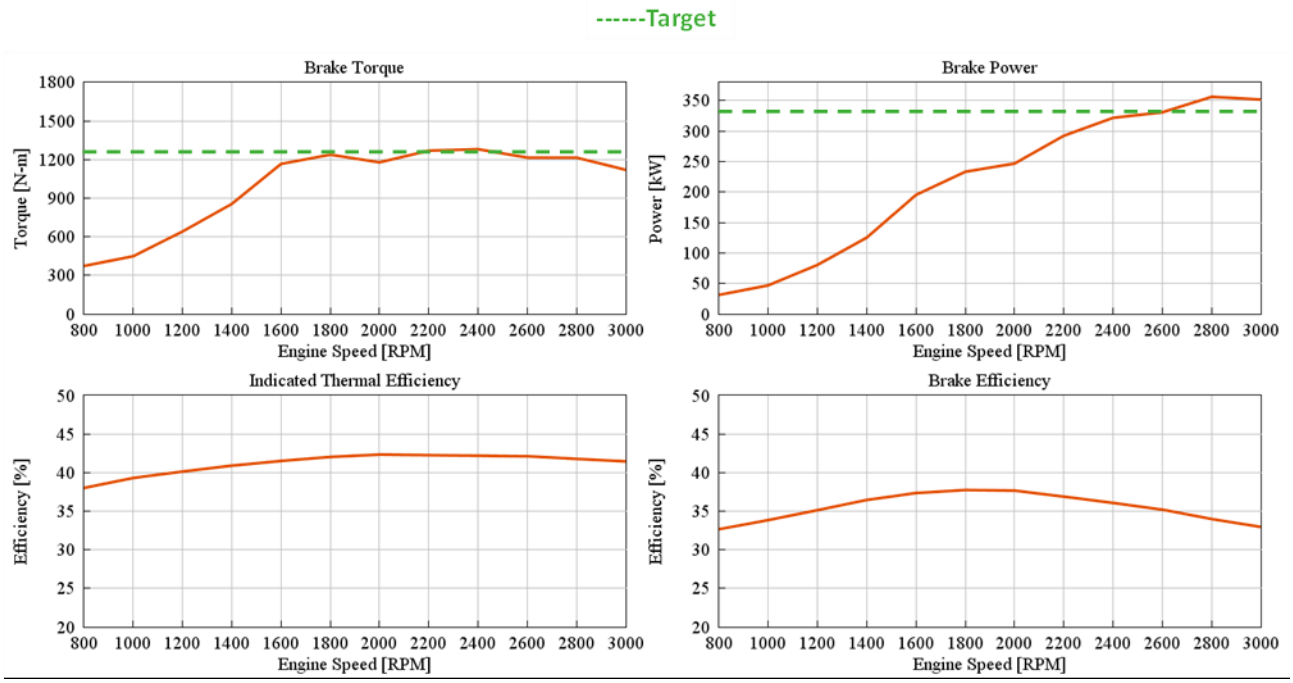

Figure 93: Brake performance curves at full load: brake torque, brake power, indicated thermal efficiency, BTE.

When compared with Dumarey's real 4S hydrogen engine, the advantages of the proposed 2S architecture become clear:

- The 2S version achieves a maximum power of 350 kW at 2800 rpm, compared to 190 kW at 2300 rpm for the 4S configuration. Even when operating at the same speed (2300 rpm), the 2S engine delivers more than 300 kW.
- At full load and 2300 rpm, the BTE of the 4S prototype was measured at 25%, while the virtual 2S counterpart reaches 36%. This result, although purely numerical, highlights the theoretical potential of the concept and warrants further experimental investigation.

In conclusion, the 0D/1D–3D integrated analysis demonstrates that the hydrogen-fuelled 2S valved engine can match the power output of the original Diesel baseline while maintaining near-zero NOx emissions and higher theoretical efficiency. These results confirm the strong potential of the proposed architecture as a viable pathway toward high-efficiency, carbon-free internal combustion for heavy-duty applications.

6.7. Conclusions and final remarks

The progressive path followed throughout this research project aimed to explore the potential of hydrogen as a viable fuel for the decarbonization of compression-ignition engines, starting from conventional Diesel operation and gradually extending toward fully hydrogen-based combustion concepts. The transition was articulated through a sequence of studies that progressively reduced diesel dependence (initially by introducing hydrogen as a secondary energy carrier in DF mode), and eventually by completely replacing Diesel with hydrogen in a dedicated spark-ignition 2S configuration.

The first stages of this work demonstrated that, in DF Diesel–Hydrogen operation, it is possible to achieve substantial reductions in pollutant emissions while maintaining high engine performance. The optimization of the diesel injection strategy, guided by 3D-CFD analyses, enabled hydrogen energy shares exceeding 95%, showing the strong potential of the concept. At the same time, the results highlighted the intrinsic limitations of DF combustion at high load (mainly related to combustion control and pressure-rise rates) which motivated the transition toward fully hydrogen-fuelled architectures.

The final step of this research focused on the complete conversion of a production Diesel engine (the Duramax 6.6 ℓ V8) into a hydrogen-fuelled, SI, 2S configuration equipped with poppet valves.

Through a combined 0D/1D-3D-CFD methodology, the new concept was extensively analysed and optimized in terms of gas exchange, scavenging, mixture preparation, and boosting system design. The redesigned combustion chamber, featuring tangentially shrouded intake valves and a shallow piston bowl, proved effective in generating a strong tumble vortex, enhancing turbulence and improving mixture homogeneity while minimizing short-circuiting losses. When integrated into the GT-Power model, the concept achieved full-load performance comparable to the original Diesel version, with near-zero NO_x emissions and high theoretical thermal efficiency. From a technological standpoint, the concept requires only limited hardware modifications (mainly to the cylinder head, piston and valve system) while retaining the base engine structure, suggesting a high Technology Readiness Level (TRL) and feasible industrial scalability.

Overall, the outcomes of this work confirm that both DF Diesel–Hydrogen and pure-hydrogen internal combustion architectures represent credible and complementary routes toward the decarbonization of HD propulsion. DF operation provides a transitional solution, capable of reducing emissions and fossil fuel consumption with minimal hardware changes, while fully hydrogen-fuelled concepts demonstrate the long-term potential for zero-carbon, high-efficiency operation using largely existing engine platforms.

In a broader perspective, the results presented here highlight the flexibility and resilience of internal combustion technology in adapting to new fuels. Both approaches (hybrid and full-hydrogen) can play a crucial role in the decarbonization of HD, long-haul, and marine applications, where high energy density, robustness, and operational autonomy remain essential requirements. The methodologies and insights developed in this thesis thus provide a solid foundation for the next generation of carbon-neutral engine systems, where hydrogen will increasingly complement or replace traditional hydrocarbons without compromising performance, reliability, or efficiency.

Future research should extend this work by experimentally validating the 2S hydrogen concept, refining the control of the scavenging and injection systems, and exploring advanced combustion modes and hybrid powertrain integrations. Such developments will be key to fully unlocking the potential of hydrogen-fuelled internal combustion engines in the global transition toward sustainable mobility and energy systems.

7. Hybrid-electric power unit for an ultralight aircraft: a complementary approach to cleaner Diesel technology

The ultralight aircraft sector represents one of the most dynamic areas of modern mobility. In recent years, the demand for compact, efficient, and environmentally sustainable propulsion systems for small aircraft and Unmanned Aerial Vehicles (UAVs) has grown rapidly, supported by both civil and defence applications [150]. This expansion reflects the broader transformation of the transport landscape, where the principles of green and intelligent mobility increasingly extend beyond the automotive domain to include general and light aviation. Within this context, propulsion technology is undergoing a phase of deep innovation, aimed at reconciling three essential and often conflicting requirements: high power-to-weight ratio, fuel efficiency, and low environmental impact.

For power classes above approximately 40 kW, the propulsion of ultralight aircraft has been traditionally dominated by 4S SI engines, such as the Rotax 912 ULS/S [151], Jabiru 2200, and HKS 700e units. These engines are lightweight, mechanically simple, and reliable, but their fuel consumption and limited compatibility with low-carbon or heavy fuels restrict their sustainability and operational flexibility. Diesel or kerosene-fuelled compression-ignition engines could, in principle, offer superior efficiency and safety (diesel fuel being less volatile than gasoline) but their adoption has been hindered by higher specific weight and mechanical complexity. The few available aviation Diesel engines, such as the Danielson 100 TD2 or the SMA SR305, confirm both the potential and the challenges of this technology: high efficiency and fuel flexibility are offset by significant mass and cost penalties.

Meanwhile, battery-electric propulsion, despite offering zero local emissions and silent operation, remains impractical for this class of aircraft due to the very low specific energy of current battery technologies (~0.2 kWh/kg). Even short take-off operations of a few minutes would require battery packs exceeding 40–50 kg, drastically reducing payload and range. These inherent limitations make hybridization the most viable pathway to combine the advantages of electric propulsion (instant torque, regenerative capability, zero-emission operation in specific phases) with the endurance and energy density provided by liquid fuels.

However, hybridization in aviation introduces additional design constraints compared to the automotive sector: every kilogram added to the power unit directly reduces payload and affects flight dynamics. Achieving a favourable mass balance is therefore essential. One effective strategy to offset the weight of electrical components is to replace the conventional 4S thermal engine with a lightweight 2S unit, which inherently offers a higher power density and simpler architecture [152].

Yet, traditional 2S designs relying on crankcase scavenging are typically penalized by high fuel consumption, poor lubrication, and limited reliability, making them unsuitable for aviation-grade applications.

The research presented in this chapter addresses these challenges by proposing an innovative Hybrid-electric Power Unit (HPU) that merges a newly developed 2S compression-ignition Diesel engine with a high-efficiency axial-flux electric motor in a parallel configuration. The thermal engine, designed as an air-cooled, four-cylinder boxer, operates on Diesel, kerosene, or Jet-A fuels, and has been optimized through CAD and CFD-supported design methods to achieve high combustion efficiency while minimizing weight. The electric subsystem, based on a commercial axial-flux motor (Emrax 188) and a compact lithium NMC battery pack, provides the capability for full-electric operation over short intervals, power assistance during take-off and climb, and energy recovery during low-load phases.

The proposed configuration aims to deliver equivalent or superior performance to the widely used Rotax 912 ULS/S engine while reducing fuel consumption and CO_2 emissions, maintaining comparable weight and compactness. The concept also offers additional advantages typical of hybrid architectures, such as reduced fuel mass for a given range, increased payload capacity, and enhanced operational flexibility at high altitudes.

While hybrid powertrains have become standard in the automotive field, their integration into aviation propulsion systems is still in its infancy. This research topic, therefore, contributes to bridging that gap by applying the design principles and analytical methodologies developed in the automotive domain (particularly those centered on Diesel engine optimization and CFD-based design) to the emerging field of light hybrid aviation. This approach is consistent with the overarching vision of the present dissertation: rather than discarding compression-ignition technology, it seeks to redefine and repurpose it within a modern framework of efficiency, safety, and environmental responsibility.

Part of the research activities presented in this chapter has been published in Pisapia, et al., “Hybrid-electric power unit for an ultralight aircraft,” Journal of Physics: Conference Series, Vol. 2648, 2023, pp. 012081, within the framework of the ATI 2023 Conference [153]. In addition, complementary computational work was carried out within a Master’s thesis supervised by the author, focusing on the spray calibration and combustion chamber geometry optimization of the 2S Diesel engine used in the HPU. These activities provided valuable insights into mixture formation and combustion behaviour under low-pressure Diesel injection, supporting the 3D-CFD-based design process

discussed in this chapter. A concise summary of their methodology, optimization and results is reported in Appendices A and B.

7.1. HPU: the layout

The proposed hybrid-electric propulsion system is based on a parallel configuration, as schematically illustrated in Figure 94. This architecture, which is among the most common in light aircraft applications, combines the mechanical power of the Internal Combustion Engine (ICE) and the electric motor (EM), enabling both joint and independent operation of the two power sources. The parallel layout offers two key advantages:

- It allows maximum power summation during take-off or emergency manoeuvres, when short-term peak output is crucial;
- It improves average thermal efficiency during cruise, where the load is typically low and the electric motor can assist the ICE, permitting the adoption of a smaller and lighter thermal engine [154];

The ICE is connected to the propeller through a dry slip clutch, which ensures smooth torque transmission even in the absence of a flywheel, thus saving mass. The electric motor, a commercial Emrax 188 axial-flux permanent magnet unit, was selected for its compactness, low weight (7.5 kg), and high specific power. It provides up to 35 kW continuous output, with a rotor external diameter of 188 mm. The motor transmits torque to the propeller shaft via the Electric Motor Gearbox (EMG), a compact gear pair with a reduction ratio of 0.75.

Downstream, a Propeller Gearbox (PG) is installed between the hybrid power unit and the propeller to match the required rotational speed of the reference aircraft. The PG was designed to deliver a maximum propeller speed equivalent to that of the Falco EVO UAV [155], powered by the Rotax 912 ULS/S engine, thus ensuring a direct comparison between the proposed system and a well-established configuration in the same power range.

The energy storage subsystem employs lithium-ion cells with Nickel–Manganese–Cobalt (NMC) chemistry, chosen for their high specific power and thermal stability [156]. Two battery pack configurations were investigated, named BP_A (smaller capacity) and BP_B (larger capacity). In addition to mass and energy storage, the battery size directly influences the maximum hybridization level and the peak electrical power that can be delivered to the propulsion system.

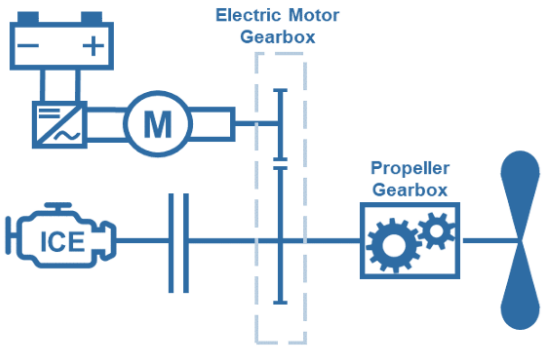

Figure 94: Schematic view of the HPU layout

The Hybridization Level (HL) is defined as the ratio between the instantaneous power provided by the battery and that delivered by the thermal engine:

$$HL = \frac{P_{batt}}{P_{eng}} \quad (24)$$

HL depends on the power-management strategy adopted by the hybrid control unit and varies with flight phase. Table 37 summarizes the main specifications of the two battery packs and the corresponding HL values under different operating conditions.

During take-off, the electric motor compensates for the lower peak output of the 2S Diesel engine by contributing ~5 kW of additional power, restoring the total propulsive power to the reference value of the Rotax 912 ULS/S. At maximum power, the electric contribution is instead limited by the discharge capability of the battery.

Table 37: Main Characteristics of the battery packs

Battery	Cell layout	Rated capacity [kWh]	Nominal voltage [V]	Max cont. discharge [kW]	Max cont. discharge @80 °C [kW]	Cells weight [kg]	Pack weight [kg]	HL @ take-off [-]	HL @ max [-]
BP_A	S34P3	1.43	122.4	12.9	16.5	7.1	7.9	0.14	0.25
BP_B	S34P5	2.39	122.4	21.4	27.5	11.9	13.1	0.14	0.41

As expected, BP_B (2.39 kWh) provides higher HL values (up to 0.41) and improved take-off performance, albeit at a slightly higher mass. Conversely, BP_A (1.43 kWh) offers a lighter configuration, suitable for missions prioritizing endurance and payload over peak power. The selection between these configurations depends on the mission profile and aircraft design constraints. A higher HL is particularly advantageous for operations at high altitude, where reduced air density

lowers the ICE performance; in such cases, electric assistance can restore propulsive power with only a marginal penalty in component cooling.

The hybrid power unit can operate under four main modes, depending on the flight phase and energy-management logic:

- ICE-only mode: the internal combustion engine provides all propulsive power.
- EM-only mode: pure electric propulsion, feasible for short-duration, low-noise operations.
- Combined ICE + EM mode: both sources deliver power simultaneously, maximizing total thrust (e.g., during take-off).
- Generator mode: the ICE drives the EM as an alternator to recharge the battery during low-load conditions.

Given the stringent mass limitations typical of ultralight aircraft, the system is classified as a mild hybrid, meaning that the electric subsystem can sustain propulsive operation only for limited periods. A full-hybrid architecture, while offering greater flexibility, would have imposed an excessive weight penalty and was therefore discarded.

7.2. HPU: the 2-stroke engine

The development of the thermal unit at the core of the hybrid power system was guided by the same simulation-driven design philosophy adopted throughout this dissertation. In particular, the 2S compression-ignition engine was conceived to achieve a high specific power, low mass, and high efficiency while ensuring reliable operation with Diesel, kerosene, or Jet-A/Jet-A1 fuels. The engine architecture derives from concepts previously introduced in earlier research on advanced 2S propulsion systems [157]. In this configuration, air exchange is controlled by piston-actuated ports, and the induction process is assisted by an external mechanical supercharger rather than by crankcase pumping. This design choice eliminates the need for crankcase scavenging and allows the implementation of a 4S-type lubrication system, where oil and air are fully separated. Consequently, the fresh charge entering the cylinder is free of both fuel and lubricant, improving mixture purity and reducing oil consumption. The decoupling of the crankcase from the scavenging process also provides significant freedom in shaping and orienting the intake ports, which can be optimized independently of the piston motion constraints typical of conventional 2S engines.

Among the various subsystems, the combustion chamber represented the most critical design challenge. In the proposed layout, the in-cylinder flow field is characterized by a dominant tumble

vortex, generated as the incoming air stream is directed along the cylinder liner and then deflected by the cylinder head. Under these conditions, the adoption of a traditional omega-bowl piston with flat head (suitable for swirl-dominated chambers) would have compromised scavenging efficiency. The absence of poppet valves, however, provided almost complete geometric freedom, which was exploited to define a novel, compact combustion system featuring a high compression ratio (>22:1) and a favourable surface-to-volume ratio.

A dedicated campaign of 3D-CFD simulations was carried out to evaluate alternative chamber geometries and injection strategies. The results demonstrated that the proposed configuration can burn Diesel fuel efficiently even with moderate injection pressures (50–350 bar) values significantly lower than those of conventional common-rail systems, thanks to the intense turbulence levels inside the cylinder. Simulations were performed up to 5000 rpm, at $\lambda \geq 1.3$ and IMEP up to 10 bar. Beyond this threshold, the rate of pressure rise increased markedly, leading to rough combustion and mechanical stress on lightweight components. As an illustrative case, Figure 95 reports the predicted in-cylinder pressure trace and burned-mass fraction for an optimized injection law at 5000 rpm and IMEP = 10.3 bar, confirming complete combustion and stable pressure development under lean conditions.

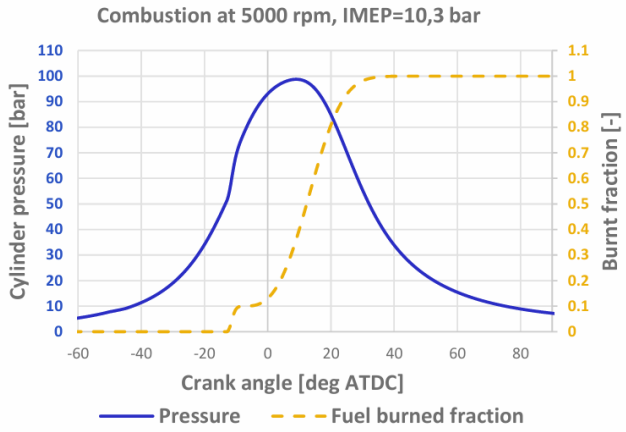

Figure 95: Cylinder pressure and burned fraction at 5000 rpm, IMEP = 10.3 bar; for an optimized injection strategy.

The preliminary sizing of the engine was based on a target brake power of 70 kW at 5000 rpm, corresponding to a BMEP of approximately 8 bar. This moderate BMEP value was intentionally selected to limit combustion roughness and maintain high mechanical reliability despite the lightweight structure. The relatively low specific heat rejection also enabled the use of air cooling, providing a further weight advantage over liquid-cooled architectures.

From these hypotheses, the resulting total displacement was set to ≈ 1050 cm³. The engine adopts a four-cylinder boxer layout, consistent with most ultralight propulsion units (including the reference

Rotax 912 ULS/S) and ensuring a smooth torque delivery that minimizes propeller stress and vibration.

The Bore-to-Stroke ratio (B/S) was defined according to the following design considerations:

- Values of B/S < 1 reduce the work required for charging and improve scavenging efficiency.
- Excessively long strokes, however, increase mean piston speed and inertia loads, reducing durability.

Assuming a maximum mean piston speed of 13.5 m/s at 5000 rpm (typical for automotive Diesel engines), the stroke limit is about 81 mm. For a unit displacement of 262.5 cm³ (1050/4), this yields a bore of 64.2 mm (B/S ≈ 0.79). After iterative optimization, the final dimensions were fixed at 65 mm × 79.5 mm, corresponding to B/S = 0.82 and a total displacement of 1055 cm³.

Given the absence of crankcase pumping, turbocharging was deemed unsuitable: the engine requires positive pressure for self-starting and steady scavenging even at idle. A mechanical supercharger was therefore adopted, driven by the crankshaft through a gear train. Two-stage boosting systems previously studied for automotive downsizing [158,159] were discarded because of their excessive weight and complexity for this power class.

The supercharger was selected and sized based on the airflow demand at rated power (70 kW @ 5000 rpm). Assuming a Brake Specific Fuel Consumption (BSFC) of 240 g/kWh, supported by preliminary 0D/1D-3D-CFD results, the corresponding fuel mass flow is:

$$\dot{m}_{fuel} = 240\ \left[\frac{g}{kWh}\right] \times \frac{70\ [kW]}{1000} = 16.8 \frac{kg}{h} \tag{25}$$

The 3D-CFD combustion analyses indicated that a trapped-air-to-fuel ratio ≥ 20 is required for complete and efficient combustion. Assuming a trapping efficiency of 80 %, the required air mass flow becomes:

$$\dot{m}_{air} = 16.8\ \left[\frac{kg}{h}\right] \times \frac{20}{0.8} = 420\ \left[\frac{kg}{h}\right] = 0.117 \frac{kg}{s} \tag{26}$$

With an ambient air density of 1.2 kg/m³, the corresponding delivery ratio DR can be evaluated as:

$$\lambda_D = \frac{0.117}{1.2 \times 1.055 \times 5000/60000} = 1.11 \quad (27)$$

A DR slightly above unity indicates that the scavenging process in the proposed engine operates under conditions comparable to those of a tuned crankcase-scavenged 2S engine. This similarity allowed the application of well-established empirical design rules from conventional 2S development, reducing the number of parameters requiring detailed CFD optimization.

Two alternatives for the mechanical supercharger were considered: positive-displacement and centrifugal types. Although their predicted performance was comparable, the centrifugal compressor was ultimately preferred for its lower weight and simpler integration within the compact engine bay of the ultralight aircraft.

To improve the reliability of the CFD models employed in the development of the 2S Diesel engine for UAV applications, a specific spray calibration was performed using experimental data from the Engine Combustion Network (ECN – Spray A, Sandia National Laboratories [160]). This activity, carried out within a parallel Master's thesis under the supervision of the author, provided a validated spray sub-model for low-pressure Diesel injection (250–500 bar) [161]. The calibrated model ensures accurate liquid and vapor penetration prediction, supporting the subsequent combustion and chamber-geometry optimization analyses. The results of the spray analysis are reported in the appendix A.

The combustion chamber design study was conducted as a supporting activity aimed at identifying an efficient geometry for a 2S Diesel UAV engine operating with low injection pressures. The 3D-CFD campaign compared three alternative chamber shapes (two truncated-conical and one bowl-type configuration), highlighting the influence of turbulence and mixture formation on combustion efficiency. The final bowl-type chamber demonstrated the highest combustion efficiency ($\eta_c = 0.97$) and the lowest BSFC (239 g/kWh), validating the design choices adopted in the present work. The results about the combustion chamber geometry optimization are reported in appendix B.

The principal design data of the optimized two-stroke compression ignition engine are summarized in Table 38.

Table 38: Design data of the optimized 2S compression ignition engine.

Parameter	Value
Total displacement	1055 cm³
Cylinders / layout	4, boxer
Stroke	79.5 mm
Bore	65 mm
Bore-to-stroke ratio	0.82
Geometric compression ratio	24 : 1
Scavenging type	Loop, valveless
Scavenge ports timing (advance/delay from BDC)	53 °/ 53 ° CA
Exhaust ports timing (advance/delay from BDC)	72 °/ 72 ° CA
Supercharging system	Mechanical centrifugal compressor
Max. corrected mass flow rate (compressor)	0.275 kg/s
Fuels	Diesel, kerosene, Jet fuel (JP8)
Max. injection pressure	350 bar
Lubrication system	Dry-sump
Operating speed range	2000 – 5000 rpm

7.3. Weight and dimensions of the HPU

In order to ensure a seamless integration with existing ultralight aircraft architectures, the newly developed HPU was designed to replace the stock engine without requiring major modifications to the fuselage or the aircraft's weight distribution. Consequently, the overall dimensions of the HPU must be equal to or smaller than those of the original engine, while maintaining a comparable total mass. The same constraint applies to the heat exchangers, which must preserve the original installation space; therefore, the total heat rejection of the new HPU should not exceed that of the reference unit.

It is worth noting that the thermal efficiency of the internal combustion engine plays a crucial role in determining the overall aircraft weight. For a given mission range, a higher efficiency results in lower fuel consumption, smaller fuel tanks, and consequently, a higher available payload.

All components of the proposed 2S engine were designed according to standard engineering practice, supported by empirical considerations based on the authors' experience. Table 39 summarizes the adopted safety coefficients for the main elements of the crank mechanism (pin, connecting rod, crack shaft) highlighting the sections used for stress evaluation.

Table 39: Components safety coefficients:

Component	Section	Safety Coefficient
Pin	Maximum shear stress section	1.46
Connecting rod	Minimum rod section (normal stress)	1.46
Connecting rod	Journal cross section (bending-torsion stress)	1.42

Once the design of all components, materials, and manufacturing processes was completed, the weight assessment was carried out using the Parametric Creo CAD software (Student Edition [162]). A full 3D model of the engine assembly was developed from scratch, allowing a precise estimation of the overall engine dimensions and total mass. Figure 96 presents the perspective view of the 2S engine, while Table 40 reports the detailed mass breakdown of the main subsystems.

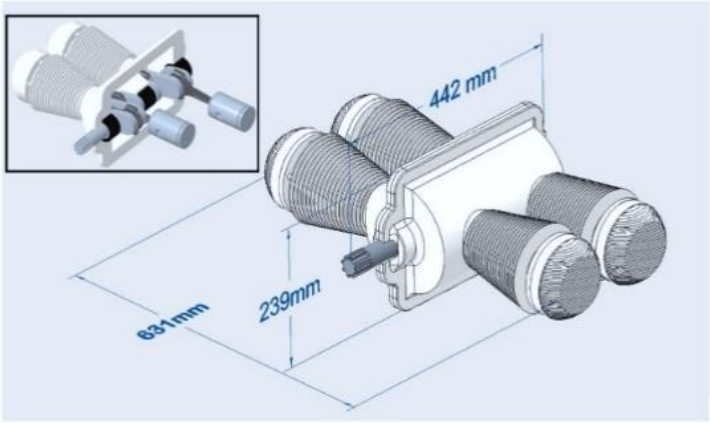

Figure 96: 2S Engine perspective view and size information.

Table 40: Components weight breakdown of the 2S engine and hybrid configuration.

Group level 0	Group level 1	Group level 2	Mass [kg]	Units [-]	Components mass [kg]	Subsystem mass [kg]
Thermal engine	Crankshaft	Piston & Pin	0.41	4	1.64	38.9
		Connecting Rod	0.41	4	1.64	
		Shaft & Bearings	8.25	1	8.25	
	Engine case	Cylinder block	7.72	2	15.43	
		Head	1.06	4	4.24	
	Supercharging system	Compressor & gears	5.10	1	5.10	
	Injection system	Injector & Rail	0.40	4	1.60	
		HP Pump	1.00	1	1.00	
Electric system	Electric motor	–	7.50	1	7.50	22.9 (28.2)
	Inverter	–	2.70	1	2.70	
	Battery (BMS & case)	–	7.88 (13.14)	1	7.88 (13.14)	
	Electrical wiring	–	4.86	1	4.86	

Configuration	Total mass [kg]
HPU 1.4kWh battery configuration	61.8
HPU 2.4 kWh battery configuration	67.1

The overall dimensions of the thermal unit are considerably smaller than those of the Rotax 912 ULS/S reference engine [151], leaving sufficient room within the fuselage for integrating the electric components (motor, inverter, battery, and wirings). While the Rotax 912 ULS/S weighs approximately 60 kg, the new HPU reaches 61.8 kg or 67.1 kg, depending on the selected battery configuration (BP_A or BP_B). As demonstrated in the following sections, this slight increase in curb weight is largely offset by a substantial improvement in fuel economy.

From a performance perspective, both HPU configurations demonstrate competitive power-to-weight ratios. Figure 97 compares the results for four cases: the standalone 2S engine, the two hybrid configurations (with different battery capacities), and the Rotax 912 ULS/S engine. Two weight scenarios were considered:

- W/O_Tank: excluding the fuel tank weight;
- W_Tank: including a 100 L tank.

Assuming a 30% reduction in fuel consumption for the HPU compared to the Rotax engine, the equivalent fuel weight for the same mission decreases from 77 kg of gasoline to 54 kg of diesel. Consequently, when the tank is included, the HPUs show significantly improved power-to-weight ratios:

- +31% for the 1.4 kWh configuration,
- +38% for the 2.4 kWh configuration, compared to the Rotax reference.

Moreover, the 2S engine alone exhibits a +40% advantage in power-to-weight ratio relative to the Rotax (curb weight basis), although its maximum power output is slightly lower at this stage of development. The HPUs with fuel tank show higher power-to-weight ratios compared to the Rotax engine, with a 31% increase for the 1.4 kWh battery configuration and a remarkable 38% increase for 2.4 kWh battery configuration.

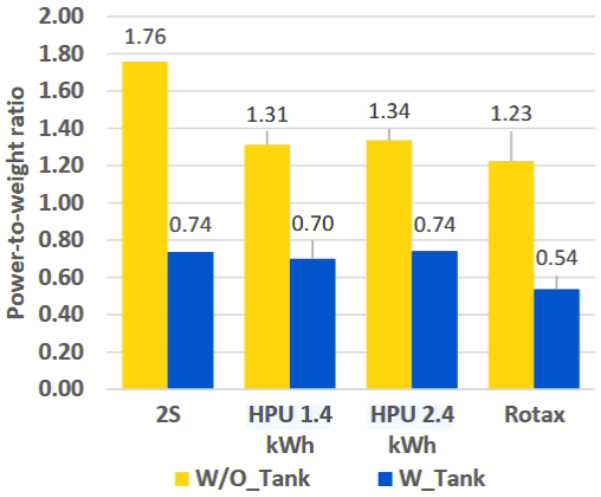

Figure 97: Power-to-weight ratio comparison among power units with and without tank (W_Tank, W/O_Tank).

7.4. 0D/1D-CFD analyses and optimization results

Computational Fluid Dynamics (CFD) simulations represent an essential tool for modern engine development. In the present work, given the absence of experimental data on the newly designed power unit, the numerical approach was not only supportive but foundational to the design process. The methodology adopted in this study follows consolidated practices widely reported in literature [163–165] and can be regarded as a standard engineering workflow for preliminary engine design. Although the lack of direct experimental validation introduces some degree of uncertainty, all numerical sub-models implemented here have been calibrated and validated in previous research activities involving comparable compression-ignition engines.

In particular, the model configuration for the scavenging process and supercharging system was derived from the validated setup described in [157], which employs the same port geometry and mechanical compressor architecture. The physical models used (covering turbulence, heat transfer, and combustion) refer to established formulations that have been extensively verified in similar operating conditions. Therefore, the numerical predictions reported in this section can be considered reliable for the intended design purpose.

The optimization campaign was primarily based on 0D/1D-CFD simulations performed in GT-Power, supported by preliminary 3D CFD analyses that guided the definition of the cylinder geometry and combustion chamber layout. The objective of the 1D campaign was to identify the best trade-off between maximum power and BTE, within the mechanical constraints of the 2S architecture.

Boundary conditions were set according to the International Standard Atmosphere (ISA): ambient temperature of 15 °C and pressure of 1.013 bar. The peak in-cylinder pressure was limited to 100 bar, while a minimum target brake power of 65 kW defined the upper engine speed boundary.

The optimization variables included:

- Scavenge and exhaust port timing (opening/closing heights);
- Transmission ratio between the engine and the mechanical supercharger;
- Layout and dimensions of the exhaust system (pipe lengths, junction volumes, silencer chambers);
- Geometry of the intake manifold between the supercharger and cylinders.

Because of the strong coupling among these parameters, the optimization relied on an iterative Design of Experiments (DOE) process, schematically represented in Figure 98.

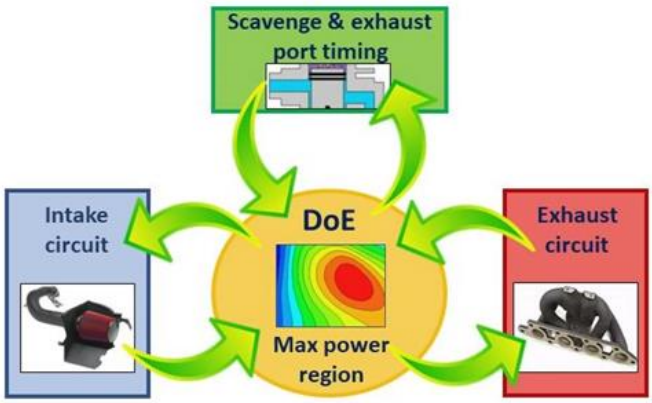

Figure 98: Flow diagram of the 0D/1D-CFD optimization process.

The resulting performance maps are shown in Figure 99, which depict the BSFC and BMEP as functions of engine speed and brake power. The full-load curve of the 2S engine and the propeller load curve of the Falco EVO aircraft (equipped with the Rotax 912 ULS/S) are also superimposed for direct comparison. The region between these curves identifies the effective operating window for aircraft use.

The analysis revealed that the 2S Diesel engine can sustain the propeller load up to 4230 rpm, corresponding to 58 kW, beyond which the electric motor contributes a limited assistance of ≈ 5 kW to match the 73.5 kW peak power of the Rotax during take-off.

Across the relevant operating field, BSFC values range between 230–240 g/kWh, with local extrema of 220 g/kWh (best case) and 265 g/kWh (worst case). These results confirm the high fuel efficiency

of the proposed 2S concept compared with the Rotax 912 ULS/S, as summarized in Table 41 along the propeller curve.

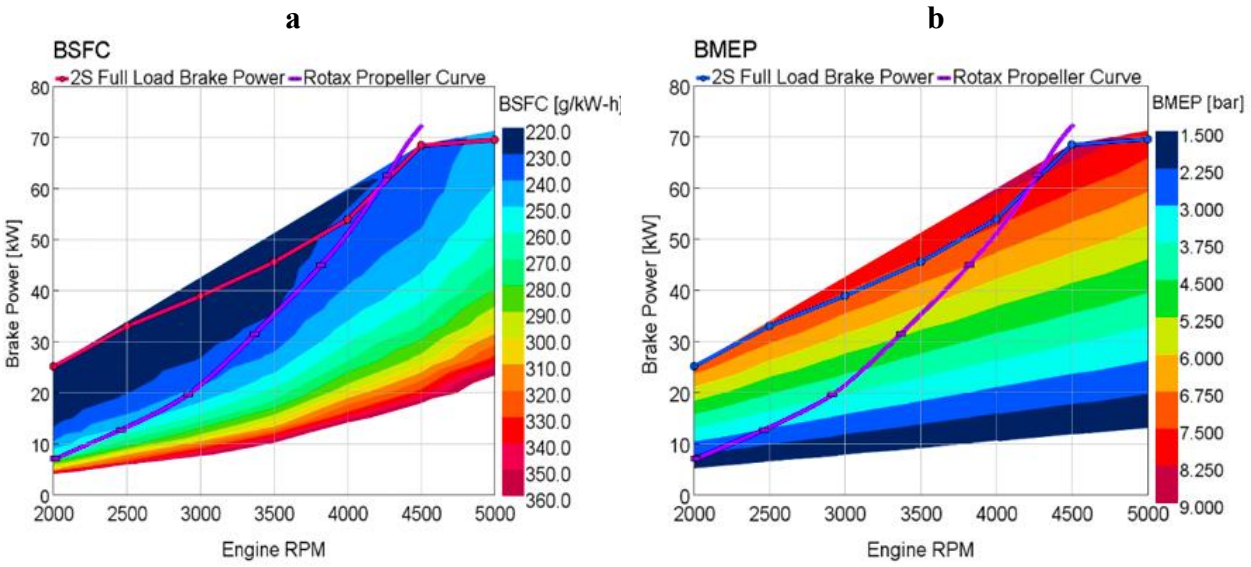

Figure 99: BSFC map and BMEP map (a, b respectively) including engine max power curve and propeller resistance curve.

Table 41: Comparison of BSFC between the proposed 2S engine and the Rotax 912 ULS/S under propeller-load conditions.)

% of max propeller power	Rotax 912 ULS/S speed	2S speed	Propeller power	Rotax 912 ULS/S power	2S power	Rotax 912 ULS/S BSFC	2S engine BSFC
[%]	[rpm]	[rpm]	[kW]	[kW]	[kW]	[g/kWh]	[g/kWh]
100	5800	4500	73.5	73.5	68.4	282.3	**232**
90	5600	4350	66.1	66.1	64.0	305.0	**232**
75	5270	4100	55.1	55.1	55.1	321.0	**233**
60	4880	3790	44.1	44.1	44.1	331.0	**233**
50	4560	3550	36.7	36.7	36.7	344.0	**233**
40	4240	3300	29.4	29.4	29.4	364.0	**235**

In terms of mean effective pressure, the operating range of interest (between propeller and full-load curves) is characterized by BMEP values from 2 to 8.7 bar, which indicates a low thermomechanical stress on the cylinder components. This aspect is very positive, as low values of BMEPs generally correspond to a low level of thermal stress on the cylinder components. Moreover, for the proposed 2S engine there is no need to distinguish between take-off and continuous operating conditions.

Since aircraft propulsion units must operate across a wide altitude range, additional simulations were performed under ISA conditions at different altitudes. Two representative cases were selected: 10 000 ft (≈ 3000 m), corresponding to a typical cruise level, and 26 000 ft (≈ 8000 m), approximately the ceiling of this aircraft class.

The results showed that the 2S engine exhibits a similar power-loss trend with altitude as the Rotax 912 ULS/S. Figure 100 report the absolute and relative variations of maximum power versus altitude. These graphs clearly illustrate the beneficial role of hybridization: at 23 000 ft, the hybrid system with the 2.4 kWh battery pack delivers ≈ 50 kW, compared to only 30 kW from the Rotax under take-off conditions.

Given that take-off typically lasts less than 5 minutes, and that the electric motor operates at roughly two-thirds of its continuous-power limit, no major thermal issues are expected for the electrical system even at high altitudes, despite reduced air density.

The operating points of the engine at full load and 26 000 ft are reported on the compressor map (Figure 101). All points remain in the region of high efficiency, safely distant from both the surge and choke limits, even when increasing the maximum engine speed from 4500 to 5500 rpm.

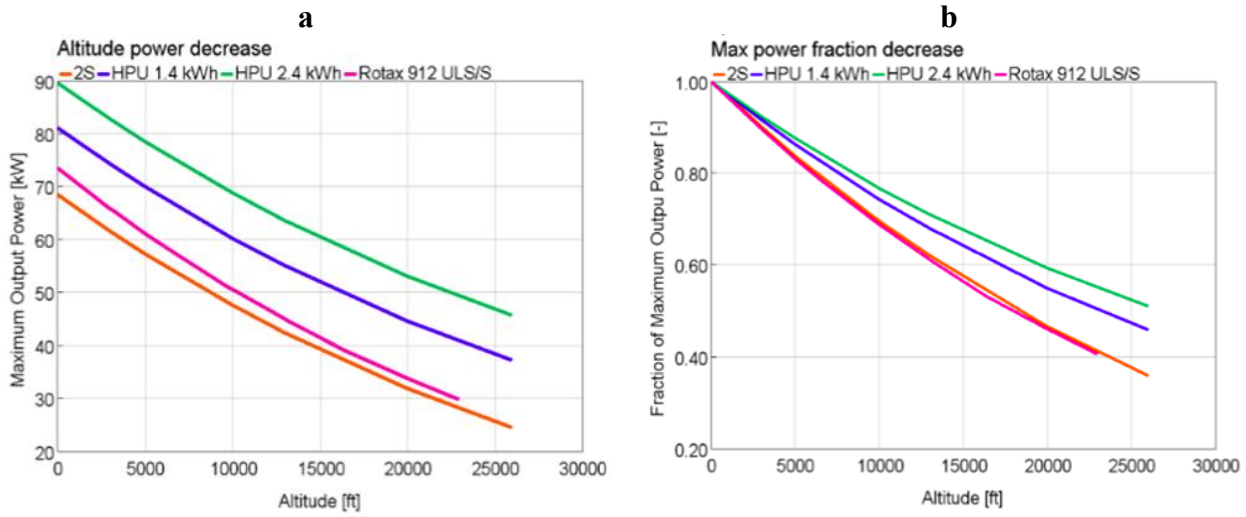

Figure 100: Altitude effect comparison among the studied power unit: a) Maximum output power vs altitude, b) Max power fraction vs altitude.

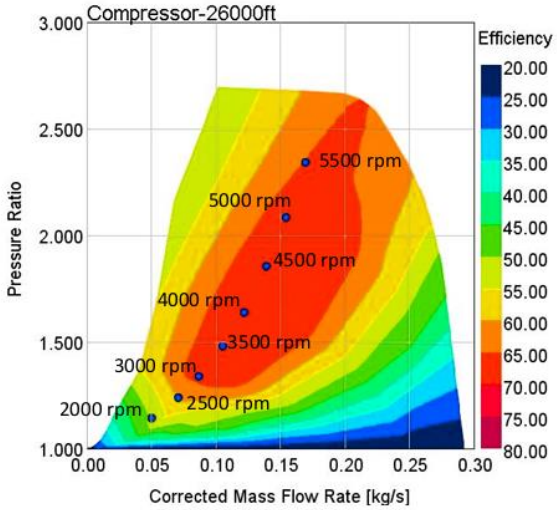

Figure 101: Compressor map with engine operation points at full load and 26000 ft altitude.

Table 42: Main parameters and efficiency comparison among the 2S engine, HPUs, and Rotax 912 ULS/S)

Power unit	Dry mass	Max continuous power	Peak power	Max BMEP	BTE* @ max cont. power	BTE* @ peak power	Mean piston speed @ peak power
	[kg]	[kW@rpm]	[kW@ rpm]	[bar]	[%]	[%]	[m/s]
2S engine	39	68.4 @ 4500	68.4 @ 4500	8.65	35.7	35.7	11.9
HPU 1.4 kWh	62	78.3 @ 4500 (*)	81.1 @ 4500 (**)	8.65	38.3 (HL = 0.19)	39.0 (HL = 0.24)	11.9
HPU 2.4 kWh	67	84.9 @ 4500 (*)	89.6 @ 4500 (**)	8.65	39.9 (HL = 0.25)	40.9 (HL = 0.31)	11.9
Rotax 912 ULS/S	60	69 @ 5500	73.5 @ 5800	11.9	28.8 (HL = 0)	29.0 (HL = 0)	11.8

(*) Power available for 5 minutes (limit due to battery capacity)
(**) Power limited by the battery thermal resistance

Table 42 summarizes the main performance and efficiency indicators for the analysed configurations:

- the stand-alone 2S engine,
- two hybrid power units (HPU) with 1.4 kWh and 2.4 kWh batteries,
- and the Rotax 912 ULS/S reference.

In the hybrid systems, the introduction of electrical components slightly increases dry mass (+2 kg for the 1.4 kWh and +7 kg for the 2.4 kWh configuration), but simultaneously provides significant performance gains. Peak power rises by +10% and +22%, respectively, while continuous-power capability remains comparable to the Rotax.

Thermomechanical loads are modest: mean piston speed at peak power (≈ 11.9 m/s) matches the reference, and maximum BMEP is 27% lower, implying improved durability margins.

To quantify overall efficiency, a corrected Brake Thermal Efficiency (BTE*) was defined as:

$$BTE^* = \frac{P_{ICE} + P_{EM}}{P_{fuel} + P_{batt}} \quad (28)$$

As visible in equation (*28*), BTE* takes into account not only the energy associated to the fuel consumed, but also the electrical energy taken from the battery. It is supposed that this energy is stored in the battery via an external charger, before take-off. As the product of the efficiencies of battery, inverter and electric motor is much higher than the BTE of the thermal engine, the higher is HL, the higher BTE*.

Under these assumptions, both HPUs exhibit markedly higher efficiency than the Rotax engine: the maximum improvement at peak power is +41%, corresponding to a proportional reduction in CO_2 emissions, assuming renewable electricity for charging. Even in the worst-case scenario (battery recharged via the 2S engine) the hybrid system remains more efficient than the conventional solution. It is important to note that the results presented in this study are inherently dependent on the underlying assumptions regarding the primary source of electrical energy. In particular, overall efficiency and fuel consumption may vary depending on the battery charging strategy adopted during the mission profile, as well as on other operational factors not addressed in the present work. A detailed optimization of these aspects lies beyond the scope of this study but represents an important topic for future investigation.

The full-load power curves (Figure 102) indicate that the 2S engine alone satisfies propeller power up to 2230 rpm, with electric support required only above this threshold. The HPU 2.4 kWh consistently exceeds the Rotax power output across all propeller speeds.

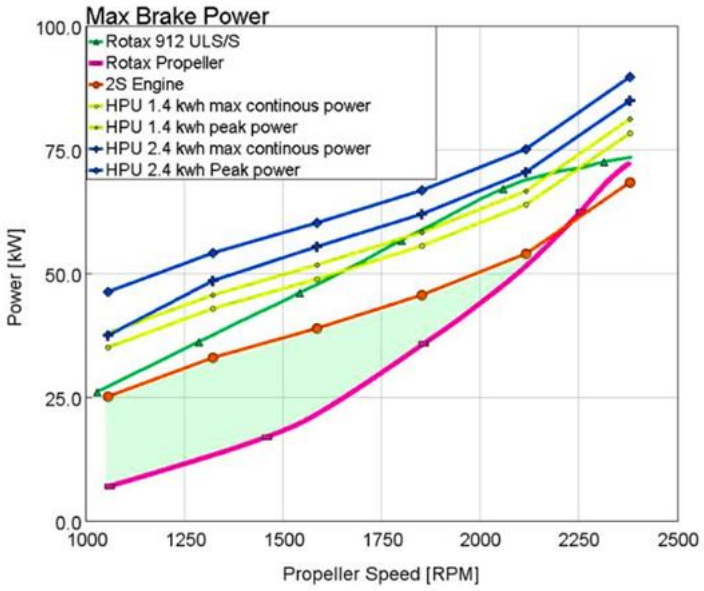

Figure 102: full load power curves.

At take-off, the HPU 1.4 kWh can sustain the 73.5 kW Rotax-equivalent power for 10 min 24 s, more than twice the conventional 5-minute limit. Alternatively, it can provide +6.5% higher power (≈ 78 kW) for 5 minutes. The HPU 2.4 kWh extends endurance even further, delivering 73.5 kW for 17 min 24 s or up to 84.5 kW (+15%) for 5 minutes.

These extended-power capabilities could significantly reduce climb time or enhance safety margins during take-off in high-altitude operations.

Table 43: Summary of power unit performance

Power unit	**Time range @ 73.5 kW**	**Max power for 5 min duration**
		[kW]
HPU 1.4 kWh	5 min	73.4
HPU 2.4 kWh	10 min 24 sec	78.3
Rotax 912 ULS/S	17 min 24 sec	84.5

The analysis of fuel and energy consumption (Figure 103) shows that electrical assistance is required only above 58 kW, while in the 55–75% propeller-power range (typical cruise regime) the hybrid system operates with zero electric propulsion and achieves a 28% reduction in fuel consumption. This improvement translates directly into a 28% increase in aircraft range without structural changes. Alternatively, maintaining the same range allows for a payload gain of ≈ 30 kg, considering the fuel mass saving, an appreciable advantage for ultralight aircraft such as the Falco EVO (maximum payload ≈ 100 kg). Further benefits arise from the electrical subsystem itself, which can supply

onboard avionics and equipment, removing the need for separate heavy-duty alternators and conventional lead-acid batteries.

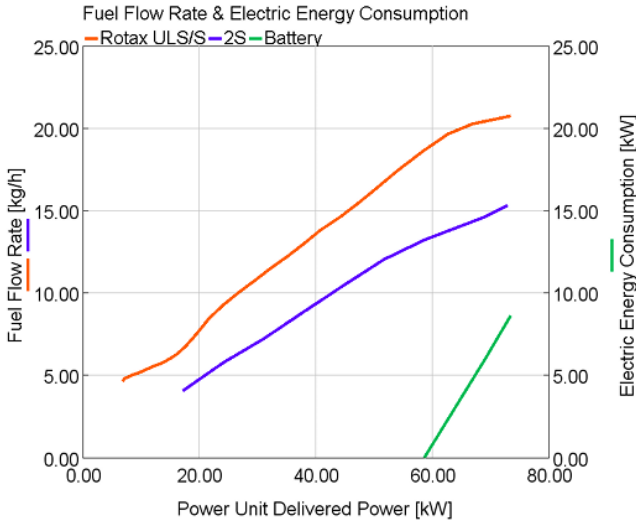

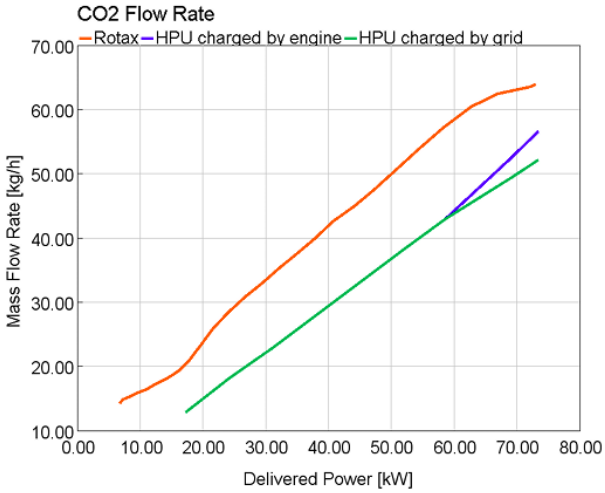

Figure 103: Fuel flow rate & electric energy consumptionFigure 104: CO2 mass flow rates comparison. comparison.

Table 44: CO2 emission factor adopted hybrid and Rotax power units.

Energy source	**Reference**	**CO_2 emission factor**
Gasoline	[23]	3.08 kg CO_2 / kg fuel
Kerosene	[23]	3.16 kg CO_2 / kg fuel
Electricity	[166]	0.48 kg CO_2 / kWh

Table 45: Efficiency factors adopted for the hybrid power unit energy balance.

Parameter	**Description**	**Value**
η_{ICE}	Internal combustion engine efficiency	Depends on ICE operating point
η_{grid}	Electrical grid efficiency	0.93
η_{EM}	Electric motor efficiency	0.90
η_{Batt}	Battery efficiency during discharge	0.90 [167]
η'_{Batt}	Battery efficiency during charge	0.90 [167]
η_{inv}	Inverter efficiency	0.95

Finally, the environmental impact of the analysed configurations was assessed through the CO_2 mass-flow rate (Figure 104). Emission factors adopted for gasoline, kerosene, and electricity are summarized in Table 44, while Table 45 lists the efficiency coefficients for the various energy-conversion processes.

The results highlight a CO_2 reduction of up to 37% for the hybrid configurations compared to the Rotax engine, with a minimum gain of 16%, depending on the energy source used for recharging. Figure 105 illustrates the energy pathways for the two charging strategies: ICE-based and grid-based. The grid-charging mode, involving fewer conversion steps, obviously yields higher overall efficiency and lower emissions.

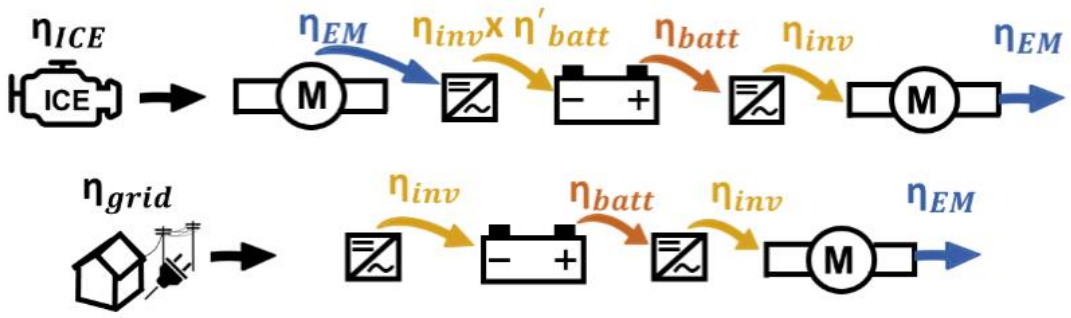

Figure 105: Energy chain for ICE recharging mode (up) and grid recharging mode (down).

The CFD-guided optimization and performance analysis demonstrated that the newly developed 2S Diesel engine, both in stand-alone and hybrid configurations, provides substantial gains in efficiency, performance flexibility, and sustainability compared with a conventional gasoline engine of equivalent size.

In particular:

- Fuel consumption reductions of up to 28%,
- CO_2 emission reductions of 16–37%,
- and a 41% improvement in corrected thermal efficiency (BTE*) at peak power confirm the feasibility of a lightweight hybrid power unit as a viable propulsion concept for ultralight and UAV applications.

These results support the overarching thesis perspective that Diesel-based technologies, when properly optimized and hybridized, remain key enablers of intelligent, low-carbon mobility.

7.5. Conclusions and final remarks

The research activity presented in this chapter represents the final stage of the broader investigation carried out in this doctoral work, which aimed at exploring and developing technological solutions capable of reducing the environmental impact of Diesel-based propulsion systems across different

application domains (from heavy-duty engines and dual-fuel configurations to advanced hydrogen and hybrid systems).

Within this framework, the study focused on the design and performance assessment of an innovative hybrid power unit (HPU) for ultralight aircraft, conceived to replace a conventional 4S spark-ignition gasoline engine (such as the Rotax 912 ULS/S) with minimum weight penalty and no modification to the aircraft structure, while operating on Jet-A or Diesel fuels. The power unit integrates a newly developed 2S compression-ignition Diesel engine, featuring piston-controlled ports and air scavenging assisted by a compact mechanical supercharger, with a high-efficiency axial-flux electric motor and a lithium NMC battery system.

The 2S architecture was selected for its inherent advantages in terms of power-to-weight ratio, simplicity, and mechanical efficiency, which allowed compensating for the additional mass of the hybrid components. The adoption of a valveless design, a dry-sump lubrication system, and the elimination of liquid cooling contributed to a substantial mass reduction of the thermal engine, estimated at 38.9 kg, more than 20 kg lighter than the Rotax 912 ULS/S reference. This weight advantage was exploited to integrate the electrical components (motor, inverter, and battery) without compromising the total mass of the propulsion system: depending on battery capacity, the final dry weight of the HPU exceeded that of the Rotax engine by only 2 to 7 kg.

The design of the combustion system, developed through3D-CFD simulations and based on a high-compression compact chamber geometry, was identified as the main innovation of the thermal unit. Although the detailed configuration remains confidential, the numerical results confirmed efficient Diesel combustion at moderate injection pressures (50–350 bar), enabling low fuel consumption and stable operation over a wide speed range.

Extensive 0D/1D-CFD analyses supported the optimization of the gas-exchange system, supercharger matching, and exhaust layout, under the constraint of maintaining peak cylinder pressures below 100 bar. The optimized 2S Diesel engine achieved a maximum brake power of 68.4 kW at 4500 rpm and exhibited a Brake Specific Fuel Consumption (BSFC) between 230–240 g/kWh, corresponding to a 28% reduction in fuel consumption compared to the Rotax 912 ULS/S at equivalent operating points.

When integrated within the hybrid configuration, the system demonstrated even greater benefits. Depending on the selected battery pack:

- The HPU 1.4 kWh provided +6.5% peak power for 5 minutes or maintained 73.5 kW for 10 minutes 24 seconds;

- The HPU 2.4 kWh delivered +15% peak power for 5 minutes or sustained the same output for 17 minutes 24 seconds.

These results highlight the potential of the hybrid power unit to enhance take-off performance, extend climb duration, and increase operational safety margins. Moreover, in typical cruise conditions (55–75% of maximum propeller power), the hybrid system achieved 28% lower fuel consumption, translating into a comparable increase in aircraft range or, alternatively, an increase of approximately 30 kg in payload without altering total mass or performance.

The environmental benefits are equally significant: depending on the charging strategy and electricity source, the CO_2 emission reduction ranged from 16% to 37% relative to the conventional gasoline-fuelled engine. These improvements stem from both the higher thermodynamic efficiency of the Diesel cycle and the superior energy conversion efficiency of the hybrid powertrain.

The results are inherently dependent on the assumptions regarding the primary energy source and the mission-specific charging strategy, which were not the focus of this study. Nevertheless, even under conservative conditions (where battery recharging is performed by the onboard thermal engine) the hybrid units maintain a clear efficiency advantage over the reference configuration.

Finally, while the absence of experimental validation introduces some uncertainty, it must be emphasized that all sub-models and methodologies employed in this work are derived from previously validated CFD frameworks developed by the author and collaborators in projects involving experimental data. Moreover, the electric subsystem relies on well-established commercial components, minimizing uncertainty in its performance assessment.

In conclusion, the proposed hybrid power unit demonstrates that Diesel-based technologies, when properly redesigned and hybridized, can effectively meet the dual challenge of performance and sustainability in light aviation. This study therefore reinforces the central message of the entire doctoral research: rather than being an obsolete technology, the Diesel engine (adapted through advanced combustion concepts, alternative fuels, and hybrid architectures) can remain a key enabler of the transition toward intelligent and low-carbon mobility, spanning from road to marine and aerial applications.

8. Conclusion

This thesis set out to lower the environmental impact of Diesel-based propulsion while preserving range, robustness, and affordability. Two complementary routes were pursued (alternative fuels and hybridization) within a calibrated 0D/1D–3D-CFD workflow (GT-Power coupled to AVL FIRE-M). The outcome is a staged, engineering-credible direction for decarbonizing applications where ICE remain essential.

This thesis begins with a system-level analysis on a 12.9-L heavy-duty Diesel engine, rated at 420 kW @ 1800 rpm in its Diesel configuration and 330 kW @ 1800 rpm in the CNG configuration used as reference. Within this fixed platform, biodiesel/HVO behaves as a true drop-in, preserving the Diesel power target (~420 kW @ 1800 rpm) and delivering the highest observed efficiency among the fuel used in this power unit ($BTE_{max} \approx 44\%$), albeit with reliance on complex aftertreatment and sustainable feedstocks. Bio-methane can be readily integrated in spark-ignited CNG architectures exploiting a simple aftertreatment system but is constrained by the lower rated power of the CNG setup (~330 kW @ 1800 rpm) and a lower peak efficiency ($BTE_{max} \approx 37\%$), with more demanding storage than liquids. Green hydrogen was modelled to match the CNG power level by design (~330 kW @ 1800 rpm) while approaching Diesel-like efficiency but in spark ignition configuration ($BTE_{max} \approx 43.8\%$). Using green hydrogen in lean or ultra-lean mixture, it offers near-zero CO_2 with low NO_x emissions (< 20 ppm). Together, these findings push hydrogen-focused solutions as a realistic path to medium- and long-term decarbonization, as long as air-handling and combustion are carefully controlled.

Building on the baseline calibration, Diesel–Hydrogen dual-fuel operation was investigated on a light-duty compression ignition engine at two operating points: low load (2400 rpm, 10.5 bar BMEP) and high load (4000 rpm, 13.5 bar BMEP). At low load, increasing the Hydrogen Energy Share (HES) improves IMEP* up to ≈40% HES thanks to faster, more thermodynamically efficient heat release; beyond this point, IMEP* declines and reaches its minimum at 80% HES due to reduced combustion efficiency from incomplete oxidation of the premixed hydrogen-air charge and wall quenching. Advancing the diesel injection further enhances performance at low HES, and at higher shares recovering most of the IMEP* losses. At high load, hydrogen substitution raises peak pressure and Peak Pressure Rise Rate (PPRR), frequently approaching structural limits; retarding SOI is therefore required, and an optimal SOI was identified for each HES to keep both peak pressure and PPRR within mechanical constrains. Representative optima include 40% HES with ΔSOI = +2.55°CA (maximizing IMEP* +6.4% vs. Diesel) and 78.4% HES with ΔSOI = +6°CA (enabling the maximum feasible HES under the imposed constraints with a modest IMEP* gain of +2.96% and a slight

efficiency decrease). Across both loads, the diesel injection law governs not only ignition onset but the entire heat-release phasing: by appropriately advancing or retarding the diesel injection, the combustion maintains CA50 ≈ 10° ATDC, containing peak pressure and PPRR. Overall, the optimized strategy enabled HES up to ~80% while respecting mechanical and acoustic limits, and it set the stage for the subsequent optimization steps that lifted HES further to 86% with stable, efficient combustion.

On this basis, a separate effort on a modified compression-ignition engine set up for diesel–hydrogen dual-fuel operation, an experimental/numerical campaign (0D/1D and 3D-CFD) examined the effect of igniting the hydrogen-air mixture with just one diesel pilot injection. Load-sweep tests showed that at low load hydrogen combustion becomes unstable and incomplete, making diesel-only operation the only configuration that guarantees reliable ignition, for this reason baseline two injection strategy was kept unchanged. At medium load, halving the main injection increased Gross Indicated Efficiency (GIE) by ~3% and substantially cut diesel (−33%), CO_2 (−32%), CO (−55%), and NOx (−7%). At higher loads (not full load), the main injection can be removed with only a small efficiency penalty (≈−1.8%), still delivering >60% reductions in diesel and CO_2, ~80% in CO, and ~30% in NO_x with respect to the dual fuel baseline case. Despite a slight rise in average in-cylinder temperature due to faster hydrogen combustion, NO_x continues to decrease as the main diesel is reduced, consistent with a transition from diffusion-controlled Diesel flames to an ultra-lean, premixed hydrogen–air regime; 3D-CFD analysis confirms more homogeneous temperature fields and the absence of hot spots in the optimized cases. Relative to the numerical study that pushed substitution up to ~80% HES chiefly via timing optimization, this campaign demonstrated that, at medium–to–high load, a single, small pilot sustains stable operation up to 86% HES without breaching mechanical limits.

Conducted at the Centre of Advanced Powertrain and Fuels (CAPF), Brunel University London during the author's international research period, the final stage of the CFD dual-fuel investigation executed a pilot-only optimization on a modified heavy-duty engine at partial load (IMEP = 6 bar) to push the HES toward its operational limit. Relative to a DF baseline at HES 67%, increasing to HES 96% engine delivered a +4.4% gain in GIE with clear reductions in CO_2, CO, and NO_x; extending to HES 98%, identified as the practical upper bound at this operating point, entailed a modest efficiency reduction (GIE −1.2%) but minimized diesel use and practically eliminated NO_x, remaining well within Euro-7-level limits. A very early pilot was calibrated to promote HCCI-like auto-ignition of the diesel, while the overall process remained RCCI with an ultra-lean premixed hydrogen charge. High-fidelity 3D-CFD confirmed the shift from diffusion-controlled Diesel burning to ultra-lean,

premixed hydrogen with more homogeneous temperature fields and suppressed most of the hot spots thanks to the HCCI-like combustion of the diesel fuel, and quantified the associated efficiency and emissions benefits.

To address high-load limitations of dual-fuel operation, the thesis culminates in a full-hydrogen, spark-ignited two-stroke concept derived from a production Diesel engine (Duramax 6.6 L V8) and equipped with poppet valves. Tangentially shrouded intake valves and a shallow piston bowl generate strong tumble and high turbulence, improving mixture homogeneity while limiting short-circuiting. Coupled 0D/1D–3D-CFD optimization of gas exchange, scavenging, mixture preparation and boosting achieves Diesel-comparable full-load performance, near-zero NO_x, and high theoretical efficiency, with limited hardware changes (head/piston/valves) that support credible scalability and a favourable technology-readiness outlook for this solution.

Finally, the thesis extends the analysis to ultralight aviation with an innovative hybrid power unit combining a light weight two-stroke Diesel engine and an axial-flux electric motor with lithium-NMC storage. The engine delivers ~68.4 kW at 4500 rpm with BSFC ≈ 230–240 g/kWh (≈ −28% if compared to a Rotax reference gasoline engine) and weighs ~38.9 kg; the complete hybrid system remains only ~2–7 kg heavier than the Rotax reference engine depending on battery size. The hybridization enables short-duration peak-power (up to –15% more than the reference gasoline engine) and, in cruise (55–75% propeller power), about 28% lower fuel and 16–37% lower CO_2 depending on battery charging strategy, translating into improved take-off/climb margins, extended range, or roughly 30 kg payload gains at constant total mass.

Taken together, these results show that the Diesel architecture remains a solid, adaptable platform for the next generation of low-carbon propulsion. Rather than discarding a technology refined over decades, the thesis demonstrated how to re-engineer Diesel platforms by combining sustainable fuels, progressing from diesel–hydrogen dual-fuel to full-hydrogen concepts, and applying targeted hybridization. This layered approach delivered large CO_2 cuts (with co-benefits on NO_x) while preserving the core virtues of Diesel systems (performance, robustness, efficiency). Ultimately, the Diesel engine is not obsolete: with modern simulation-driven design, advanced combustion, sustainable fuels, and intelligent hybridization, it can remain a relevant and effective pillar of the transport landscape for decades to come.

9. References

[1] Change NGC. Global Surface Temperature | NASA Global Climate Change. Climate Change: Vital Signs of the Planet n.d. https://climate.nasa.gov/vital-signs/global-temperature?intent=121 (accessed September 12, 2025).

[2] Filonchyk M, Peterson MP, Zhang L, Hurynovich V, He Y. Greenhouse gases emissions and global climate change: Examining the influence of CO2, CH4, and N2O. Science of The Total Environment 2024;935:173359. https://doi.org/10.1016/j.scitotenv.2024.173359.

[3] Climate change: global temperature | NOAA Climate.gov 2025. https://www.climate.gov/news-features/understanding-climate/climate-change-global-temperature (accessed September 12, 2025).

[4] Liu L, Greaver TL. A review of nitrogen enrichment effects on three biogenic GHGs: the CO_2 sink may be largely offset by stimulated N_2 O and CH_4 emission. Ecology Letters 2009;12:1103–17. https://doi.org/10.1111/j.1461-0248.2009.01351.x.

[5] Mitchell JFB. The "Greenhouse" effect and climate change. Reviews of Geophysics 1989;27:115–39. https://doi.org/10.1029/RG027i001p00115.

[6] Role of greenhouse gases in climate change n.d. https://doi.org/10.1177/0958305X17706177.

[7] Archer D, Eby M, Brovkin V, Ridgwell A, Cao L, Mikolajewicz U, et al. Atmospheric Lifetime of Fossil Fuel Carbon Dioxide. Annual Review of Earth and Planetary Sciences 2009;37:117–34. https://doi.org/10.1146/annurev.earth.031208.100206.

[8] Hamlington BD, Fournier S, Thompson PR, Marcos M. Sea level rise in 2024. Nat Rev Earth Environ 2025;6:246–8. https://doi.org/10.1038/s43017-025-00667-w.

[9] Dietz T, Shwom RL, Whitley CT. Climate Change and Society n.d.

[10] Mata F, Dos-Santos M, Cano-Díaz C, Jesus M, Vaz-Velho M. The Society of Information and the European Citizens' Perception of Climate Change: Natural or Anthropological Causes. Environmental Management 2025;75:21–32. https://doi.org/10.1007/s00267-024-01961-x.

[11] Wendler F. Climate Change Policy in the EU: From the Paris Agreement to the European Green Deal. In: Wendler F, editor. Framing Climate Change in the EU and US After the Paris Agreement, Cham: Springer International Publishing; 2022, p. 65–117. https://doi.org/10.1007/978-3-031-04059-7_3.

[12] Cifuentes-Faura J. European Union policies and their role in combating climate change over the years. Air Qual Atmos Health 2022;15:1333–40. https://doi.org/10.1007/s11869-022-01156-5.

[13] UNFCCC n.d. https://unfccc.int/ (accessed September 19, 2025).

[14] The Kyoto Protocol | UNFCCC n.d. https://unfccc.int/process-and-meetings/the-kyoto-protocol (accessed September 19, 2025).

[15] The Paris Agreement | UNFCCC n.d. https://unfccc.int/process-and-meetings/the-paris-agreement (accessed September 12, 2025).

[16] COP28. Consilium n.d. https://www.consilium.europa.eu/en/policies/paris-agreement-climate/cop28/ (accessed September 12, 2025).

[17] Fit for 55. Consilium n.d. https://www.consilium.europa.eu/en/policies/fit-for-55/ (accessed September 19, 2025).

[18] Erbach G, Jensen L, Chahri S, Claros E. Towards climate neutrality n.d.

[19] Introduction to Climate Finance | UNFCCC n.d. https://unfccc.int/topics/introduction-to-climate-finance (accessed September 26, 2025).

[20] Bracking S, Leffel B. Climate finance governance: Fit for purpose? WIREs Climate Change 2021;12:e709. https://doi.org/10.1002/wcc.709.

[21] Environment UN. Emissions Gap Report 2024 | UNEP - UN Environment Programme 2024. https://www.unep.org/resources/emissions-gap-report-2024 (accessed September 19, 2025).

[22] Intergovernmental Panel On Climate Change (Ipcc), editor. Transport. Climate Change 2022 - Mitigation of Climate Change. 1st ed., Cambridge University Press; 2023, p. 1049–160. https://doi.org/10.1017/9781009157926.012.
[23] John Heywood - Internal Combustion Engine Fundamentals-McGraw-Hill Education (2018) n.d.
[24] Mollenhauer K, Tschöke H, editors. Handbook of Diesel Engines. Berlin, Heidelberg: Springer Berlin Heidelberg; 2010. https://doi.org/10.1007/978-3-540-89083-6.
[25] Ferrari G, Onorati A, D'Errico G. Internal Combustion Engines. Società Editrice Esculapio; 2022.
[26] Avola MC. 110 Years of Turbocharging n.d.
[27] ABB group. Turbocharging in Switzerland - A history [Online] 2014.
[28] Karabektas M. The effects of turbocharger on the performance and exhaust emissions of a diesel engine fuelled with biodiesel. Renewable Energy 2009;34:989–93. https://doi.org/10.1016/j.renene.2008.08.010.
[29] Knecht W. Some Historical Steps in the Development of the Common Rail Injection System. Transactions of the Newcomen Society 2004;74:89–107. https://doi.org/10.1179/tns.2004.005.
[30] Kocher LE. Cummins 55% Brake Thermal Efficiency Project n.d.
[31] Abani N, Chiang M, Thomas I, Nagar N, Zermeno R, Regner G. Developing a 55+ BTE Commercial Heavy-Duty Opposed-Piston Engine Without a Waste Heat Recovery System. In: Siebenpfeiffer W, editor. Heavy-Duty-, On- und Off-Highway-Motoren 2016, Wiesbaden: Springer Fachmedien; 2017, p. 292–310. https://doi.org/10.1007/978-3-658-19012-5_17.
[32] Crdl T. Research History of High-speed, Direct-injection Diesel Engine Combustion Systems for Passenger Cars 2014.
[33] Cames M, Helmers E. Critical evaluation of the European diesel car boom - global comparison, environmental effects and various national strategies. Environ Sci Eur 2013;25:15. https://doi.org/10.1186/2190-4715-25-15.
[34] Dieselisation in the EEA 2011. https://www.eea.europa.eu/en/analysis/maps-and-charts/dieselisation-in-the-eea (accessed October 7, 2025).
[35] Intergovernmental Panel On Climate Change. Climate Change 2007: Mitigation of Climate Change. Cambridge: Cambridge University Press; 2007. https://doi.org/10.1017/CBO9780511546013.
[36] Trucks & buses. IEA n.d. https://www.iea.org/energy-system/transport/trucks-and-buses (accessed October 7, 2025).
[37] Brouwers A. Lightweight diesel aircraft engines for general aviation. 16th Joint Propulsion Conference, Hartford,CT,U.S.A.: American Institute of Aeronautics and Astronautics; 1980. https://doi.org/10.2514/6.1980-1238.
[38] Continental Aerospace Technologies n.d. https://continental.aero/ (accessed October 8, 2025).
[39] Gęca M, Czyż Z, Sułek M. Diesel engine for aircraft propulsion system. Combustion Engines 2017;169:7–13. https://doi.org/10.19206/CE-2017-202.
[40] Diamond Aircraft n.d. https://www.diamondaircraft.com/en/.
[41] SMA Aero Engines n.d. https://www.sma-aero-engines.com/the-product/sr305-230e-sr305-260e/.
[42] Deltahawk n.d. https://www.deltahawk.com/engines/.
[43] Johnson TV. Diesel Emissions in Review. SAE International Journal of Engines 2011;4:143–57.
[44] Long E, Carlsten C. Controlled human exposure to diesel exhaust: results illuminate health effects of traffic-related air pollution and inform future directions. Part Fibre Toxicol 2022;19:11. https://doi.org/10.1186/s12989-022-00450-5.
[45] Ge C, Peters S, Olsson A, Portengen L, Schüz J, Almansa J, et al. Diesel Engine Exhaust Exposure, Smoking, and Lung Cancer Subtype Risks. A Pooled Exposure–Response Analysis of 14 Case–Control Studies. Am J Respir Crit Care Med 2020;202:402–11. https://doi.org/10.1164/rccm.201911-2101OC.

[46] Johnson BT. Diesel Engine Emissions and Their Control: AN OVERVIEW. Platinum Metals Review 2008;52:23–37. https://doi.org/10.1595/147106708X248750.
[47] Council Directive 91/441/EEC of 26 June 1991 amending Directive 70/220/EEC on the approximation of the laws of the Member States relating to measures to be taken against air pollution by emissions from motor vehicles 1991.
[48] Regulation (EU) 2024/1257 of the European Parliament and of the Council of 24 April 2024 on type-approval of motor vehicles and engines and of systems, components and separate technical units intended for such vehicles, with respect to their emissions and battery durability (Euro 7), amending Regulation (EU) 2018/858 of the European Parliament and of the Council and repealing Regulations (EC) No 715/2007 and (EC) No 595/2009 of the European Parliament and of the Council, Commission Regulation (EU) No 582/2011, Commission Regulation (EU) 2017/1151, Commission Regulation (EU) 2017/2400 and Commission Implementing Regulation (EU) 2022/1362 (Text with EEA relevance) 2024.
[49] The California Low-Emission Vehicle Regulations 2022.
[50] US EPA O. Final Rule for Control of Air Pollution from Motor Vehicles: Tier 3 Motor Vehicle Emission and Fuel Standards 2016. https://www.epa.gov/regulations-emissions-vehicles-and-engines/final-rule-control-air-pollution-motor-vehicles-tier-3 (accessed September 29, 2025).
[51] Bazari DZ, Consultant R. MARPOL Annex VI - Prevention of Air Pollution from Ships n.d.;https://www.rempec.org/en/knowledge-centre/online-catalogue/3-zb-l01-marpol-annex-vi-regulations-final.pdf.
[52] ICAO. ANNEX 16: environmental protection. Https://Ffac.Ch/Wp-Content/Uploads/2020/10/ICAO-Annex-16-Environmental-Protection-Vol-II-Aircraft-Engine-Emissions.Pdf: ICAO; 2017.
[53] Fracarolli Nunes M, Lee Park C. Caught red-handed: the cost of the Volkswagen Dieselgate. JGR 2016;7:288–302. https://doi.org/10.1108/JGR-05-2016-0011.
[54] Robertson JA. The danger of Dieselgate: how Volkswagen's diesel scandal critically damaged the wider market. ASR 2017;3:68–9. https://doi.org/10.1108/ASR-10-2017-0010.
[55] Mądziel M. Future Cities Carbon Emission Models: Hybrid Vehicle Emission Modelling for Low-Emission Zones. Energies 2023;16:6928. https://doi.org/10.3390/en16196928.
[56] European Automobile Manufacturers' Association. New passenger car registrations breakdown by share of diesel 2014.
[57] Vehicles on European Roads 2025.
[58] Fleming KL, Brown AL, Fulton L, Miller M. Electrification of Medium- and Heavy-Duty Ground Transportation: Status Report. Curr Sustainable Renewable Energy Rep 2021;8:180–8. https://doi.org/10.1007/s40518-021-00187-3.
[59] Transport - Energy System. IEA n.d. http://www.iea.org/energy-system/transport (accessed September 30, 2025).
[60] Qazi S, Venugopal P, Rietveld G, Soeiro TB, Shipurkar U, Grasman A, et al. Powering Maritime: Challenges and prospects in ship electrification. IEEE Electrific Mag 2023;11:74–87. https://doi.org/10.1109/MELE.2023.3264926.
[61] Schwab A, Thomas A, Bennett J, Robertson E, Cary S. Electrification of Aircraft: Challenges, Barriers, and Potential Impacts. 2021. https://doi.org/10.2172/1827628.
[62] Cunanan C, Tran M-K, Lee Y, Kwok S, Leung V, Fowler M. A Review of Heavy-Duty Vehicle Powertrain Technologies: Diesel Engine Vehicles, Battery Electric Vehicles, and Hydrogen Fuel Cell Electric Vehicles. Clean Technol 2021;3:474–89. https://doi.org/10.3390/cleantechnol3020028.
[63] Lapuerta M, Armas O, Rodriguezfernandez J. Effect of biodiesel fuels on diesel engine emissions. Progress in Energy and Combustion Science 2008;34:198–223. https://doi.org/10.1016/j.pecs.2007.07.001.
[64] Knothe G. Biodiesel and renewable diesel: A comparison. Progress in Energy and Combustion Science 2010;36:364–73. https://doi.org/10.1016/j.pecs.2009.11.004.

[65] Ram V, Salkuti SR. An Overview of Major Synthetic Fuels. Energies 2023;16:2834. https://doi.org/10.3390/en16062834.
[66] Dell'Aversano S, Villante C, Gallucci K, Vanga G, Di Giuliano A. E-Fuels: A Comprehensive Review of the Most Promising Technological Alternatives towards an Energy Transition. Energies 2024;17:3995. https://doi.org/10.3390/en17163995.
[67] Deng Y, Cao K-K, Wetzel M, Hu W, Jochem P. Carbon-neutral power system enabled e-kerosene production in Brazil in 2050. Sci Rep 2023;13:21348. https://doi.org/10.1038/s41598-023-48559-7.
[68] Dec JE. Advanced compression-ignition engines—understanding the in-cylinder processes. Proceedings of the Combustion Institute 2009;32:2727–42. https://doi.org/10.1016/j.proci.2008.08.008.
[69] Kokjohn SL, Hanson RM, Splitter DA, Reitz RD. Experiments and Modeling of Dual-Fuel HCCI and PCCI Combustion Using In-Cylinder Fuel Blending. SAE International Journal of Engines 2010;2:24–39.
[70] Kokjohn S, Hanson R, Splitter D, Kaddatz J, Reitz R. Fuel Reactivity Controlled Compression Ignition (RCCI) Combustion in Light- and Heavy-Duty Engines. SAE International Journal of Engines 2011;4:360–74.
[71] Li Y, Jia M, Chang Y, Liu Y, Xie M, Wang T, et al. Parametric study and optimization of a RCCI (reactivity controlled compression ignition) engine fueled with methanol and diesel. Energy 2014;65:319–32. https://doi.org/10.1016/j.energy.2013.11.059.
[72] Guan W, Wang X, Zhao H, Liu H. Exploring the high load potential of diesel–methanol dual-fuel operation with Miller cycle, exhaust gas recirculation, and intake air cooling on a heavy-duty diesel engine. International Journal of Engine Research 2021;22:2318–36. https://doi.org/10.1177/1468087420926775.
[73] Cui Y, Liu H, Wen M, Feng L, Wang C, Ming Z, et al. Optical diagnostics and chemical kinetic analysis on the dual-fuel combustion of methanol and high reactivity fuels. Fuel 2022;312:122949. https://doi.org/10.1016/j.fuel.2021.122949.
[74] Zhang H, Zhao Z, Wu J, Wang X, Ouyang W, Wang Z. Investigation of Split Diesel Injections in Methanol/Diesel Dual-Fuel Combustion in an Optical Engine. Energies 2024;17:3382. https://doi.org/10.3390/en17143382.
[75] Pan X, Guan W, Gu J, Wang X, Zhao H. Optimization of the low-load performance and emission characteristics for a heavy-duty diesel engine fueled with diesel/methanol by RSM-NSWOA. Renewable Energy 2025;245:122819. https://doi.org/10.1016/j.renene.2025.122819.
[76] Guan W, Gu J, Pan X, Pan M, Wang X, Zhao H, et al. Improvement of the light-load combustion control strategy for a heavy-duty diesel engine fueled with diesel/methonal by RSM-NSGA III. Energy 2024;297:131190. https://doi.org/10.1016/j.energy.2024.131190.
[77] Fang W, Huang B, Kittelson DB, Northop WF. Dual-Fuel Diesel Engine Combustion With Hydrogen, Gasoline and Ethanol as Fumigants: Effect of Diesel Injection Timing, American Society of Mechanical Engineers Digital Collection; 2013, p. 373–81. https://doi.org/10.1115/ICEF2012-92142.
[78] Effect of Hydrogen Fumigation in a Dual Fueled Heavy Duty Engine 2015-24-2457 n.d. https://www.sae.org/papers/effect-hydrogen-fumigation-a-dual-fueled-heavy-duty-engine-2015-24-2457 (accessed October 2, 2025).
[79] Saravanan N, Nagarajan G. Performance and emission studies on port injection of hydrogen with varied flow rates with Diesel as an ignition source. Applied Energy 2010;87:2218–29. https://doi.org/10.1016/j.apenergy.2010.01.014.
[80] Saravanan N, Nagarajan G, Dhanasekaran C, Kalaiselvan KM. Experimental investigation of hydrogen port fuel injection in DI diesel engine. International Journal of Hydrogen Energy 2007;32:4071–80. https://doi.org/10.1016/j.ijhydene.2007.03.036.

[81] Saravanan N, Nagarajan G. An experimental investigation on manifold-injected hydrogen as a dual fuel for diesel engine system with different injection duration. International Journal of Energy Research 2009;33:1352–66. https://doi.org/10.1002/er.1550.
[82] Mathur HB, Das LM, Patro TN. Hydrogen-fuelled diesel engine: Performance improvement through charge dilution techniques. International Journal of Hydrogen Energy 1993;18:421–31. https://doi.org/10.1016/0360-3199(93)90221-U.
[83] Chintala V, Subramanian KA. An effort to enhance hydrogen energy share in a compression ignition engine under dual-fuel mode using low temperature combustion strategies. Applied Energy 2015;146:174–83. https://doi.org/10.1016/j.apenergy.2015.01.110.
[84] Hanafi Gharehlar H, Ebrahimi M, Hosseinzadeh M, Hosseini S. Hydrogen/diesel RCCI engine performance assessment at low load. International Journal of Hydrogen Energy 2024;58:200–9. https://doi.org/10.1016/j.ijhydene.2024.01.172.
[85] Duan H, Jia M, Xu Z, Li Y, Xia G. Comprehensive analysis of combustion behaviors of hydrogen (H2)/diesel reactivity-controlled compression ignition (RCCI) in a light-duty diesel engine. Fuel 2023;353:129237. https://doi.org/10.1016/j.fuel.2023.129237.
[86] Muncrief R, Sharpe B. Overview of the heavy-duty vehicle market and CO2 emissions in the European Union. Overview of the Heavy-Duty Vehicle Market and CO2 Emissions in the European Union 2015.
[87] Duarte Souza Alvarenga Santos N, Rückert Roso V, Teixeira Malaquias AC, Coelho Baêta JG. Internal combustion engines and biofuels: Examining why this robust combination should not be ignored for future sustainable transportation. Renewable and Sustainable Energy Reviews 2021;148. https://doi.org/10.1016/j.rser.2021.111292.
[88] Kuronen M, Mikkonen S, Aakko P, Murtonen T. Hydrotreated vegetable oil as fuel for heavy duty diesel engines. SAE Technical Papers 2007. https://doi.org/10.4271/2007-01-4031.
[89] COMMUNICATION FROM THE COMMISSION TO THE EUROPEAN PARLIAMENT, THE COUNCIL, THE EUROPEAN ECONOMIC AND SOCIAL COMMITTEE AND THE COMMITTEE OF THE REGIONS A hydrogen strategy for a climate-neutral Europe 2020. https://eur-lex.europa.eu/legal-content/EN/TXT/?qid=1594897267722&uri=CELEX:52020DC0301 (accessed October 9, 2025).
[90] European Clean Hydrogen Alliance - European Commission n.d. https://single-market-economy.ec.europa.eu/industry/strategy/industrial-alliances/european-clean-hydrogen-alliance_en (accessed February 16, 2024).
[91] Cheng X, Baigang S, Zhen H. Investigation on Jet Characteristics of Hydrogen Injection and Injection Strategy for Backfire Control in a Port Fuel Injection Hydrogen Engine. Energy Procedia 2017;105:1588–99. https://doi.org/10.1016/j.egypro.2017.03.508.
[92] Gao J, Wang X, Song P, Tian G, Ma C. Review of the backfire occurrences and control strategies for port hydrogen injection internal combustion engines. Fuel 2022;307. https://doi.org/10.1016/j.fuel.2021.121553.
[93] Duan J, Liu F, Sun B. Backfire control and power enhancement of a hydrogen internal combustion engine. International Journal of Hydrogen Energy 2014;39:4581–9. https://doi.org/10.1016/j.ijhydene.2013.12.175.
[94] Choi Y, Kim J, Park S, Park H, Chang D. Design and analysis of liquid hydrogen fuel tank for heavy duty truck. International Journal of Hydrogen Energy 2022;47:14687–702. https://doi.org/10.1016/j.ijhydene.2022.02.210.
[95] GT-SUITE 2022, Gamma Technologies, Westmont, IL. 2022.
[96] Volza A, Pisapia A, Caprioli S, Rinaldini C, Mattarelli E. Sustainable Fuels for Long-Haul Truck Engines: A 1D-CFD Analysis, Turin, Italy: 2024, p. 2024-37–0027. https://doi.org/10.4271/2024-37-0027.

[97] Motore Camion Cursor 13: Potenza e Affidabilità | FPT Industrial n.d. https://www.fptindustrial.com/it/engines/Onroad/Trucks/CURSOR-13 (accessed October 9, 2025).
[98] Volza A, Scrignoli F, Caprioli S, Mattarelli E, Rinaldini CA. Exploring the Potential of Hydrogen Opposed Piston Engines for Single-Cylinder Electric Generators: A Computational Study. SAE Technical Papers 2023. https://doi.org/10.4271/2023-24-0128.
[99] Bao L, Sun B, Luo Q. Optimal control strategy of the turbocharged direct-injection hydrogen engine to achieve near-zero emissions with large power and high brake thermal efficiency. Fuel 2022;325. https://doi.org/10.1016/j.fuel.2022.124913.
[100] Bao L, Sun B, Luo Q, Li J, Qian D, Ma H, et al. Development of a turbocharged direct-injection hydrogen engine to achieve clean, efficient, and high-power performance. Fuel 2022;324. https://doi.org/10.1016/j.fuel.2022.124713.
[101] EU: heavy-duty: ESC n.d. https://www.transportpolicy.net/standard/eu-heavy-duty-esc/.
[102] Elliott MA, Davis RF. Dual-Fuel Combustion in Diesel Engines. Ind Eng Chem 1951;43:2854–64. https://doi.org/10.1021/ie50504a056.
[103] Wei L, Geng P. A review on natural gas/diesel dual fuel combustion, emissions and performance. Fuel Processing Technology 2016;142:264–78. https://doi.org/10.1016/j.fuproc.2015.09.018.
[104] Nwafor OMI. Effect of advanced injection timing on emission characteristics of diesel engine running on natural gas. Renewable Energy 2007;32:2361–8. https://doi.org/10.1016/j.renene.2006.12.006.
[105] Effect of pilot injection timing, pilot quantity and intake charge conditions on performance and emissions for an advanced low-pilot-ignited natural gas engine n.d. https://doi.org/10.1243/146808704323224231.
[106] Alla GHA, Soliman HA, Badr OA, Rabbo MFA. Effect of injection timing on the performance of a dual fuel engine n.d.
[107] Shioji M, Ishiyama T, Ikegami M, Mitani S, Shibata H. Performance and Exhaust Emissions in a Natural-Gas Fueled Dual-Fuel Engine. JSME International Journal Series B Fluids and Thermal Engineering 2001;44:641–8. https://doi.org/10.1299/jsmeb.44.641.
[108] Fayaz H, Saidur R, Razali N, Anuar FS, Saleman AR, Islam MR. An overview of hydrogen as a vehicle fuel. Renewable and Sustainable Energy Reviews 2012;16:5511–28. https://doi.org/10.1016/j.rser.2012.06.012.
[109] Stępień Z. A Comprehensive Overview of Hydrogen-Fueled Internal Combustion Engines: Achievements and Future Challenges. Energies 2021;14:6504. https://doi.org/10.3390/en14206504.
[110] Mattarelli E, Rinaldini CA, Savioli T. Dual Fuel (Natural Gas Diesel) for Light-Duty Industrial Engines: A Numerical and Experimental Investigation. In: Srinivasan KK, Agarwal AK, Krishnan SR, Mulone V, editors. Natural Gas Engines : For Transportation and Power Generation, Singapore: Springer; 2019, p. 297–328. https://doi.org/10.1007/978-981-13-3307-1_11.
[111]Legrottaglie F, Mattarelli E, Rinaldini CA, Scrignoli F. Application to micro-cogeneration of an innovative dual fuel compression ignition engine running on biogas. International Journal of Thermofluids 2021;10:100093. https://doi.org/10.1016/j.ijft.2021.100093.
[112] Scrignoli F, Vecchio F, Legrottaglie F, Mattarelli E, Rinaldini CA. Numerical Investigation of Dual Fuel Combustion on a Compression Ignition Engine Fueled with Hydrogen/Natural Gas Blends. Fuels 2022;3:132–51. https://doi.org/10.3390/fuels3010009.
[113] Scrignoli F, Pisapia AM, Savioli T, Mancaruso E, Mattarelli E, Rinaldini CA. Exploring Hydrogen–Diesel Dual Fuel Combustion in a Light-Duty Engine: A Numerical Investigation. Energies 2024;17:5761. https://doi.org/10.3390/en17225761.
[114] AVL FIRE M 2023 R2, AVL List, Graz, Austria 2023.

[115] Hanjalić K, Popovac M, Hadžiabdić M. A robust near-wall elliptic-relaxation eddy-viscosity turbulence model for CFD. International Journal of Heat and Fluid Flow 2004;25:1047–51. https://doi.org/10.1016/j.ijheatfluidflow.2004.07.005.
[116] Beale JC, Reitz RD. MODELING SPRAY ATOMIZATION WITH THE KELVIN-HELMHOLTZ/RAYLEIGH-TAYLOR HYBRID MODEL. AAS 1999;9. https://doi.org/10.1615/AtomizSpr.v9.i6.40.
[117] Colin O, Benkenida A. The 3-Zones Extended Coherent Flame Model (Ecfm3z) for Computing Premixed/Diffusion Combustion. Oil & Gas Science and Technology - Rev IFP 2004;59:593–609. https://doi.org/10.2516/ogst:2004043.
[118] Mancaruso E, Robbio RD, Vaglieco BM. Hydrogen/Diesel Combustion Analysis in a Single Cylinder Research Engine. SAE Int J Adv & Curr Prac in Mobility 2022;5:1312–21. https://doi.org/10.4271/2022-24-0012.
[119] Mancaruso E, Rossetti S, Vaglieco BM, Robbio RD, Maroteaux F. Optical Diagnostics to Study Hydrogen/Diesel Combustion with EGR in a Single Cylinder Research Engine. SAE Technical Paper; 2023. https://doi.org/10.4271/2023-24-0070.
[120] Rahnama P, Paykani A, Reitz RD. A numerical study of the effects of using hydrogen, reformer gas and nitrogen on combustion, emissions and load limits of a heavy duty natural gas/diesel RCCI engine. Applied Energy 2017;193:182–98. https://doi.org/10.1016/j.apenergy.2017.02.023.
[121] Mohite A, Bora BJ, Ağbulut Ü, Sharma P, Medhi BJ, Barik D. Optimization of the pilot fuel injection and engine load for an algae biodiesel - hydrogen run dual fuel diesel engine using response surface methodology. Fuel 2024;357:129841. https://doi.org/10.1016/j.fuel.2023.129841.
[122] Saravanan N, Nagarajan G. Experimental Investigation in Optimizing the Hydrogen Fuel on a Hydrogen Diesel Dual-Fuel Engine. Energy Fuels 2009;23:2646–57. https://doi.org/10.1021/ef800962k.
[123] Rinaldini C, Pisapia AM, Scrignoli F, Volza A, Emilia R, Rossetti S, et al. CFD-Driven Optimization of Diesel Injection for a Hydrogen-Diesel Dual Fuel Engine n.d.
[124] Zeldvich YB. The oxidation of nitrogen in combustion and explosions. J Acta Physicochimica 1946.
[125] Anetor L, Odetunde C, Osakue EE. Computational Analysis of the Extended Zeldovich Mechanism. Arab J Sci Eng 2014;39:8287–305. https://doi.org/10.1007/s13369-014-1398-7.
[126] Luo Q, Hu J-B, Sun B, Liu F, Wang X, Li C, et al. Experimental investigation of combustion characteristics and NOx emission of a turbocharged hydrogen internal combustion engine. International Journal of Hydrogen Energy 2019;44:5573–84. https://doi.org/10.1016/j.ijhydene.2018.08.184.
[127] Rinaldini CA, Mattarelli E, Golovitchev VI. Potential of the Miller cycle on a HSDI diesel automotive engine. Applied Energy 2013;112:102–19. https://doi.org/10.1016/j.apenergy.2013.05.056.
[128] Dittrich PA, Peter F, Huber G, Kuehn M. Thermodynamic Potentials of a Fully Variable Valve Actuation System for Passenger-Car Diesel Engines, SAE International; 2010. https://doi.org/10.4271/2010-01-1199.
[129] Schwoerer JA, Kumar K, Ruggiero B, Swanbon B. Lost-Motion VVA Systems for Enabling Next Generation Diesel Engine Efficiency and After-Treatment Optimization, Detroit, Michigan, United States: 2010, p. 2010-01–1189. https://doi.org/10.4271/2010-01-1189.
[130] Ian Alexander MAy. An experimental investigation of lean-burn dual-fuel combustiom in a heavy duty diesel engine. A thesis submitted for the degree of Doctor of Philosophy. Brunel University of London, 2018.
[131] Wróbel K, Wróbel J, Tokarz W, Lach J, Podsadni K, Czerwiński A. Hydrogen Internal Combustion Engine Vehicles: A Review. Energies 2022;15:8937. https://doi.org/10.3390/en15238937.

[132] White C, Steeper R, Lutz A. The hydrogen-fueled internal combustion engine: a technical review. International Journal of Hydrogen Energy 2006;31:1292–305. https://doi.org/10.1016/j.ijhydene.2005.12.001.
[133] Bekdemir C, Doosje E, Seykens X. H2-ICE Technology Options of the Present and the Near Future, 2022, p. 2022-01–0472. https://doi.org/10.4271/2022-01-0472.
[134] Goyal H, Jones P, Bajwa A, Parsons D, Akehurst S, Davy MH, et al. Design trends and challenges in hydrogen direct injection (H2DI) internal combustion engines – A review. International Journal of Hydrogen Energy 2024;86:1179–94. https://doi.org/10.1016/j.ijhydene.2024.08.284.
[135] Onorati A, Payri R, Vaglieco B, Agarwal A, Bae C, Bruneaux G, et al. The role of hydrogen for future internal combustion engines. International Journal of Engine Research 2022;23:529–40. https://doi.org/10.1177/14680874221081947.
[136] Pucillo F, Millo F, Piano A, Giordana S, Rapetto N, Paulicelli F. Turbocharging System Selection for a Hydrogen-Fuelled Spark-Ignition Internal Combustion Engine for Heavy-Duty Applications, SAE International; 2024. https://doi.org/10.4271/2024-01-3019.
[137] Andrisani N, Bagal N. Benefits of Supercharger Boosting on H_2 ICE for Heavy Duty Applications, Stuttgart, Germany: 2024, p. 2024-01–3006. https://doi.org/10.4271/2024-01-3006.
[138] NOMURA K. Development of a new two stroke engine with poppet-valves : Toyota S-2 Engine. IFP Int Seminar 1993 “A New Generation of Two-Stroke Engines”, 29-30 November 1993 n.d.
[139] Stokes J, Hundleby GE, Lake TH, Chiristie MJ. Development Experience of a Poppet-Valved Two-Stroke Flagship Engine. SAE Transactions 1992;101:1549–59.
[140] Sato K, Takahashi S, Nakano M, Fujita H. On the Scavenging Action of a New Type Two Stroke Cycle Engine with Scavenging and Exhaust Valves on the Cylinder Head. Journal of the MESJ 1981;16:935–44. https://doi.org/10.5988/jime1966.16.935.
[141] Nakano M, Sato K, Ukawa H. A Two-Stroke Cycle Gasoline Engine with Poppet Valves on the Cylinder Head, 1990, p. 901664. https://doi.org/10.4271/901664.
[142] Sato K, Ukawa H, Nakano M. A Two-Stroke Cycle Gasoline Engine with Poppet Valves in the Cylinder Head - Part II, 1992, p. 920780. https://doi.org/10.4271/920780.
[143] Ukawa H, Nakano M, Sato K. A Two-Stroke Cycle Engine with Poppet Valves in the Cylinder Head - Part III: An Application of Gaseous Fuel Direct Injection System, SAE International; 1993. https://doi.org/10.4271/930983.
[144] Benajes J, Novella R, De Lima D, Tribotté P, Quechon N, Obernesser P, et al. Analysis of the combustion process, pollutant emissions and efficiency of an innovative 2-stroke HSDI engine designed for automotive applications. Applied Thermal Engineering 2013;58:181–93. https://doi.org/10.1016/j.applthermaleng.2013.03.050.
[145] Benajes J, Novella R, De Lima D, Tribotté P. Analysis of combustion concepts in a newly designed two-stroke high-speed direct injection compression ignition engine. International Journal of Engine Research 2015;16:52–67. https://doi.org/10.1177/1468087414562867.
[146] Sher E. Modeling the Scavenging Process in the Two-Stroke Engine-An Overview. SAE Transactions 1989;98:648–68.
[147] Dang D, Wallace FJ. Some single zone scavenging models for two-stroke engines. International Journal of Mechanical Sciences 1992;34:595–604. https://doi.org/10.1016/0020-7403(92)90057-N.
[148] Merker GP, Gerstle M. Evaluation on Two Stroke Engines Scavenging Models. SAE Transactions 1997;106:604–27.
[149] Caprioli S, Volza A, Mattarelli E, Rinaldini CA. High Performance and Near Zero Emissions 2-Stroke H 2 Engine. SAE Technical Paper; 2023.

[150] ltd R and M. Ultralight Aircraft Market 2024-2028 - Research and Markets n.d. https://www.researchandmarkets.com/reports/5637150/ultralight-aircraft-market-2024-2028 (accessed October 26, 2025).
[151] 912 ULS / S. Rotax Aircraft Engines n.d. https://www.flyrotax.com/it/products/912-uls-s (accessed October 26, 2025).
[152] Mattarelli E, Rinaldini CA, Cantore G, Agostinelli E. Comparison between 2 and 4-Stroke Engines for a 30 kW Range Extender. SAE Int J Alt Power 2014;4:67–87. https://doi.org/10.4271/2014-32-0114.
[153] Pisapia AM, Volza A, Savioli T, Martini P, Mattarelli E. Hybrid-electric power unit for an ultralight aircraft. J Phys: Conf Ser 2023;2648:012081. https://doi.org/10.1088/1742-6596/2648/1/012081.
[154] Frosina E, Caputo C, Marinaro G, Senatore A, Pascarella C, Di Lorenzo G. Modelling of a Hybrid-Electric Light Aircraft. Energy Procedia 2017;126:1155–62. https://doi.org/10.1016/j.egypro.2017.08.315.
[155] Sistemi uncrewed applicazioni aeree, terrestri, marittime n.d. https://aeronautics.leonardo.com/it/uncrewed-systems (accessed October 26, 2025).
[156] Chemali E, Preindl M, Malysz P, Emadi A. Electrochemical and Electrostatic Energy Storage and Management Systems for Electric Drive Vehicles: State-of-the-Art Review and Future Trends. IEEE Journal of Emerging and Selected Topics in Power Electronics 2016;4:1117–34. https://doi.org/10.1109/JESTPE.2016.2566583.
[157] Caprioli S, Rinaldini C, Mattarelli E, Savioli T, Scrignoli F. Design of a Novel 2-Stroke SI Engine for Hybrid Light Aircraft, Live Online, Pennsylvania, United States: 2021, p. 2021-01–1179. https://doi.org/10.4271/2021-01-1179.
[158] Rinaldini CA, Breda S, Fontanesi S, Savioli T. Two-Stage Turbocharging for the Downsizing of SI V-Engines. Energy Procedia 2015;81:715–22. https://doi.org/10.1016/j.egypro.2015.12.077.
[159] Mattarelli E, Caprioli S, Rinaldini CA, Scrignoli F, Sparaco D, Caso P. Numerical optimization of supercharging and combustion on a two-stroke compression ignition aircraft engine. International Journal of Engine Research 2023;24:2352–68. https://doi.org/10.1177/14680874221118174.
[160] Engine Combustion Network – Engine Combustion Network n.d. https://ecn.sandia.gov/ (accessed October 27, 2025).
[161] Alberto Caputo. Progettazione e analisi CFD 3D di un motore 2 tempi per velivoli a pilotaggio remoto. Master Thesis. Modena and Reggio Emilia University, 2025.
[162] Creo Parametric cad (student edition) n.d.
[163] Millo F, Piano A, Peiretti Paradisi B, Marzano MR, Bianco A, Pesce FC. Development and Assessment of an Integrated 1D-3D CFD Codes Coupling Methodology for Diesel Engine Combustion Simulation and Optimization. Energies 2020;13:1612. https://doi.org/10.3390/en13071612.
[164] Mattarelli E, Cantore G, Rinaldini CA, Savioli T. Combustion System Development of an Opposed Piston 2-Stroke Diesel Engine. Energy Procedia 2017;126:1003–10. https://doi.org/10.1016/j.egypro.2017.08.268.
[165] Mattarelli E, Rinaldini C, Savioli T. Port Design Criteria for 2-Stroke Loop Scavenged Engines. 2016. https://doi.org/10.4271/2016-01-0610.
[166] Aria, climatici C. Efficiency and decarbonization indicators for total energy consumption and power sector. Comparison among Italy and the biggest European countries. ISPRA Istituto Superiore per la Protezione e la Ricerca Ambientale n.d. https://www.isprambiente.gov.it/it/pubblicazioni/rapporti/efficiency-and-decarbonization-indicators-for-total-energy-consumption-and-power-sector (accessed October 27, 2025).
[167] Reddy TB, Linden D, editors. Linden's handbook of batteries. 4. ed. New York, N.Y: McGraw-Hill; 2011.

[168] Gimeno J, Bracho G, Martí-Aldaraví P, Peraza JE. Experimental study of the injection conditions influence over n-dodecane and diesel sprays with two ECN single-hole nozzles. Part I: Inert atmosphere. Energy Conversion and Management 2016;126:1146–56. https://doi.org/10.1016/j.enconman.2016.07.077.
[169] Som S, Longman DE, Luo Z, Plomer M, Lu T. Three Dimensional Simulations of Diesel Sprays Using n-Dodecane as a Surrogate n.d.
[170] Marco CAD, Mattarelli E, Paltrinieri F, Rinaldini CA. A New Combustion System for 2-Stroke HSDI Diesel Engines. SAE Technical Paper; 2007. https://doi.org/10.4271/2007-01-1255.

Appendix A: diesel spray Model Calibration

Overview

In order to ensure the reliability of the CFD simulations performed for the development of the 2S Diesel engine described in Chapter 7, a dedicated spray model calibration was carried out. This activity, developed within a Master's thesis under the supervision of the author, was aimed at reproducing the experimental behaviour of a Diesel spray under controlled conditions, using detailed numerical modelling and state-of-the-art physical sub-models for atomization, evaporation, and wall interaction.

The calibration process was based on the Engine Combustion Network (ECN) experimental data, specifically the "Spray A" configuration made available by the Sandia National Laboratories, which constitutes the international benchmark for Diesel injection model validation.

The goal of this activity was to achieve a numerical model capable of accurately reproducing the liquid and vapor penetration lengths, spray cone angle, and Sauter Mean Diameter (SMD) under conditions representative of low-pressure Diesel injection (≈500 bar), typical of small 2S engines for UAV and ultralight aircraft applications.

Physical sub-models and calibration targets

The predictive accuracy of any CFD simulation of Diesel injection strongly depends on the calibration of its constitutive sub-models. For this purpose, the following models were implemented and tuned:

Phenomenon	Sub-model	Purpose and calibration strategy
Secondary break-up	KH–RT (Kelvin–Helmholtz / Rayleigh–Taylor)	Governs droplet disintegration due to aerodynamic instabilities. Constants C_1–C_8 were tuned to reproduce the temporal evolution of the liquid penetration.
Droplet evaporation	Abramzon–Sirignano	Describes heat and mass transfer between liquid fuel and gas. The heat transfer and diffusion coefficients were calibrated to match vapor-phase penetration.
Aerodynamic drag	Shiller–Naumann	Defines the drag coefficient as a function of droplet Reynolds number; used without modification.
Wall interaction	Wall impingement model	Models droplet–wall interactions, including rebound and film formation. Coefficients were tuned to match the observed spray morphology near walls.
Initial conditions	Injection cone angle and SMD distribution	Calibrated to reproduce the experimental spray cone opening and droplet size evolution measured at Sandia.

The overall calibration strategy aimed to obtain quantitative agreement between simulation and experiment in terms of both spray penetration and phase transition dynamics, while maintaining realistic computational stability for later engine simulations.

Experimental reference: ECN “Spray A”

The ECN “Spray A” dataset provides detailed information on both the injector and the ambient thermodynamic conditions, allowing direct numerical replication.

Injector geometry

The experiments employed a Bosch second-generation single-hole mini-sac injector, representative of modern Diesel technology. The nozzle and orifice geometry are summarized in Table A.1.

Table A.1: Injector geometrical properties.

Parameter	Value
Nozzle type	Mini-sac (sac volume = 0.2 mm³)
Orifice diameter	0.0894 mm
L/D ratio	1.3
Discharge coefficient C_D	0.9
Surface finishing	Hydro-eroded, convergent (Bosch KS1.5/86)

Injection and ambient conditions

The injection and ambient parameters adopted in the calibration are summarized in Table A.2, corresponding to the standard ECN “Spray A” configuration.

Table A.2: injection and ambient parameters adopted in the calibration.

Parameter	Value
Injection pressure	500 bar
Fuel temperature	363 K
Fuel density	713 kg/m³
Ambient temperature	900 K
Ambient pressure	60 bar

These conditions are representative of pre-vaporized, high-temperature environments, analogous to those in the combustion chamber of the designed 2S Diesel engine.

Vessel geometry and numerical domain

The experiments were conducted in a pressurized combustion vessel designed for optical diagnostics of sprays. The vessel has a cubic geometry (108 mm side length) with optical access windows (Ø 105 mm) on each face, ensuring uniform illumination and image capture of the spray front.

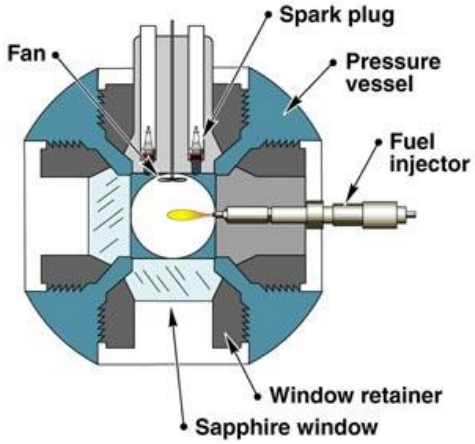

Figure A.1: schematic view of the vessel

Numerical model and physical sub-models details

The spray simulations were performed using AVL FIRE, following the methodologies outlined in [168,169]. The model allowed detailed CFD analyses of the injection, atomization, and vaporization processes under conditions representative of the ECN "Spray A" experiments.

Computational domain and mesh

The combustion vessel was reproduced in the CFD environment as a 108 mm cubic chamber, in accordance with the experimental configuration described by Sandia National Laboratories. A polyhedral mesh was generated with a base cell size of 8 mm, which provided a good compromise between computational efficiency and accuracy. To resolve the local phenomena associated with liquid jet breakup and vaporization, two levels of local refinement were applied in the injection region:

- Fine refinement: 0.2 mm cells located immediately downstream of the nozzle orifice, where the fuel jet is injected in liquid form;
- Extended refinement: 0.6 mm cells covering the surrounding region where the fuel–air mixing and evaporation occur.

The resulting computational grid consisted of approximately 230,000 control volumes, ensuring sufficient spatial resolution to capture the main flow and spray features without excessive computational cost. The same setup was used for the spry simulation. Figure A.1 shows a section of the vessel mesh, with the refined regions clearly visible near the injector.

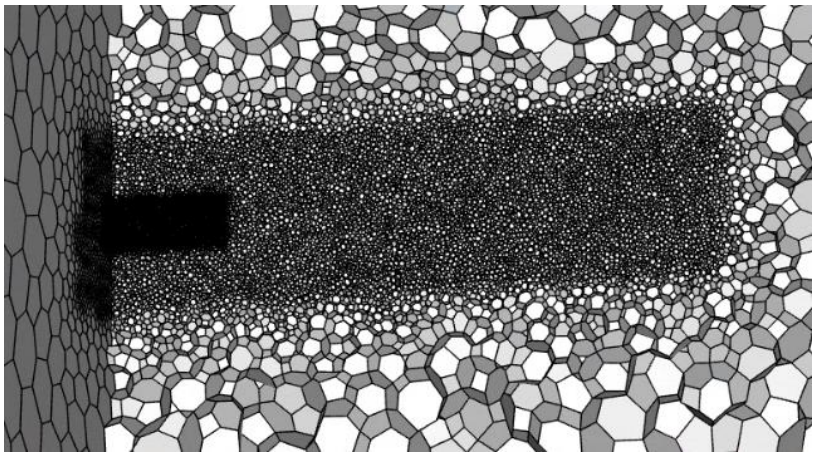

Figure A.2: Sectional view of the CFD mesh showing local refinement in the injection zone.

Aerodynamic drag model (Shiller–Naumann)

The aerodynamic drag acting on each droplet is described by the Shiller–Naumann correlation, which defines the drag coefficient as a function of the droplet Reynolds number:

$$C_D = \frac{24}{Re}(1 + 0.15\,Re^{0.687})$$

where the Reynolds number is expressed as:

$$Re = \frac{\rho_{gas}\ |\ u_{gas} - u_{drop}\ |\ d_{drop}}{\mu_{gas}}$$

This model ensures a smooth transition from the Stokes regime (for small droplets and low Re) to the fully turbulent drag regime typical of Diesel sprays.

Evaporation model (Abramzon–Sirignano)

The Abramzon–Sirignano model was adopted to describe droplet evaporation. This approach is based on the film theory, in which heat and mass transfer resistances are represented by thin gas films of constant thickness (δ_T and δ_m). These layers are corrected by factors $F_T$and F_M, accounting for Stefan flow effects. The mass and heat transfer rates are expressed as:

$$\dot{m} = \bar{\rho}_g \, \bar{\beta}_g \, D_d \, Sh^* \ln(1 + B_Y)$$

$$\dot{Q} = \pi \, \frac{\bar{k}_g}{\bar{c}_p F_T} \, D_d \, Nu^* \ln(1 + B_T)$$

where the overbars denote properties evaluated at film conditions. The modified Nusselt (Nu^*) and Sherwood (Sh^*) numbers are calculated as:

$$Nu^* = 2 + \frac{Nu_0 - 2}{F_T}, \text{with} Nu_0 = 2 + 0.552 \, Re^{1/2} \, Pr^{1/3}$$

$$Sh^* = 2 + \frac{Sh_0 - 2}{F_M}, \text{with} Sh_0 = 2 + 0.552 \, Re^{1/2} \, Sc^{1/3}$$

This formulation captures the coupled effects of convection and diffusion around each evaporating droplet, ensuring an accurate prediction of the vapor penetration length.

Break-up model (KH–RT)

The Kelvin–Helmholtz – Rayleigh–Taylor (KH–RT) model describes the disintegration of liquid jets and droplets under aerodynamic and inertial instabilities. The model combines two mechanisms:

- KH instability, driven by shear forces between the liquid jet and the surrounding gas;
- RT instability, caused by the deceleration of dense droplets in a lighter surrounding medium.

The breakup length $L$for KH-dominated regions is expressed as:

$$L = C_3 \sqrt{\frac{\rho_d}{\rho_c}} \, d_0$$

where $C_3$is a calibration constant, $d_0$the initial droplet diameter, and ρ_d, $\rho_c$the densities of the droplet and the gas. Within this length, only KH breakup is active, while downstream both KH and RT mechanisms coexist.

The characteristic wavelength Λ and breakup time $\tau_a$for KH instabilities are defined as:

$$R_a = C_1 \, \Lambda, \tau_a = \frac{3.7 \, C_2 \, R}{\Lambda \, \Omega}$$

RT instabilities are characterized by the frequency of growth $\Omega_t$and wavenumber K_t:

$$\Omega_t = \sqrt{\frac{2}{3\sqrt{3}\sigma}\frac{g_t \mid \rho_d - \rho_c \mid^{1.5}}{\rho_d + \rho_c}}, K_t = \sqrt{\frac{g_t \mid \rho_d - \rho_c \mid}{3\sigma}}$$

$$\tau_t = \frac{C_5}{\Omega_t}, \Lambda_t = \frac{C_4\pi}{K_t}$$

The velocity component normal to the droplet surface assigned to the child parcels is calculated from the wavelength and growth rate of the perturbations:

$$u_{norm} = C_8\,\Lambda\,\Omega$$

All constants ($C_1, C_2, C_3, C_4, C_5, C_8$) were adjusted iteratively to ensure the correct liquid breakup timing and penetration evolution.

Wall impingement model

The wall impingement model accounts for the interaction between droplets and the chamber walls. Given the absence of valves and the specific scavenge geometry of two-stroke engines, droplet–wall interactions are frequent and can significantly influence fuel–air mixing and HC/soot emissions. The model distinguishes among rebound, splash, and film formation, based on the Weber number (We) and impact angle, with coefficients tuned to match experimental spray morphology.

Calibration and simulation results

Following an extensive tuning of the main spray sub-model parameters, including break-up, evaporation, wall impingement, and droplet coalescence. the simulation results showed excellent agreement with the experimental evidence. As illustrated in the following figures, the CFD-predicted temporal evolution of both the liquid and vapor spray phases closely reproduces the experimental trends obtained in the ECN “Spray A” dataset. The predicted liquid and vapor penetration lengths are in good agreement with the corresponding measurements, confirming the correct representation of the atomization and vaporization dynamics.

In addition to penetration characteristics, other key parameters, such as the spray cone angle, the Sauter Mean Diameter (SMD) of the droplets, and the overall jet morphology, were accurately reproduced. These results demonstrate that the calibrated model captures not only the quantitative evolution of the spray but also its qualitative structure and symmetry, as shown in Figure A.4.

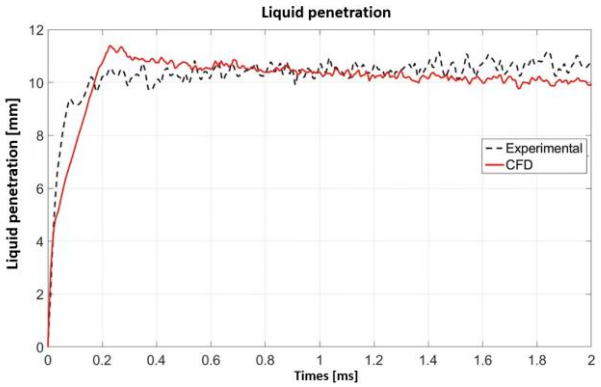

Figure A.3: Comparison of liquid penetration length: CFD vs. ECN data.

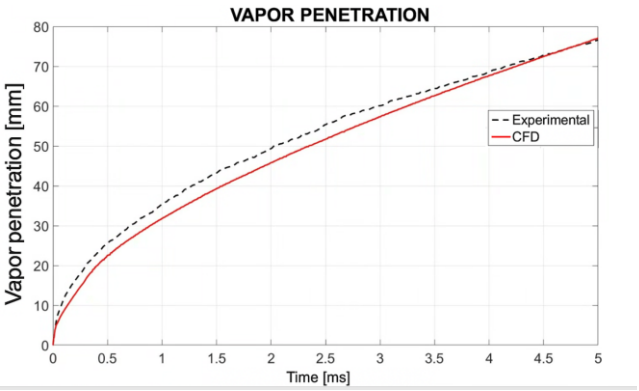

Figure A.4: Comparison of vapor penetration length: CFD vs. ECN data.

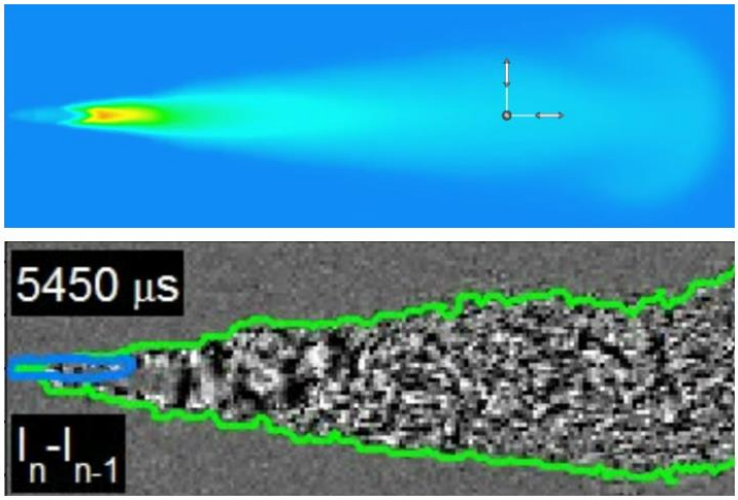

Figure A4: Comparison of spray morphology between CFD prediction and experimental visualization.

The comparison between simulation and experimental data confirms the reliability and predictive capability of the developed numerical framework. The calibrated model can therefore be confidently employed in subsequent combustion chamber simulations, where it ensures a physically consistent representation of air–fuel mixture formation, which is critical for accurate predictions of ignition behaviour, heat release rate, and pollutant emissions.

Appendix B: Combustion chamber optimization

Overview

The combustion performance of small 2S Diesel engines is highly sensitive to the shape of the combustion chamber, which governs air–fuel mixing, turbulence intensity, and flame propagation. This appendix summarizes the CFD-based optimization process performed to identify the most effective chamber geometry for the engine presented in Chapter 7. The activity, carried out within a master's thesis under the supervision of the author, consisted of three progressive stages of analysis, involving different chamber shapes:

1. Truncated-cone 1;
2. Truncated-cone 2;
3. Bowl-shaped head cavity (final optimized design).

Each configuration was evaluated in terms of pressure evolution, HRR, and combustion efficiency, allowing a quantitative comparison of performance indicators.

Numerical setup

The simulations were conducted using the same computational framework adopted for the spray studies (AVL FIRE). The initial mesh, corresponding to the truncated-cone geometry, was previously validated in the sensitivity analyses. Preliminary runs were performed to determine the optimal SOI timing and injection duration, with the aim of respecting the maximum injection-pressure constraint of 250 bar and achieving an efficient trade-off between atomization quality and mechanical stress. This pressure is also sufficiently close to the one saw in appendix 1. For this reason, the same injection setup was adopted.

The instantaneous mass-flow rate through the injector orifices is described by:

$$\dot{m} = n_f \, \rho_f \, A_{eff} \, v \quad \text{with} \quad v = \sqrt{\frac{2 \, \Delta p}{\rho_f}}$$

Combining the two expressions yields:

$$\dot{m} = n_f \, A_{eff} \sqrt{2 \, \rho_f \, \Delta p}$$

The injected-mass flow rate can also be expressed as:

$$\dot{m} = \frac{m_f}{\Delta t} = \frac{m_f \, \omega}{\Delta \theta} \, \frac{180}{\pi}$$

From these relationships, the injection pressure differential can be derived as:

$$\Delta p = \left(\frac{m_f \, \omega}{\Delta \theta \, n_f \, A_{eff}} \, \frac{180}{\pi} \right)^2 \, \frac{1}{2 \, \rho_f}$$

These equations were used to size the injector effective area and to define the mass-flow law adopted in the simulations.

3D-CFD combustion chamber geometry optimization results

Preliminary analysis with truncated-cone 1 geometry

The first combustion simulations employed the truncated-cone 1 chamber Figure A.5 shows the in-cylinder pressure profiles for four injection timings.

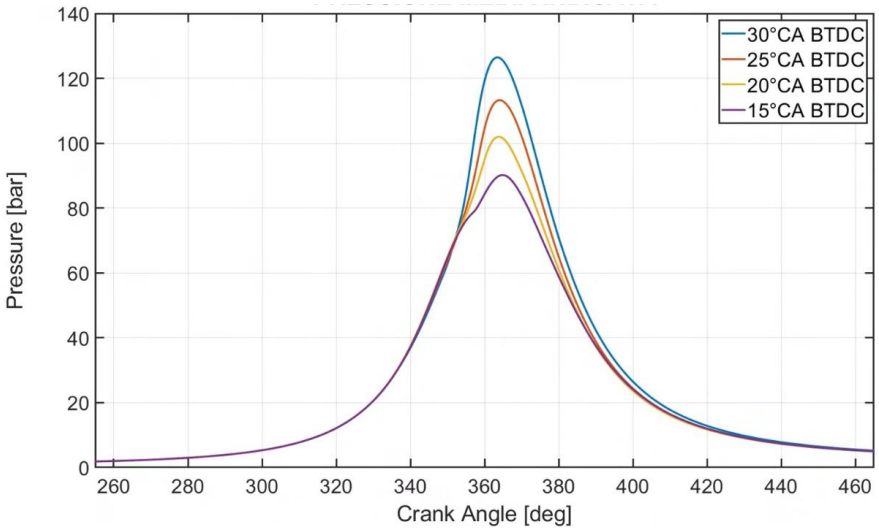

Figure A.5: In-cylinder pressure traces for different injection timigns

The analysis indicated that the optimal SOI occurs between 340° and 345° CA, i.e. 15–20° BTDC. Earlier injection timings caused an excessive increase in peak pressure, confirmed by the Peak PPRR exceeding 5 bar/°CA, leading to overly rapid combustion and potential mechanical stress on engine components.

Spatial distributions of oxygen mass fraction for the truncated-cone 1 case are reported in Figure A.6 for several crank-angle positions.

The results reveal a non-uniform mixture distribution inside the chamber. Fuel tends to accumulate in the central zone, with limited penetration toward peripheral regions where excess oxygen remains unreacted. This behaviour is attributed to the insufficient turbulence and poor air recirculation promoted by the conical shape, which hinders mixture homogenization. As a result, a portion of the injected fuel does not actively participate in combustion, reducing thermal efficiency and increasing unburned hydrocarbons.

Figure A.6: In cylinder oxygen mass fraction distribution for the truncated-cone 1 solution

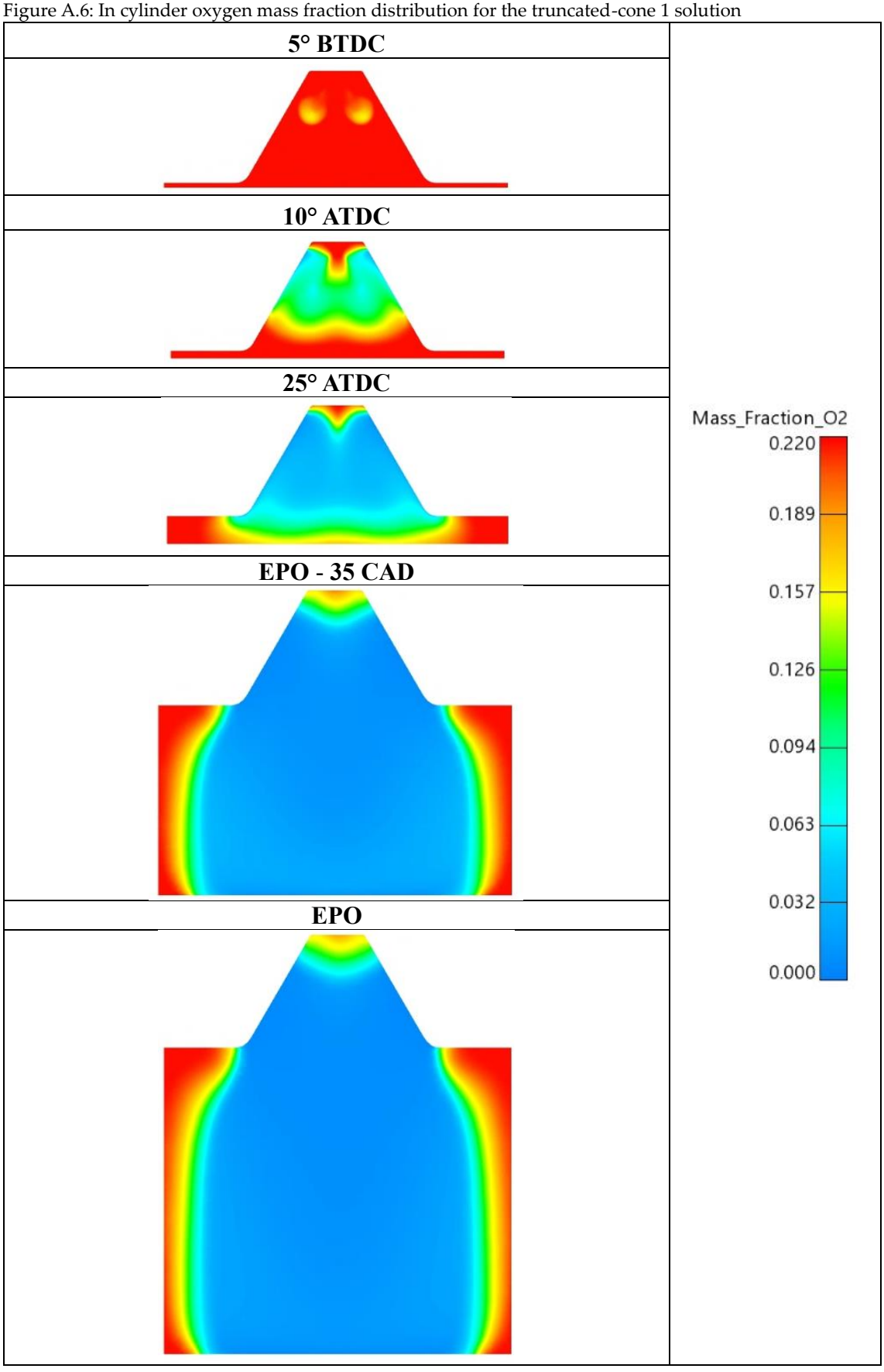

Modified truncated-cone 2 geometry

To improve mixture formation, a second geometry was designed, maintaining the conical concept but featuring a larger base diameter and reduced height (Figure A.7).

Figure A.7: Modified truncate-cone 2 geometry picture.

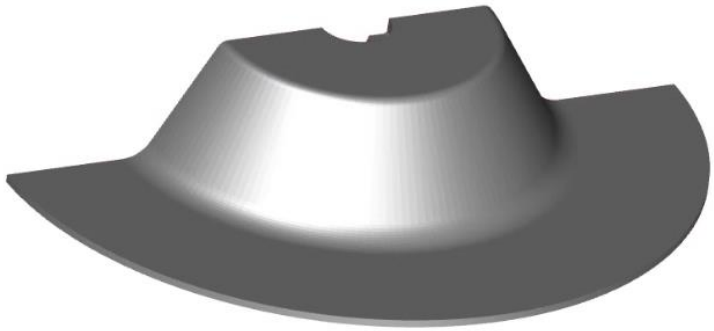

CFD simulations on this configuration, summarized in Figure A.8, show improved fuel–air mixing and more uniform oxygen distribution compared with the previous case.

The larger base promotes radial flow and stronger interaction between the jet and the surrounding air, leading to higher combustion efficiency. Nevertheless, high-oxygen pockets persist near the chamber periphery, indicating that part of the charge remains unutilized. Thus, while performance improved, the overall mixing process was still incomplete.

Figure A.8: In-cylinder oxygen distribution for the truncated-cone 2 geometry.

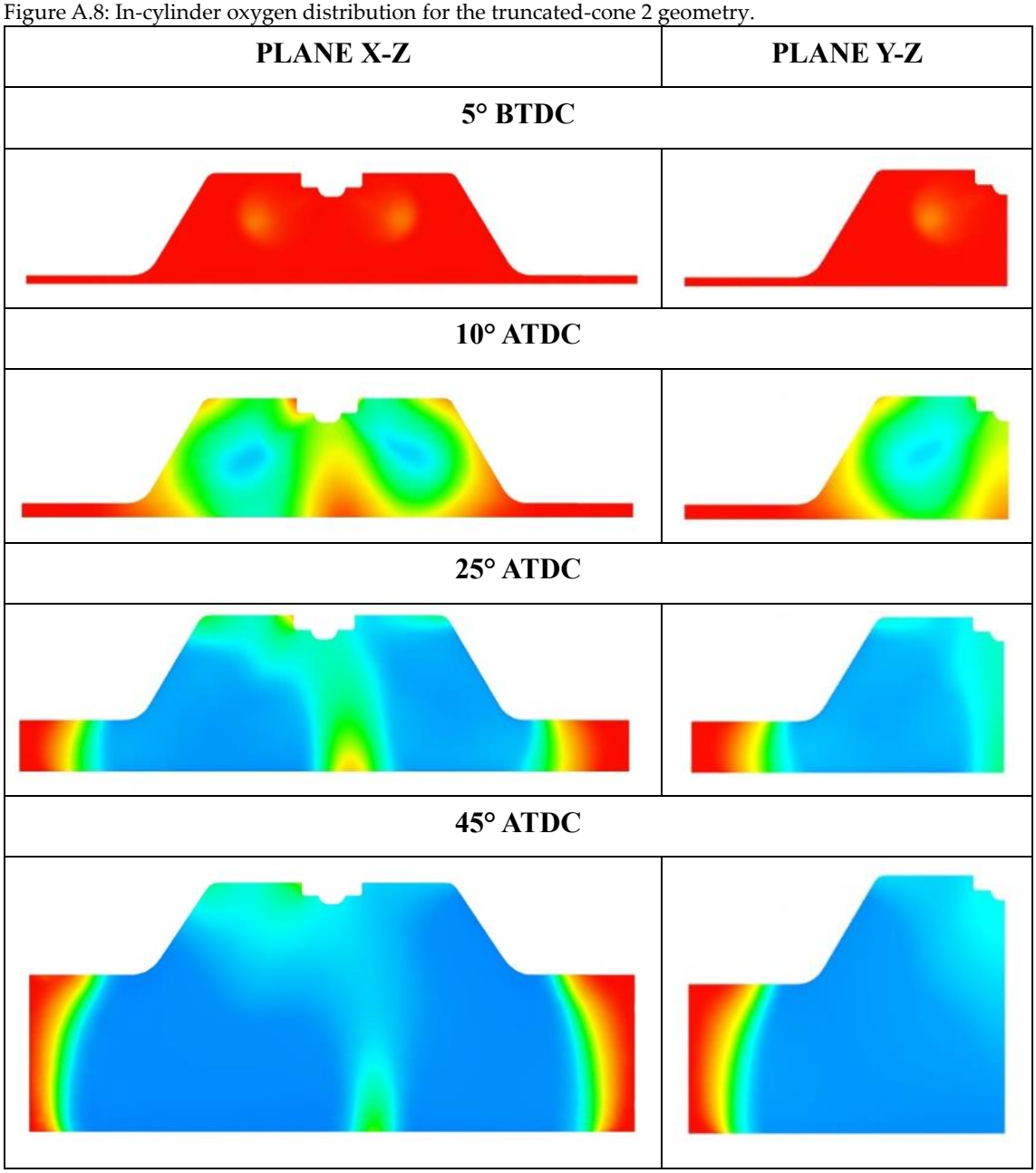

Bowl-shaped geometry (final configuration)

Based on the findings above and on literature guidelines [170], a bowl-shaped combustion chamber was developed (Figure A.9). The new cavity, machined into the cylinder head, was designed to intensify turbulence during the compression stroke and to promote a strong squish flow toward the chamber centre.

Figure A.9: Final bowl shape configuration.

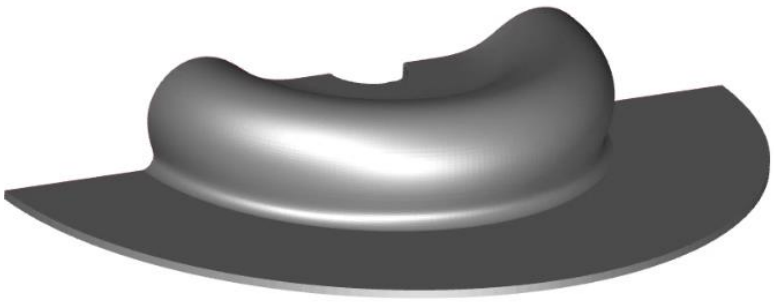

The results for the bowl mesh are reported in Figure A.10 for different crank-angle positions.

The CFD results show a marked improvement in combustion uniformity compared with the previous configurations. The oxygen field exhibits a more homogeneous distribution, with significantly fewer fuel-rich central zones. Residual oxygen concentrations near the lateral walls indicate that the majority of the air participates effectively in combustion while maintaining flame symmetry.

Figure A.10: Oxygen mass fraction fields, final bowl geometry, planes XZ and YZ.

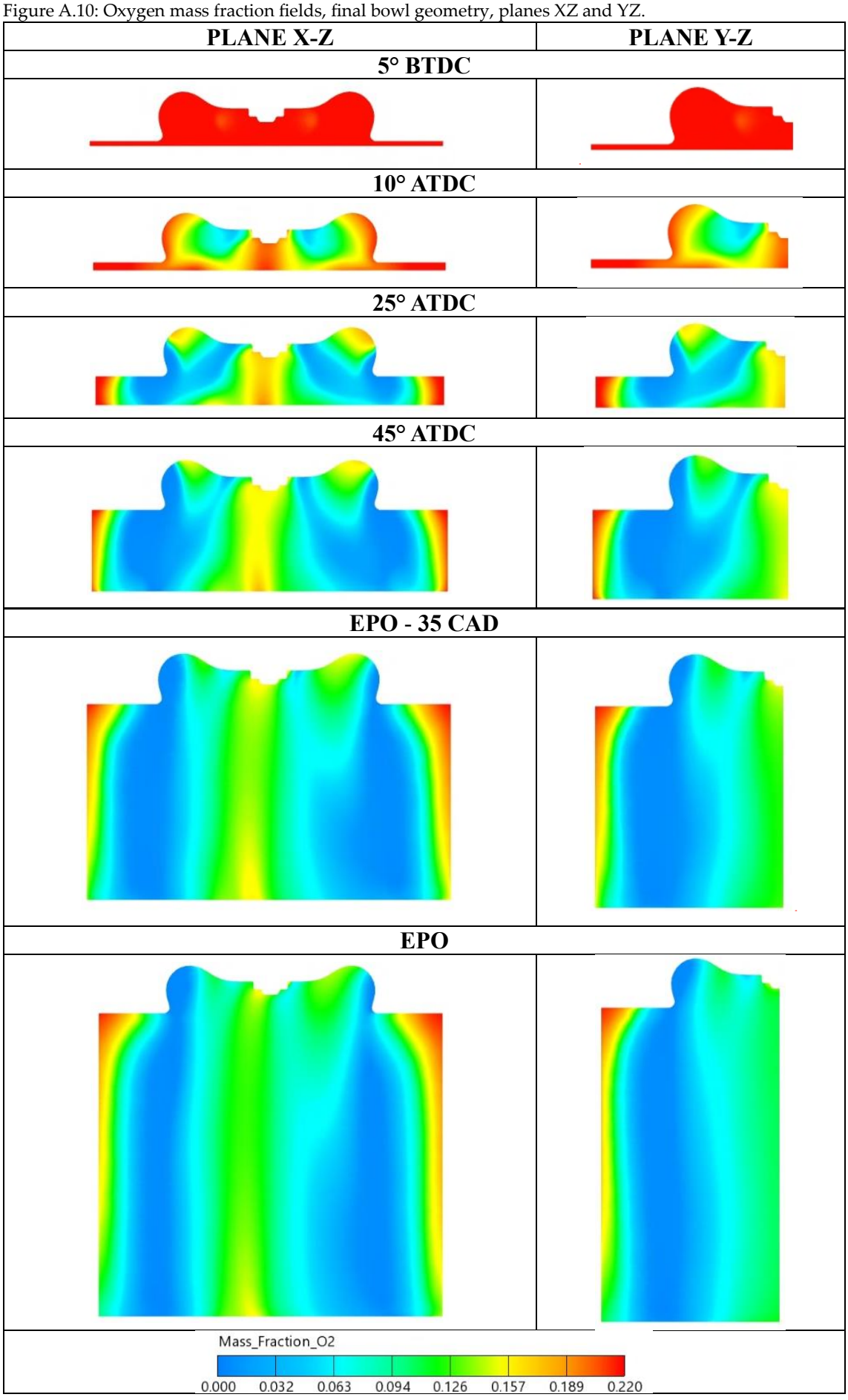

Comparative assessment of the three geometries

A comprehensive comparison among the three chamber configurations is reported in Figures A.11–A.13 and in Table A.3, considering indicated pressure, AHRR, and accumulated heat release (AHR).

Figure A.11: Mean-pressure comparison for the three chamber geometries.

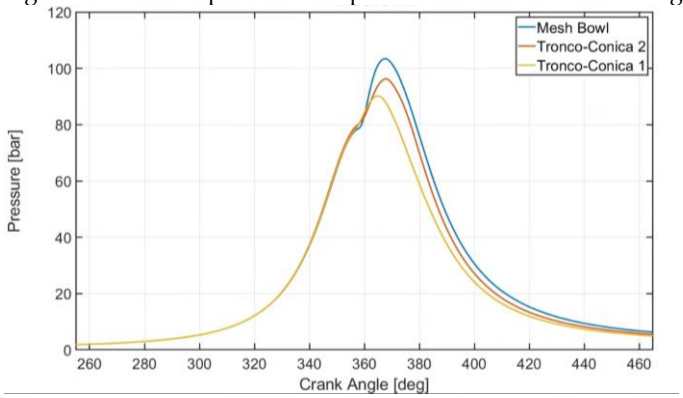

Figure A.11: HRR comparison for the three chamber geometries.

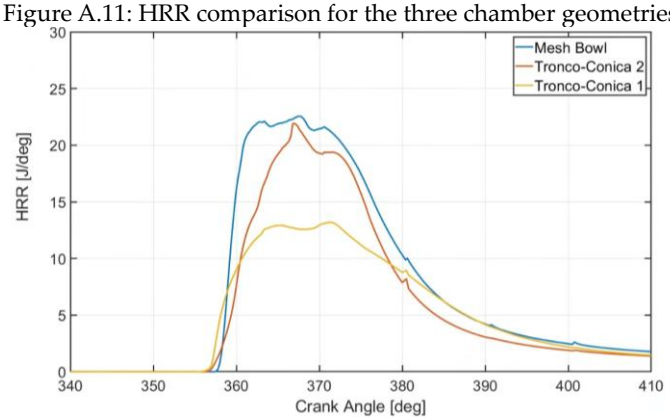

Figure A.11: AHR comparison for the three chamber geometries.

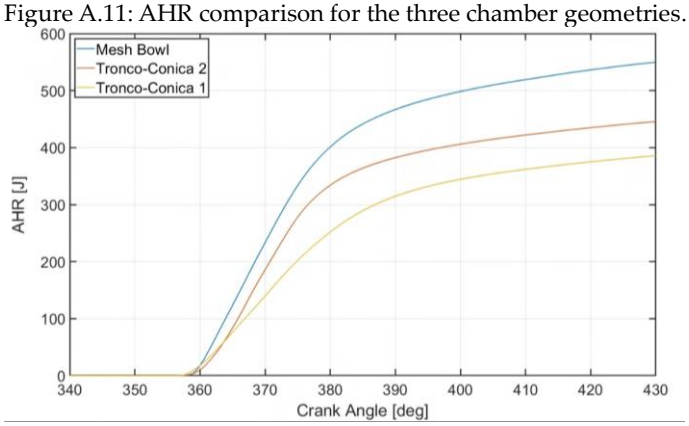

Table A.3: Summary of combustion performance for the three geometries.

Combustion chamber geometry	Comb. Efficiency	IMEP	FMEP	BMEP	Power	PPRR	BSFC
	[-]	[bar]	[bar]	[bar]	[kW]	[bar/°CA]	[g/kWh]
Truncated-cone 1	0.75	5.67	0.864	4.80	37.99	3.00	403.1
Truncated-cone 2	0.85	7.29	0.879	6.41	50.68	3.03	302.2
Omega Bowl	0.97	8.97	0.897	8.07	63.82	4.54	239.0

The results confirm the trends observed in the visual analyses showed before:

- The bowl chamber provides the highest combustion efficiency ($\eta \approx 0.97$), maximum IMEP, and lowest BSFC;
- The modified truncated-cone shows intermediate behaviour;
- The original conical design exhibits the poorest mixing and lowest efficiency.

The slightly higher PPRR observed in the bowl configuration remains within acceptable limits and reflects a faster, more complete combustion process.

Optimization discussion and conclusions

The optimization campaign clearly demonstrates the dominant influence of combustion-chamber geometry on the overall efficiency of small 2S Diesel engines. Transitioning from the initial truncated-cone design to the final omega-shaped configuration resulted in:

- A 22% increase in IMEP,
- A 36% increase in brake power,
- A 41% reduction in BSFC, and
- A marked improvement in mixture uniformity and flame propagation.

These results confirm that the omega geometry ensures a better interaction between the fuel jets and the in-cylinder air motion, promoting complete combustion and reduced unburned hydrocarbons.